Synthesis and controlled non-destructive covalent functionalization of low-dimensional carbon nanomaterials

DISSERTATION

zur Erlangung des akademischen Grades des Doktors der Naturwissenschaften (Dr. rer. nat.)

vorgelegt von

Abbas Faghani

aus Gorgan, Iran

Institut für Organische Chemie

Fachbereich Biologie, Chemie, Pharmazie

Freie Universität Berlin

August 2019

Declaration of honesty

I hereby announce and confirm this PhD thesis is completely the outcome of my own work and that no other sources than those cited have been used. All annotations, which have been used from published or unpublished sources, are identified as such. The shown illustrations have been created by myself or have been marked with the corresponding references.

Abbas Faghani

This PhD thesis was conducted within the research groups of Prof. Dr. Rainer Haag and Prof. Dr. Mohsen Adeli from **October 2015** to **August 2019** at the Institute of Chemistry and Biochemistry of the Freie Universität Berlin.

1. Reviewer: Prof. Dr. Rainer Haag, Freie Universität Berlin

2. Reviewer: Prof. Dr. Mohsen Adeli, Freie Universität Berlin

Date of Defense:
13.09.2019

Acknowledgments

Performing a PhD and writing a doctoral dissertation is not a stand-alone thing and needs the cooperation of a lot people. From the scientific and project-related point of view I would like to begin my acknowledgments: first and foremost, I would like to thank **Prof. Dr. Rainer Haag** for giving me the opportunity to work on the fascinating and challenging topic of two-dimensional carbon-based materials in his multinational group. Therefore, I sincerely thank the endless support I received from him during my work. What I am most thankful is the great freedom and independence I was given for four years, which resulted in learning the critical importance of diplomacy and communication in academia and science. I would like to express my gratitude to **Prof. Dr. Mohsen Adeli** for invaluable scientific discussion, sharing his inputs and clever ideas. I received his careful attention to experimental details and publications. It's time to mention that without his endless supervision of my master and PhD programs, I would not be where I am now. I am very grateful to **Prof. Dr. Arne Thomas** for providing access to his facilities and very helpful scientific discussion over the projects, and the generous help of his group members **Dr. Matthias Trunk**, **Dr. Pradip Pachfule**, and **Sarah Vogl**. I also would like to thank **Prof. Dr. A. Dieter Schlüter** for the great hospitality and meticulous discussions during my research stay in ETH university of Zürich as well as **Dr. Marco Servalli**. Special thanks to **Prof. Dr. Jürgen P. Rabe** for his uncountable support for providing access to SFM and other microscopies and also thanks to his PhD student who is one of my best friends **Mohammad Fardin Gholami** for really nice discussions over the results and writing papers. Many thanks go to **Prof. Dr. Stephanie Reich**, **Dr. Antonio Setaro**, and **Sabrina Jürgensen** for their performance on photoluminescence, Raman studies, and discussions on the results. I sincerely thank **Dr. Wolfgang E. S. Unger** and **Ievgen S. Donskyi** for their expertise in x-ray photoelectron spectroscopy and discussing the results. I am grateful to **Prof. Dr. Beate Paulus** and **Jingjing Shao** for their generous help with DFT simulations on 2D structure. The access to selected area electron diffraction and scanning electron microscopy set up provided by **Prof. Christoph T. Koch** and **Johannes Müller** are greatly appreciated. I would like to thank **Dr. Raul Arenal** for atomic level analyses of my materials using high-resolution transmission electron microscopy and sharing his knowledge about the projects. Each year around August, the members of Haag's group have their scientific trip where we learn and discuss a lot our projects. Hereby, I would like to thank to all the former and present members for the fantastic atmosphere. I sincerely thank, **Dr. Monika Wyszogrodzka**, **Dr. Christoph Schlaich**, **Dr. Sabine Reimann**, **Dr. Shalini Kumari**, **Dr. Manoj Kumar Muthyala**, **Dr. Priyanka Manchanda**, **Dr. Abhishek Kumar Singh**, **Dr. Olaf Wagner**, and **Mohammad Suman**

Chowdhury for all scientific discussions during our daily lab work. I am also thankful to **Dr. Pamela Winchester** and **Guy Guday** for language polishing my thesis and publications. Finally, I would like to thank **Dr. Wiebke Fischer** for taking care of all organizational and administrative matters. I cannot forget my first presentation, where we had fun debating to convince each other, which however, I believe I was right. I really thankful to our former and present secretaries, **Jutta Hass** and **Eike Ziegler**, for being always responsible and supportive. In addition, further thanks go to my other colleagues and the welcome club members **Dr. Katharina Huth** for having great discussions on the carbon nanotube project, **Dr. Nadine Rades**, **Svenja Ehrmann**, and **Isabelle Heing-Becker**, for being helpful when I started my PhD in Germany. I would like to acknowledge **Dr. Katharina Achazi** for introducing the biolab safety and our technicians, **Anja Stöshel**, **Cathleen Schlesener**, **Andrea Schulz**, **Katharina Goltsche**, and **Marleen Selent**, for their support. PhD is the stressful time life and I was not only in the lab; I want therefore to acknowledge all the people that were involved in my social life and supported me; I am sure I will forget some names. Spending the past four years in Berlin would have been impossible without the attentive presence of **Dr. Fatemeh Zabihi**, **Dr. Mazdak Asadian Birjand**, **Dr. Ehsan Mohammadifar**, **Dr. Zahra Beiranvand**, **Dr. Mahdieh Kalantari**, **Dr. Shabnam Hemmati-Sadeghi**, **Leila Amini**, **Davood Alizadeh Sanati**, **Vahid Ahmadi Soureshjani**, **Saman Salimi**, and **Paria Pouyan**. I would like to express my deepest gratitude to my esteemed friends **Marzieh Rabbani** and **Sharareh Hemmati-Sadeghi** for their care and support, I wish them both the best of the best in the world! I had memorable moments with you guys, I will never forget the great times, parties and after-parties we had.

Last but not least, I would like to mention my deepest gratitude to my family members for all their encouragement. I would like to acknowledge with words of love for my dearest mom **Shahrbano Mazraie** for her endless love during all these years. In the end, I would like to close the acknowledgments in memory of my compassionate dad **Taqi Faghani**, who is not among us, but I am sure he sees me from somewhere. I have never forgotten the time he spent to drag my attention to the magazine named “Etelaat haftegi” when I was kid and I wish God bless him.

Table of contents

List of abbreviations

3D	three dimensional
2D	two dimensional
2DPs	two-dimensional polymers
1D	one dimensional
CNTs	carbon nanotubes
TPa	terapascal
SWNTs	single-wall nanotubes
GPa	gigapascal
W	watt
FO	frontier orbital
HOMO	highest occupied molecular orbital
LUMO	lowest unoccupied molecular orbital
TRGO	thermally reduced graphene oxide
hPG	hyperbranched polyglycerol
UV-Vis	ultraviolet/visible
PTAD	4-phenyl-1,2,4-triazoline-3,5-dione
Ppy	polypyrrole
GNPs	gold nanoparticles
HRP	horseradish peroxidase
IgG	immunoglobulin G
MDR	multidrug resistance
DNA	deoxyribonucleic acid
MDa	megadalton
TaS_2	tantal(IV)-sulfide
WS_2	tungsten disulfide
$NbSe_2$	niobium diselenide
$MoSe_2$	molybdenum diselenide
MoS_2	molybdenum disulfide
CVD	chemical vapor deposition
COFs	covalent organic frameworks
2D-MOF	two-dimensional metal organic framework
STM	scanning tunneling microscopy

SC	single crystal
HRTEM	high resolution transmission electron microscopy
BHT	benzenehexathiol
CP	coordination polymer
CTFs	covalent triazine frameworks
COPs	covalent organic polymers
POFs/POPs	porous organic frameworks/polymers
TPOP	triazine-functionalized porphyrin
AFM	atomic force microscopy
TEM	transmission electron microscopy
PXRD	powder X-ray diffraction
SAED	selected area electron diffraction
PLE	photoluminescence excitation
NMR	nuclear magnetic resonance
NEXAFS	near edge X-ray absorption fine structure
XPS	x-ray photoelectron spectroscopy
EELS	electron energy loss spectroscopy
GO	graphene oxide
rGO	reduced graphene oxide
Cryo-TEM	cryogenic electron microscopy
ATR-IR	attenuated total reflection infrared
E. coli	escherichia coli

1 Introduction

Carbon nanomaterials have attracted much interest both from a fundamental point of view and for future applications due to their unique physicochemical properties.[1, 2] Carbon nanostructures are comprised of a broad range of carbon lattices with different geometries including one-, two-, or three-dimensional (3D) morphologies. In the past few decades, many carbon nanostructures including nanodiamonds, fullerene, carbon nanotubes (CNTs), graphene,[3] and other two-dimensional (2D) analogs such as graphenylene,[4-6] penta-graphene,[7-9] twin graphene,[10] graphyne,[4, 11-13] phagraphene,[14-16] and biphenylene[8, 17, 18] have been synthesized or theoretically proposed and investigated. The strong correlation between chemical structure, lattice, topography, and size of these nanostructures provides an excellent opportunity to explore many new properties and phenomena. Accordingly, many new nanodevices with extraordinary properties for a broad range of applications including electronic, composite, energy storage, and drug delivery have been constructed and successfully used[19-21] to overcome unsolved problems and challenges.[1] Consequently, carbon nanostructures and their properties can be tuned by performing chemical reactions on their lattice. This strategy diversifies carbon nanostructures in new subclasses and results in new materials with more specific properties and applications.[1]

1.1 Graphene and carbon nanotubes

Among the carbon allotropes, graphene, a planar monolayer two-dimensional honeycomb lattice, and CNT, the rolled up analog of graphene (Figure 1.1), have attracted much attention since their discovery.[22, 23] Graphene shows outstanding electrical and mechanical [22, 24, 25] properties such as Young's modulus of 1 TPa, inherent strength of 130 GPa,[26] and excessive thermal conductivity (above 3,000 W mK^{-1}).[27] Graphene has shown electron mobility of 2.5 × 10^5 cm^2 V^{-1} s^{-1},[28] which makes it greatest candidate for a high performance application in nanoelectronics. Similarly, CNTs possess various excellent features such as a high aspect ratio, great thermal conductivity, stability, very high mechanical strength, and extraordinary electronic properties.[29] Hence, CNTs are desired in practical optoelectronics as a source of nanometer light and photovoltaic tool,[30] which are a result from one-dimensional character, confined dielectric screening, and sp^2 carbon bonds.[31] CNTs can also convert the electromagnetic radiation (in optical frequencies) to direct current, illustrated as optical refining antenna.[32] On the other hand, their stability and compatibility with different environments such as biological systems, make them a desirable carrier for *in vitro* and *in vivo* studies.[33, 34]

Besides these fascinating features and applications, graphene and CNTs are also ideal candidates to pursue some chemical and physical questions such as charge transport under confined conditions, charge- and shape-dependent bindings, and release of molecules and sensing of supramolecular interactions up to a single molecule scale. However, fulfilling these exciting opportunities still needs a significant effort to circumvent obstacles such as sorting and separation, processing, and solubilization of graphene and CNTs. One of the best ways to improve the processability of graphene and other carbon nanomaterials for different applications is chemical functionalization of these nanomaterials by desired (macro)molecules. Chemical functionalization of graphene and CNTs will provide well-dispersed and even soluble nanomaterials in organic solvents and aqueous media and a simplified combination of their novel properties with other materials. Therefore, in the following subchapter, chemical covalent functionalization of graphene and CNTs will be discussed in detail as well as being given a concise explanation about the noncovalent method. Moreover, the most promising examples of covalent functionalization and also advantages/disadvantages of covalent approaches will be discussed.

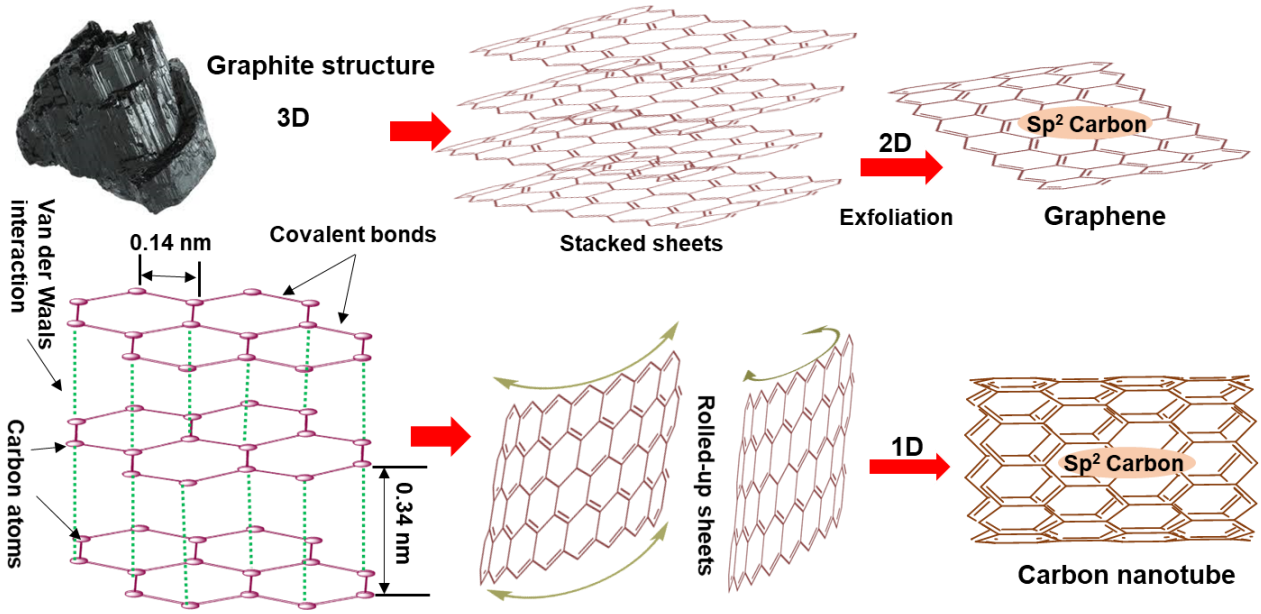

Figure 1.1. Cartoon represents graphite 3D structure (carbon source), interlayer interaction, distance, and different dimensions of allotropes (graphene and CNTs), which are fully made of sp^2 carbons. Adapted with permission from reference [35]. Copyright 2007, Springer Nature.

1.2 Functionalization of graphene and CNTs

In spite of such flourishing properties, a low processability of graphene and CNTs hamper their applications and further development. Besides the increased solubility of carbon nanomaterials,

a chemical functionalization has other consequences: introducing versatile reactive functional groups on the surface of graphene/CNTs, providing the accessibility of graphene/CNTs to interact with other objects such as polymers and biopolymers,[36] constructing hybrid structures with integrated and tailor-made properties, tuning the inherent properties of CNTs/graphene like hydrophobicity, conductivity, optical property, biocompatibility, toxicity, and developing the applications of these nanomaterials. There are two main strategies for chemical functionalization of graphene and CNTs: covalent and noncovalent functionalization. In the noncovalent pathway, functional groups are attached to the surface of graphene and CNTs by supramolecular interactions.[37, 38] By this method, the π-conjugation system of the above-mentioned carbon nanomaterials remains intact. However, the stability of functional groups is low. In complex media they can be detached from the surface of graphene or CNTs. Noncovalent functionalization is very attractive for biomolecule immobilization, also known as biofunctionalization, which is mostly employed for biosensing applications. In such biological applications, the molecule, which is attached to the surface of carbon nanomaterial, should recognize the analyte. This recognition highly depends on the type of immobilization of functional groups on the surface of carbon nanomaterials.[39-42] The immobilization method could be applied for various biomolecules such as enzyme, nucleic acids, antibodies, proteins, and so on[41, 43-46] via π-π interaction (by utilizing polymers or aromatic compounds) or CH-π interactions and electrostatic interactions between biomolecules and carbon nanomaterials.[46-49] A simple approach was shown by Wang et al.,[50] in which hydrophobin (a protein) was immobilized on the surface of CNT and employed to detect glucose using an amperometric biosensor. This biosensor with a great electron transfer demonstrated electrocatalytic capabilities with sensitivity of 116 $\mu A.mM^{-1}.cm^{-2}$ and a detection limit of 8.2 μM.[50] In another experiment, CNTs were functionalized by biotinylated pyrene derivatives via π-π interactions.[51] The functional carbon nanomaterials were successfully used for biosensing applications through antibody-antigen interactions,[52, 53] where the epitope of antigen could interact with a paratope of antibody. Such systems lead to development of immunosensors by integrating antigen or antibody with various transducers. These carbon nanomaterials could also serve as transducers due to their ability to transfer huge quantity of electroactive species, which stabilizes them. CNT-antibody-doped polypyrrole (Ppy) constructed by Tam et al. responded quickly to glucose with a low detection limit of 0.05 $\mu g.mL^{-1}$.[54] Furthermore, gold nanoparticles (GNPs) and CNTs with the horseradish peroxidase (HRP) have been used as other immunosensors for human immunoglobulin G (IgG) detection as a model protein. Presence of primary amine or mercapto groups in biomolecules led to immobilization of antibodies on

GNPs. As a result, they revealed enhanced performance of this system and a high potential for detection of other proteins.[55] However, the stability of these attachments should always be considered, since they are not covalently assembled. In comparison, covalent functionalization is very stable but with the cost of the disturbed π-conjugated system. Since most useful physicochemical properties of graphene and CNTs are strongly related to their π-conjugated system, they will be suppressed upon covalent functionalization. Changing the hybridization of graphene and CNTs from sp^2 to sp^3 by covalent attachment of functional groups to their surface induces defect sites in their structure and interferes with the mobility of electrons in these nanomaterials. This affects the electrical and optical properties of such materials. For example, luminescence of single-walled carbon nanotubes is strongly suppressed after a covalent functionalization. Therefore, an optimum method is a functionalization with the stability of covalent functionalization but a non-destructive feature of noncovalent functionalization. In this functionalization, the π-conjugated system and hybridization of carbon atoms of graphene and CNTs remain intact, while functional groups are covalently attached to the surface of these materials. In Figure 1.2, the basic methods to functionalize graphene/CNTs are shown.[56] The focus of next subchapter (1.2.1) will be the covalent functionalization methods and detailed description of highly reactive species that could interact with graphene/CNTs.

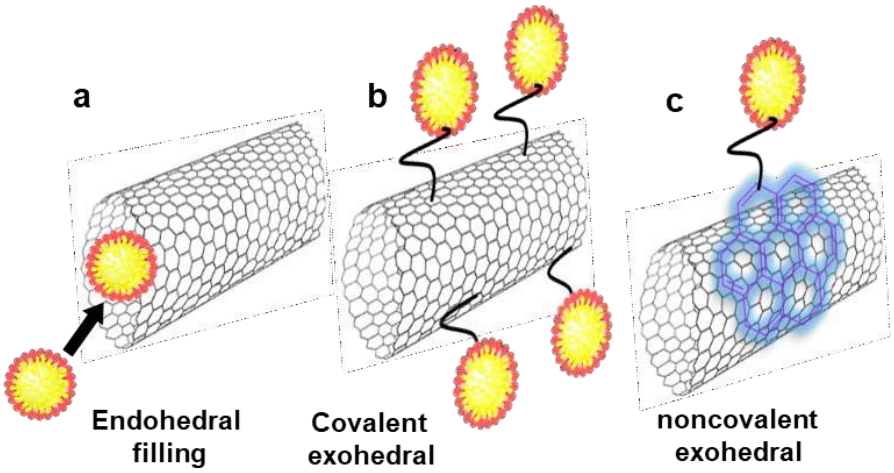

Figure 1.2. Representation of (**a**) endohedral functionalization, **(b**) covalent, and (**c**) noncovalent exohedral functionalization. The exohedral approach stands for attachment of functional groups on the external wall of the tube, in contrast, the endohedral method aims to fill the inner space of the tube. Adapted with permission from reference [56]. Copyright 2017, IOP Publishing.

1.2.1 Covalent functionalization

In terms of reactivity, graphene is fairly non-reactive compared to CNTs because, in its planar structure, the extended π-electrons can be delocalized over the entire 2D network. However, in the curved structure of CNTs the π-orbitals are misaligned.[57-59] Nevertheless, covalent functionalization can be achieved on the basal plane/edges of graphene and sidewalls of CNTs in two different ways: (a) by taking advantage of delocalized π-electron to form a covalent bond between dienophiles or free radicals and C═C bonds of the pristine graphene/CNT and (b) by forming covalent bonds between oxygen-containing functional groups (epoxy, carboxylate, and hydroxy) of graphene oxide (GO) with other (macro)molecules. An acid treatment was the pioneering method[60] for covalent functionalization of graphene, which could provide graphene oxide with versatile functionalities like epoxy group on the surface or hydroxy group at the edges (Figure 1.3). Consequently, graphene oxide was further functionalized using different chemistry like nucleophilic substitution and condensation reactions. After modifications, graphene oxide can be reduced to TRGO.[60] Nucleophilic functional groups (like amines) mainly react with epoxy groups of GO.[61, 62] For instance, Yang and coworkers performed this reaction between amine-terminated ionic liquids (IL-NH_2) and GO through the ring-opening reaction. The obtained well-dispersed solution was stable for more than three months, which was a good starting material for preparation of different composites.[63] Condensation reactions are also efficient alternatives to functionalize carbon materials covalently. Graphene-modified chitosan was prepared under microwave radiation by condensation reactions. The reaction occurred between carboxyl groups of GO and amine groups of chitosan, followed by reduction with hydrazine monohydrate.[64] However, graphene oxide contains high amount of water and requires more than four weeks to dry.[65] Also, as a starting material, it has limited use in aqueous or polar solvents for reactions. On the other hand, a reduction step is essential to omit the excess functional groups from the surface of graphene oxide.[66] Based on previous theoretical and experimental studies, the most promising method for functionalization of graphene/CNTs is to use highly reactive species like nitrene intermediates.[67] Because of high reactivity of these species, the functionalization method should be performed under milder conditions to retain the sp^2-conjugated system with a less defective structure. In the next section, cycloaddition reactions and also the most effective intermediates (nitrenes and carbene) are explained for functionalizing carbon materials.

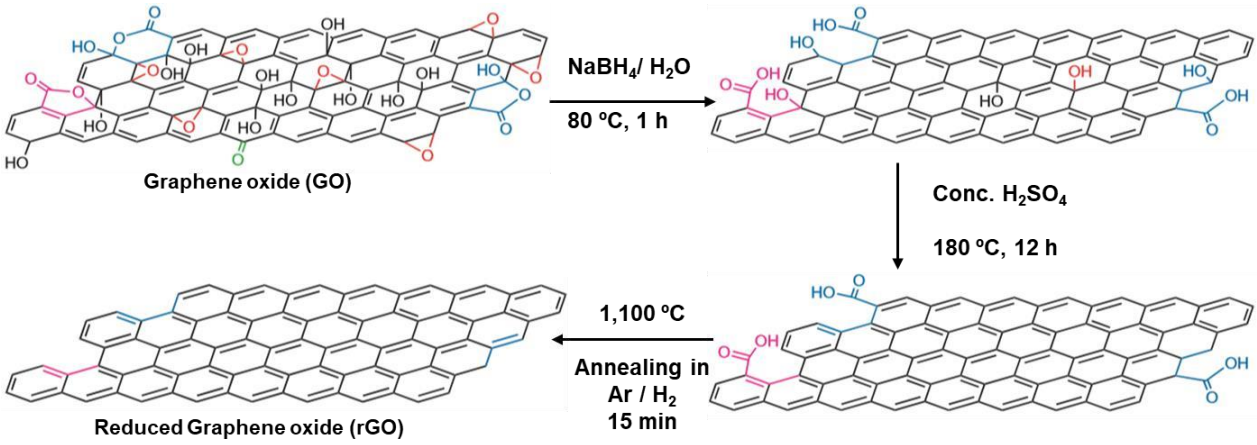

Figure 1.3. Represents graphene oxide and reduced graphene oxide (rGO). Adapted with permission from reference [68]. Copyright 2009, Springer Nature.

1.2.2 Cycloaddition covalent functionalization

Cycloaddition reactions have shown great potential to address the above-mentioned drawbacks of other covalent functionalization methods.[69] Unlike most of the typical organic reactions, in a cycloaddition reaction, formation of anions or cations are not essential, instead bond formation/cleaving processes happen simultaneously.[70] According to frontier orbital (FO) theory, this addition process takes place when electron transfers from the highest occupied molecular orbital (HOMO) of one unsaturated molecule to the lowest unoccupied molecular orbital (LUMO) of the other unsaturated molecule. Four major types of cycloaddition reactions are used for functionalization of graphene and CNTs: (a) [2+1] cycloaddition, (b) [2+2] cycloaddition, (c) [3+2] cycloaddition, and (d) [4+2] cycloaddition. Additionally, it should be mentioned that these kinds of reactions are easy to perform (like Diels-Alder reaction)[71] and do not need extra reactants or expensive catalysts. More importantly, employing these reactions could keep the π-conjugated system[72] with non or less defective structure because they are inherently exploiting π-electrons for functionalization instead of demanding dangling bonds.[72, 73]

[2+1] Cycloaddition

This reaction occurs between the π-conjugated system of carbon nanomaterials and reactive electron-deficient intermediates under relatively mild reaction conditions. In general, a [2+1] cycloaddition reaction is categorized by two main approaches; formation of aziridine adducts and cyclopropane. Nitrene is an intermediate, which results in the formation of an aziridine adduct after reaction with the π-conjugated system of carbon nanomaterials, while cyclopropane is obtained through carbene insertion reaction.[72]

Aziridine adduct

Functionalization of carbon nanotubes and graphene using nitrene chemistry were performed in a pioneering work by Holzinger et al. in 2001[74] and Kim et al. in 2009,[75] respectively. The aziridine adduct can be introduced onto the sp^2 carbon network via a nitrene intermediate, which generated under a photo- or thermo-decomposition process from an azide group. During the decomposition, nitrogen molecule is released and produces a highly reactive singlet nitrene, which subsequently undergoes a cycloaddition reaction. The mild nitrene [2+1] cycloaddition reaction based on aromatic azide has been recently reported.[76, 77] Aromatic perfluoroazides due to a high insertion efficiency were employed as nitrene precursors rather than aryl- or alkylazides.[78-80] The initial step of the reaction was decomposition of perfluoroazides under thermal and/or photolysis exposures in which a perfluoronitrene intermediate was formed. Subsequently, when three-membered rings formed on the sidewall of CNTs (so-called aziridine ring), the perfluoronitrene afforded perfluoroaziridino-CNT (Figure 1.4 and 1.5a). After functionalization of graphene by perfluorophenyl azide, a variety of long alkyl chains or ethylene oxide were grafted onto the surface of graphene, which resulted in highly soluble derivatives (stable for more than 24 hours) in o-dichlorobenzene and aqueous solution, respectively.[70]

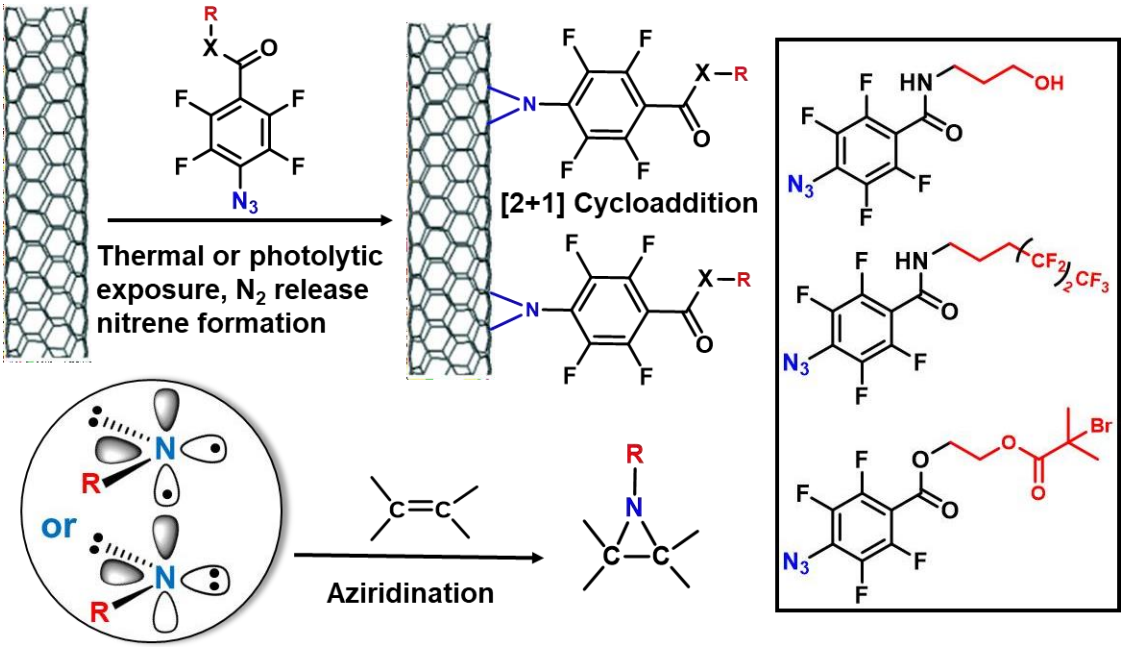

Figure 1.4. Functionalization of CNTs by perfluoroazides. This is an efficient nitrene [2+1] cycloaddition reaction on the sidewalls of tubes under ambient conditions. Adapted with permission from reference [76]. Copyright 2008, American Chemical Society.

Additionally, Hirsch's group performed a thermally-induced [2+1] cycloaddition reaction using alkyl azidoformate as a nitrene source to solubilize alkoxycarbonylaziridino- SWNTs.[74, 81] They performed a broad range of addends on CNTs and carried out comprehensive investigations using (R)-alkoxycarbonylnitrenes. This group attached crown ethers, alkyl chains, aromatic moieties, and oligoethylene glycol to carbon materials via nitrene addition. Raman and ultraviolet/visible spectroscopy (UV/Vis) revealed that defects increased in the lattice of CNTs after functionalization. These observations were used as indicators for the covalent functionalization of the above-mentioned carbon nanomaterials. However, they claimed that the electronic features of CNTs could only retained with functionalization of less than 2 wt% addend per C-atom.[81, 82]

Cyclopropane adduct (Carbene addition)

Dichlorocarbene was grafted on the π-conjugated network of graphene/CNTs.[83] A carbene intermediate was generated by α-elimination from the mixture of chloroform and sodium hydroxide (NaOH). Since in the chloroform precursor, the central carbon atom inherited two pair electrons after cleavage of the σ-band (C–H), chlorides could easily stabilize the singlet spin state due to the electron-rich character. Consequently, a singlet carbene could react as a electrophile with C═C bonds of graphene and CNTs via concerted pathway, which is presented in Figure 1.5b.[70] The concerted dichlorocarbene addition can be explained as follows: initially, since carbene has an empty P orbital (LUMO) that can interact with π-bond of C═C (HOMO). In the next step, HOMO electrons of carbene can fill the π*-antibonding orbital of carbon bond (C═C).[84] This functionalization has been reported for both graphene and CNTs with a strong effect on their electronic features.[75] Moreover, Lu et al. theoretically investigated functionalization of CNTs by oxycarbonylnitrenes, silylene, germylene, and dichlorocarbene via [2+1] cycloaddition reaction.[85] They observed that this kind of addition reaction is site-selective and a three-membered (aziridine) ring formation is favorable for carbon nanomaterials. However, in the case of dichlorocarbene and oxycarbonylnitrenes additions, slight activation energy is required for functionalization.[72] Moreover, Cho et al. revealed electronic properties of the network (i.e., CNTs), which strongly relied on the site of the cycloaddition reaction and the place of CCl_2 attachment on the tube. In some cases, they showed that the energy gap of semiconducting nanotubes was reduced, which implies manipulation of the band gap could be possible with a precise modification. Furthermore, carbene could act as a nucleophile to react with the π-conjugated system of graphene/CNTs as an electrophile to provide polyadducts like dipyridyl imidazolidene on the sidewalls of tubes. The covalent bond

of imidazolidene with a positive charge resulted in n-doping of nanotubes, which renders a new way for their modification as well as intervention into electronic characters of tubes.[74, 86]

[2+2] Cycloaddition

Benzyne or an aryne intermediate is needed for forming four-electron cycloaddition reaction on surface of graphene/CNTs via elimination-addition mechanism (Figure 1.5c). However, aryne intermediate formation needs harsh reaction conditions such as using a strong base. Therefore, an alternative mild method could be served by means of fluoride-induced decomposition on an o-trimethylsilyl-phenyl triflate. The formation of a strong F–Si bond can stimulate a desilylation step by fluoride ion, which gives a filled sp^2 orbital carbanion in the ring continued by elimination of the triflate group to provide benzyne as an electrophile. Eventually, a [2+2] cycloaddition reaction could occur by nucleophilic attachment via the C=C bond of graphene/CNTs, shown in Figure 1.5c. Ma et al. functionalized graphene with benzyne cycloaddition reaction and successfully attached three derivatives of benzyne with hydrogen, methyl, and fluoride groups onto the surface of graphene.[87]

Apart from benzyne, a photochemical reaction could also take place[88] with a charge-transfer between graphene/CNTs and 4-phenyl-1,2,4-triazoline-3,5-dione (PTAD). In this regard, PTAD is a strong dienophile for cycloaddition reaction with CNT, which acts as an electron donor species.[89] Interestingly, this cyclization process has been employed to build a new hybrid system called nanobuds, where a fullerene molecule is covalently attached on the outer layer of single-wall nanotubes by means of [2+2] cycloaddition reaction. It was shown that the nanobuds have new electronic properties that originated from charge transfer between CNT and fullerene, which neither CNT nor fullerene showed individually. A new nanobud hybrid system showed that both optical and electrical properties could be adjusted using cycloaddition reaction, which implies many applications in quantum dots and memory devices.[90-92]

[3+2] Cycloaddition

The [3+2] cycloaddition, also called 1,3-dipolar cycloaddition and/or Prato reaction, is extensively employed for functionalization of carbon-based nanomaterials such as fullerene. For instance, graphene as a dipolarophile reacts with a 1,3-dipolar molecule towards a five-membered ring through a six-electron cycloaddition reaction. According to the literature, in the case of graphene, the used 1,3-dipolar molecule comprised azomethine ylides that were obtained from a decarboxylation reaction of carbonyl species and N-methylgylcine. A decarboxylation approach is the most feasible route in terms of reaction conditions in comparison with other mechanisms such as iminium salt, aziridine, oxazole, and carbene/imine

to provide an azomethine ylide product. Ultimately, the product of [3+2] cycloaddition reaction between C═C bond of graphene and azomethine ylide forms (as depicted in Figure 1.5d).[93]

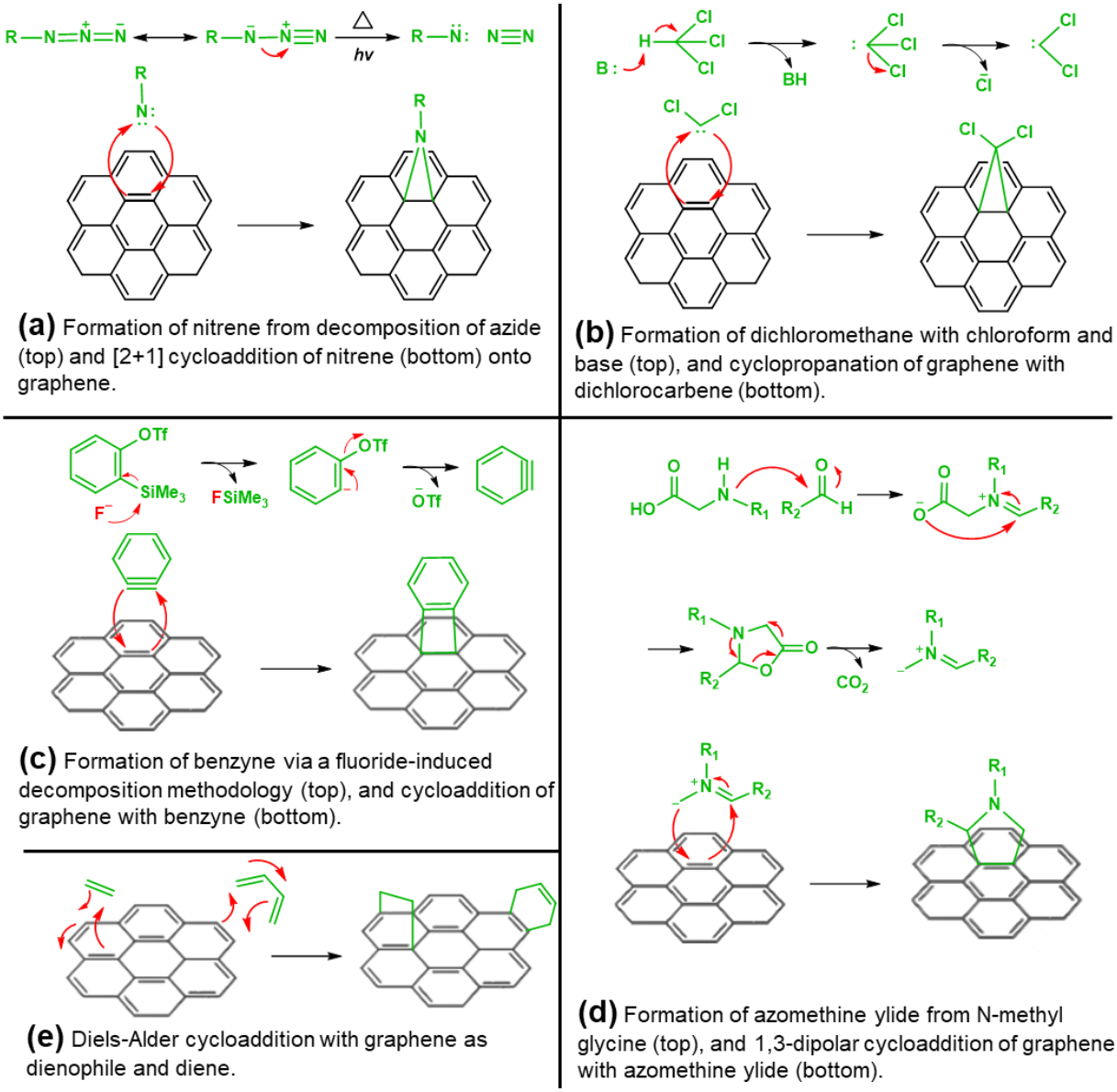

Figure 1.5. Representation of the mechanisms of possible cycloaddition reactions for the functionalization of carbon nanomaterials. Adapted with permission from reference [70]. Copyright 2013, Royal Society of Chemistry.

[4+2] Cycloaddition (Diels–Alder reaction)

The most popular pericyclic reaction in organic synthesis is Diels–Alder cycloaddition reaction, which occurs through a thermal treatment in one step to provide a six-membered ring product. In this mechanism, a conjugated system consists of four π-electrons of a 1,3-diene (electron rich) and two π-electrons from a dienophile (electron deficient). By conjugating the withdrawing groups (halogen atom, nitro group, etc.) with dienophile, the reaction proceeds

easier. However, the reaction happens only when the diene is in the s-*cis* conformation (Figure 1.5e). The [4+2] cycloaddition reaction was carried out between CNTs and o-quinodimethane, which was released *in situ* from 4,5-benzo-1,2-oxathiin-2-oxide under microwave irradiation.[94] Theoretical evaluation revealed that, in the transition state of quinodimethane cycloaddition reaction, the aromaticity stabilization made this reaction achievable. Otherwise, in another case, for example, the reaction between 1,3-butadiene and CNTs was not favorable.[95] Since the fluorine is an electron-withdrawing substituent, the rate of the reaction increased for fluorinated single-wall nanotubes (SWNTs).[96] Moreover, a transition metal was used in another similar work, which led to speed up this reaction.[97] More interestingly, Haddon et al.[98] confirmed the dual nature (i.e., diene and dienophile) of graphene in the Diels–Alder reaction. For instance, graphene as a dienophile also reacted with 9-methylanthracene and 2,3-dimethoxy-1,3-butadiene and changed the metallic to non-metallic character over a temperature range of 100-300 K.

1.2.3 Advantages of covalent functionalization

The most promising covalent functionalization method (i.e., cycloaddition reactions) on graphene and CNT was explained in the last section. The main advantage of this functionalization is that functional groups are strongly attached onto the graphene surface and sidewalls of CNTs. Nevertheless, beside this advantage, two points should be taken into account: (i) why graphene and CNT require covalent functionalization and (ii) which properties can be improved by new functionalities. Graphene and CNT are intrinsically insoluble in water, and even organic solvents, which cause challenges to process them for different applications. For instance, tube-tube interactions resulted in aggregation and bundles and caused serious problems for observing the intrinsic properties of CNTs.[99] This issue disturbed electronic structure of the tubes and made them useless for construction of composite photonic and electronic devices. Likewise, the irreversible agglomeration through π-π stacking and van der Waals interaction is a frequent challenge in graphene, which hampers utilizing graphene for practical applications. On the other hand, graphene has a zero band gap, which gives brilliant conductivity. However, for construction of transistors, semiconducting graphene is desired therefore the band gap of this compound should be opened. Apart from that, due to insolubility of graphene, the physical handling of sheets is still a big challenge.[100] Additionally, in optoelectronic applications based on CNT, the tube needs to be characterized individually, which is impossible for pristine tubes.[36] Therefore, an appropriate covalent functionalization of graphene and CNT represents a wise strategy for solving these problems and transforming

them to processable materials for different applications. Therefore, covalent-functionalized CNTs can provide different electrical and mechanical features in comparison with unfunctionalized nanotube, which can be further employed for fine-tuning the chemistry of carbon nanotubes. Another example is selecting electron withdrawing and/or donating group for covalent functionalization of graphene, which could result in n- and p-doped graphene. Eventually, sufficient doping would affect the band gap opening close the Fermi level of graphene, which could convert the 'metallic' nature to 'semiconductor' nature and finally control the electronic properties of graphene.[101]

1.2.4 Disadvantages of covalent functionalization

Covalent functionalization methods are chosen to pursue a dichotomy between maintenance of rigidity and quantum properties of carbon nanomaterials, which is commonly expected. In fact, the nature of the covalent approach leads to dangling bonds by changing hybridization of the carbon atom, the creation of defects, and consequently quenching the emission of tubes. All cycloaddition reactions and other covalent functionalization methods provide derivatives with wide range of applications, nevertheless a mild reaction condition within a short time could destroy graphene/CNTs π-conjugated structures and bleach the tubes' emission (Figure 1.6a).[102] A remarkable exception is aryl attachment, in which the product showed high emission yields.[103] However, this is at the cost of the structural integrity of the conjugated structure of the functionalized CNT.[103] Although, covalent functionalization is the prepared way for carbon nanomaterials' modification and application, their implementation interrupts the conjugated structure and changes hybridization of sp^2 carbon to sp^3 (Figure 1.6b).[67, 104-106] This matter opens another challenge for some (but not all) applications of these nanomaterials. Covalent functionalization influences electrical properties of graphene/CNT via three mechanisms: (a) disrupting the lattice by hybridization state, altering the electron density, and increasing the electron-hole puddles (b) the interaction between graphene/CNT with functionalities results in improvement of doping because of quantum capacitance and interruption of integrity. (c) hybridization of electronic band (in graphene/CNTs) with molecular orbital.[107] For instance, traditional chemical oxidation on graphene provides graphene oxide, which reduction process convert it to reduced graphene oxide (rGO). The carrier mobility of graphene is about 10,000–50,000 $cm^2/V/s$ at room temperature, however, because of a few remaining oxygen species, the carrier mobility of rGO extremely decreased (0.05–200 cm 2 /V/s).[108] It is worth mentioning that, even though noncovalent functionalization is known as a nondestructive method to introduce chemical groups on the

surface of graphene and CNT, at least it can affect the doping density, increase the electron hole, and create scattering sites. Consequently, covalent functionalization still needs to be optimized and the best trade-off between strengthening of functionalities should be found and structural interruption should be avoided.

1.2.5 Optimal covalent functionalization

New covalent functionalization is necessary for rendering stability along with unchanged π-conjugated structure of carbon nanomaterials (graphene/CNTs). Hence, [2+1] cycloaddition reactions have great potential to rebuild a fully conjugated system after covalent functionalization on graphene/CNT. [2+1] cycloaddition reactions operate under mild reaction conditions and, more importantly, the π-electrons (of graphene/CNT) exploit the attachment of functional groups instead of demanding dangling bonds.[72] Electron-poor aromatic azides,[76, 77] in which two π-electrons of the graphene network transform to a covalent bond in a three-membered aziridine ring (close configuration), are pioneer examples for such mild [2+1] cycloaddition reactions. However, the strained carbon bond on the bridge can be opened, the sp^2 carbon rebuilds again, and the aromaticity of the functionalized carbon material is restored. The lifetime of nitrene is a key point in this process. Therefore, precursors of nitrenes with a long lifetime, e.g., perfluorophenyl azides (PFPAs), are being developed for the functionalization of CNTs and graphene. The activation energy of this reaction increased due to high electronegative fluorine substituents, which are in the ortho position to the azide groups, leading to increase the life time of the singlet phenyl nitrene in comparison to nonfluorinated phenyl azide.[109] Apart from the experiments that proved the potential of nitrene covalent addition, theoretical studies[110] have also done to understand details of aziridine ring configuration. The results proposed an open configuration for the aziridine ring, which could finally solve the challenge of restoring sp^2 carbon after functionalization. Marzari and Lee et al. recommended that the open configuration for dichlorocarbene could preserve integrity of CNTs,[111] whereby, in this form, the properties of metallic CNT remained intact. However, these have not yet been done experimentally for both nitrene and carbene additions.[72, 73, 82, 112] Therefore providing a nitrene intermediate with long lifetime is an unsolved challenge, which is vital to perform a nondestructive covalent functionalization.

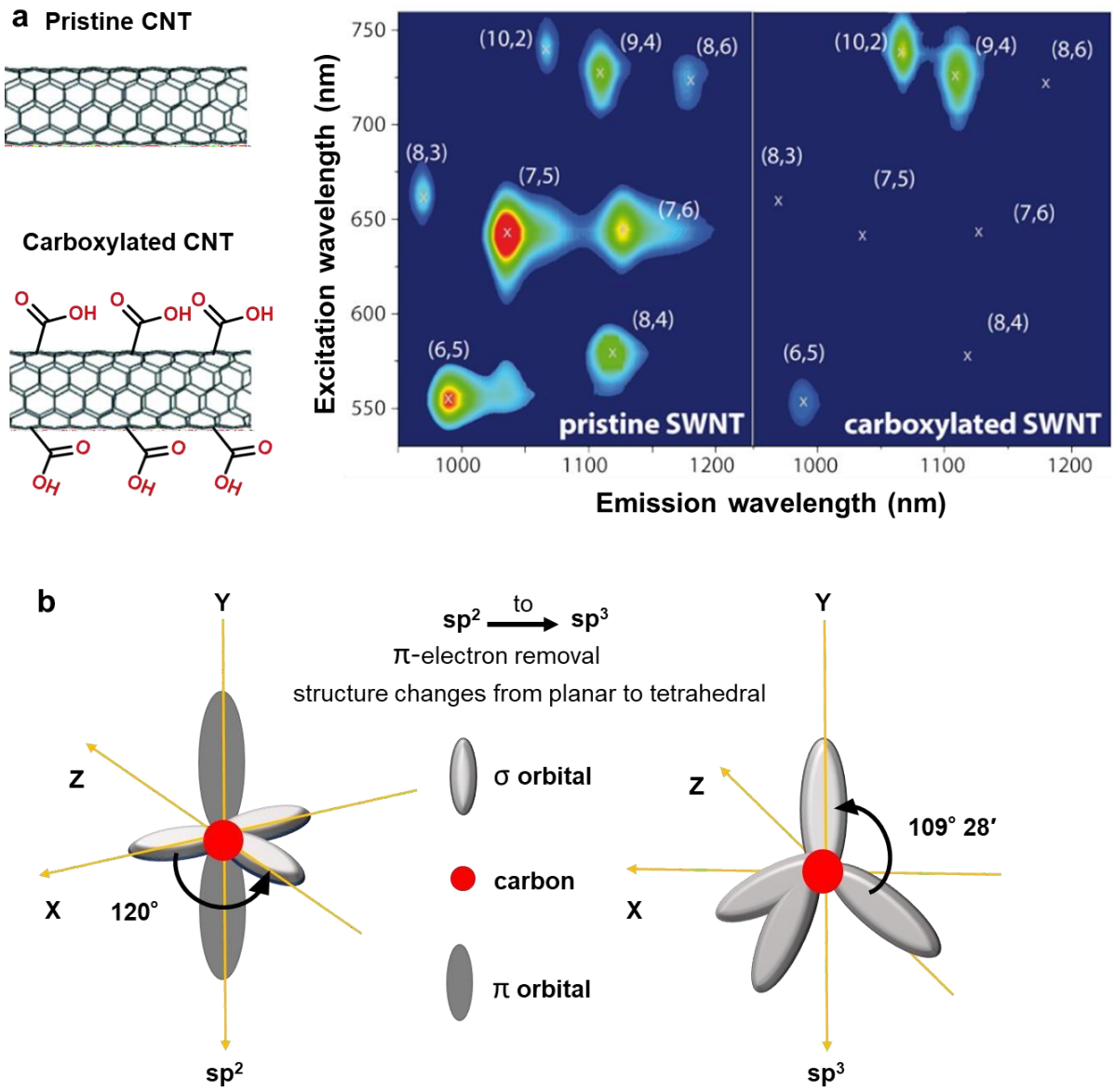

Figure 1.6. (**a**) The structure of non-functionalized and functionalized CNTs, photoluminescence maps comparison of CNT (left) and carboxylated CNT (right panel). Adapted with permission from reference [102]. Copyright 2016 John Wiley and Sons. (**b**) Cartoon represents how covalent functionalization of carbon nanomaterials can change the hybridization of carbon atoms and drastically diminish the electronic features of CNT and graphene. Adapted with permission from reference [107]. Copyright 2013, John Wiley and Sons.

1.3 Nondestructive covalent functionalization by triazine derivatives

Our group used for first time an azidodichloro-triazine with an ability for a nitrene [2+1] cycloaddition reaction for nondestructive functionalization of CNTs under ambient conditions.[113] This intermediate (azidodichloro-triazine) is highly strained on CNT and, as predicted theoretically,[111] needed an aziridine ring change to open configuration, which

induced fully conjugated hetero-bridged CNT in a one-step process by rehybridization. The bridging nitrogen atom shares its lone pair of electrons with the π-conjugated structure of CNT, which resulted in a higher electron density in system. Even at high density of functionalization (one triazine ring per 25 carbon atoms of CNT), the intensity of the disorder band (D-mode) remained constant (in Raman spectroscopy). Since the ratio between the D and G bands can provide the fraction of defects and sp^3 atoms in the functionalized CNT, it has been used for the investigation of nondestructive character of the above-mentioned functionalization. Accordingly, the ID/IG ratio of the functionalized and nonfunctionalized CNTs were similar indicating the π-preserving character of this type of functionalization and fully π-conjugated system for the triazine-conjugated CNTs. Additionally, non-destructive functionalization of high quality nanographene (size <100 nm) was recently verified in our group using a similar nitrene [2+1] cycloaddition reaction.[114] After functionalization of nanographene sheets with azidodichloro-triazine, the triazine functional group was tilted on the graphene surface and distorted bond lengths. This resulted in the triazine group no longer sitting coplanarly on graphene, but the hexagonal structure had been preserved. The local lattice was distorted by triazine group due to the opening of the C–C bond at the bridge site, which led to a noncrystalline sp^2 carbon structure. The conductivity of triazine-functionalized nanographene sheets significantly increased, which was expected because of the ring-opening configuration of the bridging N-atom towards n-type doping and a fully conjugated derivative.

1.3.1 Controlled post-functionalization based on triazine functional groups

Introducing a triazine moiety on carbon nanomaterials not only solved the destructive challenge of covalent functionalization methods, but also showed great potential for the controlled and stepwise post-functionalization. This section describes some research work from our group, which employed this chemistry, as well as other interesting reports. Multidrug resistance (MDR) is a big problem for chemotherapy treatment. To solve this problem, the Tu et al. addressed the precise functionalization of graphene as a multifunctional drug delivery system.[115] In a similar work, they investigated the effect of surface charge and size on the uptake pathways of graphene sheets with defined functionality.[116] Moreover, our group has also shown the great potential of graphene-grafted-hPG for multivalent interactions with pathogens such as Escherichia coli (*E. coli*) and Bacillus cereus. They also evaluated the mechanism of deactivation of pathogens by functionalized graphene sheets. They have shown that the antibacterial activity of graphene sheets strongly relies on area accessibility, the mean basal plane, the edges of the graphene sheets, and polymer content of the graphene platform.[117]

Additionally, they investigated graphene-based heparin biomimetics using polyglycerol sulfate. The heparin sulfate mimic could transform passive surfaces into a very affective platform for virus binding.[118] Many other graphene-based platforms with defined functionality were synthesized by this controlled post-modification method and were used for different biomedical applications.[119-124]

1.4 Synthetic approaches for two-dimensional polymers (2DPs)

Undoubtedly, the polymer concept was one of the noteworthy scientific achievements of the past century. In the 1920s Hermann Staudinger coined the term macromolecules with high molecular weights up to 1 MDa. He was awarded the Nobel Prize for chemistry in 1953.[125] Staudinger proposed a revolutionary concept for macromolecules,[126] that are composed of linear molecular chains containing a large number of repetitive units linked to each other by covalent bonds. He transformed the former idea: "the self-assembly of small molecules which connected to each other by weak intramolecular forces" rather than robust covalent bonds to form macromolecules.

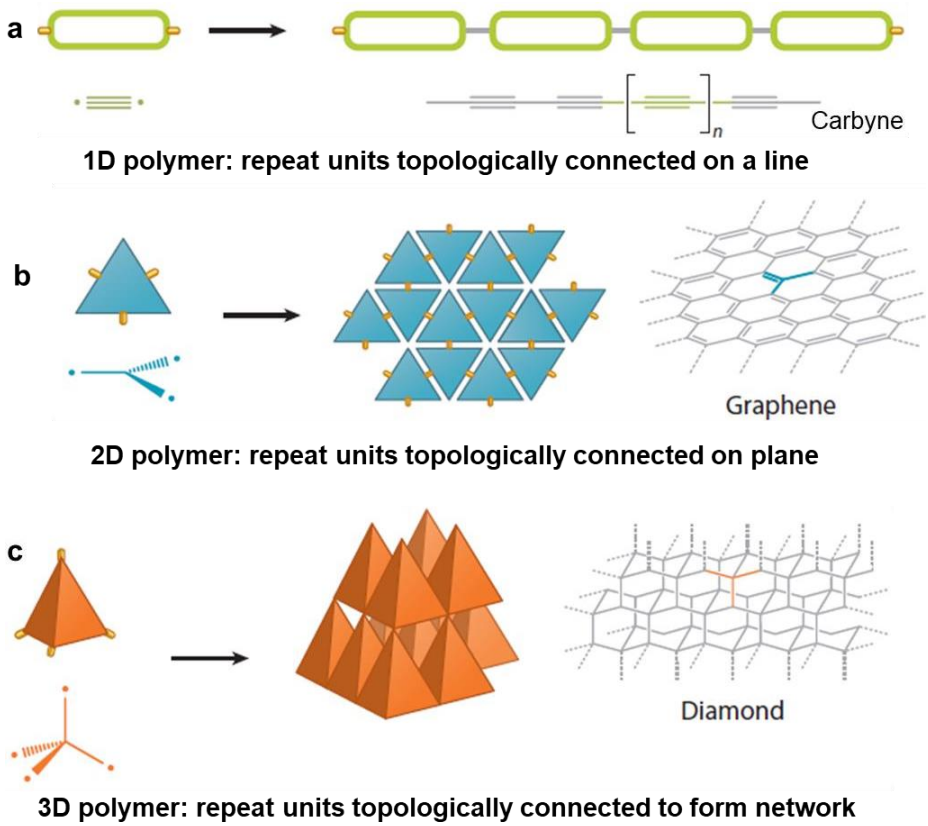

Figure 1.7. Diverse repeat units result in different topologies of polymers. (**a**) One-dimensional linear carbyne polymer based on linear acetylenic monomer polymerization. (**b**) Graphene as a natural 2D polymer that is made of trigonal carbon atom (sp^2-hybridized). (**c**) A diamond three-

dimensional structure made of the tetrahedral carbon atom (sp^3-hybridized). Adapted with permission from reference [127]. Copyright 2016, Annual Reviews.

From the topological point of view, linking of repeat units could happen in different dimensions: one-dimension (1D), two-dimensions (2D), and three-dimensions (3D). Generally, an n-dimension polymer could be synthesized when a monomer with a (n+1) binding site is available. As an example, a diamond is the result of repetition of sp^3-hybridized carbon atoms (with four binding sites) in a 3D structure.[128] This rule could be extended to all carbon allotropes, where a carbon allotrope with specific unit is attached to similar counter parts by repeating a pattern in various spatial dimensions (Figure 1.7). Further, in graphene as natural 2D polymer (2DPs), carbon is a repeated unit with three binding sites connected to each other by covalent bonds (Figure 1.7b). Since 2004 graphene has been isolated and characterized, which made work on the other 2D materials dramatically increase.[22] This was due to its outstanding features, the unique structure, and especially the 2D character of graphene. Other 2DPs, like inorganic metal dichalcogenides, TaS_2, WS_2, $NbSe_2$, $MoSe_2$, and MoS_2,[129] have been explored and they have shown great potential for different applications. Moreover, a variety of elemental allotropes such as hexagonal boron nitride,[128, 130] germanene,[26] and phosphorene[35] could also be considered as 2D materials. Nevertheless, single or thin layers of 2DPs are desired for structural characterization and some applications. Therefore, two main approaches were employed for accessing these materials in thin layers which are generally categorized into: (1) bottom-up methods like thermolysis[131, 132] and chemical vapor deposition (CVD)[133-135] and (2) top-down methods like liquid exfoliation or micromechanical techniques.[35, 129, 136, 137] The top-down approach needs harsh conditions; however, it provides 2D materials in a layered form. As a chemist, if one takes a closer look at these 2D structures, their applications are limited due to the lack of functionality in their structures. Nevertheless, organic chemistry comes to play an important role to create synthetic 2DPs like hexagonal boron nitride,[138, 139] silicone,[140, 141] and graphene[60, 67, 142] using mild conditions. Although, there is no debate about the importance of 2D polymers and their fascinating properties have been explored both theoretically and experimentally, new synthetic methods are very appealing to construct desired 2D polymers. Pioneering efforts to synthesize 2D polymers date back to 1935 at the air/water interface[143, 144] (the method explained in Subchapter 1.4.3) and after that other reports were appeared in literature.[145-147] However, their synthesis relied on linear polymerization, which is not an actual 2D growth reaction. Eventually, in 2012, a breakthrough synthetic 2DP was obtained by the Schlüter group[148] which proved that a synthetic 2D polymer

would be attainable by designing the repeating unit. Nevertheless, before venturing into the synthetic part, it is however, vital to answer two questions: what is a 2DP and what characteristics should a macromolecule have to be classified as a 2DP? Schlüter's group presents five main parameters for 2DPs (Figure 1.8).[149-151] However, other interpretations on the 2DPs definition are suggested including non-periodical and multilayer structures:

1. Planarity: A 2D polymer is a topologically planar sheets and repeating unit has a planar topology with 3 and 4 or 6 binding sites.
2. Repeat units: 2DPs have repeat units (ordered structure) and exhibit crystallinity in at least one conformation.
3. Covalent bonds: The repeating units of 2DPs are linked to each other by strong covalent bonds, which result in a stable sheet where no substrate is needed for support.
4. Thickness: A 2DP should have thickness of the constituent repeat unit.
5. Separability: 2D polymers have strong bonds and could be exfoliated into a single sheet without collapsing.

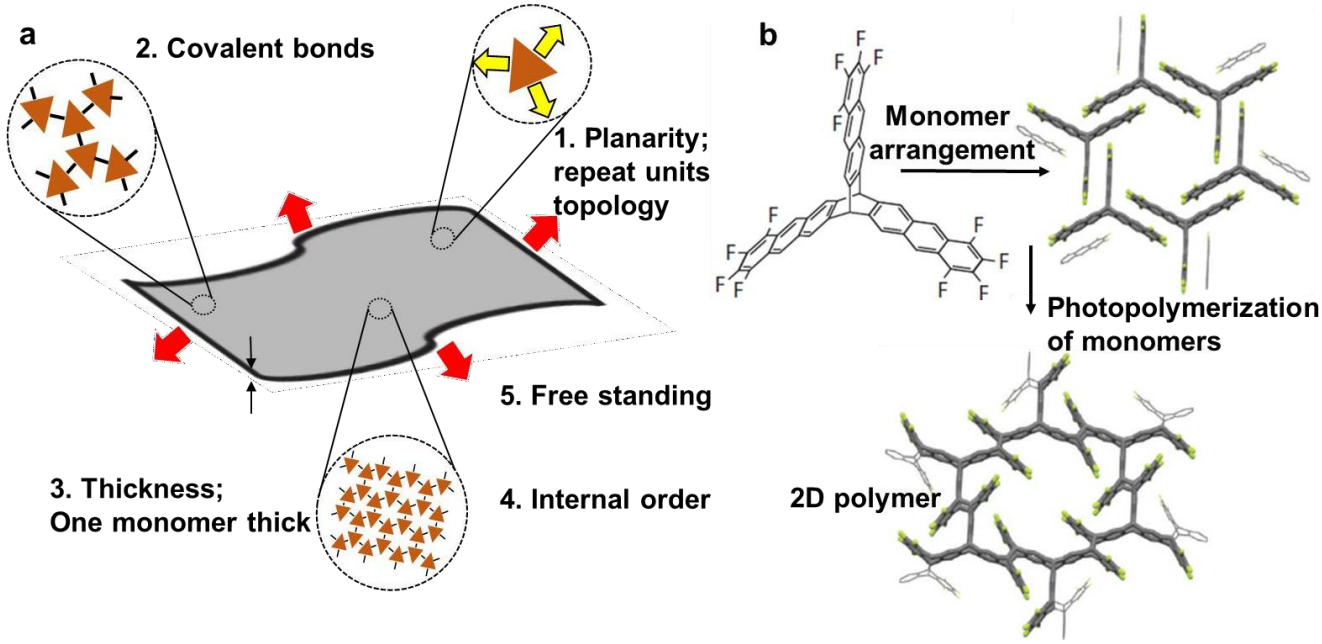

Figure 1.8. (**a**) Cartoon representation of five criteria for two-dimensional polymers. (**b**) Chemical structure of the fluorinated fantrip, which leads to 2D polymer upon photo-polymerization. Adapted with permission from reference [152]. Copyright 2014, Springer Nature.

From the chemistry point of view, there are generally some approaches for synthesizing 2DPs but two methods, air/water interface and single crystal, have shown great potential that rely on pre-organization of monomers. The critical point of these methods is monomer design,

where a monomer has to be wisely thought in terms of binding sites as well as the reaction method for synthesizing a 2DP. The confinement of the reaction is the main challenge, where the structure should grow into 2D manner and avoid its deformation into a third dimensional (3D) network. This challenge can be circumvented by performing pre-organization on the monomers, in which monomers should have a three-, four-, or six-fold symmetry before polymerization.[127, 153] In the following subchapter, the air/water interface, single crystal, and covalent organic frameworks (COFs) are chosen for synthetic methods for 2DPs. Moreover, a very attractive synthetic method will be discussed following an in-solution method in the next sub-chapters. The focus will be on employing triazine heterocycle as monomer, its chemistry, and reactivity and exploring some recent synthetic 2D polymers based on triazine monomer.

1.4.1 Triazine (cyanuric chloride) chemistry

We used cyanuric chloride (CC and/or triazine) as monomer for both 2D polymer synthesis and [2+1] cycloaddition reaction. CC with its three highly reactive chlorine atoms used to synthesize a variety of organic compounds, due to its chemoselectivity for reaction with nucleophiles. Moreover, use of a nucleophile and manipulating temperatures in CC chemistry led us to prepare mono-, di-, and tri-substituted cyanuric chloride derivatives. Mono-substitution of CC occurred below or at 0 °C, the di-substitution occurred at 25 °C, and the third chlorine could be replaced at temperatures above 60 °C, which created tri-substituted triazine derivatives (Figure 1.9) in a one-pot reaction.[154] Additionally, other parameters, such as the structure of the nucleophile, solvent, steric hindrance, and time, should be optimized to accomplish the reaction. Consequently, CC has shown widespread application in the pharmaceuticals.[155] It is also very cheap and commercially available reagent for organic synthesis.[156]

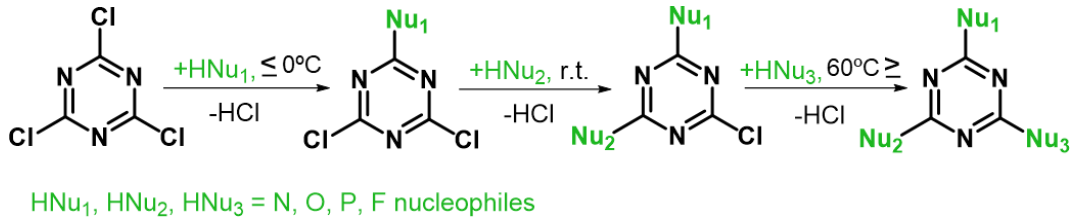

Figure 1.9. Represents step-wise substitution of 2,4,6-Trichloro-1,3,5-triazine (CC) by manipulating the temperature. Adapted with permission from reference [154]. Copyright 2006, Elsevier.

1.4.2 2DPs based on triazine derivatives

How CC could be served as a monomer for preparation of 2D polymers in-solution? To answer this question, we need to explain the in-solution method for the preparation of 2D polymers. In this method, there is no pre-organization in monomer arrangements and no substrate for monomers as a platform to be arranged on a surface. Therefore, polymerization of monomers should create 3D-like structures. We need to use a monomer with high rigidity and planarity or hindered bond rotations during the irreversible bond formation (here polymerization).[157] Another path to solve this obstacle is a regular supramolecular self-assembly that is formed in two-dimensions in solution connected by covalent bonds. Häner's group recently demonstrated a supramolecular hexagonal network by trifunctional monomers with anthracene moiety, which could be connected through [4+4] cycloaddition reaction. Häner's group also used the self-assembly of monomers (DNA chains) to create a 2D polymer, but periodicity of the obtained 2D could not be proven.[158] Kim et al. also introduced a unique in solution method to prepare free-standing, covalently bonded 2D polymer, where preorganization of monomers on the substrate was not employed. Their observations were based on three criteria: (1) designing rigid and disk-like units bearing reactive sites at the periphery, (2) for high-bending rigidity short linkers are required, and (3) solvent plays a very important role not only in the better solubility of intermediates but also would lead to remaining intermediates flat as they grow into 2D sheets.[159] Interestingly, Kim et al. proved the role of the solvent in experimental and theoretical studies, where poor solvent and low bending rigidity of monomers generated intermediate curvatures, whereas good solvent and high bending rigidity of monomers allowed a lateral growth of the intermediates without bending.[160] Another interesting procedure of supramolecular 2D in solution synthesis could be found in the report by Zhao[161] and other research groups.[160, 162, 163] Lastly, there is still an argument about which is covalent fixation of supramolecular networks, low stability and polymerization efficiency. Coordinative covalent bonds are alternatives to confine monomers in 2D conformation and increase their rigidity. This complexation is strong and could be controlled by choosing the right metal ligand composition. As a matter of fact, this concept has already led to the construction of stable organometallic, two-dimensional polymers,[164, 165] which rendered great electrical optical and physicochemical features.[166] Recently, a copper coordination 2D polymer was synthesized using benzenehexathiol (BHT) as multidentate ligand with six-fold symmetry, which could be transferred on the other surface as well. This coordination polymer (CP) showed electrical conductivity up to 1,580 S cm^{-1} at 300 K, which is the highest value among all other synthetic CPs. Consequently, limitations of the interface-assisted strategy could be overcome by taking

advantage of this possibility to organize monomers in a sheet-like structure, which connect to each other by covalent bonds. On the other hand, CC itself creates a separate class of synthetic 2D polymer that is named covalent triazine frameworks (CTFs)[167] in a solution method. For the first time, Thomas's group made CTF via trimerization reaction of carbonitrile, where $ZnCl_2$ acts as a solvent and catalyst.[168] Müllen et al. used a free-catalyst Schiff-base reaction and they synthesized a series of porous organic frameworks/polymers (POFs/POPs). One-pot polycondensation of aminal linkage in triazine monomers with different aldehydes afforded polymers including >40 wt% nitrogen content.[169, 170] Bhaumik et al. employed hydrothermal treatment of 1,3,5-tris-(4-formyl-phenyl) triazine (TFPT) for polymerization under acidic conditions.[171] Moreover, Sonogashira cross-coupling and Yamamoto coupling reactions have also shown great potential to make COPs by 2,4,6-tris-(4-bromophenyl)-[1,3,5]triazine and 2,4,6-tris(4-bromophenyl)-1,3,5-triazine as monomers.[172, 173] Aforementioned in-solution synthetic methods are used and some covalent organic polymers,[174, 175] which are based on triazine, have been synthesized with excellent applications in catalysis, drug delivery, gas storage/separation, and energy conversions fields.[176, 177]

1.4.3 Air/water interfacial and single crystal approaches

In 1917 Langmuir initiated to work on amphiphilic fatty acids at the water/air interface[178, 179] to study monolayer sheet that eventually led to discovery of the Langmuir trough. The preorganization monomer process happens, when they spread over the air/water interface and use mechanically forces to compact the monomer.[147, 180-182] When monomers are packed and reactive sites are well arranged for interaction to each other, an external stimulant could be applied for the polymerization (Figure 1.10a). For instance, in light irradiation or in the case of metal-ligand coordination method, reactants from the water sub-phase could diffuse[183-185] to reactive sites and applying to polymerization of monomers (Figure 1.10c). Eventually, after polymerization process, a micrometer sized monolayer polymer is obtained and can be transferred onto a substrate or used *in situ* in the interface for further characterization. However, characterization of the obtained polymer is the main issue since the quantity of monomers is in the microgram range. Murray et al.[186] have designed a rigid trigonal star monomer, an amphiphilic (diethylene glycol chain) monomer, consisting of three anthraceno arranged on a central triptycene core. After spreading this monomer, diethylene glycol was attached to the monomer on the water surface and the anthraceno lying on the interface for photopolymerization at the air/water interface. As a result, they prepared a porous polymer (6.8 × 1013 pores/cm^2) and macroscopic monolayer (cm^2) with the thickness of 1.2 nm. This stable

polymer could be transformed on to the other substrate. The scanning tunneling microscopy (STM) image proved the honeycomb lattice and local periodicity of the polymer (Figure 1.10b). Consequently, the main advantage of the air/water interface method compared with the other synthetic approaches (like single crystal) is a monolayer polymer formation as a final 2DP. However, it makes the characterization process complicated due to sensitivity of the monolayer besides monomer behavior in interface to form monolayer for polymerization.

Alternatively, a topochemical (or thermal) synthetic process for 2DPs is single crystal method.[187] This method requires crystallization of monomers as single crystals and subsequent packing of monomers in a way that reacting sites could be close to their neighbors in each layer. In an ideal preorganization, the layers cannot be crosslinked to each other, but they can stay together by weak intermolecular interactions. The reaction growth is restricted in two dimensions, since, in each layer, the direction of bonding sites of monomers is confined two dimensionally. Finally, upon photo irradiation and/or by thermal process, a 2DP is obtained.[153] Cycloaddition reactions like [2+2],[188, 189] [4+4],[190] and [4+2],[148] are employed as effective choices to alter the monomer crystal toward the polymer crystal. However, there are still three challenges for the SC method: first packing the crystal into an optimized and desirable level, second directing the reaction toward a single crystal formation, and third exfoliation to gain a single layer 2D polymer.

1.4.4 2D covalent organic frameworks (COFs)

In general, COFs polymerization is the method most commonly used, because it has a porous multilayer polycrystalline of 2D materials, in which monomers compact under a reversible bond-forming process.[191-195] Reversibility (dynamic chemistry) is the key point of COF formation because it requires both crystallization and polymerization at the same time. In forming the reversible bonds (such as imine bond or boronate ester creations),[196, 197] structural defects are expected. These methods are practically simple, since the right stoichiometry is the most important factor and the process is easy to mix in solution . However, a remaining challenge is how to obtain single layer sheets from a scalable method.[198] One could think of exfoliating this 2D material, which is an open issue, to obtain a few layer sheets.[198, 199] Growing single sheet on the substrate[194] and air/water interface[185, 200] methods are other alternatives for this purpose.

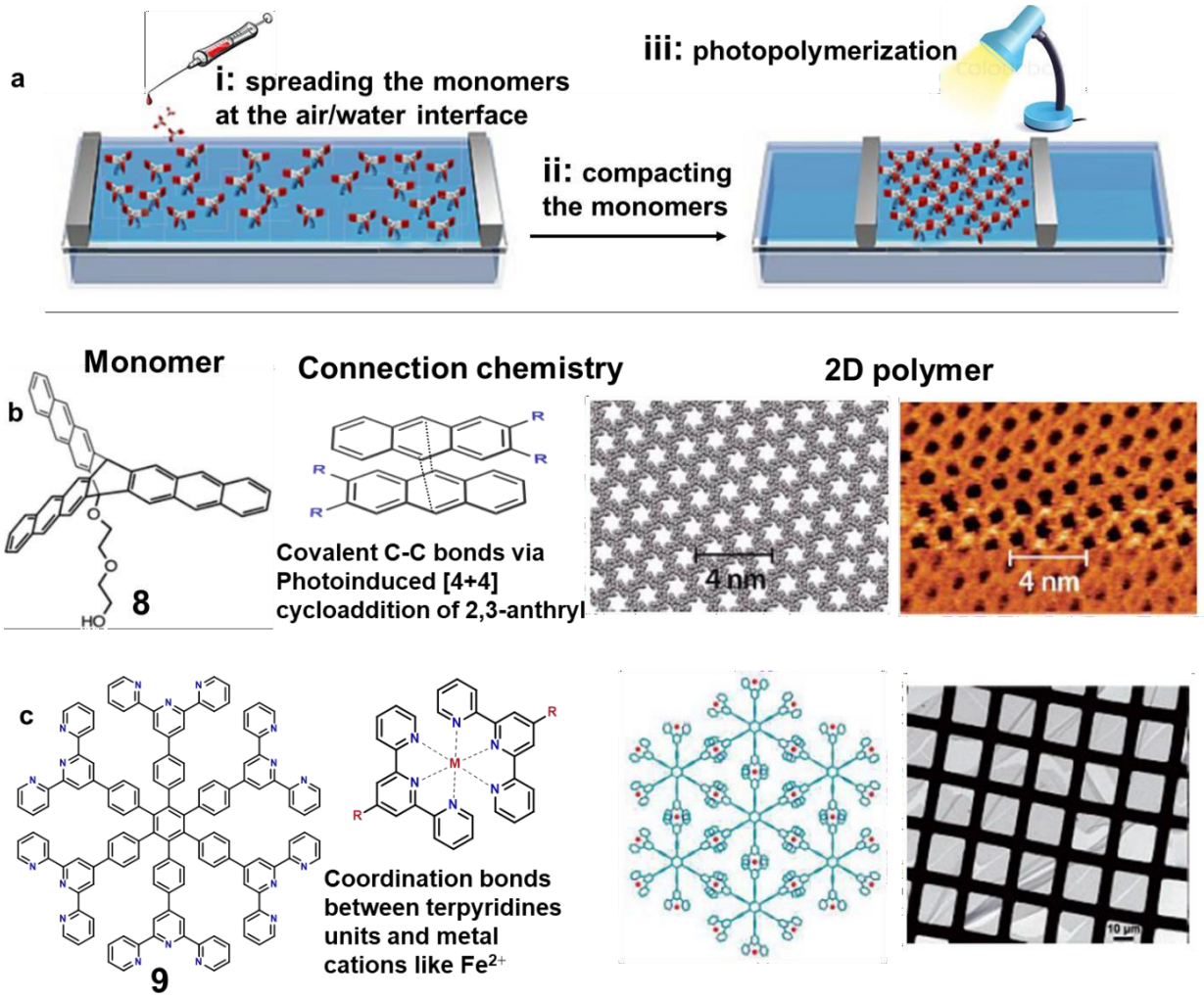

Figure 1.10 Cartoon (**a**) showing the Langmuir trough method and chosen examples of monomers with different external stimulus sources for polymerization. Adapted with permission from reference [127]. Copyright 2016, Annual Reviews. (**b**) Amphiphilic monomer **8** and STM image of polymer. Adapted with permission from reference [186]. Copyright 2015, American Chemical Society. (**c**) Two-dimensional metal organic framework (2D-MOF) synthesized with terpyridine-based monomer **9** and SEM image, which verified free-standing monolayer. Adapted with permission from reference [201]. Copyright 2011 John Wiley and Sons.

1.5 Calcium carbide as a monomer to synthesis 2DPs

Unlike the acetylene gas, calcium carbide is easy to handle, cheap, and safe to use in laboratory and industry as a source of *in situ* acetylene gas. Friedrich Wöhler discovered this method of acetylene gas release in 1862.[202, 203] In 2006, Cheng et al. used calcium carbide to synthesis symmetric diaryl ethynes from aryl bromide. So far calcium carbide has been utilized as a source of triplet bond in just few reports of organic synthesis.[204] On the other hand, in two-dimensional structure synthesis, the crucial points are intermediate planarity and rigidity.

Therefore, based on our experience, the calcium carbide is an ideal candidate to fulfill these requirements, because Ca ions derived from calcium carbide could coordinate with metal or other atoms bearing rigidity of a monomer. As a result, calcium carbide can be considered a new monomer in 2D polymer. It can provide (1) a source of triplet bond and (2) act as a chelating agent to make the intermediate rigid and provide enough geometrical barrier for in plane rotation. Recently, highly crystalline graphene (few-layers) was formed from reaction between calcium carbide and water at room temperature, and no pressure applied.[205] In this reaction C_2^{2-} anions contribute their electrons to oxidative species which are presenting in water (like H^+), followed by coupling reaction to synthesis a graphene as 2D conjugated sp^2 network. More recently calcium carbide was used to form a N-doped carbon porous network at room temperature inside a ball mill (mechanochemical synthesis).[206] There was an inverse relation between electrical conductivity and nitrogen content, in which carbon network with 16 wt% nitrogen (highest) shows less electrical conductivity compare to that of with less nitrogen content. Therefore, we believe CaC_2 with a mild condition is promising monomer for synthesis of different layered networks for broad applications.

2 Scientific goals

Within the emerging field of nanomaterials, graphene and carbon nanotubes are of high interest for many applications due to their unique chemical and physicochemical properties, which can be tailored for specific purposes. In this thesis two different challenges for the future applications of carbon nanotubes and graphene will be addressed and solved. First challenge is to establish and characterize a new method to solve the long standing problem in CNT covalent functionalization. Typically, useful physicochemical properties of CNTs are due to the disruption of the π-conjugated system of this nanomaterial upon covalent functionalization. This problem leads to creation of defects and consequently quenching the photoluminescence emission of tubes. Therefore, we will establish a new non-destructive covalent approach (by nitrene [2+1] cycloaddition reaction), which rebuilds the structural integrity of CNTs after functionalization, thereby retaining the opteoelectronic features of carbon nanotubes. Moreover, we pursue current challenges for the preparation of graphene derivatives with defined functionality and exposure. The problem originated from the uncontrolled reaction for the functionalization of graphene and lack of step-wise controlled functionalization methods.[207] Consequently, it was planned to use the nitrene [2+1] cycloaddition reaction based on triazine-azide to functionalize graphene at low temperature, unlike the often reported reactions at high temperature[73] (above 100 °C). A mild reaction condition to control functionalization of graphene by nitrene [2+1] cycloaddition reaction will be demonstrated. After conjugation of triazine groups on to the surface of graphene, they will be used for the controlled and stepwise post-modification of this nanomaterial.

Apart from natural 2D structure (graphene), in the 2D synthetic polymers, the designing of a monomer, its polymerization toward a 2D structure and control the two-dimensionality of final structure are still big problems. Therefore, in the last project, we have developed a new strategy to improve the 2D synthesis approaches using triazine and calcium carbide as monomers. Cyanuric chloride contributes as the source of triazine units in the structure, while calcium carbide provided both acetylide linkages and calcium ions. During the *in situ* polymerization calcium ions can coordinate to the nitrogen atom of triazine and provide enough rigidity to induce a two-dimensional triazine heterostructure with several micrometer lateral sizes.

3 Publications and manuscripts

3.1 Controlled Covalent Functionalization of Thermally Reduced Graphene Oxide to Generate Defined Bifunctional 2D Nanomaterials

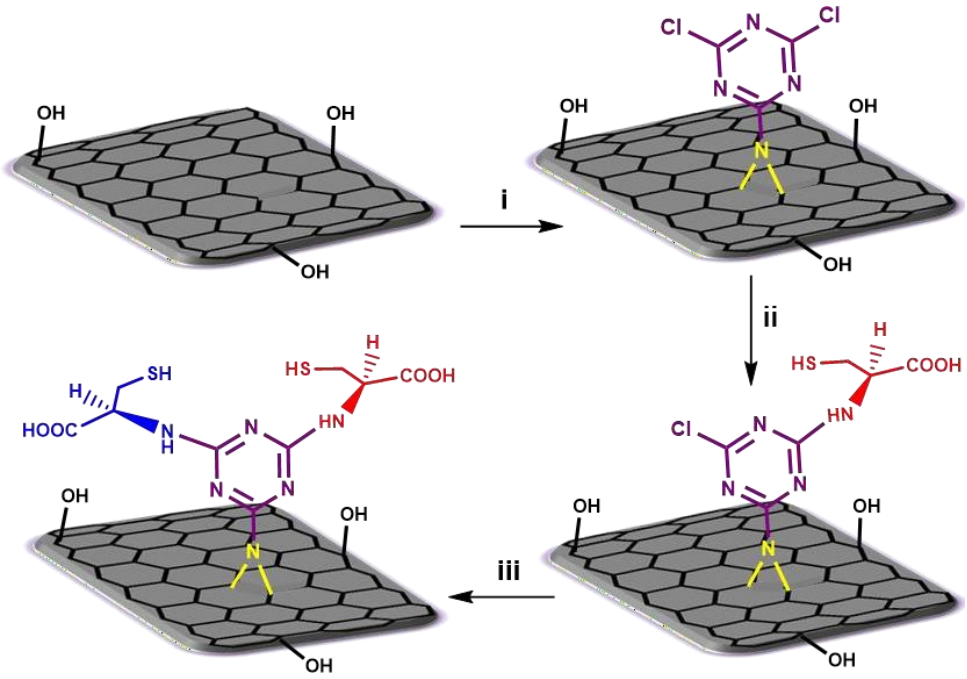

Abbas Faghani, Ievgen S. Donskyi, Mohammad Fardin Gholami, Benjamin Ziem, Andreas Lippitz, Wolfgang E. S. Unger, Christoph Böttcher, Jürgen P. Rabe, Rainer Haag and Mohsen Adeli.

Angew. Chem. Int. Ed. **2017**, 56, 2675–2679.
DOI: 10.1002/anie.201612422.

Author contributions

Abbas Faghani carried out all syntheses, main experiments, and wrote the manuscript. Ievgen S. Donskyi, Andreas Lippitz and Wolfgang E. S. Unger performed XPS and NEXAFS analyses. Mohammad Fardin Gholami and Jürgen P. Rabe performed the SFM and analyzed the data. Benjamin Ziem provided the thermally reduced graphene oxide (TRGO). Christoph Böttcher helped by the Cryo-TEM analysis. Mohsen Adeli and Rainer Haag conceived and supervised the project, as well as corrected the manuscript.

Preserving π-Conjugation in Covalently Functionalized Carbon Nanotubes for Optoelectronic Applications

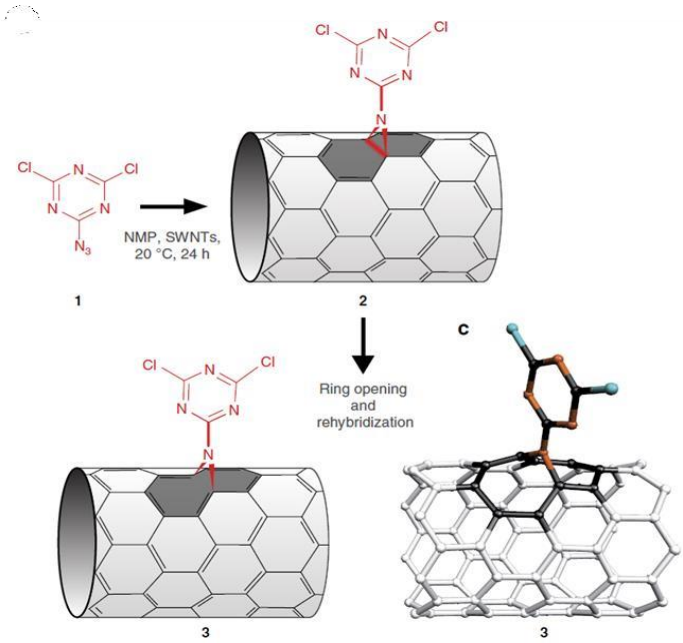

Antonio Setaro, Mohsen Adeli, Mareen Glaeske, Daniel Przyrembel, Timo Bisswanger, Georgy Gordeev, Federica Maschietto, **Abbas Faghani**, Beate Paulus, Martin Weinelt, Raul Arenal Rainer Haag & Stephanie Reich.

Nat. Commun. **2017**, 8, 14281-14287.
https://doi.org/10.1038/ncomms14281

Author contributions

Abbas Faghani and Mohsen Adeli performed the chemistry part including synthesis and characterizing the functionalized SWNTs as well as intermediates and participate in writing the manuscript. Antonio Setaro, Mohsen Adeli, Rainer Haag, and Stephanie Reich conceived the experiment, analyzed the data, and wrote the manuscript. All authors discussed the data and helped writing the manuscript. Mareen Glaeske and Antonio Setaro did the optical measurements. Timo Bisswanger, Antonio Setaro, and Mareen Glaeske followed the AuNPs attachment onto the tubes. Georgy Gordeev performed the Raman measurement. Daniel Przyrembel and Martin Weinelt performed XPS analysis. Raul Arena did the TEM and EELS studies. Federica Maschietto and Beate Paulus did computational calculations.

nature COMMUNICATIONS

ARTICLE

Received 4 Nov 2016 | Accepted 15 Dec 2016 | Published 30 Jan 2017

DOI: 10.1038/ncomms14281 OPEN

Preserving π-conjugation in covalently functionalized carbon nanotubes for optoelectronic applications

Antonio Setaro[1], Mohsen Adeli[2,3], Mareen Glaeske[1], Daniel Przyrembel[1], Timo Bisswanger[1], Georgy Gordeev[1], Federica Maschietto[3], Abbas Faghani[3], Beate Paulus[3], Martin Weinelt[1], Raul Arenal[4,5], Rainer Haag[3] & Stephanie Reich[1]

Covalent functionalization tailors carbon nanotubes for a wide range of applications in varying environments. Its strength and stability of attachment come at the price of degrading the carbon nanotubes sp^2 network and destroying the tubes electronic and optoelectronic features. Here we present a non-destructive, covalent, gram-scale functionalization of single-walled carbon nanotubes by a new [2π1] cycloaddition. The reaction rebuilds the extended π-network, thereby retaining the outstanding quantum optoelectronic properties of carbon nanotubes, including bright light emission at high degree of functionalization (1 group per 25 carbon atoms). The conjugation method described here opens the way for advanced tailoring nanotubes as demonstrated for light-triggered reversible doping through photochromic molecular switches and nanoplasmonic gold-nanotube hybrids with enhanced infrared light emission.

[1] Department of Physics, Free University Berlin, Arnimallee 14, 14195 Berlin, Germany. [2] Faculty of Science, Department of Chemistry, Lorestan University, Khorram Abad 68151-44316, Iran. [3] Institute of Chemistry and Biochemistry, Free University Berlin, 14195 Berlin, Germany. [4] Laboratorio de Microscopias Avanzadas (LMA), Instituto de Nanociencia de Aragon, Universidad de Zaragoza, 50018 Zaragoza, Spain. [5] Fundacion ARAID, 50018 Zaragoza, Spain. Correspondence and requests for materials should be addressed to M.A. (email: aadeli@zedat.fu-berlin.de) or to R.H. (email: haag@zedat.fu-berlin.de) or to S.R. (email: sreich@zedat.fu-berlin.de).

The unique optoelectronic properties of carbon nanotubes originate from their singular mixture of sp^2 carbon bonding, one-dimensional character and suppressed dielectric screening[1]. This makes them ideal building blocks for applied optoelectronics as nanometre-scale light sources, photodetectors and photovoltaic devices[2]. Nanotubes were demonstrated as optical rectifying antennas converting electromagnetic radiation at optical frequencies to direct current[3] and as single-photon sources at room temperature[4]. Their stability and compatibility with many environments, including biological systems, makes them optically detectable carriers of drugs and radiotracers as demonstrated for *in vivo* localization and imaging[5]. Bio-imaging greatly benefits from the wavelength at which single-walled carbon nanotubes (SWNTs) emit light; it lies in the second window of tissue transparency (1,100–1,400 nm) with a large penetration depth, but low tissue scattering and autofluorescence[6,7].

Optoelectronic applications heavily rely on the read-out of the SWNT fluorescence. For this, the p-conjugated structure of the individual nanotube needs to be preserved[8], as optical excitation and emission of SWNTs are ruled by the p-electrons of the carbon backbone[1,8,9]. A disruption of the p-network by rehybridization from the sp^2 to the sp^3 configuration degrades the conjugation, increases the number of non-radiative scattering centres and quenches the overall SWNTs luminescence[10]. At the same time, the p-conjugation and p–p interactions are the driving force of a strong tube bundling. This prevents luminescence through energy transfer into metallic tubes followed by non-radiative recombination[8].

Only individual SWNTs are strong light emitters and various types of functionalization have been pursued to isolate, stabilize and tailor them[11]. Endohedral functionalization fills the nanotubes, whereas covalent and non-covalent exohedral functionalizations operate onto the SWNT sidewalls[11]. Endohedral filling preserved the electronic properties of SWNTs[12,13] but is limited to small molecules that fit into the tubes (inner diameter $\mathbf{O}2$ nm). The exohedral non-covalent approach is based on physisorption of the targeted functionality onto the SWNTs[11]. It preserves the p-conjugation of the sp^2 network. However, changes in the environment easily reverse the functionalization and trigger desorption making this method inherently unstable. The covalent exohedral approach is advantageous in that it strongly binds the functionalities onto the SWNTs by converting a fraction of the sp^2 into sp^3 carbons. Its current implementations, however, interrupt the electronic properties of the nanotubes and quench their luminescence[8,10,11,14]. Alternative approaches such as mechanically interlocking nanotubes likewise resulted in reduced light emission[15].

New covalent methods are needed, which combine the p-conjugation of the SWNTs with a stable functionalization. They will have to operate under mild conditions and rebuild a fully sp^2 p-conjugated system. The [2þ1] cycloaddition reactions have the potential to solve this challenge, because they exploit the p electrons for attachment instead of requiring dangling bonds[16–18]. A first example of such mild [2þ1] cycloaddition has been recently reported based on an electron-poor aromatic azide[19,20]. This reaction initially transforms two p-electrons of the carbon network to a covalent three-membered ring bridge (closed configuration). A subsequent rehybridization step that releases the strained C–C bond underlying the bridge and reconverts the two C atoms back to the sp^2 state recovering the aromaticity of the system (open configuration) has only been studied theoretically[21–23]. Lee and Marzari[21] proposed to exploit the open configuration with dichlorocarbene to not disrupt the transport properties of metallic SWNTs. Experimentally, however, neither the carbene nor the nitrene addition have yielded the open structure and no improvement of the optoelectronic properties of the nanotubes has been reported[16,18,24,25].

Here we develop a [2þ1] cycloaddition reaction based on electron-poor aromatic nitrenes that preserves the p-conjugated electronic structure and infrared light emission. Our functionalization method is universal and may conjugate many different functionalities to the surface of SWNTs. It is highly robust, but non-destructive for the unique properties of carbon nanotubes. The functional groups become an integral part of the extended conjugated network. We show light-triggered reversible doping of SWNTs for nanotubes with photochromic molecular switches. Gold nanoparticles (AuNPs) offer a covalent attachment of plasmonic structures, leading to an enhanced luminescence. The two examples highlight the versatility of our platform for hybrid systems with distinctive photoelectronic properties.

Results

p-Preserving triazine conjugation onto the SWNTs. We introduce a [2þ1] reaction based on azidodichloro-triazine 1 (Fig. 1) that *in situ* generates the corresponding nitrene to form the intermediate SWNT adduct (2). As predicted for such highly strained intermediates, ring-opening and rehybridization forms fully conjugated hetero-bridged nanotubes (3) in a single synthetic step. In this way, the electron lone pair of the bridging nitrogen atom becomes part of the p-conjugated system of the SWNT, increasing its electron density.

The highly reactive electron-poor precursor monoazidodichloro-triazine 1 was selectively prepared at 0 C *in situ* from commercially available compounds[26,27] (Supplementary Fig. 1 and Supplementary Note 1). It conjugates onto SWNT through [2þ1] cycloaddition at 20 C to form intermediate 2, which ring opens to the final rehybridized structure 3. Quantum chemical calculations predict that the entire reaction proceeds without activation barrier at room temperature (300 K; Supplementary Fig. 17). In the fully relaxed structure (Fig. 1c), the triazine covalently bridges onto the nanotubes with a binding energy of 4.2 eV. The covalent attachment was also proven by thermogravimetric analysis (Supplementary Fig. 5). The obtained open configuration minimally distorts the carbon p-orbitals (Supplementary Note 2). The number of functional groups attached to the nanotubes is adjusted by the reaction temperature (20–70 C)[28,29]. We present exemplary a low-density functionalization with one triazine ring per 100 carbon atoms (SWNT-low) and a high-density functionalization with one triazine ring per 25 carbon atoms (SWNT-high). For details on the synthesis, the characterization of the intermediate products and the functionalized SWNTs, please refer to the Method section and Supplementary Notes 1 and 3.

X-ray photoelectron spectroscopy of the N1s level shows that the pristine SWNT sample was free of nitrogen (Fig. 2a). The triazine conjugated samples 3 (SWNT-low and SWNT-high) clearly display nitrogen peaks (Fig. 2a), which increased by a factor of 4.3 ± 0.5 between the two samples, in agreement with the elemental analysis (see Supplementary Note 3). This proves the successful tuneable decoration of the nanotubes with dichlorotriazine. With increasing nitrogen coverage we observe an exponential and uniform shift of the C1s XP spectra to higher binding energy (up to 200 meV for SWNT-high, see Supplementary Fig. 29). This reflects an increasing Fermi energy, because the nitrogen lone pair interacts with the nanotube. High-resolution scanning transmission electron microscopy (STEM) and electron energy loss spectroscopy (EELS) prove the outcome of the functionalization on a single nanotube level[30]. In Fig. 2b, we show a high-angle annular dark field high-resolution STEM micrograph of a SWNT-high together with spatially resolved

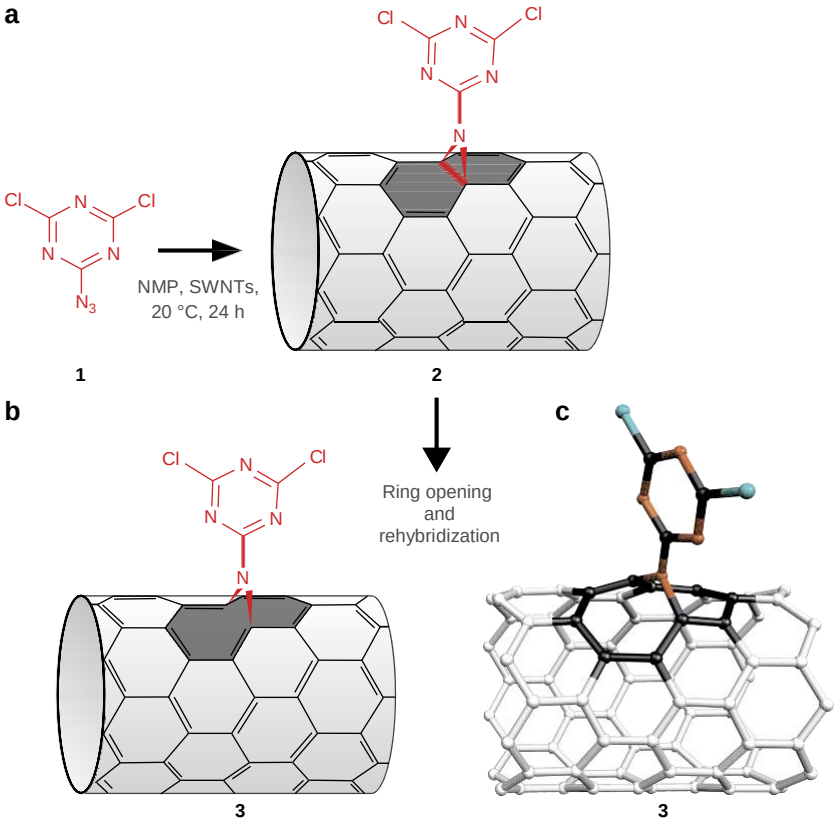

Figure 1 | One-pot functionalization of carbon nanotubes by heterocyclic [2þ1] cycloaddition reaction. (a) After establishment of the heterocyclic bridge between azidodichloro-triazine 1 and SWNTs, (b) the cycloaddition product (2) undergoes ring opening and rehybridization of the C atoms underlying the bridge and is converted into the form (3) with regenerated p-conjugation. (c) Quantum chemically optimized molecular configuration of the triazine on an (8,0) nanotube.

EELS spectra at the nitrogen edge. The spectra, taken in the regions marked by squares in the STEM image, clearly prove the localization of nitrogen in the external sidewall of the SWNTs (region ii, Fig. 2b right).

Our covalent functionalization is unique as it preserves the sp^2 character of the conjugated carbon nanotubes, see EELS analyses in Supplementary Note 1. Raman spectra show a constant intensity of the defect-induced D-mode (Fig. 2c)[9]. The ratio between the D and G bands reflects the fraction of sp^3 atoms and other defects in an sp^2 carbon system. Even at highest functionalization (SWNT-high, one triazine ring per 25 carbon atoms) the ratio remained identical to the pristine material $I_D/I_G \approx 0.1$, proving that no conversion of C atoms from sp^2 to sp^3 occurred. The outcome of conjugating triazine (1) onto the SWNT is thus the ring-open compound (3).

The triazine-functionalized SWNTs show strong light emission, because the p-network was kept intact. The overall two-dimensional luminescence intensity of SWNT-high is identical to that of the pristine tubes (Fig. 2d). Each of the spots in Fig. 2d univocally confirms the presence of a specific (n,m) SWNT species[8] and their unperturbed p-conjugated system for the SWNT-high sample[10]. Some functionalized species show even brighter emission than their pristine counterparts (compare, for example, the (9,4) tube in the left and right panel of Fig. 2d). The increase in light emission is due to the change in chemical potential by the triazine conjugated onto the tubes. Raman measurements showed an initial position of the Fermi level 70 meV away from the Dirac point (see Supplementary Fig. 30, Supplementary Table 6 and Supplementary Note 4). For SWNT-high, the Fermi level is within 20 meV of the intrinsic value, which increases the luminescence intensity. Emission from highly covalently functionalized carbon nanotubes has never been reported before and disproves the dogma that covalent functionalization always quenches nanotube emission.

Advanced photoelectronic applications of SWNTs require further customization of the tubes. For optoelectronics, for example, the emission should be controlled through external parameters. Sensing and imaging in biological environment, on the other hand, benefit from enhanced overall emission. With such applications in mind, we present two functional examples for covalently tailored luminescent SWNTs: A conjugated photochromic molecular switch to control the emission from the SWNTs and covalently attached AuNPs to plasmonically enhance the nanotubes optical response.

Photochromic molecular switches-based conjugation. Photochromic molecular switches are molecular systems displaying two or more (meta-)stable configurations with distinctive chemo-physical features[31]. On irradiation with photons, they change their configuration and properties. As a prominent example, spiropyran (SP) on irradiation with ultraviolet light (λ = 350 nm) passes from the closed to the open merocyanine (MC) form (see Fig. 3). We covalently connected SP to SWNTs, which made the switch an active part of the extended p-network (Fig. 3a, see Methods and Supplementary Note 1 for the synthesis and characterization).

The SWNTs carried one SP group every 100 carbon atoms. Under ultraviolet irradiation the SP-functionalized SWNTs (SP-SWNTs) hybrids convert into MC-SWNTs by the molecular

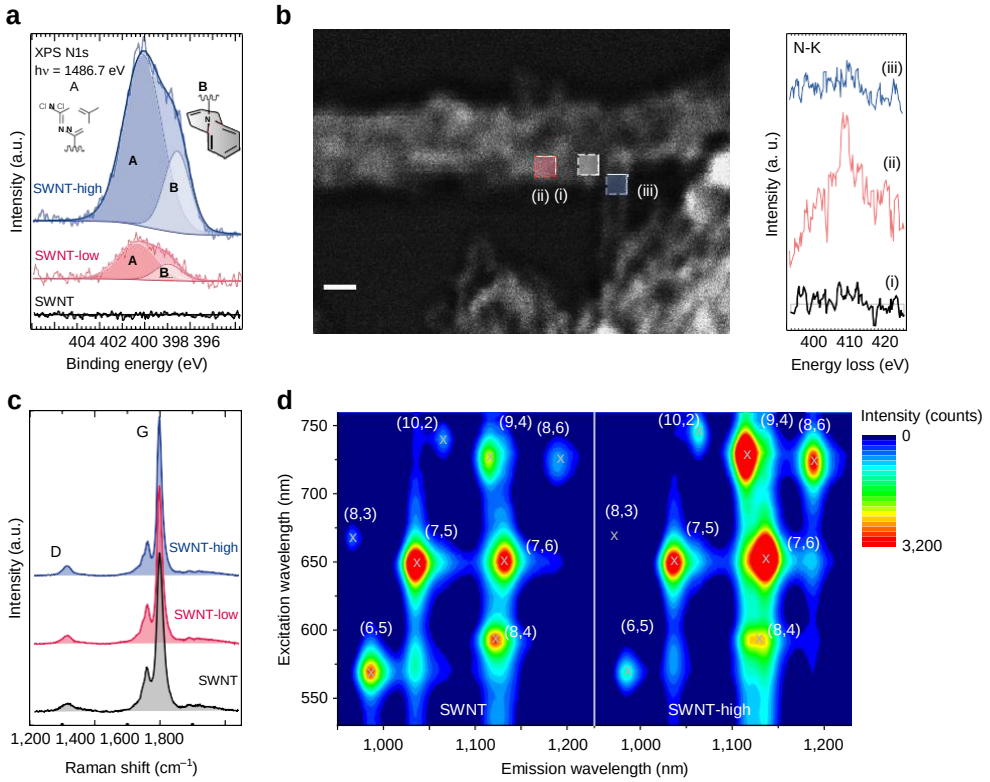

Figure 2 | Demonstration of p-conjugation preserving functionalization. (a) X-ray photoelectron spectroscopy (XPS) spectra of the N1s level of pristine and functionalized SWNTs. (b) High-resolution STEM–high-angle annular dark field (HRSTEM–HAADF) micrograph of the SWNT-high sample, showing a bundle of SWNTs and an individual tube. Scale bar, 2 nm. The regions marked by squares were investigated by EELS, see Supplementary Information. The inset on the right shows the corresponding N-K edge EEL spectra. (c) Raman spectra showing the D and G bands of samples with different density of functional groups. (d) Two-dimensional (2D) luminescence maps of pristine SWNTs compared with SWNT-high. The (*n*,*m*) indices specify the SWNT species associated with each emission spot.

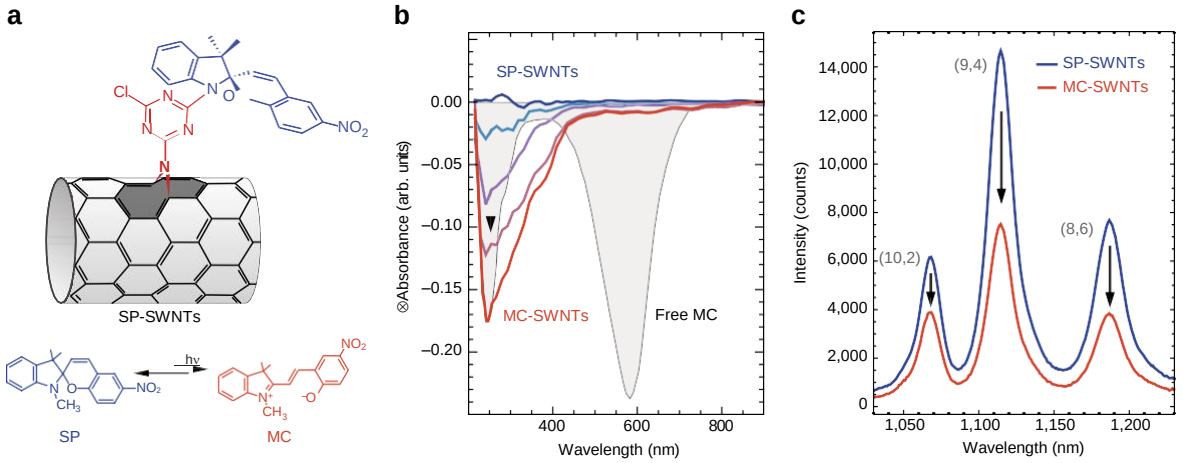

Figure 3 | SP-conjugated SWNTs. (a) Schematic representation of the SP-SWNTs. (b) Absorption spectrum of the SP-SWNTs under ultraviolet light irradiation at 367 nm. Grey: absorption spectrum of free MC. (c) Emission spectra of the SP-SWNTs (blue) and of the MC-SWNTs (red), obtained after ultraviolet irradiation.

switching from SP to MC as seen by the characteristic change in the ultraviolet absorption band in Fig. 3b and Supplementary Fig. 33. The isomerization is reversible by keeping the sample in darkness for 24 h. Interestingly, the light-induced back isomerization, MC-to-SP, is supressed for functionalized SWNTs. Indeed, MC-SWNTs display no characteristic band in the visible reminiscent of the free MC (Fig. 3b). This absorption is observed for free MC and ascribed to the p-electron delocalized along the MC structure[32]. For MC-SWNT, the p-electron is no longer confined to the MC but can extend over the whole conjugated MC-SWNTs network. This delocalization over a few hundreds of nanometres shifts the transition energy in the far infrared outside of our measurement windows[33]. The net effect of the SP to MC isomerization on the SWNTs is a further increase in the Fermi level. We effectively and reversibly dope the SWNTs by exposing them to ultraviolet photons. This idea is supported by a shift of

the Raman G-band from SP-SWNTs to MC-SWNTs (see Supplementary Fig. 32)[34].

The shift of 2 cm ^{1} in semiconducting tubes corresponds to 0.2 eV change in the energy of the Fermi level[34]. This also reduced the rate of radiative exciton emission[35–37]. We observed a quenching of 50% emission intensity when passing from SP- to the MC-SWNTs (see Fig. 3c). The intensity fully recovers when MC thermally isomerizes back to SP.

Covalently functionalizing SWNTs with SP thus offers a novel controlled, non-disruptive and reversible way to tailor the optoelectronic properties of nanotubes. Through ultraviolet photons we change the Fermi level and modulate light emission by SWNTs. SP-SWNTs could lead to light-switchable ballistic transport channels.

Plasmonically enhanced emission. In a second application we demonstrate nanoplasmonic-hybridized SWNTs as brighter fluorophores, for example, for increasing resolution in bio-imaging[6,7]. The collective oscillations of free electrons in metal nanoparticles give rise to electromagnetic resonances (plasmons) that strongly enhance optical signals from nearby molecules[38–40]. To bind plasmonic AuNPs onto the SWNTs, we exploit covalently anchored thiol groups onto the tubes (thiol-functionalized SWNT (SH-SWNT)) as sketched in Fig. 4a, in the Methods section and summarized in Supplementary Fig. 1. TEM microscopy of the resulting Au@SWNT hybrids shows the AuNPs assembled along the sidewall of the SWNTs (see Fig. 4b). This assembly is stable towards environmental changes yet again confirming the covalent nature of the functionalization method.

The functionalization with plasmonic particles markedly increased the luminescence of the SWNTs, which neither happened for defect functionalization nor simple assembly (Supplementary Note 5). The emission of Au@SWNT hybrids in Fig. 4c is two to three times stronger than for uncoated tubes. As only a small fraction of the nanotubes spatially overlaps with the AuNP near field, the increase in the emission cross-section is much higher. Luminescence peak position and width remained constant between pristine and Au@SWNT. The intensity increase originated from an enhanced excitation (absorption) through the strongly localized near-fields around the metallic particle. Interestingly, the maximum enhancement efficiency is obtained for species with excitation windows red-shifted from the AuNP plasmonic resonance (Supplementary Fig. 36), consistent with other coupled emitter-nanometal systems[41].

The functionalization of carbon nanotubes with dichloro-triazine preserves the electronic and optoelectronic properties of SWNTs. Such functionalized nanotubes are versatile building blocks for nanophotonic hybrids as we demonstrated with two exemplary structures.

Methods

Synthesis of the functionalized tubes. HiPCO SWNTs (length: 0.2–1.2 μm, diameter: 0.8–1.2 nm) were purchased from Unidym (batch SP0295). The 2,4,6-trichloro-1,3,5-triazine (cyanuric chloride or triazine), 2,3,3-trimethylindolenine and 5-nitrosalicylaldehyde were purchased from Sigma-Aldrich. Sodium azide and *N*-methyl-2-pyrrolidone were purchased from Merck. A schematic depiction of the reaction steps described below can be found in Supplementary Fig. 1.

Conjugating triazine onto the SWNTs: SWNT-low and SWNT-high. Pristine SWNTs (1 g) were added to *N*-methyl-2-pyrrolidone (150 ml), sonicated for 1 h and then stirred at room temperature for an additional 1 h. The 2,4,6-1,3,5-trichloro-triazine (10 g, 54 mmol) dissolved in *N*-methyl-2-pyrrolidone (50 ml) was added to the mixture at 0 C and stirred for 20 min. Sodium azide (1.76 g, 27 mmol) in solid state was gradually added to the reaction flask at 0 C; the mixture was stirred at this temperature for 2 h. The temperature was raised to 25 C and stirred for 1 h. Operating at low temperature ensures the substitution of only one chlorine atom[42,43]. We thus converted 2,4,6-trichloro-1,3,5-triazine into 2-azido-4,6-dichloro-1,3,5 triazine and prevented the creation of more complicated structures such as di- or tri-azide derivatives, or C_3N_4 graphitic materials[44]. Details of the characterization of the intermediate product can be found in the Supplementary Information. Thereafter, the suspension was stirred overnight at a temperature of 25 C (SWNT-low) and at 70 C (SWNT-high). The mixtures were centrifuged (5,000 r.p.m. for 5 min) and the crude products were dispersed in acetone and centrifuged again under the same condition. Dispersion and centrifugation of the product was repeated in water, toluene and chloroform to obtain the purified compounds. The products were lyophilized to obtain 1.08 g black solid compound of SWNT-low and 1.03 g black solid compound of SWNT-high.

Synthesis of SP-SWNTs. The synthesis of the SP derivatives for the SP-SWNTs was performed by the Wagenknecht method[45]. The conjugation of SP onto the SWNTs is a two-step process requiring first the attachment of the indole group onto the triazine to be used for the growth of the SP. SWNT-low (0.2 g) was dispersed in *N*-methyl-2-pyrrolidone (150 ml) and sonicated for 1 h. The 2,3,3-Trimethylindolenine (2 ml, 12.47 mmol) dissolved in *N*-methyl-2-pyrrolidone (10 ml) was added to this mixture at 0 C and stirred for 1 h. The mixture was sonicated at room temperature for 1 h and the temperature was raised to 65 C. Finally, the mixture was stirred under nitrogen atmosphere for 4 days. It was centrifuged at 7,000 r.p.m. for 10 min, washed by acetone, chloroform,

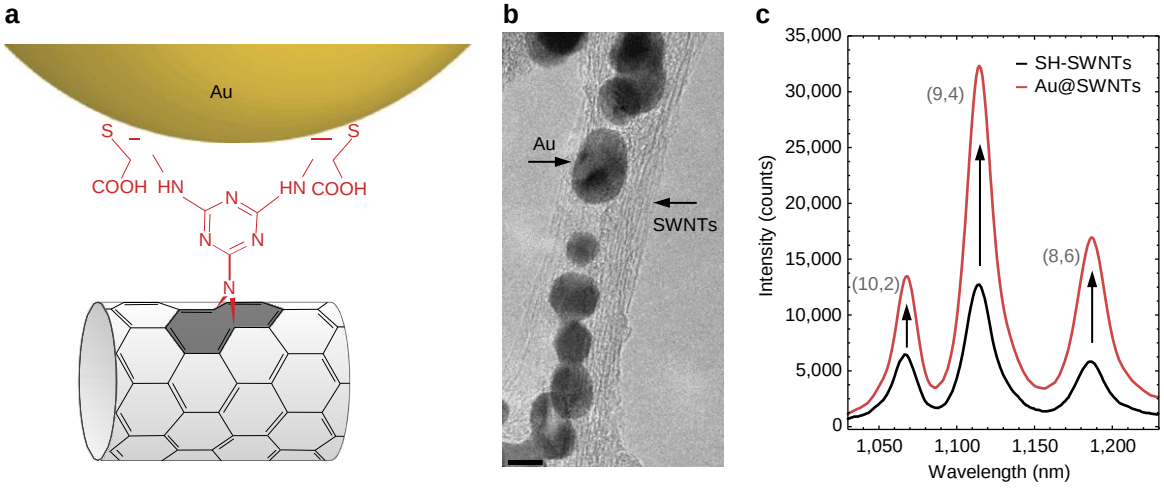

Figure 4 | Plasmonic hybrids of AuNP and SWNT. (a) Molecular sketch of AuNPs covalently anchored to SH-SWNTs. (b) TEM micrograph of Au@SWNTs hybrids. Scale bar, 5 nm. A few-SWNTs bundle can be observed and AuNPs assembled along the tubes. (c) Enhancement of the luminescence emission of SWNTs after covalent attachment of AuNPs onto their surface: comparison of the emission of the Au@SWNT hybrids (red curve) with the one of SH-SWNT (black curve).

tetrahydrofuran (THF) and water, and collected by centrifugation. The product was lyophilized overnight obtaining 0.19 g black solid compound of SWNT-indole. The intermediate step required SWNT-indole to be added to a saturated solution of NaOH in water and sonicated for 30 min. The mixture was stirred for 5 h at room temperature and the final product (SWNT-indolene) was purified by repeated washing with water and centrifugation. For the characterization of the reaction of dichlorotriazene with dimethyl indoline, please refer to Supplementary Note 1. The final step required to add an excess amount of 5-nitrosalicylaldehyde (2.5 g, 1.19 mmol) at 25 C to a well-sonicated and degassed dispersion of SWNT-indolene (0.1 g) in dry ethanol (70 ml). The mixture was sonicated at 25 C with 35 kHz for 2 h and stirred at 70 C overnight. Finally, the solvent was evaporated, the mixture dispersed in ethanol, chloroform, water, toluene and acetone, and collected by centrifugation at 5,000 r.p.m. for 5 min.

Synthesis of SH-SWNT. Based on the protocols for the nucleophilic substitution of the chlorine atoms of the triazine reported in literature, cysteine was conjugated to the triazine functional groups[42,43,46]. SWNT-high (100 mg) was dispersed in dimethylfomamide (50 ml) and sonicated for 15 min at room temperature. Next, cysteine (1 g, 8.2 mmol) and triethylamine (1.72 ml, 12.3 mmol) were added to the mixture that was stirred at 65 C for 2 days. The mixture was then dialysed for 1 week in water. We lyophilized the product and 90 mg black compound of SH-SWNT was obtained.

Sample preparation. To solubilize the carbon nanotubes, we dissolved them in water (density of tubes 0.1 g l ^{1}) and added sodium cholate (SC, 1 wt %). Following the routine described in our past works[47,48], the solution was sonicated with a tip-sonicator (Bandelin Sonopuls HD 2070) for 1 h at 60 W and then centrifuged (Hettich Mikro 220 R centrifuge) at 30,000 *g* for 1 h. The supernatant was collected and used for optical measurements. For the functionalized nanotubes, we corrected the values of the density of functionalized nanotubes dissolved in water by taking into account the mass change due to the attachment of the functionalities (fraction of SWNT enlisted in Supplementary Table 4).

The AuNPs were synthesized according to the Turkevich method[49]. We obtained spherical AuNPs with diameters 10–20 nm. The plasmon absorption band peaked at 520 nm (Supplementary Fig. 34). The Au@SWNT hybrids were created by adding 200 ml of 0.1 g l ^{1} thiol-SWNTs into 1,000 ml of the AuNP solution. The mixture was stirred overnight. To promote further debundling we added SC (1 wt%) to the solutions and applied mild sonication for 1 h at 20 W. After decantation, the supernatant was used for spectroscopic characterization. For TEM imaging of the Au@SWNTs, we dropped 5 ml of the solution onto a nickel grid covered with a lossy carbon film. The grid was placed over a heating plate until complete evaporation of the liquid.

Experimental details. Two-dimensional luminescence was recorded with a Nanolog spectrofluorometer from Horiba, equipped with a Xenon lamp and a liquid-Nitrogen cooled InGaAs detector. Ultraviolet–visible–infrared absorption spectra were taken with a Perkin-Elmer Lambda 950 spectrophotometer. Kinetic absorption measurements under ultraviolet illumination were performed with a spectrophotometer from Thermo-Fisher. The ultraviolet light source was a hand-held ultraviolet lamp emitting at 365 nm. The Raman spectra were acquired with a Horiba LabRam spectrometer equipped with an He-Ne laser (633 nm). The TEM measurement of the Au@SWNTs were taken with a transmissions electron microscope FEI Tecnai G^{2} 20 S-TWIN with LaB6-cathode, 120 kV acceleration voltage and a GATAN MS794 CCD acquistion camera, with 1,024 1,024 pixels and point resolution of 0.24 nm. Details on the X-ray photoelectron spectroscopy as well as on the HR(S)TEM and EELS setups can be found in the Supplementary Methods.

Quantum chemical calculations. Calculations were performed using MOPAC2016 (http://openmopac.net/). The geometries of the (8,0) nanotube, the nitrenes and the nanotube-addend (nitrenes) systems were fully optimized at the PM7 level using a minimal basis set[50]. The climbing image nudged elastic band method[51] was used to determine transition state configurations and barrier energies for the cycloaddition reaction (see Supplementary Note 2 for details).

Data availability. The data supporting the findings of this study are available within the article and its Supplementary Information files, and from the corresponding author upon reasonable request.

References

1. Wang, F., Dukovic, G., Brus, L. E. & Heinz, T. F. The optical resonances in carbon nanotubes arise from excitons. *Science* 308, 838–841 (2005).
2. Avouris, P., Freitag, M. & Perebeinos, V. Carbon-nanotube photonics and optoelectronics. *Nat. Photonics* 2, 341–350 (2008).
3. Sharma, A., Singh, V., Bougher, T. L. & Cola, B. A. A carbon nanotube optical rectenna. *Nat. Nanotechnol.* 10, 1027–1032 (2015).
4. Ma, X., Hartmann, N. F., Baldwin, J. K. S., Doorn, S. K. & Htoon, H. Room-temperature single-photon generation from solitary dopants of carbon nanotubes. *Nat. Nanotechnol.* 10, 671–675 (2015).
5. Hong, S. Y. *et al.* Filled and glycosylated carbon nanotubes for *in vivo* radioemitter localization and imaging. *Nat. Mater.* 9, 485–490 (2010).
6. Welsher, K. *et al.* A route to brightly fluorescent carbon nanotubes for near-infrared imaging in mice. *Nat. Nanotechnol.* 4, 773–780 (2009).
7. Hong, G. *et al.* Multifunctional *in vivo* vascular imaging using near-infrared II fluorescence. *Nat. Med.* 18, 1841–1846 (2012).
8. O'Connell, M. J. *et al.* Band gap fluorescence from individual single-walled carbon nanotubes. *Science* 297, 593–596 (2002).
9. Thomsen, C. & Reich, S. Raman scattering in carbon nanotubes, light scattering in solid IX. *Topics Appl. Phys.* 108, 115–232 (2007).
10. Cognet, L. *et al.* Stepwise quenching of exciton fluorescence in carbon nanotubes by single-molecule reactions. *Science* 316, 1465–1468 (2007).
11. Hirsch, A. Functionalization of single-walled carbon nanotubes. *Angew. Chem. Int. Ed.* 41, 1853–1859 (2002).
12. Cambré, S. *et al.* Asymmetric dyes align inside carbon nanotubes to yield a large nonlinear optical response. *Nat. Nanotechnol.* 10, 248–252 (2015).
13. Gaufrès, E. *et al.* Giant Raman scattering from J-aggregated dyes inside carbon nanotubes for multispectral imaging. *Nat. Photonics* 8, 72–78 (2014).
14. Piao, Y. *et al.* Brightening of carbon nanotube photoluminescence through the incorporation of sp^{3} defects. *Nat. Chem.* 5, 840–845 (2013).
15. de Juan, Y. *et al.* Mechanically interlocked single-wall carbon nanotubes. *Angew. Chem. Int. Ed.* 53, 5394–5400 (2014).
16. Kumar, I., Rana, S. & Cho, J. W. Cycloaddition reactions: a controlled approach for carbon nanotube functionalization. *Chem. Eur. J.* 17, 11092–11101 (2011).
17. Holzinger, M. *et al.* Sidewall functionalization of carbon nanotubes. *Angew. Chem.* 40, 4002–4005 (2001).
18. Gao, C., He, H., Zhou, L., Zheng, X. & Zhang, Y. Scalable functional group engineering of carbon nanotubes by improved one-step nitrene chemistry. *Chem. Mater.* 21, 360–370 (2009).
19. Park, J. & Yan, M. Covalent functionalization of graphene with reactive intermediates. *Acc. Chem. Res.* 46, 181–189 (2013).
20. Pastine, S. J. *et al.* A facile and patternable method for the surface modification of carbon nanotube forests using perfluoroarylazides. *J. Am. Chem. Soc.* 130, 4238–4239 (2008).
21. Lee, Y.-S. & Marzari, N. Cycloaddition functionalizations to preserve or control the conductance of carbon nanotubes. *Phys. Rev. Lett.* 97, 116801 (2006).
22. Chen, Z. *et al.* Side-wall opening of single-walled carbon nanotubes (SWCNTs) by chemical modification: a critical theoretical study. *Angew. Chem. Int. Ed.* 43, 1552–1554 (2004).
23. Li, J., Jia, G., Zhang, Y. & Chen, Y. Bond-Curvature effect of sidewall [2 1] cycloadditions of single-walled carbon nanotubes: a new criterion to the adduct structures. *Chem. Mater.* 18, 3579–3584 (2006).
24. Zhang, K., Zhang, Q., Liu, C., Marzari, N. & Stellacci, F. Diameter effect on the sidewall functionalization of single-walled carbon nanotubes by addition of dichlorocarbene. *Adv. Funct. Mater.* 22, 5216–5223 (2012).
25. Holzinger, M. *et al.* Functionalization of single-walled carbon nanotubes with (R-)oxycarbonyl nitrenes. *J. Am. Chem. Soc.* 125, 8566–8580 (2003).
26. Hart, C. V. Carbonic acid azides. *J. Am. Chem. Soc.* 50, 1922–1930 (1928).
27. Kayama, R., Hasunama, S., Sekiguchi, S. & Matsui, K. The thermal reactions of azido-1,3,5-triazines. *Bull. Chem. Soc. Jpn* 47, 2825–2829 (1974).
28. Bucher, G., Siegler, F. & Wolff, J. Photochemistry of 2-azido-4,6-dichloro-s-triazine: matrix isolation of a strained cyclic carbodiimide containing four nitrogen atoms in a seven-membered ring. *J. Chem. Commun.* 20, 2113–2114 (1999).
29. Adeli, M., Beyranvand, S. & Kabiri, R. Preparation of hybrid nanomaterials by supramolecular interactions between dendritic polymers and carbon nanotubes. *Polym. Chem.* 4, 669–674 (2013).
30. Arenal, R. & O. Stephan. Local TEM Spectroscopic Studies on Carbon and Boron Nitride-Based Nanomaterials, Ch 5, pp 139–170 (2015).
31. Klajn, R. Spiropyran-based dynamic materials. *Chem. Soc. Rev.* 43, 148–184 (2014).
32. Setaro, A., Bluemmel, P., Maity, C., Hecht, S. & Reich, S. Non-covalent functionalization of individual nanotubes with spiropyran-based molecular switches. *Adv. Funct. Mater.* 22, 2425–2431 (2012).
33. Gaude, D., Le Baccon, M., Guglielmetti, R. & Gautron, R. Photochromisme de spiropyrannes. Étude de la photodégradation de dérivé indoliniques substitués et polymériques. *Bull. Soc. Chim. Fr.* 9–10, 489–498 (1979).
34. Das, A. *et al.* Doping in carbon nanotubes probed by Raman and transport measurements. *Phys. Rev. Lett.* 99, 136803 (2007).
35. Kinder, J. M. & Mele, E. J. Nonradiative recombination of excitons in carbon nanotubes mediated by free charge carriers. *Phys. Rev. B* 78, 155429 (2008).
36. Steiner, M. *et al.* Gate-variable light absorption and emission in a semiconducting carbon nanotube. *Nano Lett.* 9, 3477–3481 (2009).
37. Yasukochi, S. *et al.* Gate-induced blue-shift and quenching of photoluminescence in suspended single-walled carbon nanotubes. *Phys. Rev. B* 84, 121409(R) (2011).

38. Maier, S. A. *Plasmonics: Fundamentals and Applications* (Springer, 2007).
39. Heeg, S. *et al.* Plasmon-enhanced Raman scattering by carbon nanotubes optically coupled with near-field cavities. *Nano Lett.* 14, 1762–1768 (2014).
40. Glaeske, M. & Setaro, A. Nanoplasmonic colloidal suspensions for the enhancement of the luminescent emission from single-walled carbon nanotubes. *Nano Res.* 6, 593–601 (2013).
41. Anger, P., Bharadwaj, P. & Novotny, L. Enhancement and quenching of single-molecule fluorescence. *Phys. Rev. Lett.* 96, 113002 (2006).
42. Whitesides, G. M. *et al.* Noncovalent synthesis: using physical-organic chemistry to make aggregates. *Acc. Chem. Res.* 28, 37–44 (1995).
43. Lim, J., Mintzer, M. A., Perez, L. M. & Simanek, E. E. Synthesis of odd generation triazine dendrimers using a divergent, macromonomer approach. *Org. Lett.* 12, 1148–1151 (2010).
44. Guo, Q. *et al.* Synthesis of carbon nitride nanotubes with the C_3N_4 stoichiometry via a benzene-thermal process at low temperatures. *Chem. Commun.* 1, 26–27 (2004).
45. Bayer, C. & Wagenknecht, H. A. Synthesis of spiropyrans as building blocks for molecular switches and dyads. *J. Org. Chem.* 75, 2752–2755 (2010).
46. Mathias, J. P., Seto, C. T., Simanek, E. E. & Whitesides, G. M. Self-assembly through hydrogen bonding: preparation and characterization of three new types of supramolecular aggregates based on parallel cyclic CA_3*M_3 'Rosettes'. *J. Am. Chem. Soc.* 116, 1725–1736 (1994).
47. Setaro, A. *et al.* Polyglycerol-derived amphiphiles for single walled carbon nanotube suspension. *Chem. Phys. Lett.* 493, 147–150 (2010).
48. Popeney, C. S. *et al.* Polyglycerol-derived amphiphiles for the solubilization of single-walled carbon nanotubes in water: a structure-property study. *Chem. Phys. Chem.* 13, 203–211 (2012).
49. Turkevich, J., Stevenson, P. C. & Hillier, J. A study of the nucleation and growth processes in the synthesis of colloidal gold. *Discuss. Faraday Soc.* 11, 55–75 (1951).
50. Stewart, J. J. P. Optimization of parameters for semiempirical methods VI: more modifications to the NDDO approximations and re-optimization of parameters. *J. Mol. Model.* 19, 1–32 (2013).
51. Henkelman, G. & Jónsson, H. Improved tangent estimate in the nudged elastic band method for finding minimum energy paths and saddle points. *J. Chem. Phys.* 113, 9978–9985 (2000).

Acknowledgements

We gratefully acknowledge the German Research Foundation (DFG via SFB 658, subprojects A6, B7 and Z) and the Focus Area NanoScale of the Freie Universität Berlin for financial support. We thank S. Selve of the ZELMI (Technical University of Berlin) for the TEM measurements of the Au@SWNT hybrids, and A. Wimmer and K. Huth for their support. High-resolution STEM and EELS studies were conducted at the Laboratorio de Microscopias Avanzadas, Instituto de Nanociencia de Aragon, Universidad de Zaragoza, Spain. R.A. acknowledges the Spanish Ministerio de Economia y Competitividad (FIS2013-46159-C3-3-P), the Government of Aragon and the European Social Fund under the project "Construyendo Europa desde Aragon" 2014–2020 (grant number E/26), the European Union Seventh Framework Program under Grant Agreements 312483- ESTEEM2 (Integrated Infrastructure Initiative – I3) and 604391 and 696656 Graphene Flagship, as well as from EU H2020 ETN project "Enabling Excellence" Grant Agreement 642742.

Author contributions

A.S., M.A., R.H. and S.R. conceived the experiment, analysed the data and wrote the manuscript. All authors discussed the results and commented on the manuscript. M.A. and A.F. synthesized and characterized the functionalized SWNTs. M.G. and A.S. performed the optical characterization of the samples. T.B., M.G. and A.S. pursued the AuNPs attachment onto the tubes. G.G. and S.R. performed the Raman characterization of the metallic SWNTs. D.P. and M.W. performed and evaluated the X-ray photoelectron spectroscopy analysis. R.A. performed the TEM and EELS studies. F.M. and B.P. performed quantum chemical calculations.

Additional information

Supplementary Information accompanies this paper at http://www.nature.com/naturecommunications

Competing financial interests: The authors declare no competing financial interests.

Reprints and permission information is available online at http://npg.nature.com/reprintsandpermissions/

How to cite this article: Setaro, A. *et al.* Preserving p-conjugation in covalently functionalized carbon nanotubes for optoelectronic applications. *Nat. Commun.* 8, 14281 doi: 10.1038/ncomms14281 (2017).

Publisher's note: Springer Nature remains neutral with regard to jurisdictional claims in published maps and institutional affiliations.

Supplementary Figures

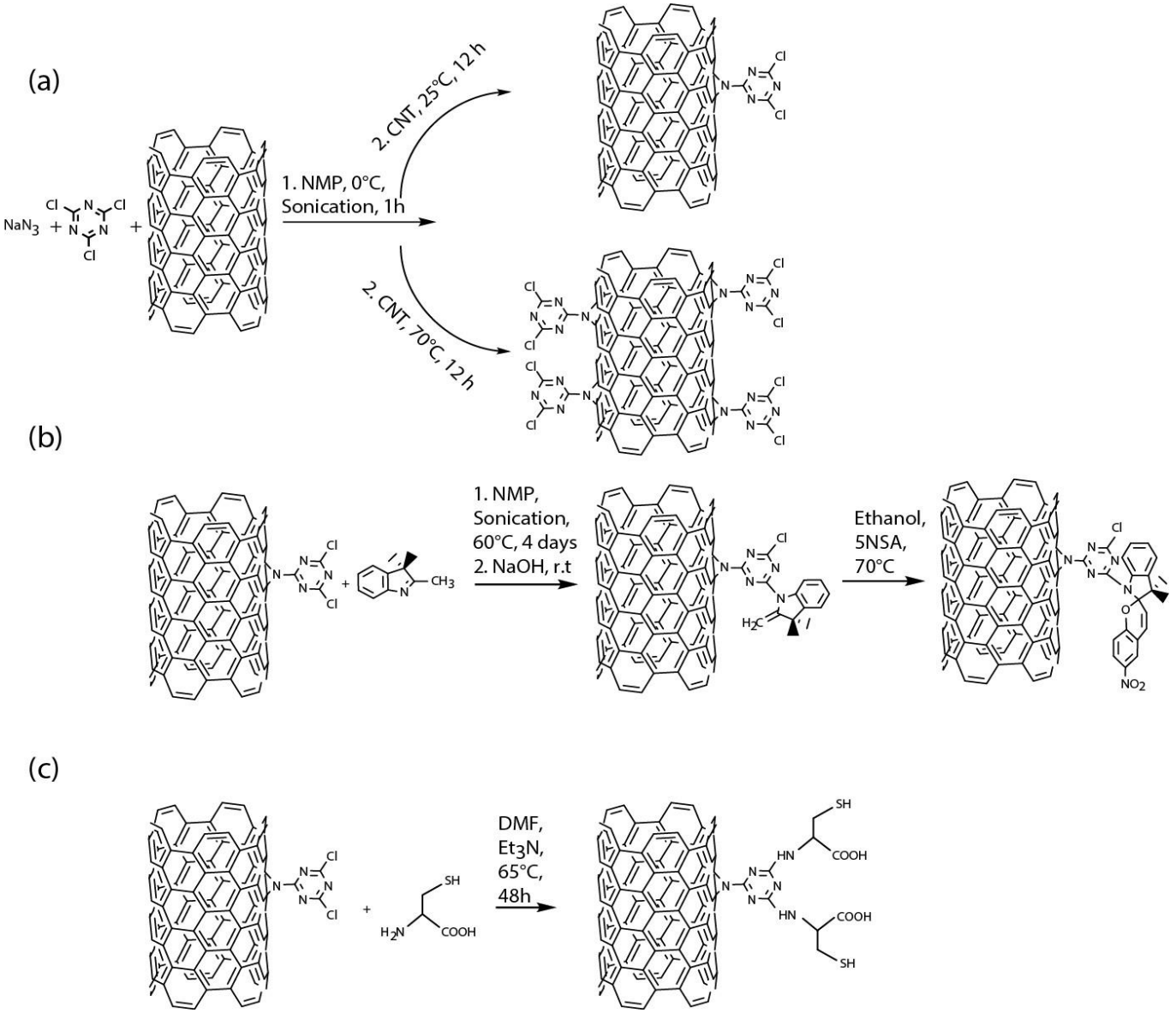

Supplementary Figure 1. Molecular sketches of the synthesis of: (a) SWNT-low and SWNT-high, (b) SP-SWNT via SWNT-indole, and (c) SH-SWNT.

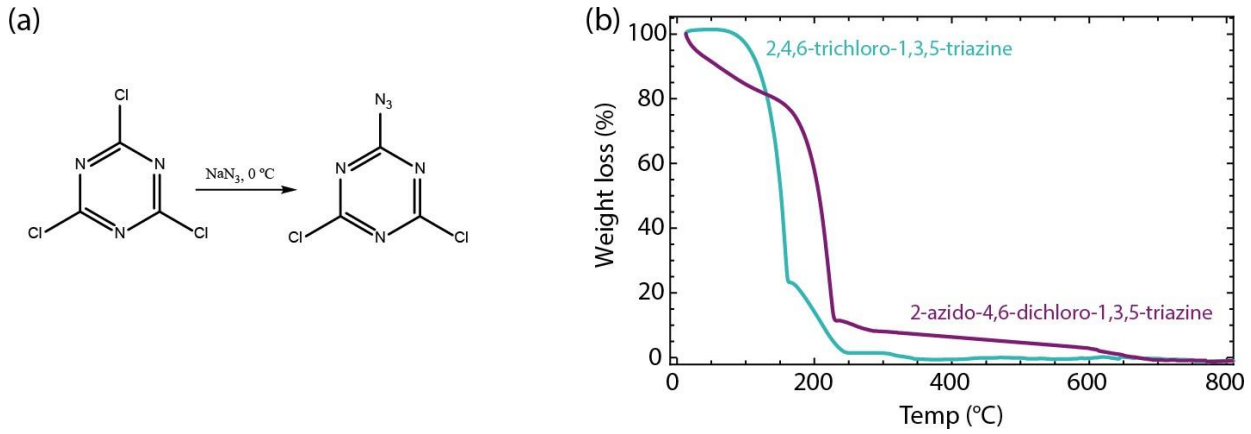

Supplementary Figure 2. (a) The reaction between sodium azide and 2,4,6-trichloro-1,3,5-triazine at low temperature results in the formation of 2-azido-4,6-dichloro-1,3,5-triazine. (b) TGA thermograms of 2,4,6-trichloro-1,3,5-triazine and 2-azido-4,6-dichloro-1,3,5-triazine.

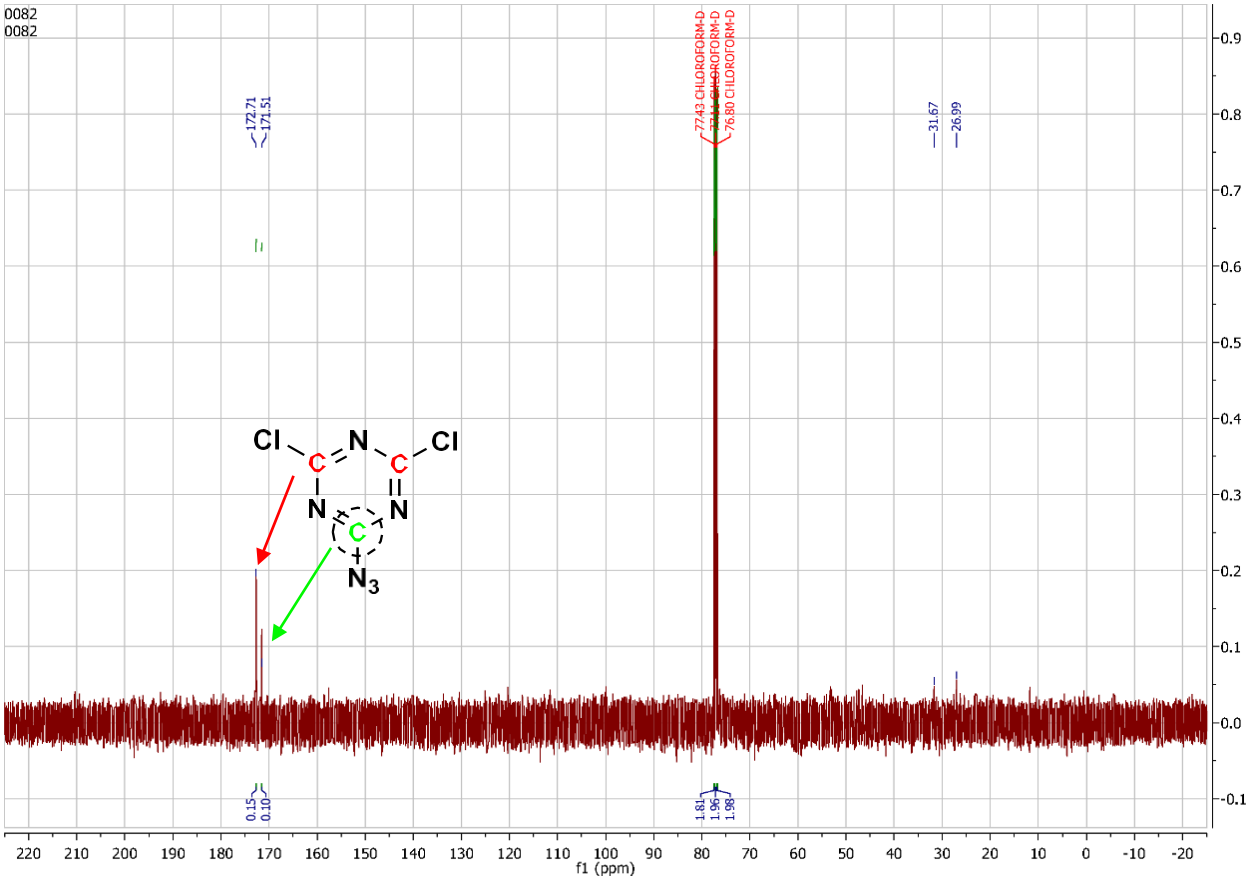

Supplementary Figure 3. ^{13}C NMR spectra of 2-azido-4,6-dichloro-1,3,5-triazine in $CDCl_3$.

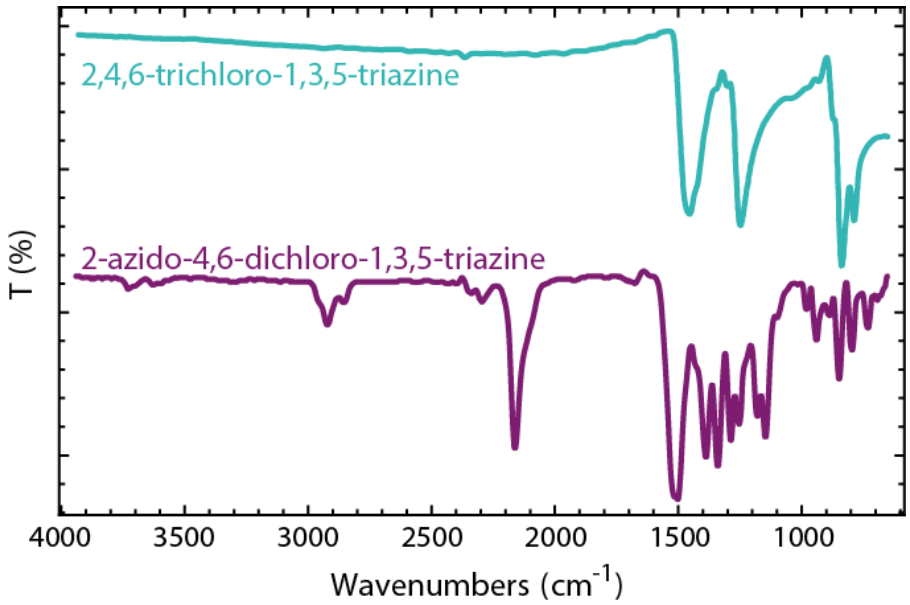

Supplementary Figure 4. IR spectra of 2,4,6-trichloro-1,3,5-triazine and 2-azido-4,6-dichloro-1,3,5-triazine.

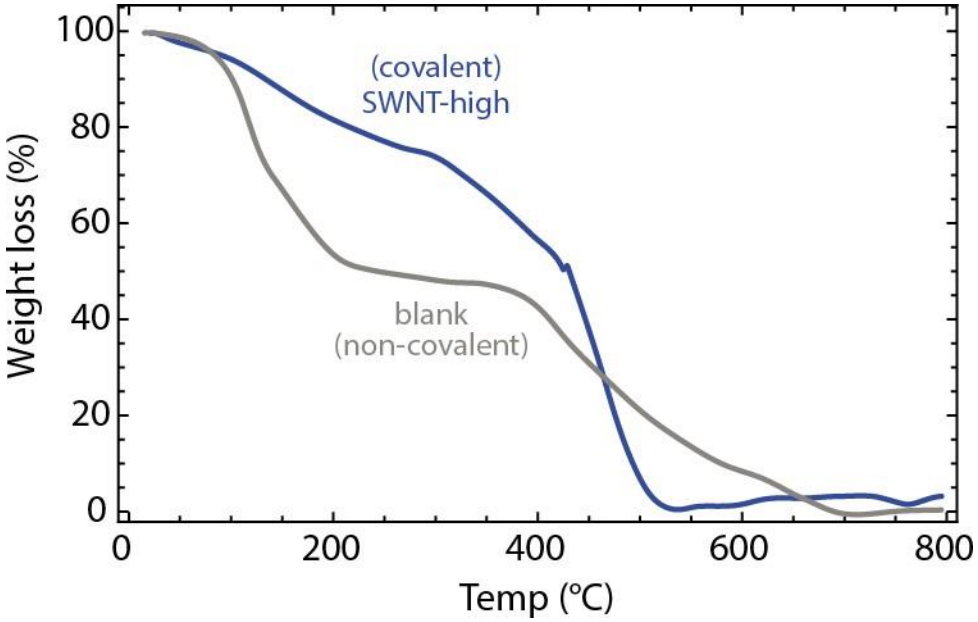

Supplementary Figure 5. TGA thermogram of mixture of SWNTs and 2,4,6-1,3,5-trichloro-triazine (blank) and SWNT-high (SWNT-high).

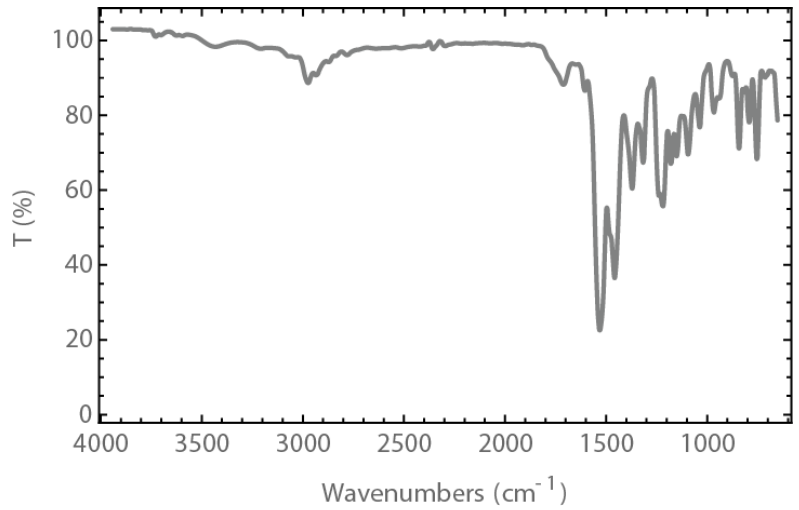

Supplementary Figure 6. IR spectra of 1-(4,6-dichloro-1,3,5-triazine)-2,3,3-trimethylindolinium chloride.

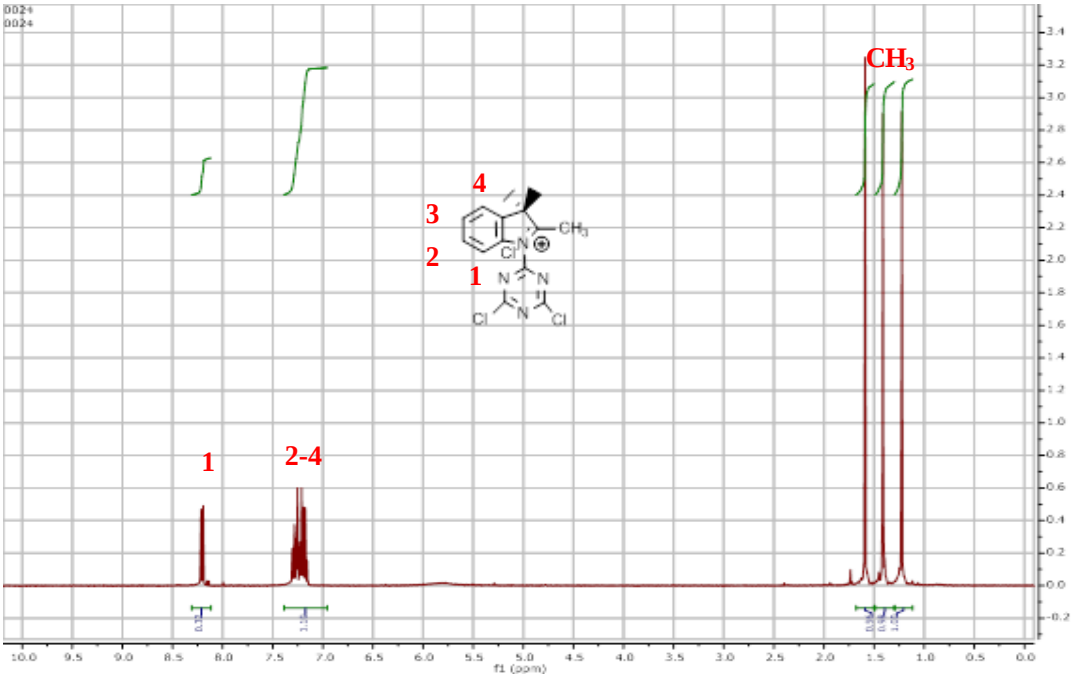

Supplementary Figure 7. ^{1}H NMR spectra of 1-(4,6-dichloro-1,3,5-triazine)-2,3,3-trimethylindolinium chloride in $CDCl_3$.

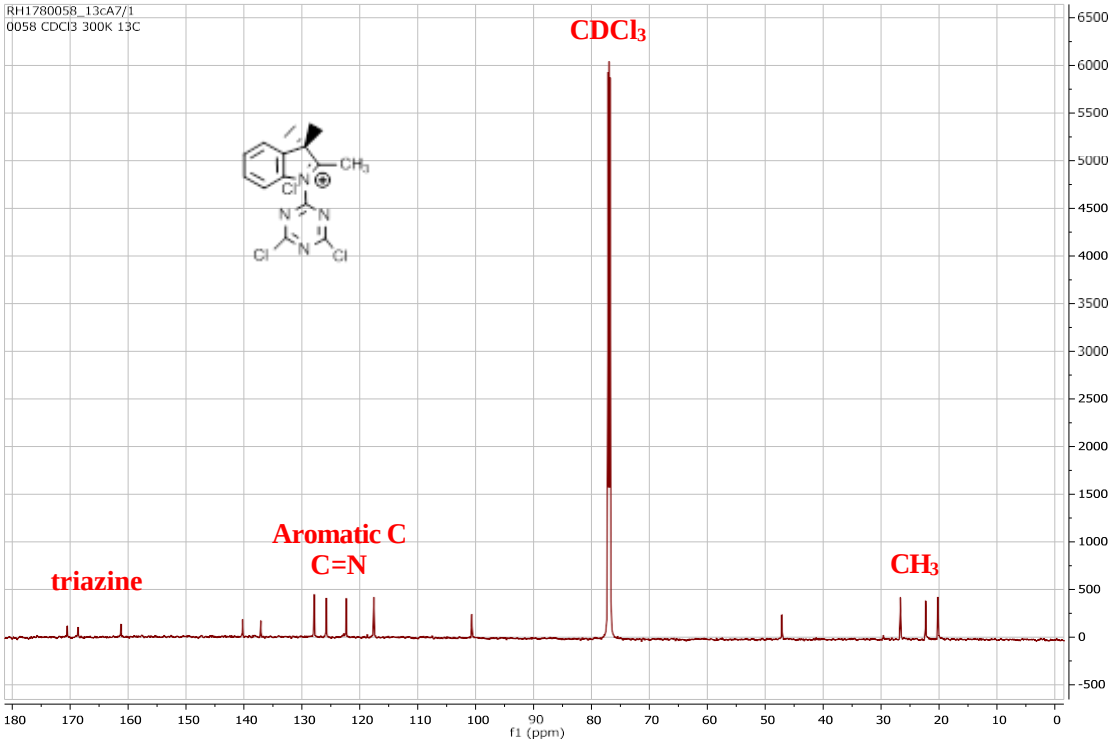

Supplementary Figure 8. ^{13}C NMR spectra of 1-(4,6-dichloro-1,3,5-triazine)-2,3,3-trimethylindolinium chloride in $CDCl_3$.

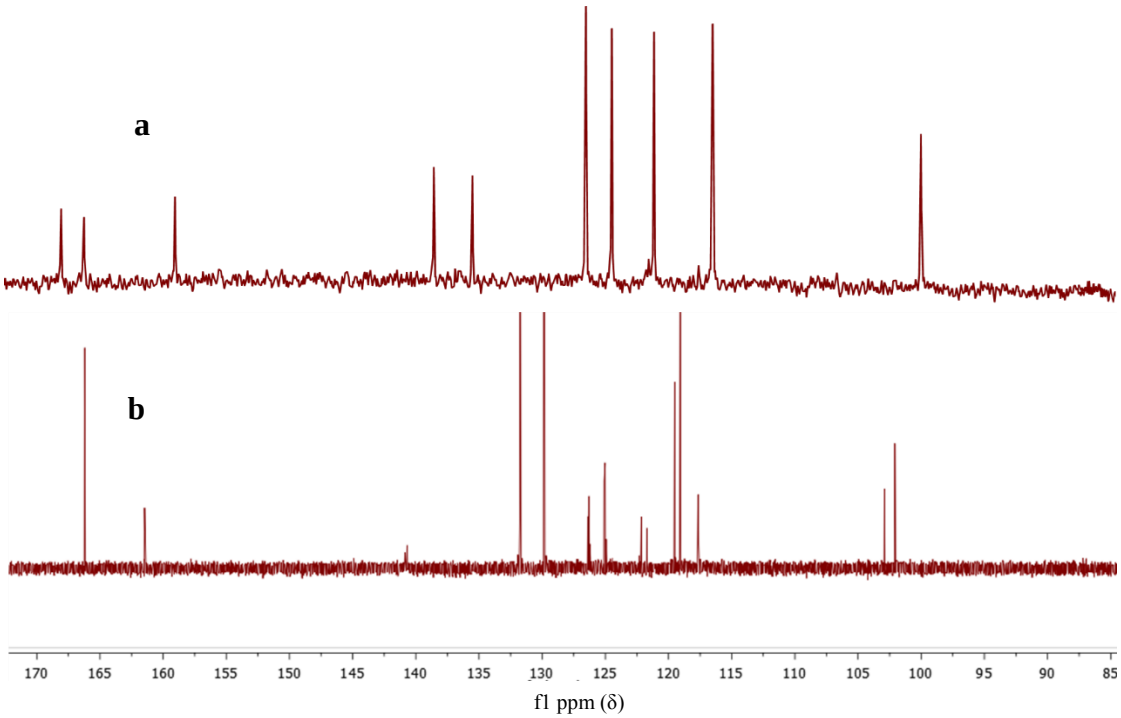

Supplementary Figure 9. ^{13}C NMR spectra of (a) 1-(4,6-dichloro-1,3,5-triazine)-2,3,3-trimethylindolinium chloride and (b) Synthesis of (R)-6-(3',3'-dimethyl-6-nitrospiro[chromene-2,2'-indolin]-1'-yl)-1,3,5-triazine-2,4-diol.

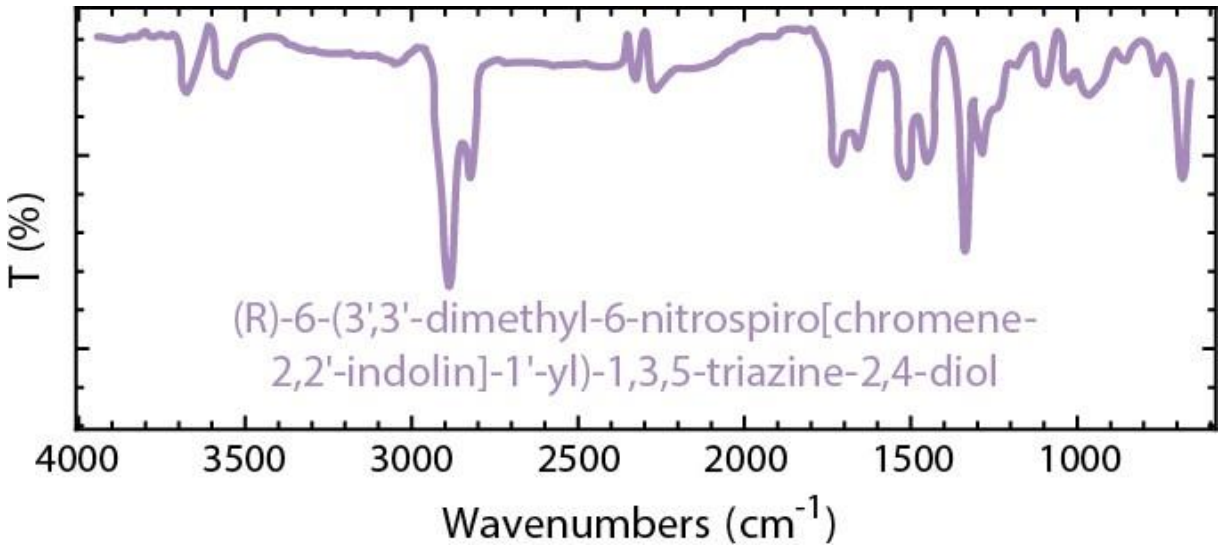

Supplementary Figure 10. IR spectrum of (R)-6-(3',3'-dimethyl-6-nitrospiro[chromene-2,2'-indolin]-1'-yl)-1,3,5-triazine-2,4-diol.

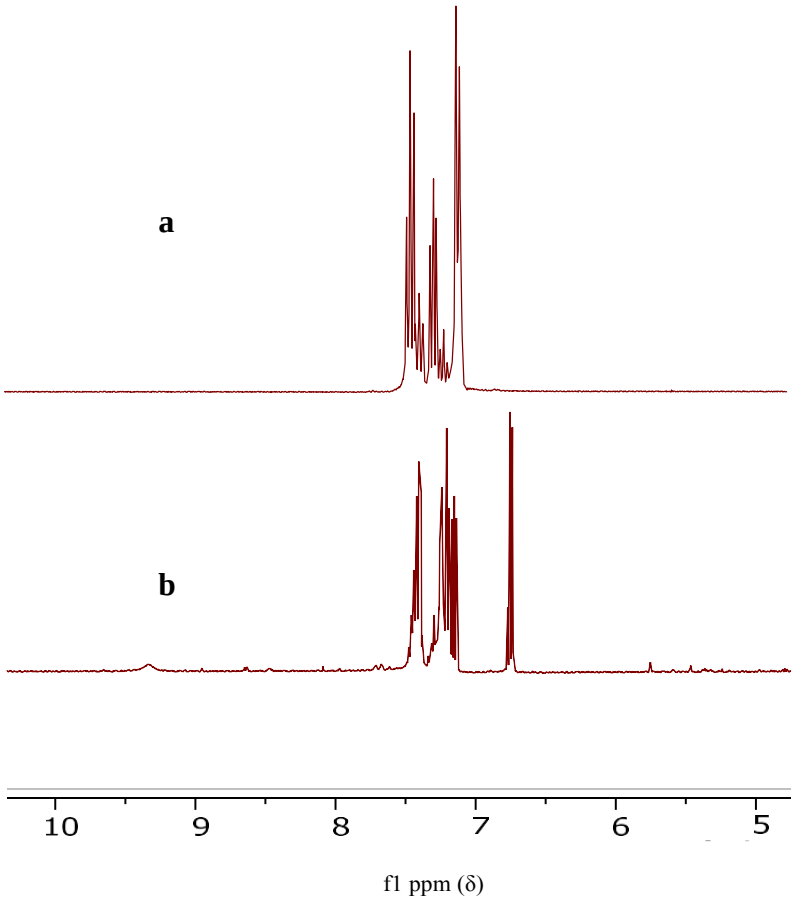

Supple me ntary Figure 11. ^{1}H NMR spectra of (a) 2-chloro-4,6-diphenoxy-1,3,5-triazine and (b) (4,6-diphenoxy-1,3,5-triazin-2-yl)-L-cysteine.

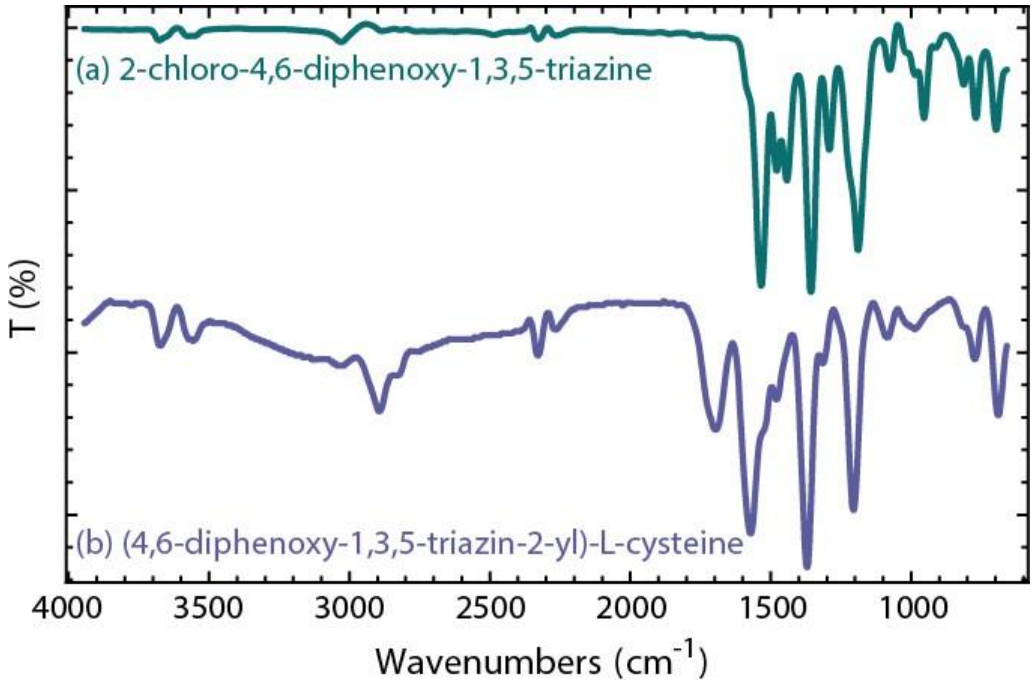

Supple me ntary Figure 12. IR spectra of a) 2-chloro-4,6-diphenoxy-1,3,5-triazine and b) (4,6-diphenoxy-1,3,5-triazin-2-yl)-L-cysteine.

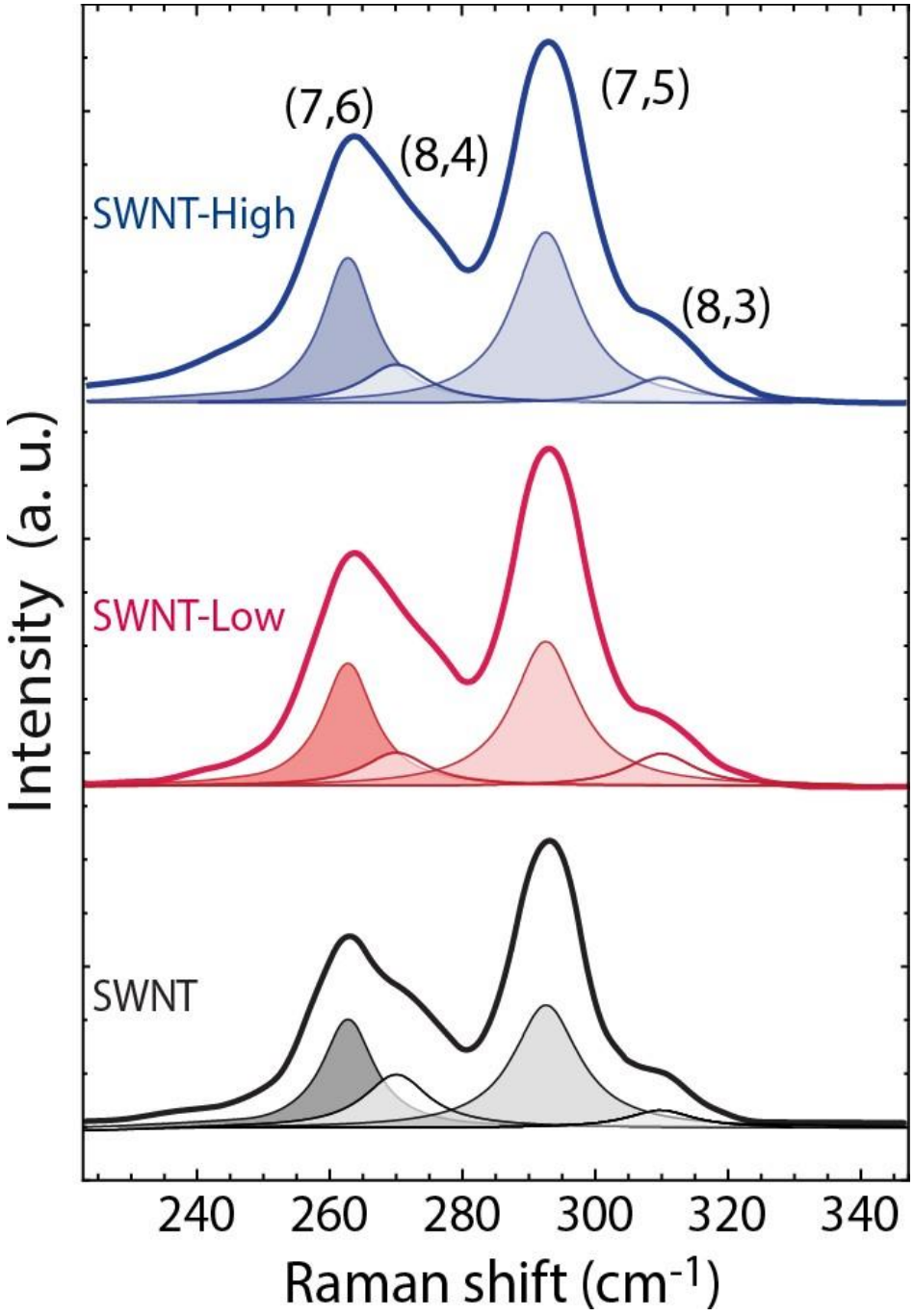

Supplementary Figure 13. Raman spectra in the RBM region of pristine and triazine-functionalized nanotubes.

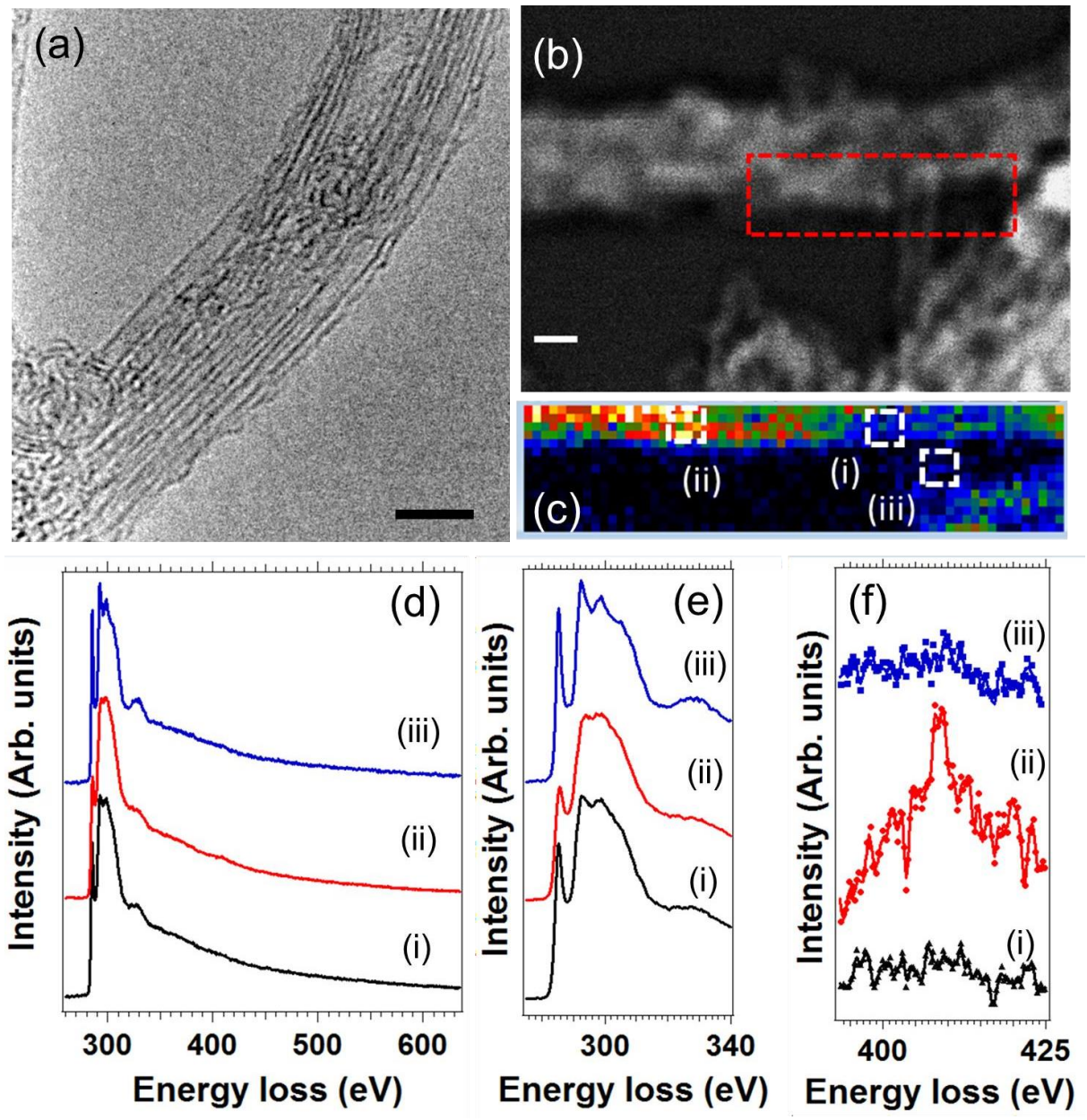

Supplementary Figure 14. (a) HRTEM micrograph of a bundle of single-walled nanotubes (SWNT-high sample). The scale bar is 5 nm. (b) HAADF-STEM image of another rope of 3 or 4 single-walled CNTs. An EELS SPIM has been recorded in the red marked area of this image. The scale bar is 2 nm. (c) Nitrogen map extracted from the EELS-SPIM. (d) Sums of 9 selected EEL spectra collected from the three different marked areas in the SPIM, Fig. 14b. While the C-K edge is visible in all the spectra, the N-K edge is only visible in the red (Fig. 14d-(ii)) EEL spectrum. (e) and (f) C- and N-K edges extracted from the EEL spectra of the Fig. 14d, respectively. To filter noise, spectra of Fig. 14f were smoothed using a Savitzky−Golay filter (second-order polynomial).

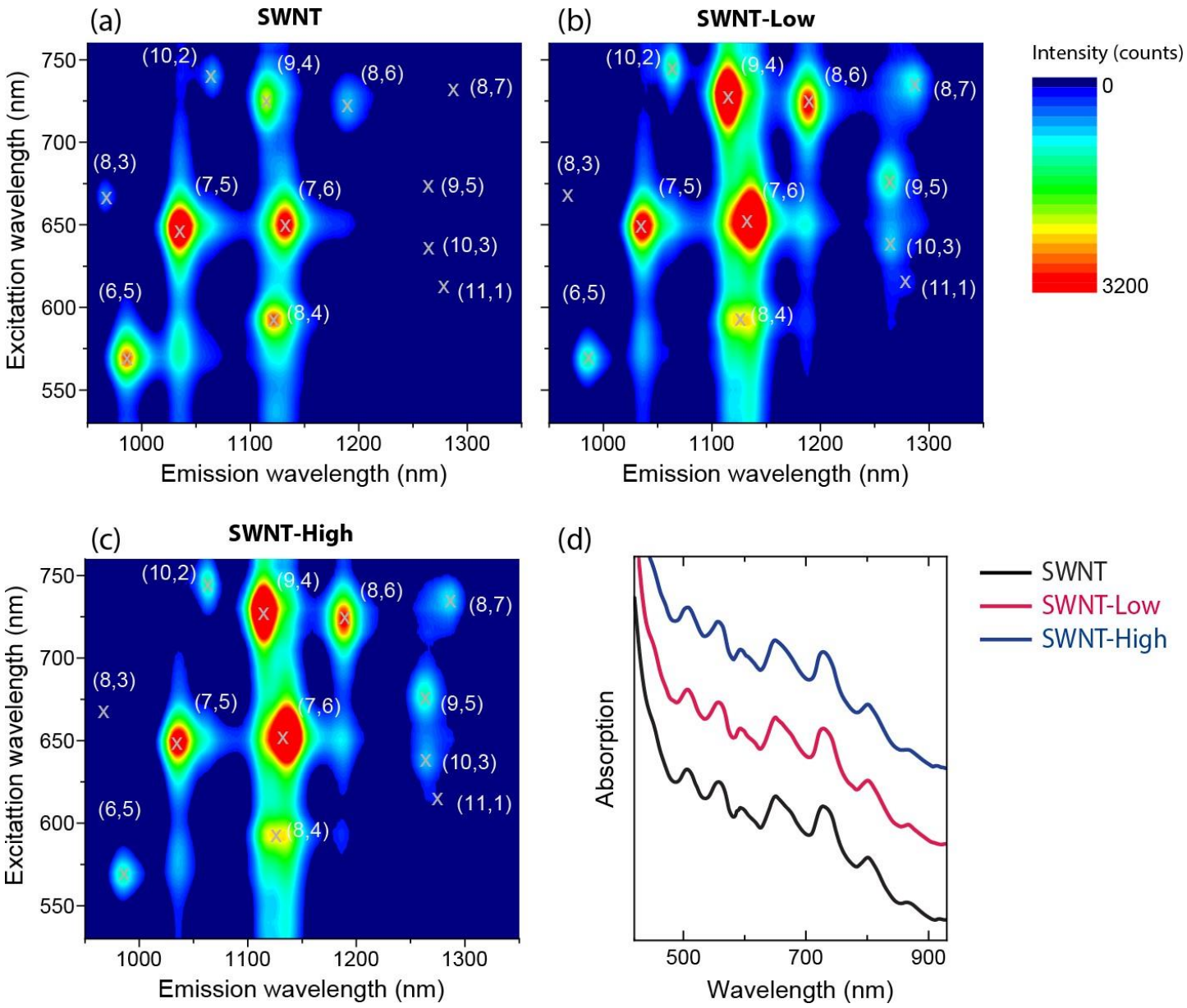

Supplementary Figure 15. Excitation-emission maps of the (a) pristine SWNTs, (b) SWNT-low and (c) SWNT-high. (d) Absorption spectra of the SWNT samples.

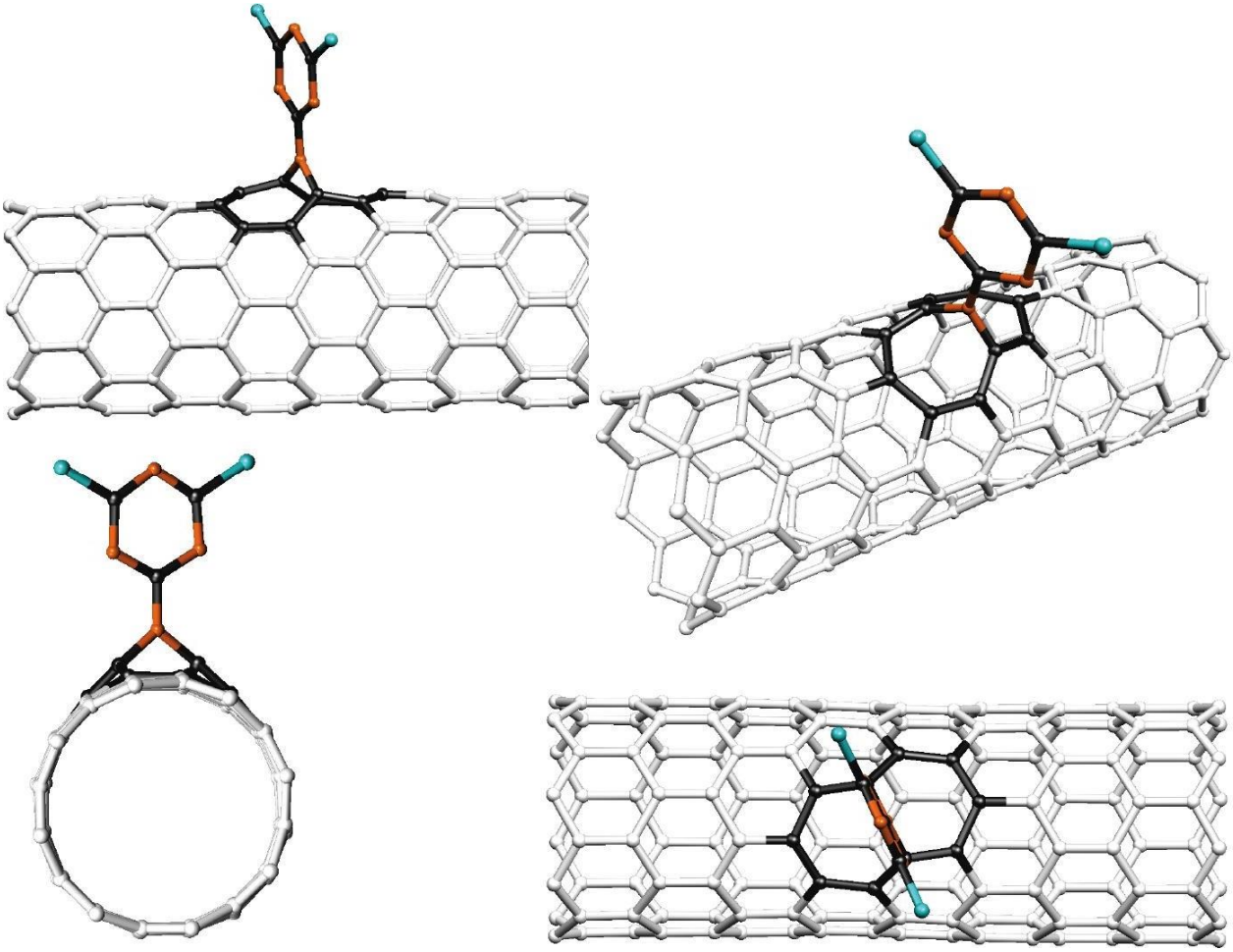

Supplementary Figure 16. Molecular configuration of the triazine on an (8,0) nanotube under different points of view and perspectives. Carbon atoms of the triazine and CNT atoms close to the triazine are highlighted in black. Hydrogen atoms were omitted for clarity.

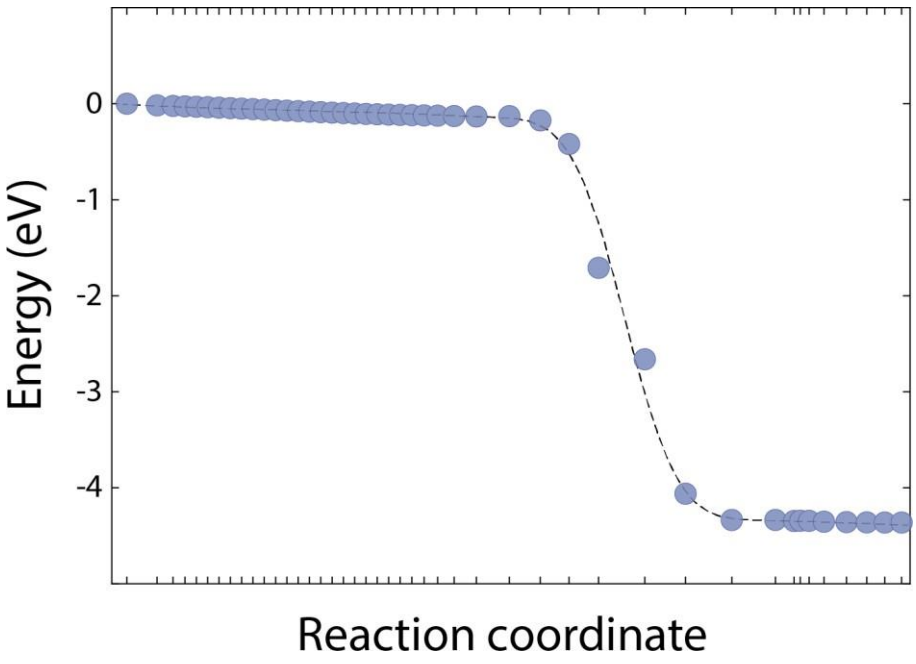

Supplementary Figure 17. Energy profile for the MEP of the cycloaddition with the CI-NEB method.

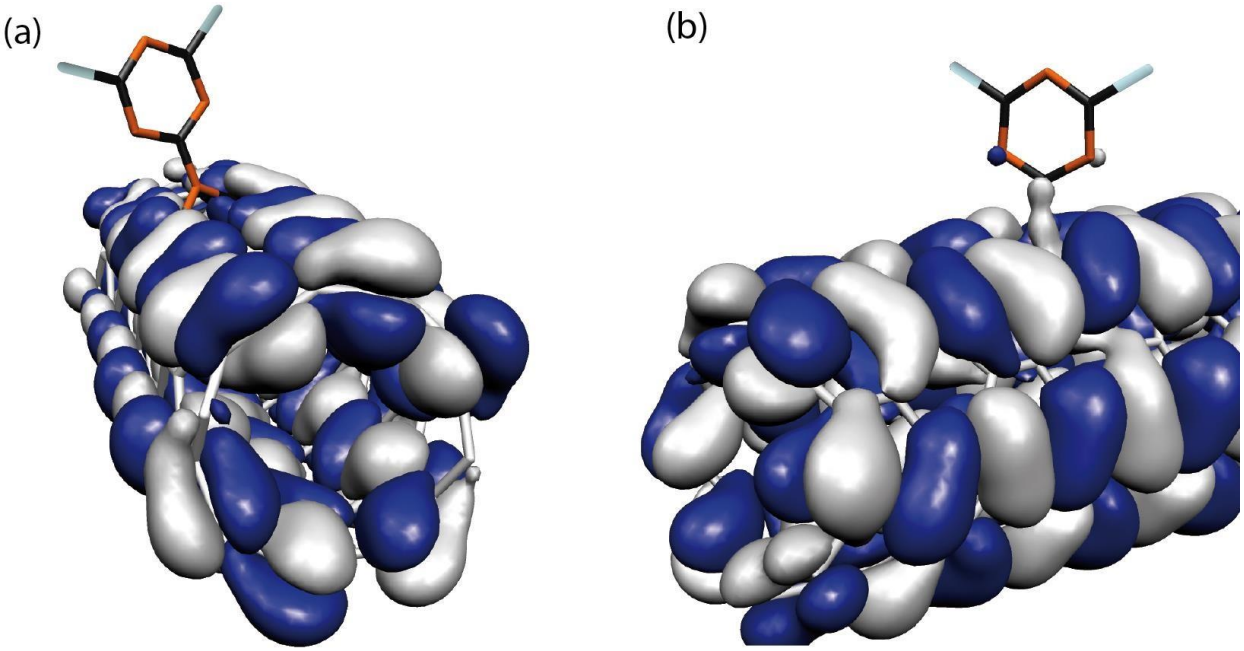

Supplementary Figure 18. HOMO of the triazine-functionalized (8,0) nanotube for the isosurface at (a) $7.6 \cdot 10^{-3} e^{-} nm^{-3}$ and (b) $2.5 \cdot 10^{-3} e^{-} nm^{-3}$.

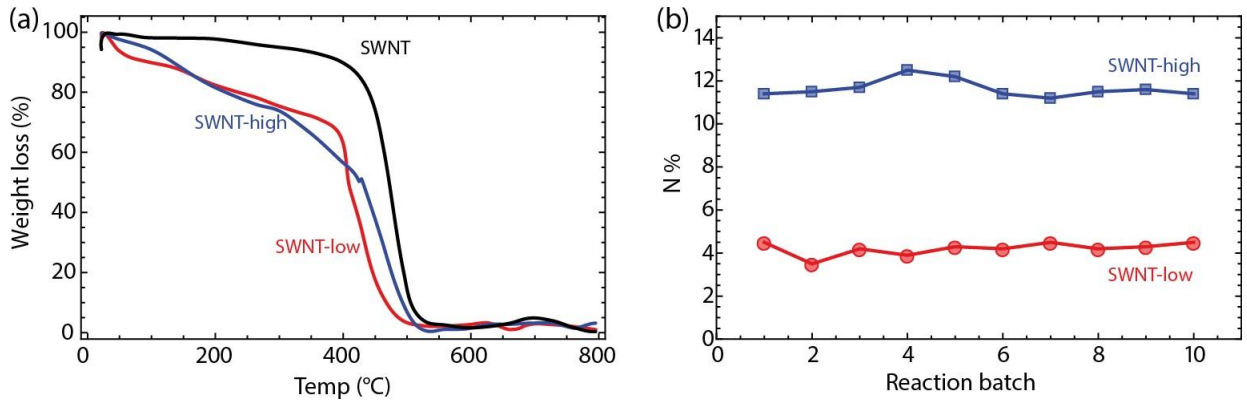

Supplementary Figure 19. (a) TGA diagrams for pristine nanotubes (black curve), SWNT-low (red curve) and SWNT-high (blue curve), at air atmosphere. (b) Variation in the nitrogen content of SWNT-low and SWNT-high obtained from ten different reaction batches.

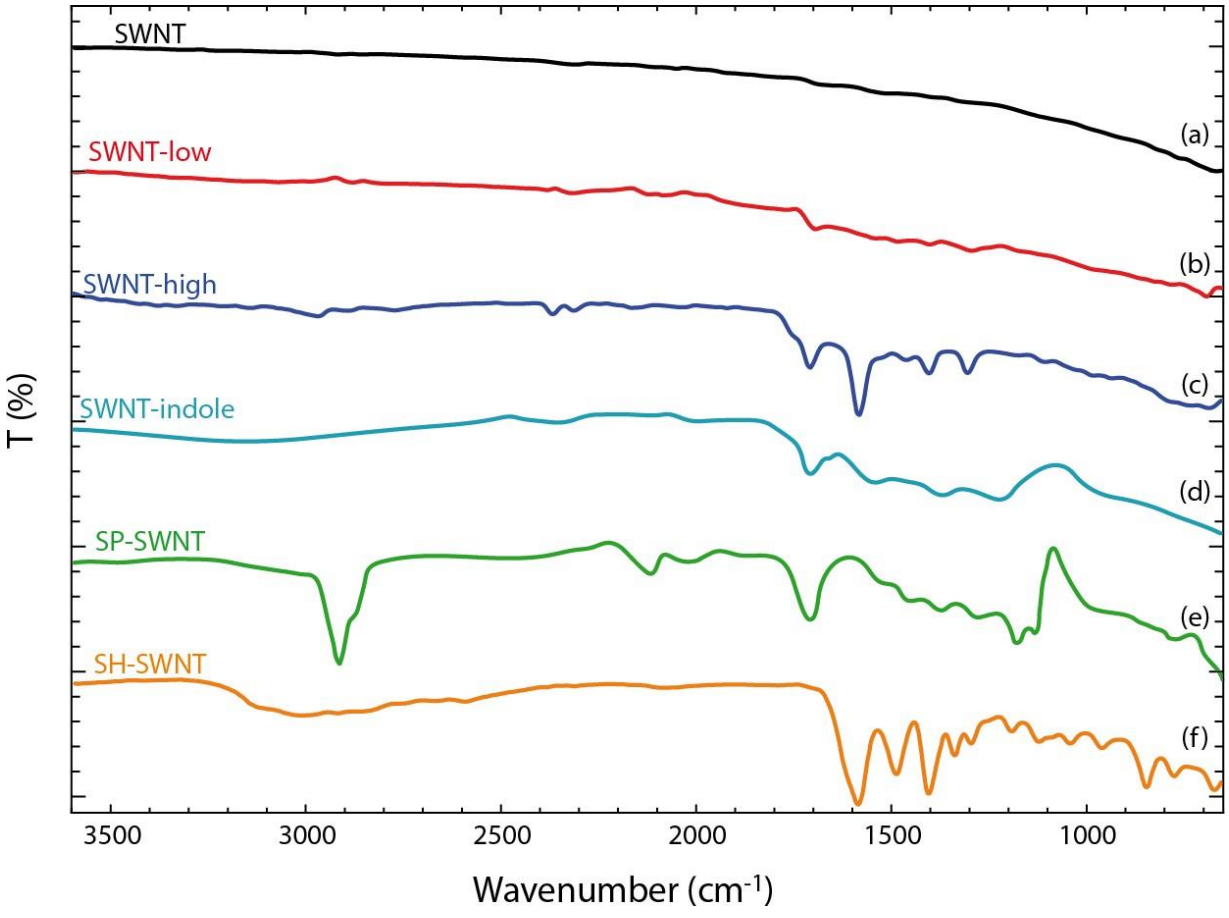

Supplementary Figure 20. IR spectra of the functionalized SWNT samples (see Supplementary Figure 1): (a) pristine SWNT, (b) SWNT-low, (c) SWNT-high, (d) SWNT-indole, (e) SP-SWNT, and (f) SH-SWNT.

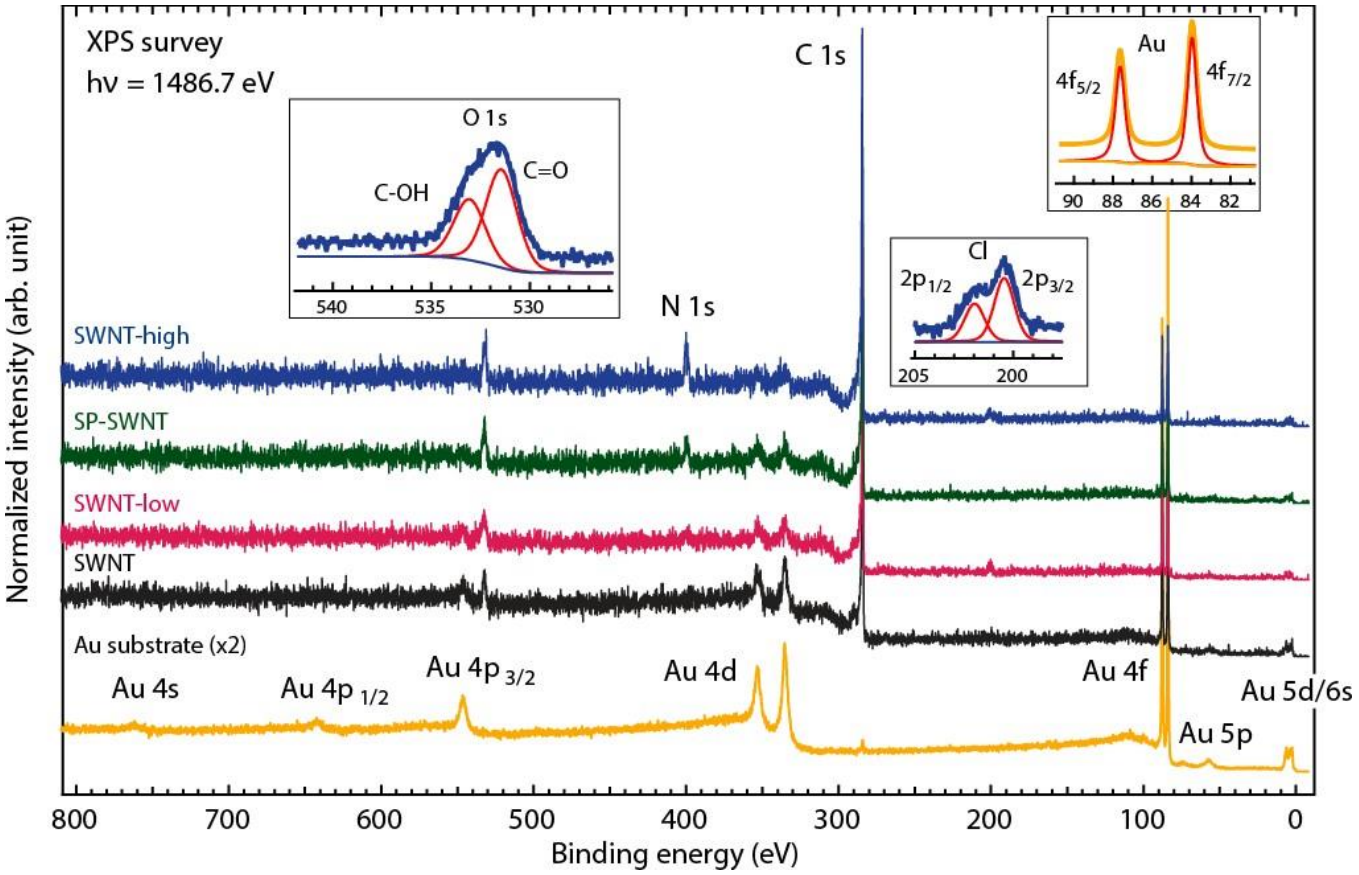

Supplementary Figure 21. Survey spectra of the functionalized SWNTs along with pristine SWNT and a reference Au substrate. All SWNT spectra are normalized on the sp^2-hybridized C 1s component of SWNT. The Au spectrum is normalized to twice the Au 4f peaks of SWNT. Insets show selected spectral details.

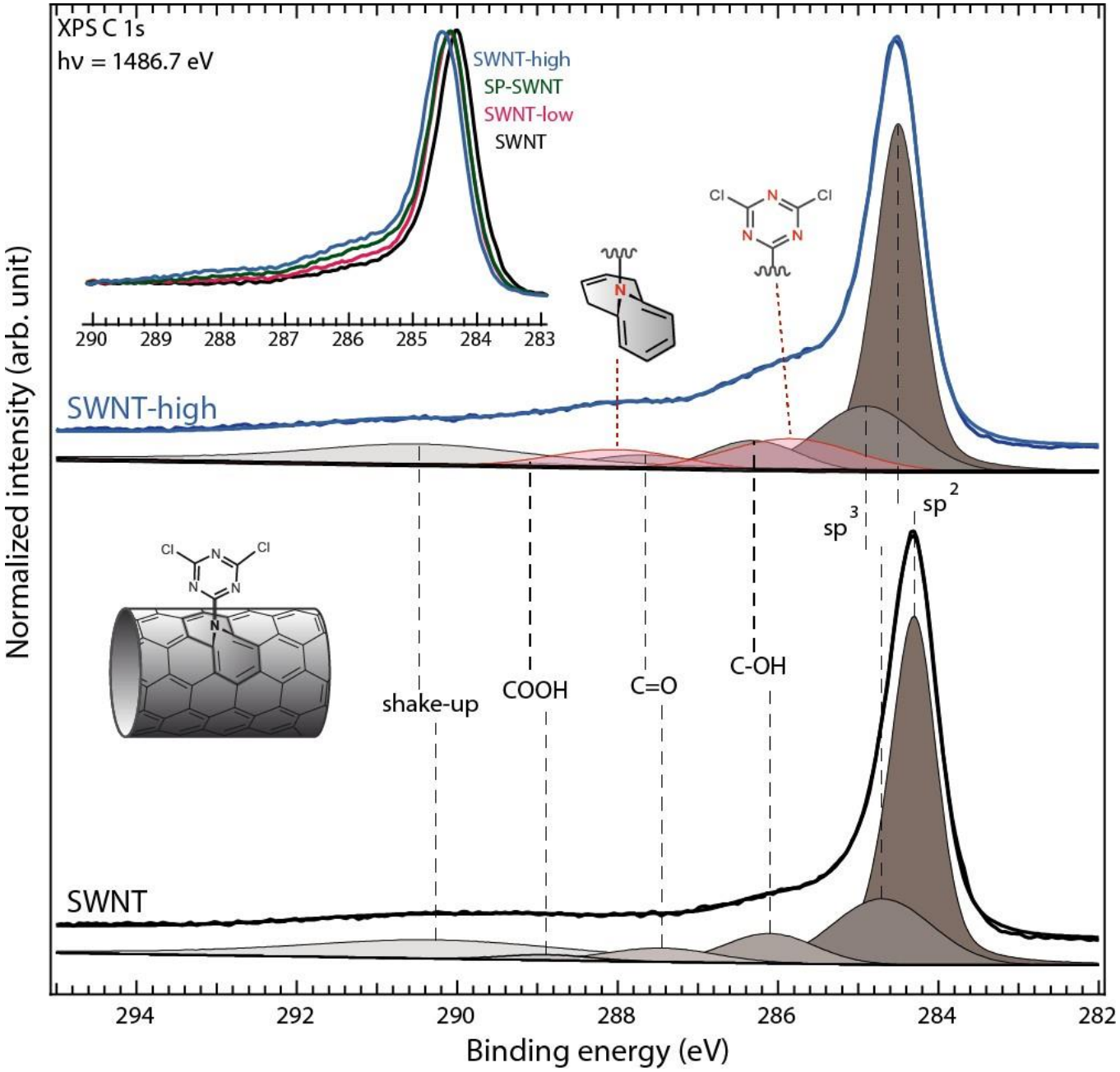

Supplementary Figure 22. C 1s XP spectra of SWNT and SWNT-high along with their spectral decomposition. All spectra are normalized on their respective sp^2 components. The inset shows that the closely related C 1s XP spectra of the SWNT samples shift to higher binding energy with increasing covalent functionalization.

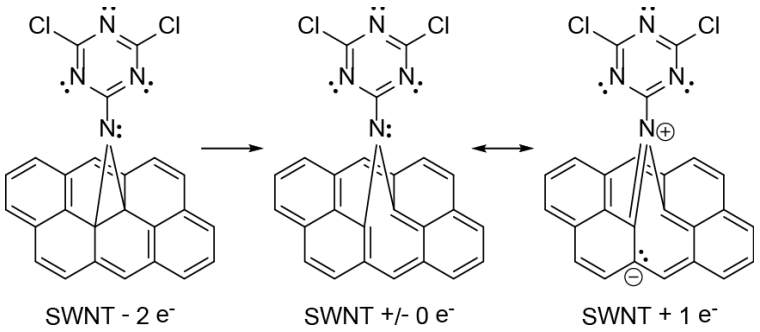

Supplementary Figure 23. Restoration of the sp^2-conjugated π-electron system of the SWNT by ring opening of the aziridine moiety after covalent functionalization. After that the electron lone pair of the bridging nitrogen atom connects the conjugated π-electron systems of the SWNT and the triazine unit. By mesomerism the electron density in the SWNT is increased.

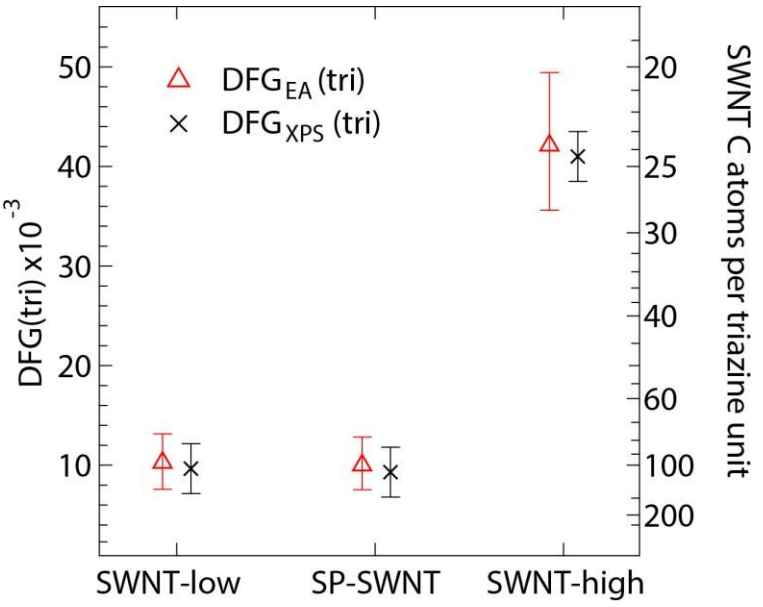

Supplementary Figure 24. Determination of the degree of functionalization: Comparison between elemental analysis and XPS results.

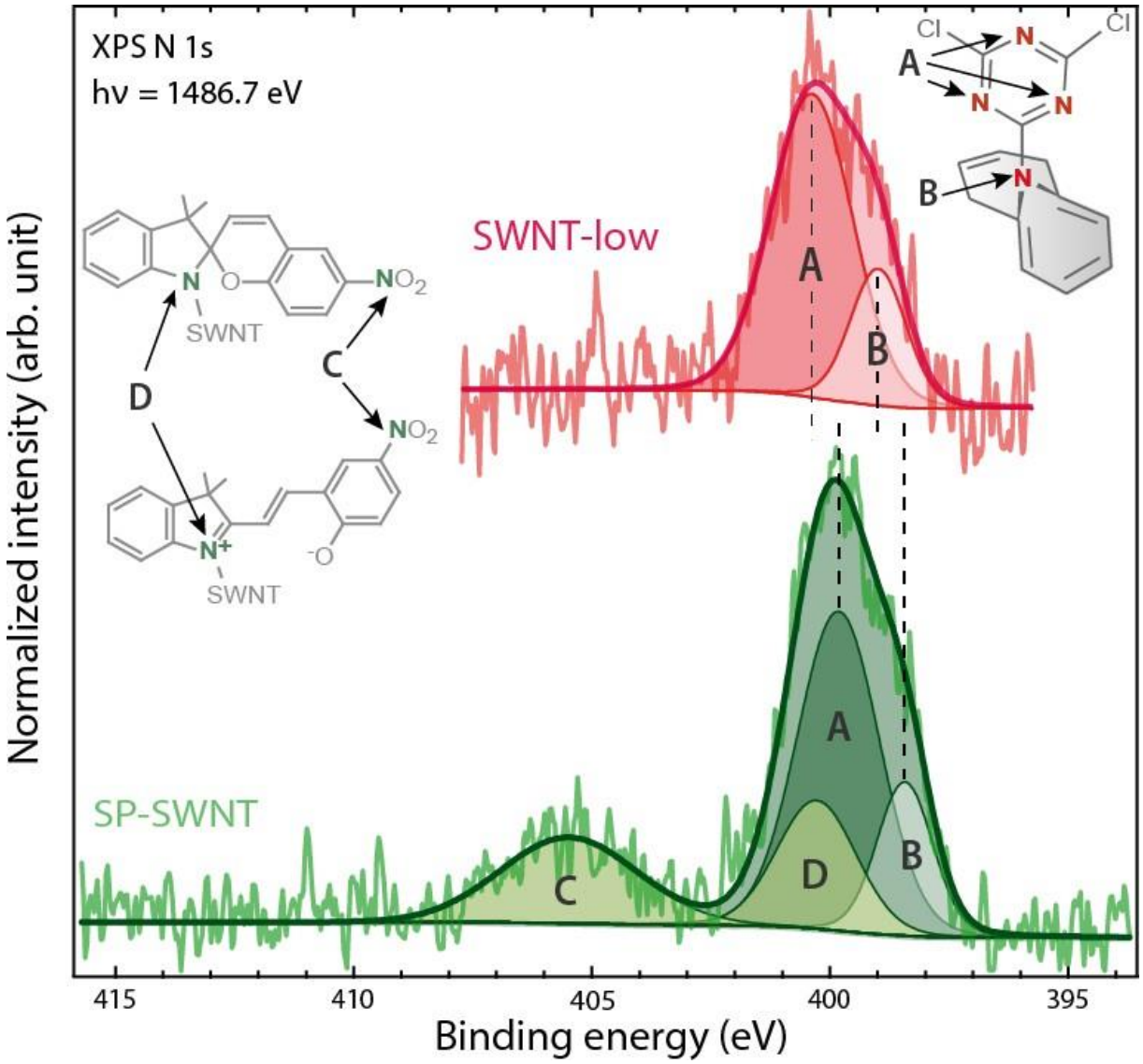

Supplementary Figure 25. N 1s XP spectra of SWNT-low and SP-SWNT along with their spectral decompositions. The triazine peaks are equal in both spectra, but shifted with respect to each other. The combined peak area for the indoline/indole iminium cation is set equal to that of NO_2.

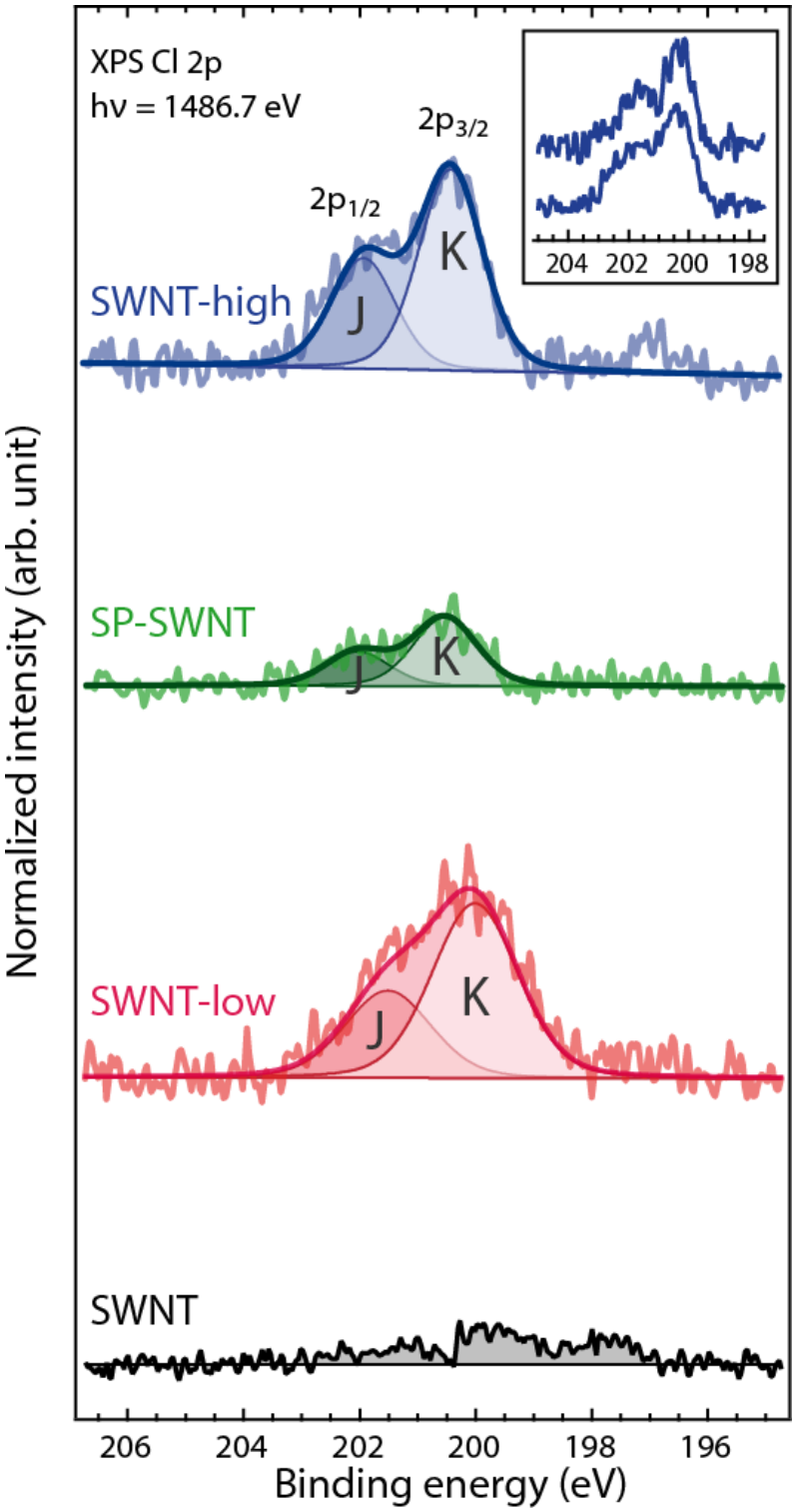

Supplementary Figure 26. Cl 2p XP spectra of pristine and functionalized SWNTs. The inset shows two subsequent measurements on the same sample: No observable X-ray beam-induced Cl loss occurs. The small artifact in SWNT-high around E_B = 197 eV is ascribed to additional residual Cl contaminations from the solvent.

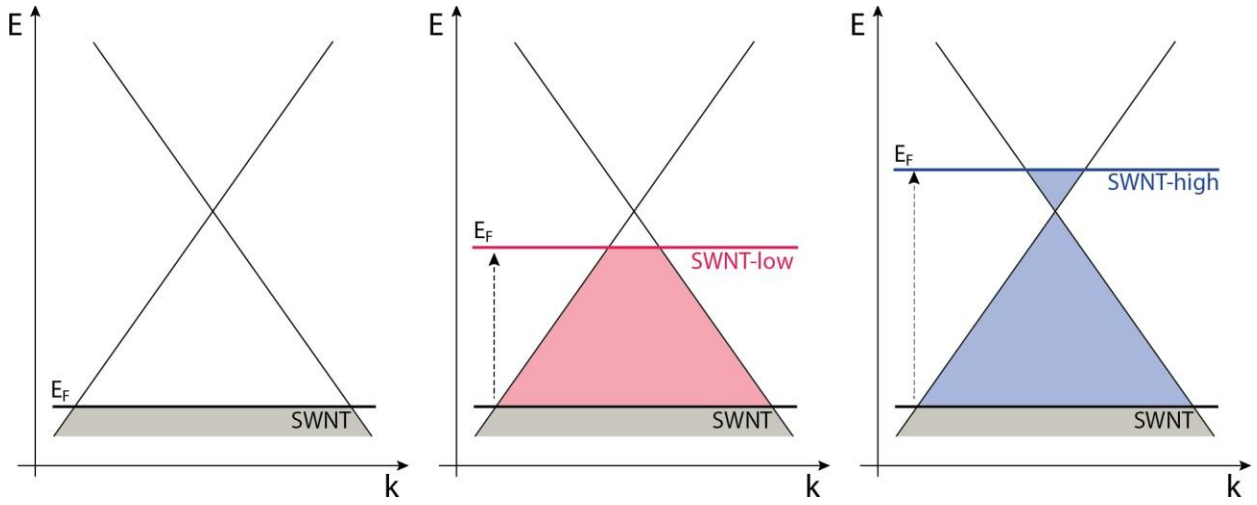

Supplementary Figure 27. Schematic illustration of the functionalization effect onto the Fermi energy of the nanotubes.

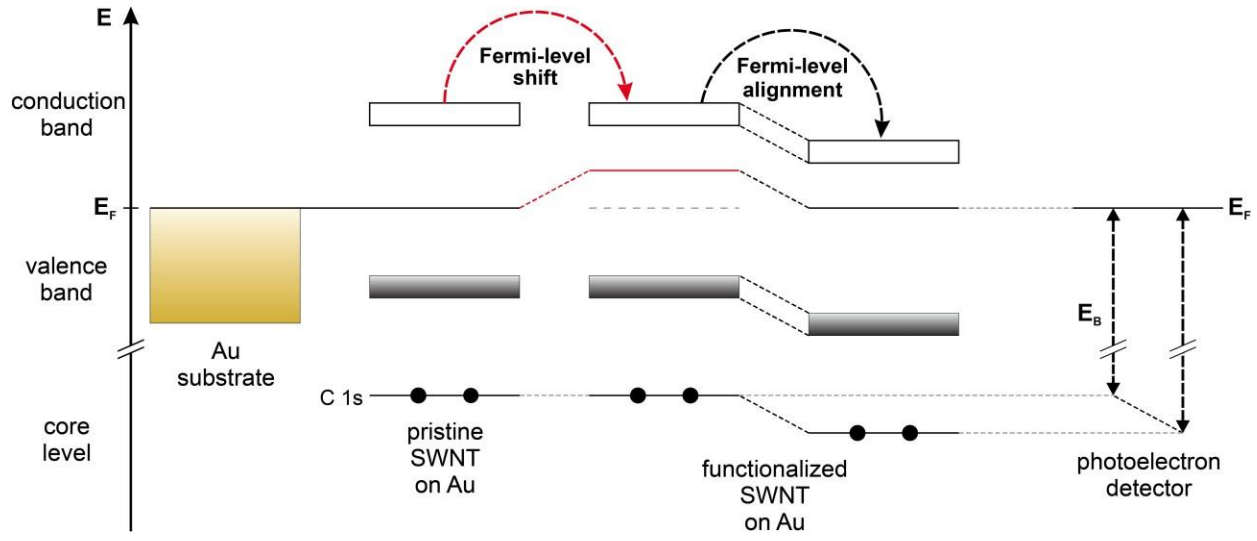

Supplementary Figure 28. XPS schematic of the C 1s peak shift upon SWNT functionalization.

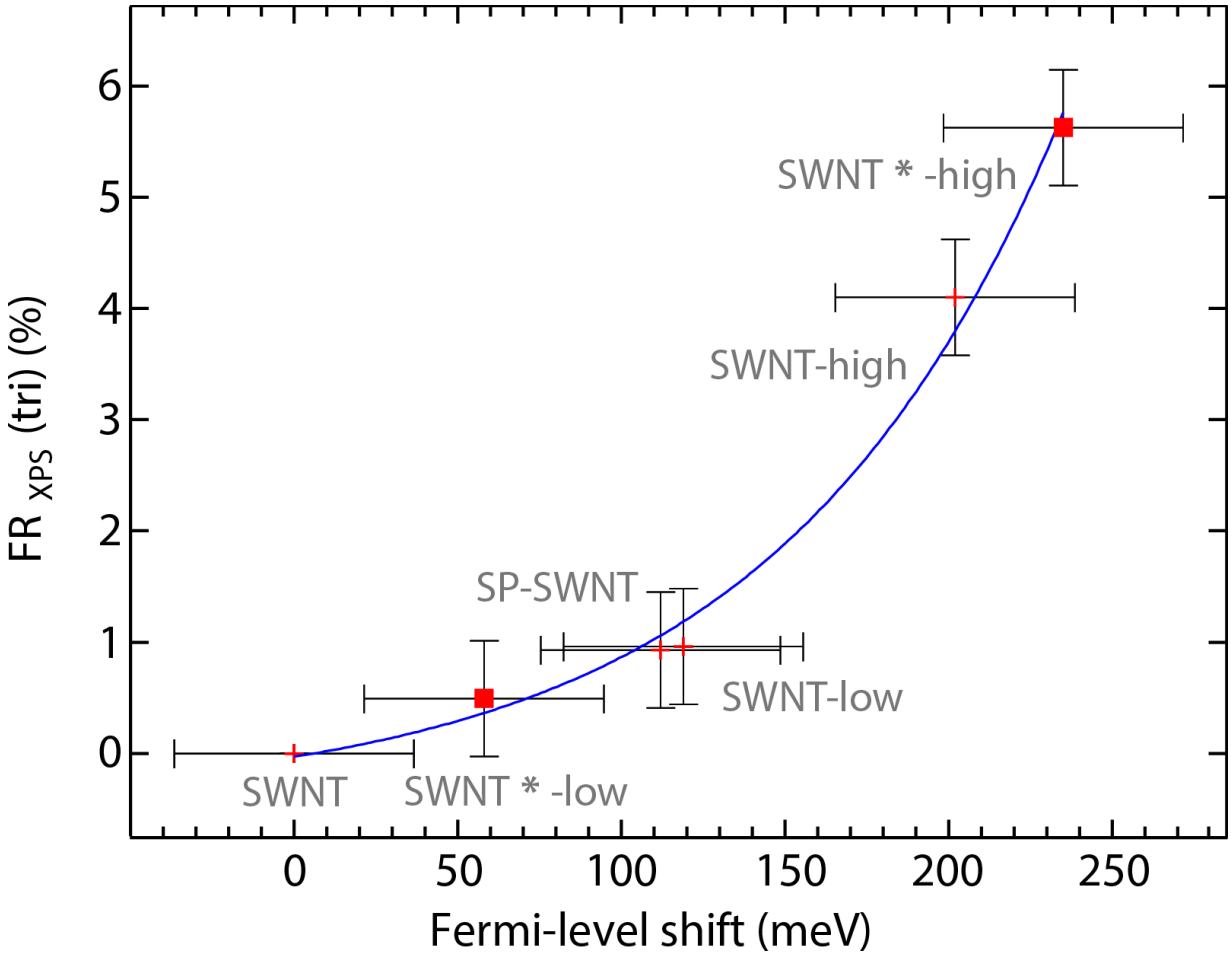

Supplementary Figure 29. Plot of the functionalization ratios of the triazine-unit FR_{XPS}(tri) against Fermi-level shifts obtained by comparing the spectral shifts of the XPS C 1s peaks of functionalized SWNTs with the pristine SWNTs (Supplementary Table 5). The data were fitted with the exponential model $FR_{XPS} \sim \exp[\beta^{-1} \Delta E]$ with β=(90±10)meV.

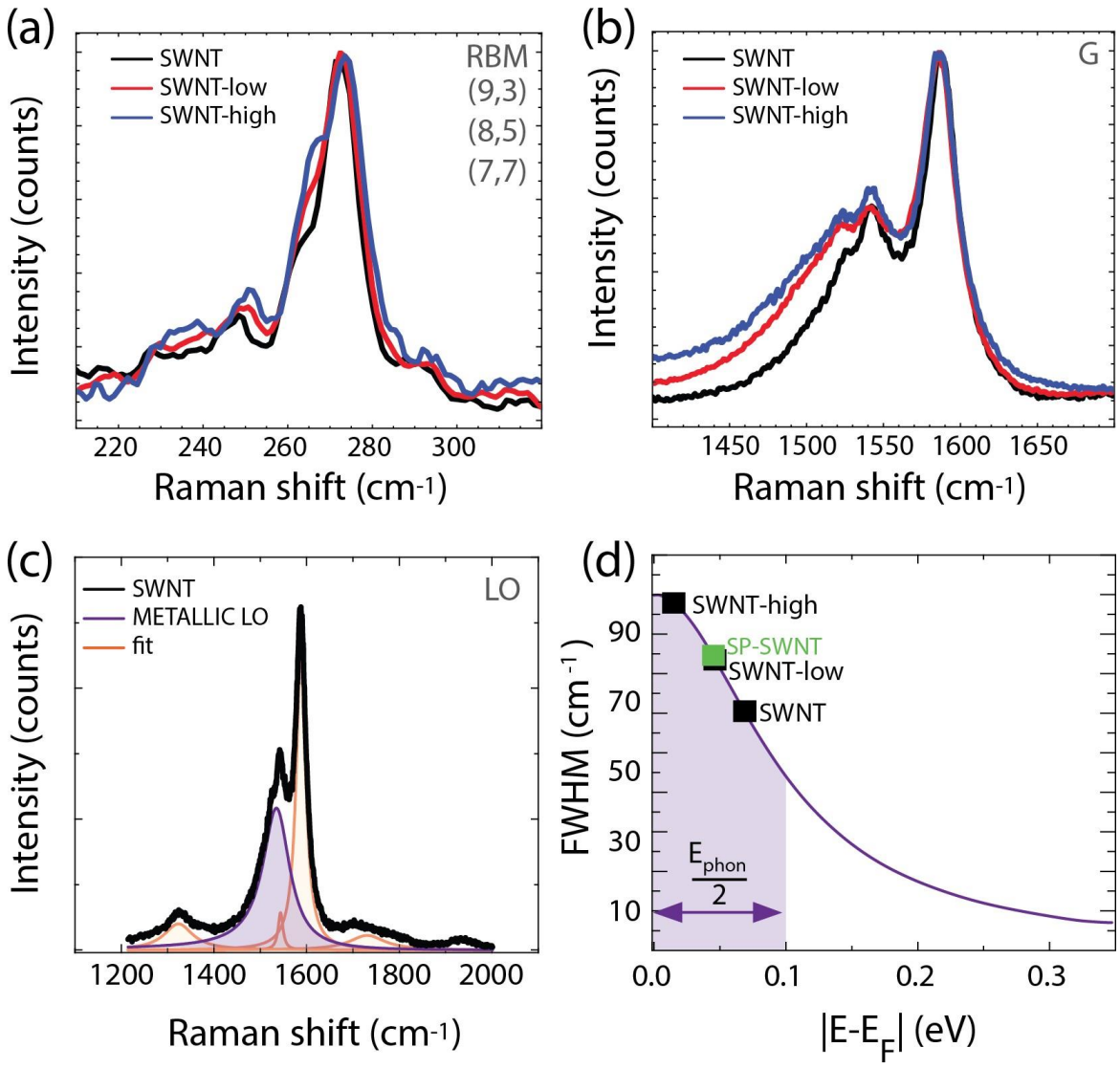

Supplementary Figure 30. RBM (a) and G (b) spectra of the three samples with different functionalization levels. The LO position shifts to lower energies by 14 cm^{-1}, the linewidth increases by 30 cm^{-1}. (c) G band fit of the SWNT sample, the metallic LO band is highlighted in purple. (d) Metallic LO broadening by shift of the Fermi level, FWHM is adjusted to the phonon energy.

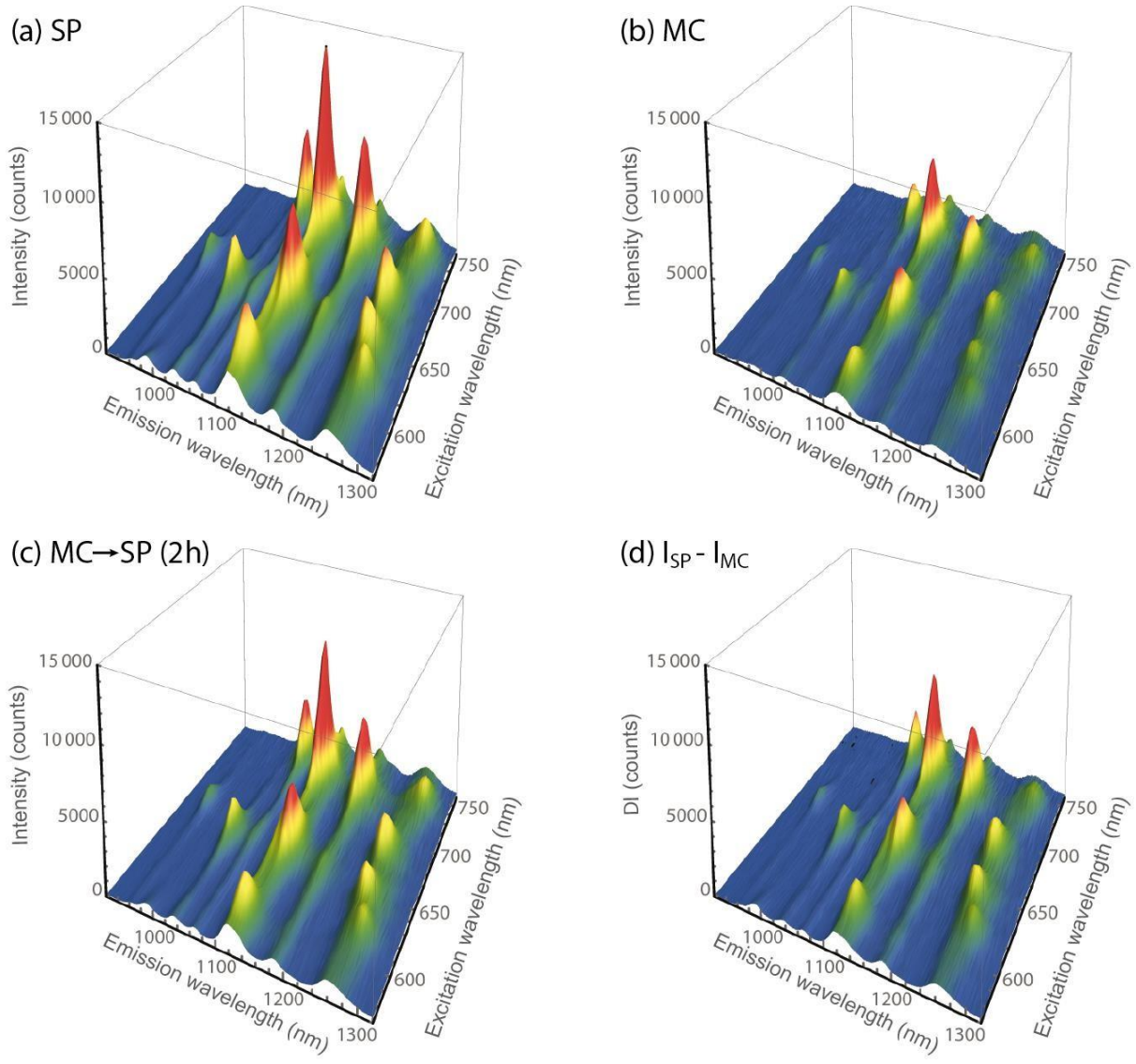

Supplementary Figure 31. Excitation-emission maps of the (a) SP-SWNTs, (b) MC-SWNTs after 1 h of UV irradiation at 367 nm and (c) mixed MC/SP-SWNTs sample, left in darkness for two hours. (24 h of darkness are required for complete back conversion to the SP-SWNT form). (d) PLE difference map obtained by subtracting the intensity of the SP-SWNT sample (a) from the MC-SWNT sample (b).

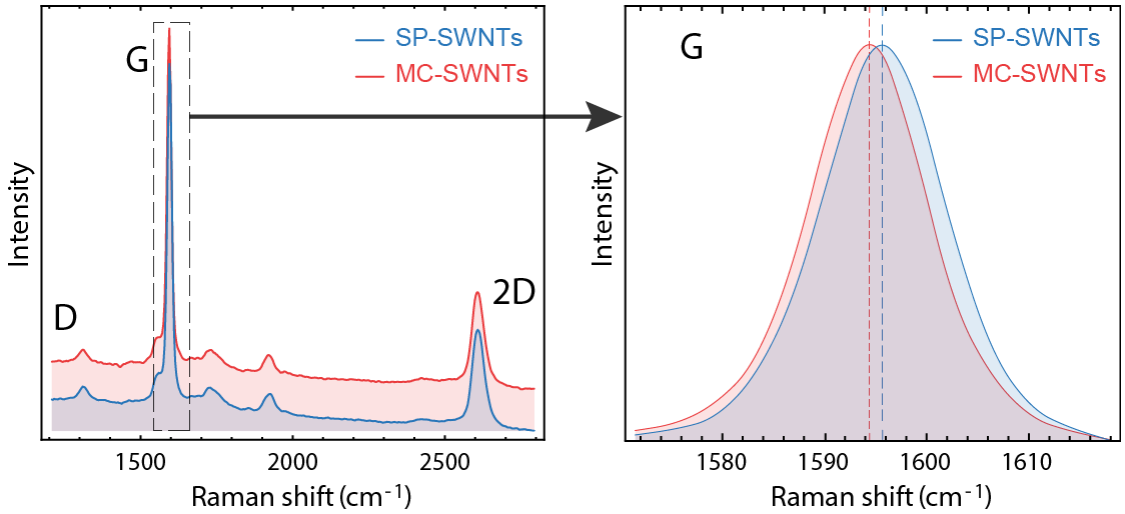

Supplementary Figure 32. (a) Comparison between the Raman signal of SP-SWNT and MC-SWNT, excitation wavelength 633 nm. (b) After SP-to-MC isomerization, a shift of the G band occurs. No appreciable shifts can be observed between the other bands.

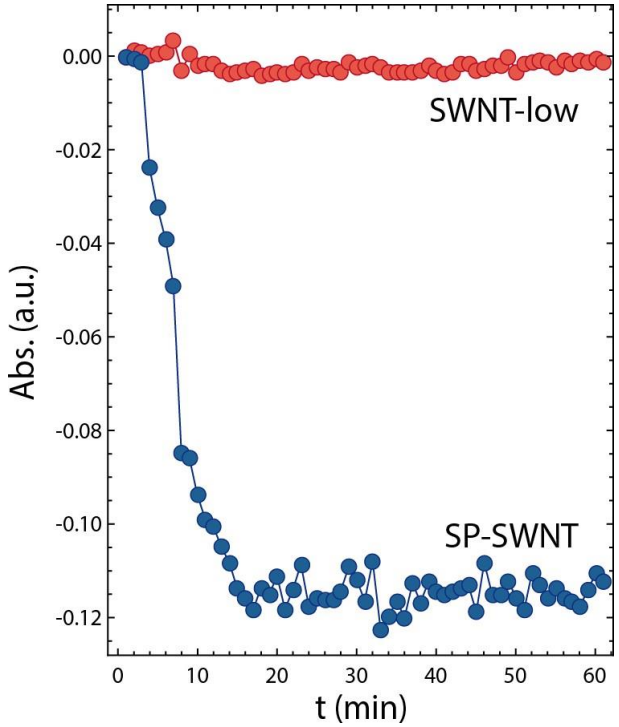

Supplementary Figure 33. Control experiment: Comparison of the intensity of the absorbance at 300 nm of the SWNT-low and SP-SWNT samples under UV light irradiation

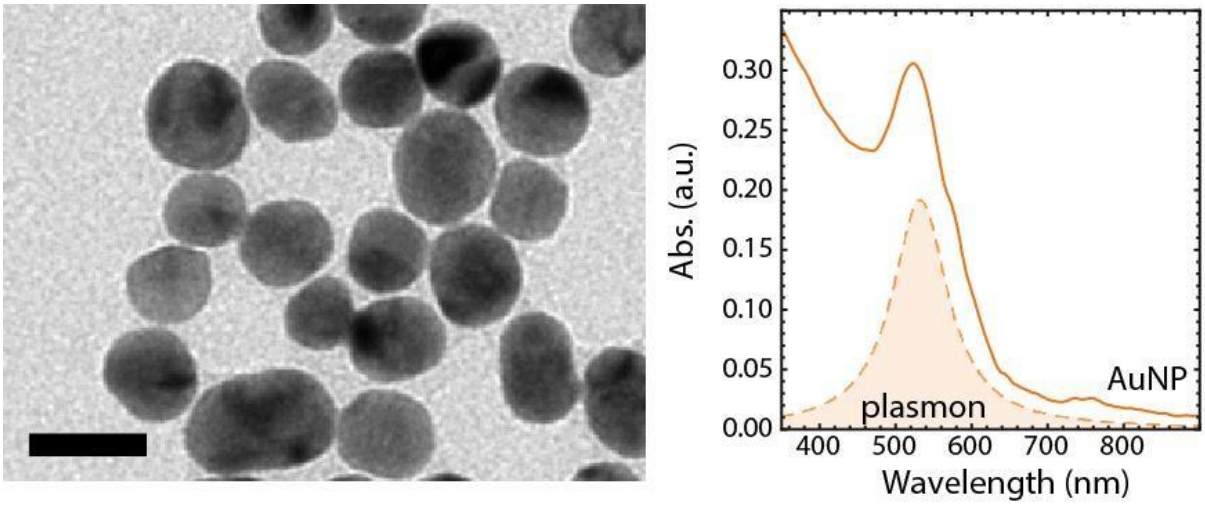

Supplementary Figure 34: TEM micrograph and absorbance of our AuNPs (scale bar 20 nm).

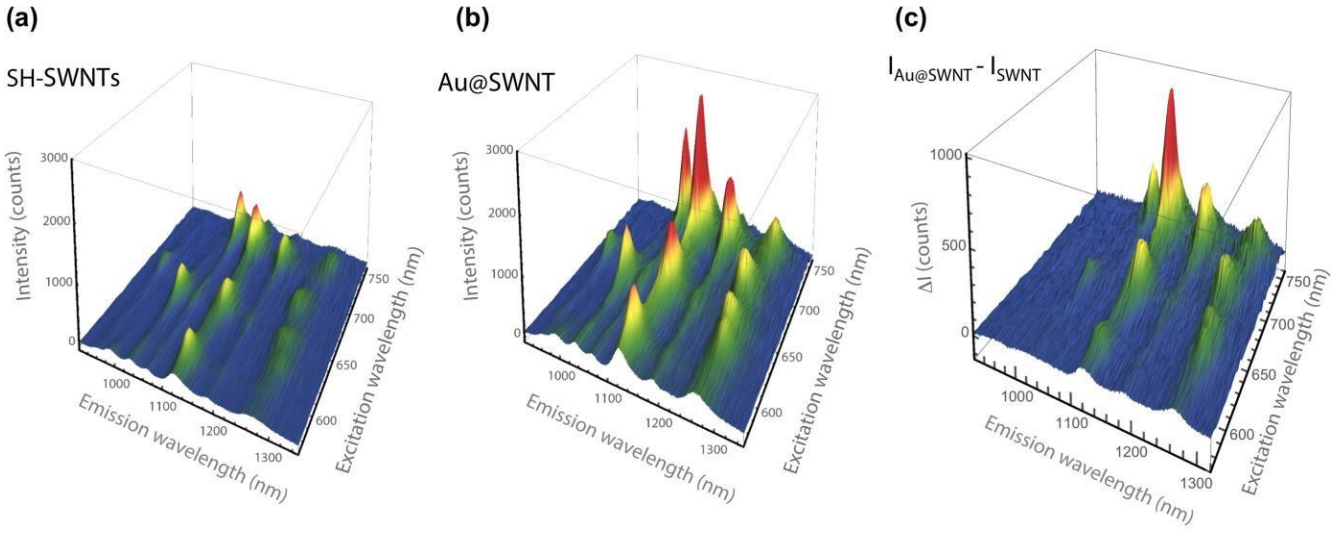

Supplementary Figure 35: Excitation-emission maps of the thiol-functionalized SH-SWNT (a) and Au@SWNT (b). The PLE difference map obtained by subtracting the intensity of the reference SWNT sample from the hybrid Au@SWNT sample is shown in panel (c).

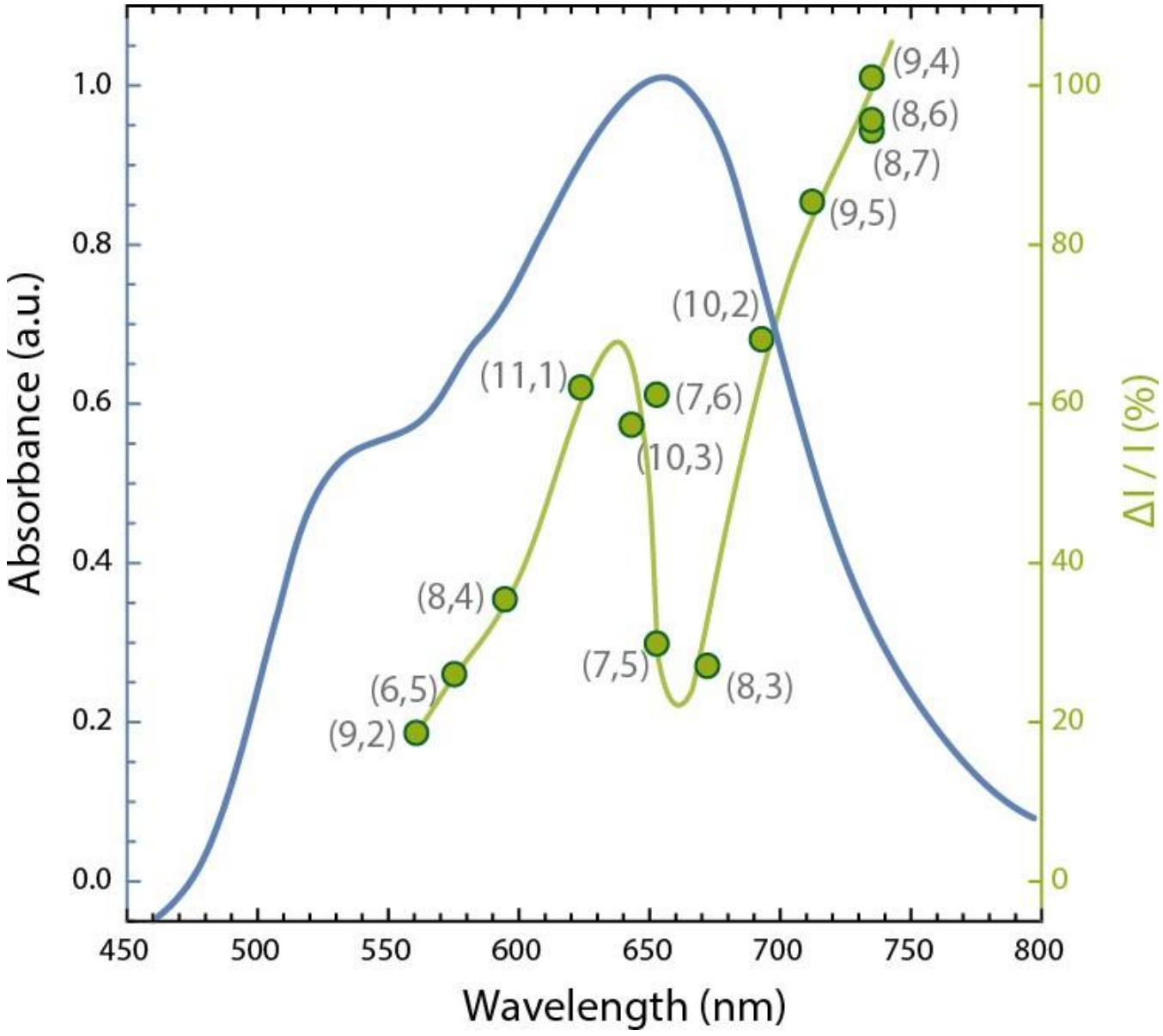

Supplementary Figure 36: Comparison between the absorption spectrum (blue curve) and the relative intensity increase of various Au@SWNT hybrid species (green dots, the line is a guide to the eye).

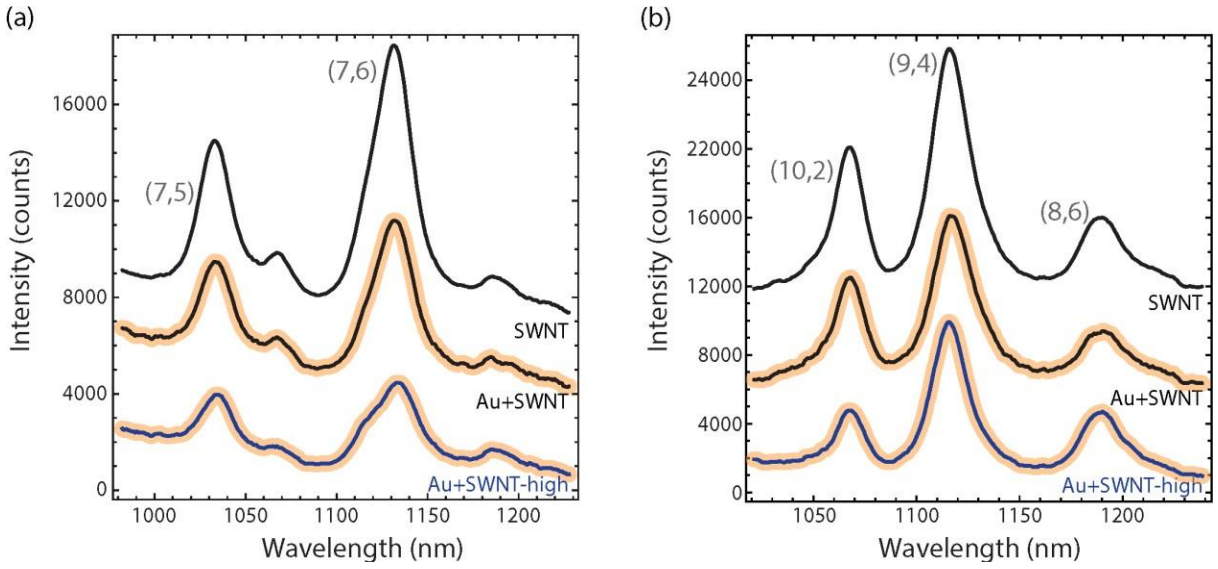

Supplementary Figure 37. Comparison between the emission spectra of the (7,5) and (7,6) (panel a) and the (10,2), (9,4), and (8,6) (panel b) nanotube species from: Pristine nanotubes (SWNT), pristine tubes mixed to AuNPs (Au+SWNT), and triazine-functionalized mixed with AuNPs (Au+SWNT-high).

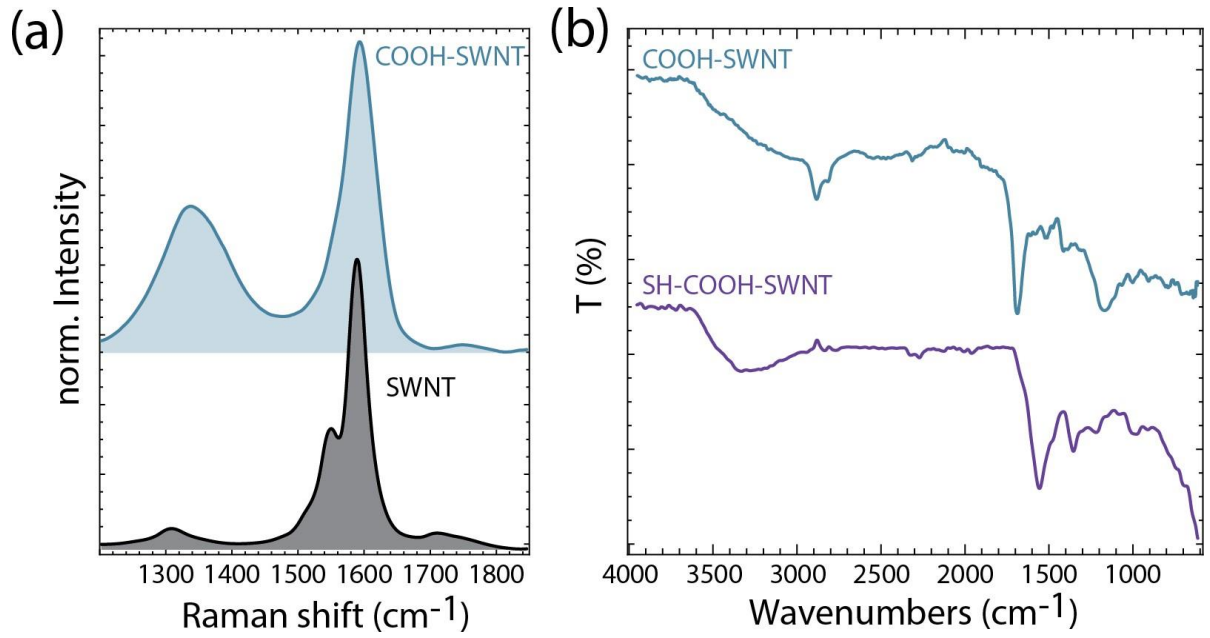

Supplementary Figure 38. (a) Comparison between the D and G lines of pristine (SWNT) and carboxylated (COOH-SWNT) nanotubes. (b) Comparison between the IR spectra of COOH-SWNT and SH-COOH-SWNT.

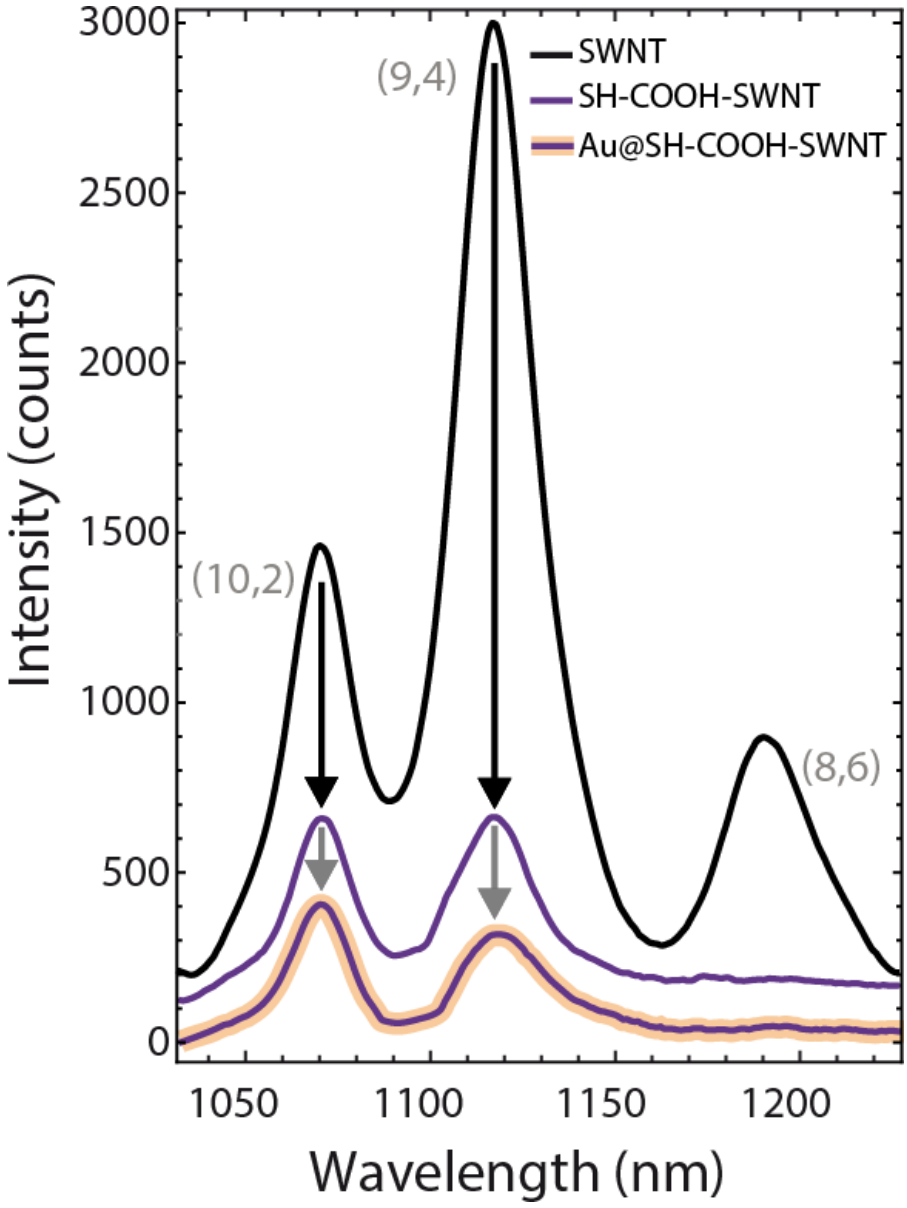

Supplementary Figure 39. Comparison between the emission of thiol-terminated carboxylated nanotubes before (SH-COOH-SWNTs) and after (Au@SH-COOH-SWNTs) AuNPs attachment.

Supplementary Tables

Supplementary Table 1. Results of the elemental analysis for 2-azido-4,6-dichloro-1,3,5-triazine.

Element	Experimental	Calculated
C%	19.1	18.8
H%	0.8	0
N%	45.1	44.0

Supplementary Table 2. Elemental analysis results for 1-(4,6-dichloro-1,3,5-triazine)-2,3,3-trimethylindolinium chloride.

Element	Experimental	Calculated
C%	16.4	16.0
H%	3.8	3.8
N%	48.7	48.9

Supplementary Table 3. Elemental analysis results for (4,6-diphenoxy-1,3,5-triazin-2-yl)-L-cysteine.

Element	Experimental	Calculated
C%	57.2	56.2
H%	4.5	4.2
N%	13.9	14.5

Supplementary Table 4. Summary of the elemental analysis for functionalized SWNTs: Fraction of N, C, H, S, density of functional groups, and fraction of SWNTs with respect to the total product. The element composition does not sum up to 100%, due to the metal catalyst and the chlorine not reported in here.

Sample	%N	%C	%H	%S	DFG	SWNT %
SWNT	0.1	81.1	0.8	0	0	100%
SWNT-low	4.2	70.8	1.9	0	1/100	88%
SWNT-high	12.5	68.2	2.0	0	1/25	64%
SWNT-indole	4.9	79.6	1.8	0	1/95	80%
SP-SWNT	5.1	74.1	2.1	0	1/100	73%
SH-SWNT	6.5	76.1	2.1	1.48	1/80	74%

Supplementary Table 5 Quantification of the SWNT functionalization by XPS. Summary of the functionalization ratio (FR) and density of functional groups (DFG) with respect to the SWNTs and the observed shift of the C 1s XP spectra. Additionally also the FRs of the triazine groups with respect to their chlorine and spiropyran content are given. The two samples denoted with a (*) were made with the same methods but based on SWNTs from different batches and processes (CoMoCAT® nanotubes).

Sample	FR_{XPS}(tri) (%; ±0.5%)	DFG_{XPS}(tri)	C 1s XPS shift (meV; ±37 meV)
SWNT	0	0	0
SWNT-low	1.0	1/104	119
SP-SWNT	0.9	1/108	112
SWNT-high	4.1	1/24	202
SWNT(*)-low	0.5	1/205	58
SWNT(*)-high	5.6	1/18	235

Supplementary Table 6. Results of the Raman characterization of the metallic tubes.

Sample	**$\|E_F$ shift|** **(me V)**	**G^- Position** **(cm^{-1})**	**G^- FWHM** **(cm^{-1})**
SWNT	70	1536	71
SWNT-low	40	1524	84
SWNT-high	20	1522	100
SP-SWNT	40	1528	85

Supplementary Table 7. Summary of the elemental analysis for COOH-SWNTs and SH-COOH-SWNTs: Fractions of N, C, H, S.

Sample	%N	%C	%H	%S
COOH-SWNT	0.9	62.5	2.4	0.032
SH-COOH-SWNT	3.8	49.1	2.8	10.4

Supplementary Note 1: Synthesis and characterization of the functionalized tubes

In this supplementary note we characterize our functionalization products. The intermediate azide and the final product are examined by thermogravimetric analysis (TGA), nuclear magnetic resonance (NMR), elemental analysis (EA), and infrared spectroscopy (IR). Raman spectroscopy identifies the nanotube species. High-resolution scanning transmission electron spectroscopy, coupled with local electron energy loss spectroscopy, allows to locally detect the presence of the functionality onto the nanotube sidewalls. 2-D excitation-emission spectroscopy proofs that the functionalized nanotubes emit light.

Schematic summary of the reaction steps

The synthetic steps towards the functionalized SWNTs are described in the methods section of the main manuscript text and schematically summarized in Supplementary Figure 1.

Characterization of the 2-azido-4,6-dichloro-1,3,5-triazine intermediate

The synthesis of 2-azido-4,6-dichloro-1,3,5-triazine through the reaction between sodium azide and 2,4,6-trichloro-1,3,5-triazine at low temperature was reported previously. [1] This compound is an interesting precursor for highly reactive nitrene intermediates. [2] To prove the successful creation of the product of reaction of sodium azide with 2,4,6-trichloro-1,3,5-triazine (Supplementary Figure 2a), we purified and characterized the intermediate azide at 0ºC. Supplementary Figure 2b shows the TGA thermograms of 2,4,6-trichloro-1,3,5-triazine and 2-azido-4,6-dichloro-1,3,5-triazine. The substitution of one of the chlorine atoms of cyanuric chloride dramatically changes the thermal behaviour. While 2-azido-4,6-dichloro-1,3,5-triazine starts losing weight at low temperature (purple line), its main decomposition temperature is

higher (ca. 200°C) than 2,4,6-trichloro-1,3,5-triazine (blue line). Elemental analysis (Supplementary Table 1), ^{13}C NMR (Supplementary Figure 3) and IR spectroscopy (Supplementary Figure 4) prove that the intermediate of the functionalization of SWNTs is 2-azido-4,6-dichloro-1,3,5-triazine.

In the ^{13}C NMR spectrum of 2-azido-4,6-dichloro-1,3,5-triazine, the two signals at 171 ppm and 172 ppm are assigned to the two types of carbon atoms of the compound as sketched in Supplementary Figure 3.

Supplementary Figure 4 shows the IR spectra of 2,4,6-trichloro-1,3,5-triazine (blue) and 2-azido-4,6-dichloro-1,3,5-triazine (purple). The appearance of the strong absorbance band at 2133 cm^{-1} in the IR spectra of 2-azido-4,6-dichloro-1,3,5-triazine due to the azide group proves the substitution of one of the chlorine of the cyanuric chloride by azide.

Comparison between covalently and non-covalently triazine-functionalized SWNTs

To prove the effective covalent attachment of the triazine onto the SWNTs, we performed a blank reaction designed to prevent the covalent attachment of the triazine onto the SWNTs. We followed the synthetic steps of the original reaction but without adding the sodium azide and thus without converting the 2,4,6-1,3,5-trichloro-triazine into 2-azido-4,6-dichloro-1,3,5-triazine. In this way the 2,4,6-1,3,5-trichloro-triazine can only non-covalently attach to the SWNTs.

For performing the blank reaction, SWNTs (1 g) were added to N-methyl-2-pyrrolidone (150 ml) and sonicated for 1 h. The mixture was then stirred at room temperature for one additional hour. 2,4,6-1,3,5-trichloro-triazine (1 g) dissolved in N-methyl-2-pyrrolidone (50 ml) was added at 0°C and stirred for 20 min. The temperature was raised to 25°C and it was stirred for 1 h. Finally, we left the mixture stirring at 70°C overnight. To compare the TGA response of covalently and non-covalently functionalized SWNTs, we evaporated the solvent of the blank

mixture at 70°C under vacuum. The results of the TGA analysis are shown in Supplementary Supplementary Figure 5. The TGA thermogram of the noncovalent sample is completely different from the covalently functionalized one. We observe (gray line in Supplementary Figure 5) two distinct onsets of decomposition at 140 and 440°C, which are due to the triazine and to the SWNTs. Our blank mixture consists of two separate compounds. The TGA of the SWNT-high (blue line in Supplementary Figure 5) does not show such an onset for the weight loss. The decomposition starts below 100°C and continues up to 430°C. This is assigned to the loss of trapped water molecules (low T), followed by the detachment of triazine molecules from the SWNT and their decomposition. Such broad decomposition spectra for functionalized tubes are well-known and abundantly reported in the literature. [3-5]

Synthesis and characterization of 1-(4,6-dichloro-1,3,5-triazine)-2,3,3-trimethylindolinium chloride and spiropyran

The reaction of dichlorotriazine with dimethyl indoline was performed for the first time in our experiments. Details of the synthesis are reported in the methods section of the main manuscript text. The results of the elemental analysis (reported in Supplementary Table 2) of the 1-(4,6-dichloro-1,3,5-triazine)-2,3,3-trimethylindolinium chloride are very close to the calculated contents, confirming the successful synthesis of the compound.

^{1}H NMR ($CDCl_3$): δ 8.25, 7.15-7.35 (aromatic segment), 1.25, 1.4, and 1.6 (-CH_3).

^{13}C NMR ($CDCl_3$): δ 170, 168, and 161 (triazine segment), 140, 136.9, 127.7, 125.6, 122.2, 117.7, 100 (aromatic segment and C=N), 26.4, 22.1, 20.2 (CH_3).

FTIR: 2890 (ν_{CH}), 1612 ($\nu_{C=C}$), 1557 ($\nu_{C=N}$) cm^{-1}.

In the IR spectra of 1-(4,6-dichloro-1,3,5-triazine)-2,3,3-trimethylindolinium chloride (see Supplementary Figure 6), the absorbance bands at 1612 and 1557 cm^{-1} are assigned to C=C and C=N bonds, respectively. The absorbance band of the aliphatic C-H bond is observed at 2890 cm^{-1}. In the ^{1}H NMR spectra of 1-(4,6-dichloro-1,3,5-triazine)-2,3,3-trimethylindolinium chloride (Supplementary Figure 7), the signal at 8.25 ppm is assigned to the proton 1, while the multiple signals at 7.15-7.35 ppm correspond to the protons 2, 3 and 4. Signals from the methyl groups are detected at 1.25, 1.4, and 1.6 ppm. In the ^{13}C NMR spectra of the compound (Supplementary Figure 8), signals at 170, 168, and 161 ppm are assigned to the carbon atoms of the triazine ring. Moreover, six signals from the aromatic ring as well as from the carbon of C=N bond are seen in the 100-140 ppm region. Three additional signals from the methyl carbons occur in the 20-27 ppm region.

Synthesis of 6-(3,3-dimethyl-2-methyleneindolin-1-yl)-1,3,5-triazine-2,4-diol

A solution of sodium hydroxide (0.2 g, 5×10^{-3} mol) in water (5 ml) was added to a degassed suspension of 1-(4,6-dichloro-1,3,5-triazine)-2,3,3-trimethylindolinium chloride (0.14 g, 4.1×10^{-4} mol) in water (30 ml) and then stirred at 80 °C for 15 min. The reaction was then cooled down to room temperature and diethyl ether (30 ml) was added to the solution. The organic phase was separated and the product was extracted from water by dichloromethane (4×20 ml). Sodium sulfate (1 g) was added to the organic phase and stirred for 1 h. After filtration the solvent was evaporated. The product was used for the next reaction without further purification.

Synthesis of (R)-6-(3',3'-dimethyl-6-nitrospiro[chromene-2,2'-indolin]-1'-yl)-1,3,5-triazine-2,4-diol

6-(3,3-dimethyl-2-methyleneindolin-1-yl)-1,3,5-triazine-2,4-diol (0.04 g, 1.48×10^{-4} mol) was dissolved in dry ethanol (15 ml) and degassed. 5-nitrosalicylaldehyde (0.037 g, 2.22×10^{-4} mol) was added to the solution and the mixture was sonicated at 25°C with 35 kHz for 2 h. The solvent was evaporated and the residue was dried under vacuum and purified by column chromatography using dichloromethane/methanol (50/2) as eluent.

^{1}H NMR ($CDC1_3$): δ 11.6 (-OH), 8.4, 8.1, 7.2, 7.1, 6.9 (aromatic segments), 5.6, 5.5 (vinylic segment), 1.3-1.2 ($-CH_3$).

^{13}C NMR ($CDC1_3$): δ 166.1, 161.6 (triazine segment), 140.5, 131.8, 129.8, 126.4, 124.9, 121.5, 119.4, 119.1117.4 (aromatic segments), 103.1, 102 (vinylic segment).

MS (ESI-TOF): calcd. for $C_{21}H_{17}N_5O_5$ 420.1263 $[M+H]^+$, found 420.1334 $[M+H]^+$

FTIR: 2920 (ν_{CH3}), 1734 ($\nu_{C=O}$), 1670 ($\nu_{C=C}$), 1525 ($\nu_{C=N}$), 1457-1341 (ν_{NO2}) cm^{-1}.

The compound was characterized by mass spectroscopy, ^{13}C NMR, and IR spectroscopy.

In the mass spectra, a peak at m/z = 420 proves that (R)-6-(3',3'-dimethyl-6-nitrospiro[chromene-2,2'-indolin]-1'-yl)-1,3,5-triazine-2,4-diol is successfully synthesized.

After the condensation reaction between 5-nitrosalicylaldehyde and 6-(3,3-dimethyl-2-methyleneindolin-1-yl)-1,3,5-triazine-2,4-diol, two new signals appear in the ^{13}C NMR spectrum of the product at 102 ppm and 103 ppm, Supplementary Figure 9(a). These signals are assigned to the carbon atoms of the vinylic bond of (R)-6-(3',3'-dimethyl-6-nitrospiro[chromene-2,2'-indolin]-1'-yl)-1,3,5-triazine-2,4-diol [Supplementary Figure 9(b)].

In the IR spectra of (R)-6-(3',3'-dimethyl-6-nitrospiro[chromene-2,2'-indolin]-1'-yl)-1,3,5-triazine-2,4-diol, the absorbance bands at 2920 cm^{-1}, 1734 cm^{-1}, 1670 cm^{-1}, 1525 cm^{-1}, and 1457-1341cm^{-1} are assigned to the methyl groups, tautomeric of hydroxyl groups to carbonyl, C=C

bond of aromatic ring, C=N bond of triazine ring and nitro group, respectively (Supplementary Figure 10).

Characterization of the reaction of dichlorotriazine with cystein

Synthesis of 2-chloro-4,6-diphenoxy-1,3,5-triazine

2-chloro-4,6-diphenoxy-1,3,5-triazine was synthesized and purified according to the reported procedure [6]. Briefly, a solution of phenol (1 g, 1.05×10^{-2} mol) and sodium hydroxide (0.42 g, 1.05×10^{-2} mol) in 10 ml water was added to a solution of cyanuric chloride (0.96, $5.2\ 10^{-3}$ mol) in dichloromethane (40 ml), dropwise at 0 °C. The mixture was stirred at room temperature for 1 hour and then refluxed for additional 6 hours. After that, the reaction was cooled down and filtered and the solvent evaporated. The crude product was dissolved in dichloromethane (5 ml) and then filtered. The product was precipitated in methanol, yield 70%.

^{1}H NMR ($CDC1_3$): a) δ 7.10-7.40 (phenoxy segments)

^{13}C NMR ($DMSO_{d6}$): δ 173.7, 172.4, (triazine segment), 151.2, 129.7, 126.7, 121 (phenoxy segments).

FTIR: 1557 ($\nu_{C=C,}$ $\nu_{C=N}$), 1261 ($\nu_{C-O)}$ cm^{-1}.

Synthesis of (4,6-diphenoxy-1,3,5-triazin-2-yl)-L-cysteine

2-chloro-4,6-diphenoxy-1,3,5-triazine (0.1 g, 3.34×10^{-4} mol) was dissolved in NMP (15 ml) and triethylamine (0.05 ml, 3.5×10^{-4} mol). Cysteine (0.04 g, 3.3×10^{-4} mol) was added to the solution and the mixture was stirred at room temperature for 10 min. The temperature of the reaction was then raised to 70 °C and stirred for 24 h. After that, the mixture was cooled down and the solvent was evaporated under vacuum. The crude product was dissolved in water (20 ml) and extracted by dichloromethane (3 × 15 ml). Yield 45%.

^{1}H NMR ($DMSO_{d6}$): δ 7.1-7.4 (phenoxy segments), 6.7 (-NH-), 3.25-3.35 ($-CH_2$), 2.1-2.2 (-CH).

^{13}C NMR ($DMSO_{d6}$): δ 174, 166 (triazine segment), 172.2 (C=O), 152.2 130, 126, 122.4, (phenoxy segments).

MS (ESI-TOF): calcd. for $C_{18}H_{16}N_4O_4S$ 384.0892 $[M+H]^+$, found 384.3532 $[M+H]^+$.

FTIR: 3334 (ν_{OH}), 2863 (ν_{CH}), 2375 (ν_{SH}), 1731 ($\nu_{C=O}$), 1612 ($\nu_{C=C,}$ $\nu_{C=N}$) cm^{-1}.

After conjugation of cysteine to the 2-chloro-4,6-diphenoxy-1,3,5-triazine, a new signal in the ^{1}H NMR spectra of the product appeared at 6.7 ppm, see Supplementary Figure 11. This signal is assigned to the proton of the amine group which is conjugated to the triazine ring. This result proves that the nucleophilic reaction between the triazine ring and cysteine occurs mostly through the amino group of cysteine.

In the IR spectra of (4,6-diphenoxy-1,3,5-triazin-2-yl)-L-cysteine (Supplementary Figure 12) the absorbance band at 2375 cm^{-1} is assigned to the thiol group. This result proves that cysteine is attached to the triazine ring through amino functional group and that the thiol group remains unreacted.

In the mass spectra, the peak at m/z = 384.3 proves the successful synthesis of (4,6-diphenoxy-1,3,5-triazin-2-yl)-L-cysteine. The results of the elemental analysis (Supplementary Table 3) are consistent with the ^{1}H NMR (Supplementary Figure 11) and the mass spectra, proving the successful reaction between cysteine and 2-chloro-4,6-diphenoxy-1,3,5-triazine.

Raman Scattering

Supplementary Figure 13 depicts the Raman spectra of the radial breathing modes (RBM) of pristine (SWNT) and triazine functionalized (SWNT-low and SWNT-high) nanotubes excited at

633 nm. The lines of the (7,6), (8,4), (7,5), and (8,3) nanotube species are observed at these excitation energies. [7] No change in the RBM is observed for the different degrees of functionalization. The D and G bands of the Raman spectra are reported in Fig. 2c of the main text.

HR(S)TEM and EELS studies

Transmission electron microscopy (TEM) and spatially-resolved electron energy loss spectroscopy (SR-EELS) studies were performed on the functionalized nanotubes. Supplementary Figure 14a is a high resolution (HRTEM) micrograph where a bundle of single-walled nanotubes is visible. Some moieties are observed at the surface of these SWNTs. In order to locally analyse these objects, having access to chemical information, we performed spatially-resolved EELS (SR-EELS) measurements. This is a powerful tool to investigate such nanomaterials at (sub-) nanometer scale [8-15].

We acquired a spectrum-image (SPIM) in the entire area shown in the high angle annular dark field (HAADF) image (Supplementary Figure 14b). Supplementary Figure 14d shows three EEL spectra extracted in the different areas marked in Supplementary Figure 14b. Each of these EEL spectra corresponds to the sum of nine spectra (3x3 probe positions of the SPIM). The carbon K edge at ~285 eV is present in all these EEL spectra. This C-K edge shows the characteristic peaks of sp^2 materials at 285 eV and 292 eV, corresponding to the π^* and σ^* contributions, respectively [8-11, 15]. The C-K edge displayed in Supplementary Figure 14d-(ii) is slightly different to the other two. Indeed, we observed that the fine structures near the edge (ELNES) of this spectrum indicate that we are dealing with a material less graphitic than those ones recorded in the other two regions (clean individual SWNT (iii) or a clean region of the bundle). Nitrogen

is also detected, see Supplementary Figure 14d-(ii). The ELNES analysis of this N-K edge indicates that this nitrogen corresponds to a pyrrolic-like atomic configuration [8-13]. Thus, the presence of this nitrogen, its atomic configuration, and the atomic configuration of the associated carbon, reveal that this nitrogen is associated to the presence of triazine.

Furthermore , it is also confirmed by the fact that these molecules are the only source of nitrogen in the samples. From the local TEM analyses, we conclude that the observed moieties correspond to the triazine functionalized molecules localized at the surface of the SWNTs.

Absorption and 2D emission spectroscopy of the SWNTs-low and SWNTs-high

Supplementary Figure 15a-c shows the full 2D luminescence map of pristine SWNT, SWNT-low and SWNT-high (cp. Fig. 2). Chiral species are labelled with the (*n*,*m*) indices.[8,9,16] Supplementary Figure 15d shows their absorption spectra.

Supplementary Note 2: Computational studies

The structure of triazine-functionalized carbon nanotubes were calculated for armchair and zig-zag nanotubes. For this paper we concentrate on the exemplary (8,0) nanotube: Calculations were performed on non-periodic structures in which dangling bonds at both ends were terminated by hydrogen bonds (Supplementary Figure 16). The convergence thresholds for energy change, maximum force, and maximum displacement between optimization cycles were set at $2.0 \cdot 10^{-7}$ kcal·mol, 0.01 kcal/mol/Å and 0.0001 Å respectively. The optimization stopped when the energy convergence was satisfied along with either the displacement or gradient criterion. The default optimization algorithm (EF) was used. The NEB calculation were performed using the ASE package.[17].

We calculated the reaction pathway for the covalent attachment of triazene onto the nanotube using climbing image nudged elastic band (CI-NEB) method [46] with the ASE package.[17] It constructs a series of atomic configurations along a minimum energy path (MEP), which follows atomic configurations corresponding to neighboring local minima. The CI-NEB showed that the MEP for the cycloaddition of the nitrene on the (8,0) nanotube lacks an activation barrier and the reaction of a single triazene with the clean SWNT occurs without an evident transition state. Initial and final structures were optimized and characterized by means of a force calculation in order to verify that two minima structures are used. The MEP was delimited by 42 intermediate configuration. Supplementary Figure 17 was calculated considering an initial separation of ca. 6 Å between the barycenters of the two endpoints. The forces on all atoms in each image of the CI-NEB chain were converged to 0.05 eV.

The nanotube orbitals of the functionalized (8,0) tubes showed the characteristic π-orbitals structure of semiconducting nanotubes. [16] Particularly impressive is the minimum amount of

distortion by the triazine in Supplementary Figure 18a (isosurface at $7.6 \cdot 10^{-3}$ $e^- nm^{-3}$). The HOMO (π-character) contains contributions from the nanotube and the triazine as visible for the isosurface in Supplementary Figure 18b (isosurface at $2.5 \cdot 10^{-3}$ $e^- nm^{-3}$).

Supplementary Note 3: Quantification of the functionalization product

In this Supplementary Note we characterize our functionalized carbon nanotubes and compare the results from different experimental methods. Elemental analysis, thermogravimetry, and X-ray photoelectron spectroscopy are used to prove the efficient attachment of the triazine groups onto the SWNTs as well as to quantify the amount of functional groups conjugated onto the tubes. Infrared absorption spectroscopy confirms the presence of the additional vibrational modes of the groups attached to the tubes.

Calculation of the density of functional groups and of the carbon nanotubes fraction

Single walled carbon nanotubes with different but well-defined numbers of functional groups were synthesized by in situ [2+1] cycloaddition reaction with azidodichloro-triazine (compound **1**) at ambient conditions. An estimation of the amount of functional groups conjugated onto the SWNTs is obtained by evaluating the density of functional groups (DFG), defined as the number of triazine rings per number of carbon atoms of the SWNT. The DFG from elemental analysis (EA) is given by the ratio between the total mass of N atoms within the functional group divided by the total nitrogen content of the product. The results of the elemental analysis, the estimated DFG, and the density of SWNTs are summarized in Supplementary Table 4 for various samples.

TGA analysis

Thermogravimetric analysis (TGA) showed that the amount of SWNT was reduced by 12% and 36% due to the triazine functional groups of the SWNT-high and SWNT-low samples, respectively (Supplementary Figure 19a). Based on these mass ratios, the DFG of SWNT-high was 1/25 and of SWNT-low was 1/100. These results are in excellent agreement with the elemental analysis results.

Each reaction was repeated at least ten times for evaluating the reproducibility of the functionalization. The nitrogen contents slightly changes from batch to batch, with a maximum deviation from the mean value of 1% (SWNT-low) and 1.3% (of SWNT-high), respectively (Supplementary Figure 19b). The nitrogen content is an indicator for DFG, proving that our approach produced SWNT with a well-defined amount of functionalities.

IR spectroscopy

In the IR spectra, characteristic bands of aziridine rings usually appear in the 1000-1250 cm^{-1} region and are assigned to symmetric aziridine ring breathing modes and to the C-N bonds in which carbon is sp^3 hybridized (sp^3C-N bonds) [18]. Instead of those peaks, new absorbance bands, not present in pristine SWNT, arise at 1296 cm^{-1} and 1305 cm^{-1} for SWNT-low and SWNT-high, respectively (Supplementary Figure 20a-c). They are assigned to sp^2C-N bonds and indicate efficient attachment of triazine groups onto SWNTs through carbon atoms with sp^2 hybridization. In the IR spectrum of SWNT-indole (Supplementary Figure 20d), the absorbance bands at 1612, 1567 and 1297 cm^{-1} are assigned to the C=C, C=N and C-N bonds, respectively. The IR spectrum of SP-SWNT (Supplementary Figure 20e) exhibits absorbance bands at 2920, 1670, 1516, 1300, and 1150 cm^{-1}, that correspond to the C-H, C=C, C=N, C-N, and C-O bonds, respectively.

In the IR spectrum of SH-SWNT (Supplementary Figure 20f) the broad band in the 3300-2400 cm^{-1} region is due to the carboxyl functional group of cysteine. The band in the 1540-1680 cm^{-1} region corresponds to the absorbance of the carbonyl group of cysteine overlapped with the absorbance of C=C and C=N bonds of SWNT and triazine.

X-ray photoelectron spectroscopy (XPS)

Sample Composition

Supplementary Figure 21 shows survey XPS spectra of SWNT, SWNT-low, SP-SWNT, SWNT-high, and a gold reference that was handled the same way as the drop-coated samples. All spectra show Au features, in particular the spin-orbit-split 4f doublet at E_B = 83.96 and 87.64 eV as shown in the upper right inset. The full widths at half maximum (FWHM) of the respective peaks of 0.57 and 0.58 eV indicate an instrumental resolution of 380 meV. The Au reference shows negligible traces of adventitious carbon at E_B = 284.4 eV and no other contaminations. The SWNT samples show a large carbon (C 1s) signal around E_B = 284.4 eV and smaller peaks due to oxygen species (O 1s) around E_B = 532 eV. SWNT-low, SP-SWNT, and SWNT-high also contain nitrogen (N 1s, at ca. E_B = 400 eV) and chlorine[a] (Cl 2p, at ca. E_B = 201 eV), which proves the successful SWNT functionalization. The occurrence of oxygen in the SWNT samples is mainly due to their inherent oxidation at defect sites.

Carbon 1s Spectra

Supplementary Figure 22 details the C 1s XP spectra of the pristine SWNT and the highly functionalized SWNT-high. The spectrum of SWNT is clearly dominated (52.4% of the total area) by an asymmetric peak [19] with a maximum at E_B = 284.30 eV due to the graphitic sp^2-hybridized carbon backbone of the SWNT. In the long asymmetric tail on the higher-binding-energy side of the spectrum we allocated additional Voigt-shape peaks ascribed to sp^3-hybridized carbon (E_B = 284.70 eV, 17.9%), hydroxy (**C**-OH, E_B = 286.10 eV, 7.4%), carbonyl (**C**=O, E_B = 287.45 eV, 4.2%), and carboxyl groups (**C**OOH, E_B = 288.89 eV, 1.4%), and a π-π^* shake-up

[a] We found very small traces of chlorine in the pristine SWNT as well. They are most probably due to residues from molecular sieves added to the solvent we used for sample preparation.

process in the sp^2 carbons [20] (E_B = 290.27 eV, 16.7%) on top of a Tougaard background [21]. The sp^3 and carbon-oxygen species are due to defect sites in the SWNTs and their inherent oxidation. These constitute 30.9% of the total carbon content, leaving 69.1% of sp^2-hybridized carbon.

The inset graph of Supplementary Figure 22 shows the C 1s spectra of the functionalized samples. They closely resemble the spectra of the pristine SWNT but are energetically shifted. We fitted the spectrum of SWNT-high by combining the same peak-area ratios and peaks we used for SWNT, but shifted in E_B by +202 meV, with two additional Voigt peaks at E_B = 285.84 eV and 288.01 eV. The latter two peaks have a peak-area ratio of 3:2 and are assigned to the three carbon atoms of the triazine unit and the two carbon atoms of the SWNT to which the bridging nitrogen is attached (C_2 unit). The C 1s spectra of all other functionalized SWNTs were fitted by the identical procedure.

The appearance of the additional peaks for SWNT-high and SWNT-low proves the actual *covalent* functionalization. The large chemical shift in E_B by +3.5 eV of the peak ascribed to the attachment C_2 units is striking. It suggests that the functionalization did not end with the formation of an aziridine moiety but rather resulted in the local restoration of the SWNT's conjugated sp^2-hybridized carbon system by ring opening. The bridging nitrogen atom's electron lone pair than joins the conjugated π-electron system of the SWNT by mesomerism with the corresponding iminium-cation state, Supplementary Figure 23. The chemical shift observed in XPS agrees reasonably well with the calculated binding energy (4.2 eV, see main text). This increases the electron density in the SWNT and explains the strong shift of the peak we ascribed to the attachment C_2 unit. As illustrated by the inset graph of Supplementary Figure 22, the C 1s spectra of the samples shift as wholes according to the functionalization. The values of the shifts

are summarized in Supplementary Table 5. A discussion of the phenomenon is presented in Supplementary Note 4.

Quantification of the Covalent Triazine Functionalization

The functionalization ratios of triazine groups (FR_{XPS}(tri)) on the SWNTs were determined by relating the respective total triazine N 1s spectral area of each sample to its sp^2 C1s area (i.e., the sum of sp^2 and attachment C_2-unit peak areas). To this end measurement statistics, relative elemental sensitivity factors [22], and the stoichiometry were taken into account. We define FR_{XPS}(tri) as the percentage of functionalized sp^2-carbon C_2 units. [b] To compare the XPS results with those of the elemental analyses (EA) we also determined the respective densities of functional groups (DFGs), Supplementary Figure 24. [c] The results are summarized in Supplementary Table 5. While our EA determined the mass percentage (wt%) of the elements C, H, N, and S contained in our samples, XPS quantified the relative amounts of *all* constituting elements (C, N, O, and Cl) but H. Elemental analysis, TGA, and XPS excellently agree in the obtained density of functional groups.

Nitrogen 1s Spectra

The N 1s spectra shown in Figure 2 of the main text and depicted in Supplementary Figure 25 (normalized to the sp^2 carbon peak) were each decomposed into Voigt peaks on a Shirley-type

---

[b] $FR_S(\ ) \quad \frac{rea^{N\ 1s}_S(tri)}{rea^{C\ 1s}_S(sp^2\ C_2\ units)}$, with $rea^{i}_{S}(\ )$ as core level i XPS peak area of constituent j.

[c] $FG_S(tri) \quad \frac{rea^{N\ 1s}_S(tri)}{rea^{C\ 1s}_S(sp^2\ atoms)} - FR(tri)$; and $FG(tri)^{t(N)} \quad \frac{\_\_N(tri)}{\_\_(tri)} / (\ )C$ with

(i) as molar mass of compound i and (i) as molar mass of compound i with respect to element j.

background [23]. SWNT-high and SWNT-low were fitted with two peaks having an area ratio of 1:3 that we assigned to the single bridging (peak B) and the three triazine nitrogen atoms (peak A). The total triazine N 1s peak areas were used to determine the FR_{XPS}(tri) and DFG_{XPS}(tri) values given in Supplementary Table 5.

In the N 1s spectrum of the spiropyran-functionalized SP-SWNT an additional signal at E_B = 405.49 eV (peak C) is clearly visible. We assigned it to the nitro group of the spiropyran molecule assembled at the triazine anchor group [24], thereby proving its successful synthesis. The N 1s signal between E_B = 397 and 402 eV for SP-SWNT is similar to that of SWNT-low. The additional intensity is due to the second nitrogen atom of the molecular switch (peak D).

We determined the FR_{XPS}(spiro) of the spiropyran groups with respect to the available triazine units by comparing the N 1s XPS peak areas. The result of 65% gives the average number of spiropyran units per triazine anchor as 1.3. Statistically 30% of the triazine units substituted both of their chlorine atoms with a spiropyran switch, while 70% carry a single switch. This proves the effectiveness of this preparation.

Chlorine 2p Spectra

Cl 2p spectra for SWNT, SWNT-low, SP-SWNT, and SWNT-high are depicted in Supplementary Figure 26. The finite background in the SWNT spectrum (black) hints at trace amounts of chlorine. It originates most likely from the molecular sieves added to the solvent used for sample preparation. We took the SWNT Cl 2p spectrum as background for all other Cl spectra, scaling it to match their respective secondary-electron signals. The subtracted spectra were decomposed into doublets with peak-area ratios of 2:1 and a spin-orbit splitting of 1.5 eV on top of linear backgrounds. The $2p_{3/2}$ components (peak K) were found at E_B = 200.48 eV for SWNT-high and SP-SWNT and at E_B = 200.01 eV for SWNT-low.

By relating the Cl 2p peak areas to the respective triazine N 1s peak areas we determined the number of Cl atoms per triazine unit and the FR_{XPS}(Cl) (in brackets). For SWNT-low it is ca. 2 (100%), for SP-SWNT ca. 0.7 (35%), and for SWNT-high ca. 0.5 (25%).

These numbers indicate the following. First, during the low-temperature triazine-functionalization reaction for SWNT-low (and SP-SWNT) no chlorine was lost. We covalently couple intact dichlorotriazine functional groups to SWNTs. Second, the assembly of the spiropyran via SWNT-indole did not lead to any additional losses of chlorine atoms apart from the ones substituted. In SP-SWNT all triazine units carry on average 1.3 spiropyran molecular switches and 0.7 Cl atoms. In other words, 30% of the triazine units are doubly substituted with spiropyran, 70% have a spiropyran and a Cl atom attached. This proves that the synthesis of the spiropyran at the SWNT actually proceeds quantitatively. It also shows that all triazine groups that are covalently coupled to an SWNT may be further functionalized effectively. Third, the triazine functionalization at 70°C for SWNT-high caused a large but not complete loss of 75% of the Cl atoms. [d] Optimized reaction conditions will find an ideal trade off between functionalization density and preserving triazine Cl content.

[d] When XPS measurements were repeated with samples, there was no indication of any losses of functional groups by X-ray beam damage (cf. the inset in Supplementary Figure 26).

Supplementary Note 4: Change in Fermi energy

In the previous Supplementary Notes we focused on the chemical and morphological properties of the functionalized products, demonstrating the presence of the covalently attached functional groups and quantifying the density of groups attached onto the nanotube sidewall. We have, moreover, shown the 2-D excitation-emission charts for the nanotubes with different degrees of coverage, proving that the conjugation of the functional groups preserves the π-conjugation of the carbon network. Even if the covalent functionalization of the SWNTs does not perturb their optoelectronic structure, it can still contribute with additional charges to the nanotubes' delocalized π-system. In this Supplementary Note we focus on the investigations of this charge-transfer effect/doping and its quantification. For a careful characterization, we resort to different experimental techniques. Supplementary Figure 27 summarizes their results: The Fermi level of the functionalized tubes shifts upwards when increasing the density of functional groups. The p-doping of the pristine SWNTs gets (Supplementary Figure 27, left) compensated by the functionalization, uplifting the Fermi energies of the functionalized tubes close to the neutral point for SWNT-low (middle) and above in SWNT-high (right). The C 1s levels in the XPS spectra are sensitive to the functionalities conjugated onto the tubes. Their binding energy shift provides a useful indicator of the Fermi energy shift induced by the covalent attachment of functional groups. Raman investigations on small-diameter metallic nanotubes complement the XPS findings. Beyond the effect induced by the covalent attachment of the functional groups, in the last part of this note we analyse the optically-triggered effects due to the spiropyran-to-merocyanine isomerization when SP-SWNT are exposed to UV radiation.

X-ray photoelectron spectroscopy

Our XPS study provided strong evidence for an electronic interaction between the triazine unit and the functionalized SWNT. The C 1s XP signal of a C_2 unit under the bridge to the triazine unit shifted by 3.5 eV to higher binding energy. A corresponding shift to lower binding energy was observed for the N 1s signal of the bridging nitrogen atom with respect to the nitrogen in the triazine. The large opposite chemical shifts suggest that the electron lone pair of the bridging nitrogen atom contributes to the conjugated π-electron system of the SWNT, see the scheme in Supplementary Figure 23. This likewise manifests by an increase in Fermi energy. As illustrated in Supplementary Figure 28 the shift of the C1s XP level to higher binding energy directly reflects an upward shift of the Fermi level towards the SWNT conduction-band. Interestingly, a deposition of triazine on graphene without chemical interaction results in the opposite behavior (lower C 1s binding energy and decrease in Fermi energy). [24]

The XPS peak shifts were independent of the actual amount of SWNT material covering the substrate. This implies the induction of a negligible photovoltage and/or a low-resistance junction between the Au substrate and the drop-coated SWNT film. Therefore the Fermi levels E_F of the electron analyzer and the sample were aligned in the XPS measurements and the observed shift of the C 1s peak position with increasing functionalization ratio directly reflected the shift of the SWNT Fermi level. E_F shifts upwards towards the conduction band of the semiconducting SWNT. When referenced to the analyzer Fermi level the C1s XPS signal must shift downwards towards higher binding energy E_B (see Supplementary Figure 28).

In Supplementary Figure 29 we plot FR_{XPS}(tri) as a function of the observed C 1s peak shift ΔE for the SWNTs. We also investigated two additional triazine-functionalized samples, prepared with the same procedures, one with less ($SWNT^{(*)}$-low) and one with more ($SWNT^{(*)}$-high)

functional groups based on SWNTs coming from different production methods and batches (CoMoCAT®) and referenced against their respective pristine SWNTs.

Raman characterization of the metallic tubes.

The Raman spectra confirm the functionalization of metallic nanotubes through changes in peak width. The G band of metallic carbon nanotubes consists of two bands, labelled as G^+ at ca. 1580 cm^{-1} due to the transverse optical phonon (TO), and G^- at ca. 1540 cm^{-1} due to the longitudinal optical phonon (LO). The LO mode responsible for the G^- band is very sensitive to shifts of the Fermi energy level and its broadening can be used to quantify the doping in metallic SWNTs [26]. We monitored the G band of metallic nanotubes with various functionalization levels under 532 nm laser excitation, where metallic tubes were resonantly excited. For each sample we acquired at the same spot the G and the radial-breathing mode (RBM) spectra to control the CNT chirality distribution at the analysed position (Supplementary Figure 30a,b). We identified the metallic (9,3), (8,5), and (7,7) species.

To calculate the Fermi energy shift, we used the model of the LO peak broadening discussed in Ref. [26]. A shift in the Fermi level away from its intrinsic position (crossing of valence and conduction band) continuously increases the LO phonon lifetime and decreases the full width at half maximum (FWHM) of the LO peak. As a rule of thumb one half of the maximum FWHM indicates the E_F at half the LO energy. The maximum FWHM value for the analysed species (d=0.85 nm) is 100 cm^{-1} and the phonon energy is 187 meV. [27] We considered a Lorentzian dispersion model for fitting our data (Supplementary Figure 30d), obtaining values of the doping levels of -70 meV for the pristine SWNT, -40 meV for SWNT-low and SP-SWNT, and +20 meV for SWNT-high. The positive sign of the E_F shift was obtained from the 6 cm^{-1} decrease in frequency of the 2D Raman mode between the pristine SWNT and SWNT-high. [26,28] It agrees

with the increase in Fermi energy obtained from the XPS data. Overall, ΔE_F from Raman is smaller than observed in XPS. This is explained by the limited number of small-diameter tubes accessed in Raman scattering, whereas XPS obtains a mean doping level across all nanotubes.

Effect of the SP-to-MC isomerization

Under UV irradiation, SP converts into MC. As a consequence of the SP-to-MC isomerization, the emission of the tubes gets quenched. In Supplementary Figure 31a we report the excitation-emission map (in 3-*D* to highlight the intensity changes) displaying all the nanotube species contained within the SP-SWNT sample. After the conversion, the emission is quenched in the MC-SWNT sample (Supplementary Figure 31b). Unlike free MC, MC-SWNT does not isomerize back to the SP-SWNT upon visible light irradiation. It thermally gets back to the SP-SWNT if left in darkness. Supplementary Figure 31c shows the recover of 75% of the emission intensity after 2 h of darkness. For a full recovery of the emission, the samples needed to remain in darkness for 24 h. The net effect of the SP-to-MC conversion is quenching of the SWNT emission, without any change in the spectral position of the emission bands (Supplementary Figure 31d). To quantify the amount of doping due to the isomerization, we focused on the Raman analysis of semiconducting SWNTs. Similarly to the metallic nanotubes, semiconducting nanotubes' G band consists of two sub-bands, labelled G^+ and G^- as well but arising from different modes than in metallic tubes. [26,27] For semiconducting SWNTs, the LO phonon contributes to the G^+ band (at 1590 cm^{-1}) while the TO contributes to the G^- band (at ca. 1565 cm^{-1}). Doping thus affects differently semiconducting SWNT than the metallic SWNT, shifting the position of the G^+ band. This can be used to quantify the shift of the Fermi energy [28]. The Raman spectra of SP-SWNT and MC-SWNT (obtained by UV light irradiation of the SP-SWNT to promote SP-to-MC conversion) are shown in Supplementary Figure 32. The only difference

between the two spectra is given by a shift of 2 cm^{-1} of the G^+ band position, suggesting an upshift of 0.2 eV of the Fermi energy from comparing with the result of Ref. [28].

Control experiment on the effect of UV irradiation

To confirm that the observed effects are due to the SP-to-MC conversion and rule out UV exposure damages, we exposed to UV irradiation two samples with similar characteristics but one with- (SP-SWNT) and the other without (SWNT-low) spiropyran. In Supplementary Figure 33 the temporal change of the absorbance at 300 nm is monitored. While the onset of the merocyanine absorption band can be observed in SP-SWNT, no changes occur in the SWNT-low sample, ruling out any damage by the UV light exposure.

Supplementary Note 5: Nanoplasmonic hybrids

In this Supplementary Note we report on the characteristics of the nanoplasmonic hybrids Au@SWNTs. Additionally, we discuss a set of control experiments for plasmonic enhancement in SWNTs.

Optical and morphological properties of the AuNPs

For the synthesis of the AuNPs, please refer to the Methods section of the main manuscript text. TEM micrographs of the AuNPs show a distribution of the particle size between 10 and 20 nm (Supplementary Figure 34). For such an ensemble absorption spectroscopy reveals the presence of the plasmon absorption band of the AuNPs peaked at 520 nm.

2D emission spectroscopy of the Au@SWNTs hybrids: Emission enhancement

Once coated with the AuNPs, we observe enhancement of the emission of the nanotubes. Supplementary Figure 35a reports the excitation-emission map (in 3-*D* to highlight the intensity changes) displaying all the nanotube species contained within the thiol-functionalized SH-SWNT sample. After the attachment of the gold nanoparticles, the emission of Au@SWNT is enhanced (Supplementary Figure 35b). The net effect of the interaction with the plasmonic particles is the enhancement of the emission of the different species, without any change in the spectral position of the emission bands (Supplementary Figure 35c).

The relative change of the emission intensity depends on the specific species and ranges between 20% and 100%. In Supplementary Figure 36 we plot the relative change of the emission intensity *vs.* excitation wavelength of the considered species (green dots, the curve is a guide to the eye) and compare it with the absorption spectrum of the Au@SWNT hybrids (blue curve).

Interestingly, there is a systematic red-shift between the plasmonic bands of the gold particles and the excitation resonance profile of the carbon nanotubes. The dependence of the enhancement on excitation wavelength with respect to the plasmonic response will be studied in a future paper.

Nanoplasmonic hybrids - control experiments: Role of the covalently-bound thiols and contribution of the triazine-based covalent attachment

To highlight the importance of the thiol-based attachment in our hybridization process, we performed two sets of control experiments: One control shows the relevance of the thiol-triazine based immobilization of the Au nanoparticles on the SWNTs and the other compares standard covalent functionalization with our cycloaddition-based method.

The first set of control samples were prepared following the very same procedure as for the Au@SWNTs hybrids but starting each time from different sets of tubes, one for each step of the synthesis leading to the SH-SWNTs. In Suppplementary Figures 37a,b we compare the emission of the pristine tubes (SWNT) with the emission of the hybrids obtained by mixing gold with pristine tubes (Au+SWNT) and tubes functionalized with triazine groups but without the thiol-termination (Au+SWNT-high). The emission from the hybrids is always weaker than the emission from the pristine tubes, highlighting the key role of the thiol-induced immobilization of the AuNPs at the nanotubes sidewalls.

In the second set of control experiment, we show that the other key element towards successful emission enhancement is the preservation of the pristine optoelectronic properties of the tubes. We generate a set of COOH-covalently functionalized carbon nanotubes (COOH-SWNTs) by following the standard acid treatment. [29] To produce the carboxylic groups onto the tubes sidewalls, we dissolved 1 g of SWNTs in a mixture of 150 ml of H_2SO_4 and 50 ml of HNO_3,

which was heated up to 60°C and stirred for 45 min. Afterwards, the solution was filtered and washed repeatedly with distilled water to reach a pH value of 7. Subsequently, the sample was dried overnight at 60°C. Figure 38a compares the Raman spectra of pristine (SWNT) and carboxylated (COOH-SWNT) tubes. The increase in the intensity of the D band after the carboxylation of the tubes is a clear indication of the increased defectivity introduced by the covalent approach. The optical properties of the tubes are destroyed by the functionalization. We ensured a mild functionalization to preserve some emission from the functionalized tubes.

To attach the thiol-groups onto the tubes, 100 mg of the COOH-SWNTs were dispersed in thionyl chloride (10 ml) by 30 min sonication. Then they were refluxed for 6 h. The excess of thionyl chloride was evaporated and dry DMF was added to the residual compound. Cystein (100 mg) and triethylamine (0.11 ml) were added to the mixture, which was then stirred for 2 h at 25°C and for 12 h at 70°C, respectively. The mixture was cooled and centrifuged (1100 rpm, 1 hour). The product was dialyzed in the alkali aqueous solution (pH 8) for 2 days and then lyophilized.

The IR spectra of COOH-SWNT and SH-COOH-SWNT, reported in Supplementary Figure 38b, and the results of their elemental analysis, reported in Supplementary Table 7, confirmed the successful functionalization: The appearance of a broad absorbance band in the 3015-3630 cm^{-1} region of the IR spectra of SH-COOH-SWNT as well as the shift of the carbonyl absorbance band from 1726 cm^{-1} for COOH-SWNT to 1596 cm^{-1} for SH-COOH-SWNT indicate conjugation of cysteine molecules to the sidewall of carbon nanotubes. The 10% sulfur content of SH-COOH-SWNT also indicates the attachment of cysteine to SWNTs.

Figure 39 compares the emission of pristine tubes with the one of thiol-terminated carboxylated nanotubes before and after gold attachment. After attaching gold nanoparticles, the nanotube

emission gets quenched. This might be a genuine quenching process due to energy transfer between AuNPs and SWNTs. An additional reduction in intensity may arise from reabsorption and scattering in the solution.

Supplementary Methods

Infrared (IR) spectra were recorded using a JASCO spectrometer. Ultrasonic bath (Model: SONOREX, RK255 HZ) was used to disperse materials in solvents. TGA measurements were recorded by a STA 409 apparatus (from Netzsch) in temperatures ranging from 25-800ºC with a 10ºC/min heating rate under air. Elemental analysis was performed using ELEMENTAR apparatus with three columns and detector for carbon, nitrogen, hydrogen and sulfur elements.

XPS measurements were carried out on SWNT, SWNT-low, SWNT-high, and SP-SWNT samples. For this the substances were dispersed in THF and the suspensions carefully dropped onto thin-film gold substrates (300 nm Au(111) on mica, Georg Albert PVD) and left on the bench until the solvent was evaporated. Samples were then brought into ultra-high vacuum (UHV) and measured with a monochromatic high-resolution XPS setup (VG Scienta MX 650 and SES-200) in perpendicular take-off geometry with constant analyzer pass energy of 200 eV. All binding energies (E_B) were referenced to the Au substrate $4f_{7/2}$ peak at E_B = 83.96 eV and are correct within 40 meV. The zero of the binding energy scale corresponds to the Fermi level of the Au substrate. Due to the drop-coating preparation the samples did not contain equal absolute amounts of substance and their spectra needed to be normalized. Considering the comparable shape of the C 1s spectra and the fact that the SWNTs were not exposed to any harsh treatments, we assumed that their carbon backbones remained intact and that the established functionalization ratios (FR) did not significantly reduce the amount of sp^2-hybridized carbon atoms. Therefore we chose to normalize all SWNT XP spectra with respect to the carbon backbone, i.e., the intensity of the sp^2-carbon component.

High resolution TEM was performed employing an imaging-side aberration-corrected FEI Titan-Cube microscope working at 80 kV, equipped with a Cs corrector (CETCOR from CEOS

GmbH). Spatially-resolved electron energy loss spectroscopy (EELS) measurements were performed on probe-corrected scanning TEM (STEM) FEI Titan Low-Base operating at 80keV (fitted with a X-FEG® gun and Cs-probe corrector (CESCOR from CEOS GmbH)). Furthermore, in order to avoid the effects of electron beam damage, these measurements have been performed using a liquid-nitrogen-cooled cryo-holder at -170º C. EEL spectra were recorded using the spectrum-imaging (SPIM in 2D or spectrum-line (SPLI) in 1D) mode [15,30] in a Gatan GIF Tridiem ESR 865 spectrometer. The convergent semi-angle was of 25 mrad, the collection semi-angle was of 30 mrad and the energy resolution ~ 1.0 eV. To filter the noise in the experimental data, the background corrected EEL spectra showed in Supplementary Figure 14f were smoothed using a Savitzky-Golay filter (second-order polynomial).

The transmission electron microscopy (TEM) samples were prepared by dispersing the NTs powders in ethanol. The dispersions were ultrasonicated and subsequently deposited on holey carbon 3 mm copper grids.

Raman spectra of metallic nanotubes were acquired using an XploRa spectrometer (Horiba), excitation wavelength at 532 nm, equipped with charge-coupled device, 2400 lines/mm gratings and edge filter to block Rayleigh-scattered light. Frequencies were calibrated using a cyclohexane reference sample.

The electrospray ionization-time of flight (ESI-TOF) measurements were performed on an Agilent 6210 ESI-TOF from Agilent Technologies, Santa Clara, CA, USA. The solvent flow rate was adjusted to 4 µL/min and the spray voltage set to 4 kV. The drying gas flow rate was set to 15 psi (1 bar). All the other parameters were adjusted for a maximum abundance of the relative $[M+H]^+$. ^1H NMR and ^{13}C NMR spectra were recorded on a Bruker Avance 400 spectrometer

(Bruker Corporation, Billerica, MA, USA) (at 295 K). Tetramethylsilane was used for internal calibration at 125 MHz with complete proton decoupling.

Supplementary References

1. Mori K, Matsuno Y, Mori K, Kudo T. *Bonding method, bondability improving agent, surface modification method, surface modifying agent, and novel compound.* US patent 2013, US20130177770 A1.
2. Bucher G, Siegler F, Jens Wolff J. *Photochemistry of 2-azido-4,6-dichloro-s-triazine: matrix isolation of a strained cyclic carbodiimide containing four nitrogen atoms in a seven-membered ring*. Chemical Communications **20,** *2113-2114* (1999).
3. Gebhardt B, Syrgiannis Z, Backes C, Graupner R, Hauke F, Hirsch A. *Selective Polycarboxylation of Semiconducting Single-Walled Carbon Nanotubes by Reductive Sidewall Functionalization*. J. Am. Chem. Soc. **133**, *7985-7995* (2011).
4. Gao C, He H, Zhou L, Zheng X, Zhang Y. *Scalable Functional Group Engineering of Carbon Nanotubes by Improved One-Step Nitrene Chemistry*. Chem. Mater. **21**, *360-370* (2009).
5. Yadav S. K, Kim J, Kim H. J, Kim J, Hong S. M, Koo C. M. *PDMS/MWCNT nanocomposite actuators using silicone functionalized multiwalled carbon nanotubes via nitrene chemistry*. J. Mat. Chem. C **1**, *5463-5470* (2013).
6. H. Namazi and M. Adeli. *Synthesis of barbell-like triblock copolymers, dendritic triazine-block-poly(ethylene glycol)-block-dendritic triazine and investigation of their solution behaviors*, Polymer **46**, *10788-10799* (2005).
7. J. Maultzsch, H. Telg, S. Reich, and C. Thomsen, *Radial breathing mode of single-walled carbon nanotubes: Optical transition energies and chiral-index assignment*, Phys. Rev. B **72**, *205438* (2005).

8. P. Ayala, R. Arenal, M. Rummeli, A. Rubio, T. Pichler, *Doping carbon nanotubes with Nitrogen: a route towards applications*, Carbon **48**, *575-586* (2010).

9. P. Ayala, R. Arenal, A. Loiseau, A. Rubio, T. Pichler, *The physical and chemical properties of heteronanotubes*, Rev. Mod. Phys. **82**, *1843-1885* (2010).

10. R. Arenal, K. March, C.P. Ewels, X. Rocquefelte, M. Kociak, A. Loiseau, O. Stephan, *Atomic Configuration of Nitrogen-Doped Single-Walled Carbon Nanotubes*, Nano Lett. **14**, *5509−5516* (2014).

11. R. Arenal, X. Blase, A. Loiseau, *Boron-nitride and boron-carbonitride (BCN) NTs: synthesis, characterization and theory*, Adv. in Phys. **59**, *101-179* (2010).

12. L. Alvarez, Y. Almadori, R. Arenal, R. Babaa, T. Michel, R. Leparc, J-L.Bantignies, P. Hermet, J-L.Sauvajol, *Transfer evidence between carbon nanotubes and encapsulated conjugated oligomers*, J. Physical Chem. C **115**, *11898-11905* (2011).

13. R. Arenal, L. De Matteis, L. Custardoy, A. Mayoral, M. Tence, V. Grazu, J.M. de la Fuente, C. Marquina, M.R. Ibarra, *Spatially-Resolved EELS Analysis of the Antibody Distribution on Bio-functionalized Magnetic Nanoparticles*, ACS Nano **7**, *4006-4013* (2013).

14. R. Arenal, F. de la Pena, O. Stephan, M. Walls, A. Loiseau, C. Colliex, *Extending the analysis of EELS spectrum-imaging data, from elemental to bond mapping in complex nanostructures*, Ultramicroscopy **109**, *32-38* (2008).

15. A. Mayoral and R. Arenal, *Advanced Transmission Electron Microscopy: Applications to Nanomaterials*, Eds. L. Francis, Springer (2015).

16. S. Reich, C. Thomsen, J. Maultzsch, *Carbon Nanotubes: Basic Concepts and Physical Properties*, Wiley-VCH (2004).

17. S. R. Bahn and K. W. Jacobsen, *An object-oriented scripting interface to a legacy electronic structure code*, Comput. Sci. Eng. **4,** *56-66* (2002).

18. H.L. Spell, Infrared spectra of N-substituted aziridine compounds. *Anal. Chem.*, **39**, *185–193* (1967).

19. M. Schmid, H.-P. Steinrück, J.M. Gottfried, *A new asymmetric Pseudo-Voigt function for more efficient fitting of XPS lines*, Surf. Interface Anal. **46,** *505–511* (2014).

20. M. Filippi, L. Calliari, *Measuring the energy of the graphite π + σ plasmon peak*, Surf. Interface Anal. **38**, *595–598* (2006).

21. S. Tougaard, *Quantitative analysis of the inelastic background in surface electron spectroscopy*, Surf. Interface Anal. **11**, *453–472* (1988).

22. C.D. Wagner, L.E. Davis, M.V. Zeller, J.A. Taylor, R.H. Raymond, L.H. Gale, *Empirical atomic sensitivity factors for quantitative analysis by electron spectroscopy for chemical analysis*, Surf. Interface Anal. **3,** *211–225* (1981).

23. D.A. Shirley, *High-Resolution X-Ray Photoemission Spectrum of the Valence Bands of Gold*, Phys. Rev. B. **5**, *4709–4714* (1972).

24. J. Allouche, A. Le Beulze, J.-C. Dupin, J.-B. Ledeuil, S. Blanc, D. Gonbeau, *Hybrid spiropyran–silica nanoparticles with a core-shell structure: sol–gel synthesis and photochromic properties*, J. Mater. Chem. **20**, *9370-9378* (2010).

25. J. Cervenka *et al. Graphene field effect transistor as a probe of electronic structure and charge transfer at organic molecule–graphene interfaces*, Nanoscale **7**, *1471* (2015).

26. B. Hatting, S. Heeg, K. Ataka, J. Heberle, F. Hennrich, M.M. Kappes, R. Krupke, and S. Reich, *Fermi energy shift in deposited metallic nanotubes: A Raman scattering study* , Physical Review B **87**, *165442* (2013).

27. M. Lazzeri, S. Piscanec, F. Mauri, A.C. Ferrari, and J. Robertson, *Phonon linewidths and electron-phonon coupling in graphite and nanotubes*, Physical Review B **73**, *155426* (2006).

28. Das, A. Sood, A. K. Govindaraj, A. Marco Saitta, A. Lazzeri, M. Mauri, F. and Rao, C.N.R *Doping in carbon nanotubes probed by Raman and transport measurements.* Phys. Rev. Lett. **99**, 136803 (2007).

29. R. Yu *et al.*, *Platinum Deposition on Carbon Nanotubes via Chemical Modification* , Chem. Mater.**10**, *718-722* (1998).

30. C. Jeanguillaume, C. Colliex, *Spectrum-image: the next step in EELS digital acquisition*, Ultramicroscopy **28**, *252-257* (1989).

3.3 Gram-Scale, Metal- and Solvent-mediated Synthesis of Two-Dimensional Triazine Heterostructures

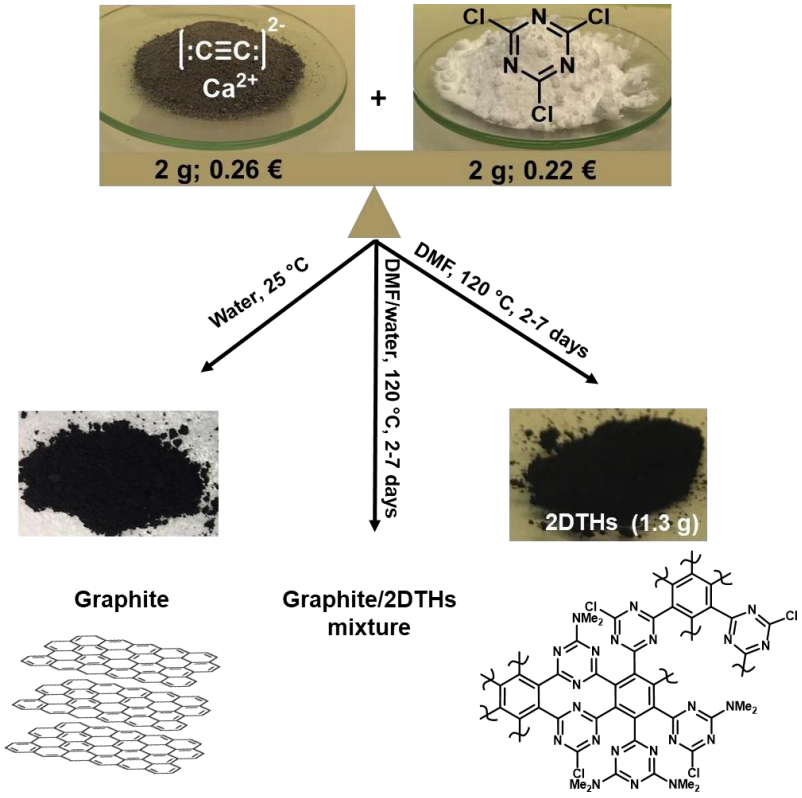

Abbas Faghani, Mohammad Fardin Gholami, Matthias Trunk, Pradip Pachfule, Johannes Müllerb, Philip Nickl, Sarah Vogel, Jingjing shao, Sabrina Jürgensen, Antonio Setaro, Wolfgang E. S. Unger, Raul Arenal, Christoph T. Koch, Beate Paulus, Jürgen P. Rabe, Stephanie Reich, Arne Thomas, Rainer Haag, Mohsen Adeli.

Note: This titled manuscript has online number: ja-2020-023999, which was submitted to the **Journal of the American Chemical Society (JACS)**.

Author contributions

Abbas Faghani performed all the syntheses, main experiments, and wrote the paper. Mohammad Fardin Gholami and Jürgen P. Rabe performed SFM and Raman experiments, analyzed the data. Matthias Trunk, Pradip Pachfule and Arne Thomas did NMR, P-XRD and ATR-IR mesurements. Johannes Müller, Christoph T. Koch discussed SAED. Philip Nickl and Wolfgang E. S. Unger conducted the XPS. Jingjing Shao and Beate Paulus simulated the intermediate compound. Raul Arenal carried out the HRTEM and EELS analyses. Stephanie Reich and Antonio Setaro performed and analyzed the PLE measurements. Mohsen Adeli and Rainer Haag conceived and supervised the project. They corrected the manuscript as well.

Gram-Scale, Metal- and Solvent-mediated Synthesis of Two- Dimensional Triazine Heterostructures

Abbas Faghani,[a] Mohammad Fardin Gholami,[b] Matthias Trunk,[c] Johannes Müller[b], Pradip Pachfule,[c] Sarah Vogel,[c] Philip Nickl,[a] Jingjing shao,[a] Sabrina Jürgensen,[d] Antonio Setaro,[d] Wolfgang E. S. Unger,[e] Raul Arenal,[f] Christoph T. Koch,[b] Beate Paulus,[a] Jürgen P. Rabe,[b] Stephanie Reich,[d] Arne Thomas,[c] Rainer Haag,[a] Mohsen Adeli,*[a,g]*

[a] *Institut für Chemie und Biochemie, Freie Universität Berlin, Takustraße 3, Berlin 14195, Germany.*

[b]*Department of Physics & IRIS Adlershof Humboldt Universität zu Berlin Newtonstrasse 15, 12489 Berlin Germany.*

[c]*Department of Chemistry / Functional Materials, Technische Universität Berlin, BA2, Hardenbergstraße 40, 10623 Berlin, Germany.*

[d]*Department of Physics, Free University Berlin, Arnimallee 14, 14195 Berlin, Germany*

[e]*BAM – Federal Institute for Material Science and Testing, Division of Surface Analysis and Interfacial Chemistry, Unter den Eichen 44-46, 12205 Berlin, Germany*

[f]*Laboratorio de Microscopias Avanzadas (LMA), Instituto de Nanociencia de Aragon, Universidad de Zaragoza, 50018 Zaragoza, Spain. 5 Fundacion ARAID, 50018 Zaragoza, Spain.*

[g]*Faculty of Science, Department of Chemistry, Lorestan University, Khorramabad, Iran*

Abstract: This work elucidates a metal- and solvent-mediated reaction between calcium carbide and cyanuric chloride, as cheap and commercially available precursors, to synthesize two-dimensional triazine heterostructures (2DTHs). Reaction between dimethylformamide and cyanuric chloride was promoted by calcium carbide and resulted in dimethylamino-triazine intermediates which in turn undergo nucleophilic substitutions. This reaction was directed in two dimensions by calcium ions derived from calcium carbide and induced the formation of 2DTHs. The role of calcium ions in two-dimensionality of the resulted structure was simulated using DFT and further it was proven by synthesizing some intermediates. The water content of the reaction medium was found to be a crucial factor that affected the structure of the products dramatically. While 2DTHs were obtained at dry conditions, graphite/2DTHs mixture or only graphite was obtained in aqueous solutions. Taking advantage of their straightforward and gram-scale synthesis, as well as fluorescence, photothermal and photodynamic properties, the synthesized two-dimensional triazine heterostructures are promising materials for a wide range of the future applications.

Keywords: Triazine two-dimensional polymer, metal-assisted polymers, calcium carbide reaction.

Introduction

Synthetic polymers are categorized topologically in one-, two- and three-dimensional structures.[1] In spite of the long history of one- and three- dimensional polymers,[1-2] their two-

dimensional (2D) analogs have been explored in the recent decades.[3-5] The only recent synthetic success of 2D polymers is due to the limiting factors to confine monomers in a sheet-like structure.[3] Two-dimensional preorganization of monomers, which is mostly derived by supramolecular forces, followed by polymerization that leads to 2D polymers.[4, 6-8] For example, polymerization of a monolayer of amphiphilic monomers in liquid/gas[9-11] and liquid/liquid[12-16] interfaces or their assemblies on/in a platform[17-19] is triggered by an external stimuli factor to catenates monomers into a 2D structure. In another approach, monomer crystals are directly polymerized to a crystalline 2D polymer by appropriate reactions.[20] Moreover, self-assembly of amphiphilic monomers into a sheet-like structure in aqueous solutions and *in situ* polymerization results in sheet-like polymers with a high surface area.[21] In these approaches, non-covalent interactions between the functional groups of monomers are driving forces to form supramolecular two-dimensional structures as precursors for the polymerization process.[20, 22] Most of the mentioned strategies are interface assisted techniques and are influenced by chemical, physical and mechanical properties of the interfaces.[23] For example, interactions between monomers or co-monomers and subphases, orientational structure and mobility of monomers at interface, low temperature variations, transfer processing of 2D polymers from interfaces as well as roughness and type of interface (gas/liquid, liquid/liquid, gas/solid or liquid/solid) affect the structure and properties of 2D polymers significantly.[23-29] In addition, interface polymerizations are often limited to the microgram scale and require synthetic monomers, which hamper the large scale production of these materials both technically and economically.[23] The single-crystal-to-single-crystal synthesis of 2D polymers, on the other hand, can be performed in gram-scale but limited to monomers with the ability of single crystal formation.[20, 22, 30-32]

The common aspect of all synthetic strategies for the production of 2D polymers is preorganization of monomers to create sheet-like supramolecular precursors.[8] This is a very efficient strategy but with the mentioned challenges that are related to the low stability of the supramolecular monomer organizations and interface limitations.[29] 2D directed polymerization by strong but controlled forces such as coordinate covalent bonds is an alternative to overcome these challenges. Coordinate covalent bonds are strong enough to construct stable organometallic 2D polymers[33-34] with the outstanding optical, electrical and physicochemical properties.[33-36] As an outcome, coordinate covalent bonds are able to organize monomers in sheet-like structures.[37-43] Taking advantage of this property and susceptibility of these bonds to strong ligands, the coordinated sheet-like structures of reactive monomers can be converted to

2D polymers upon polymerization and removal of the metal ions. Such chemistry can be performed in solution, circumventing the limitations of the interface assisted strategy.

In this work, we have used this strategy for the synthesis of two-dimensional triazine heterostructures. Reaction between calcium carbide and cyanuric chloride in dimethylformamide (DMF) resulted in 2DTHs with several micrometer lateral sizes. While cyanuric chloride contributed as the source of triazine units, calcium carbide provided both acetylide linkages and calcium ions. Reaction was mediated by DMF and directed in two dimensions by calcium ions, leading to 2DTHs after trimerization of acetylide linkages. The water content of the reaction medium changed the structure of the product from 2DTHs, in dry DMF conditions, to purely graphitic in water as solvent.

Results and discussion

Reaction between cyanuric chloride and DMF at different conditions results in versatile intermediates in organic chemistry.[44-48] Herein, we demonstrate that this reaction in the presence of calcium carbide renders 4,6-dichloro-N, N-dimethyl-1,3,5-triazin-2-amine which undergo consecutive acetylide nucleophilic substitutions and produce two-dimensional triazine heterostructures after trimerization (Figure 1). Calcium ions directed the C─C coupling of monomers in two dimensions and were eventually removed by washing process (See page S8). This reaction was performed at different conditions and effect of water on the structure of products was monitored (Figure 1). Scanning electron microscopy (SEM) and high resolution transmission electron microscopy (HRTEM) images demonstrated a layered structure with few micrometer lateral sizes for the products of reactions at different conditions (Figures 2d,e). However, further investigations explored different structures for the materials synthesized at different water content. While 2DTHs were formed in dry conditions, crystalline graphitic derivatives were obtained in aqueous solutions (Figure 2d). It is already shown that reaction between water and calcium carbide results in crystalline graphite sheets.[49] Accordingly, the product of our reaction in aqueous solution showed a crystalline structure also with a unit cell close to graphene (Figures 2e,f and S1). In dry condition, however, the product of reaction was not crystalline. Electron energy loss spectroscopy (EELS) spectra of the product in dry condition, 2DTHs, showed discrete peaks at 295 eV and 412 eV which are assigned to the carbon and nitrogen elements in the backbone of this material (Figure S2). The nitrogen content of the product as an indicator for the triazine rings, was measured by elemental analysis.

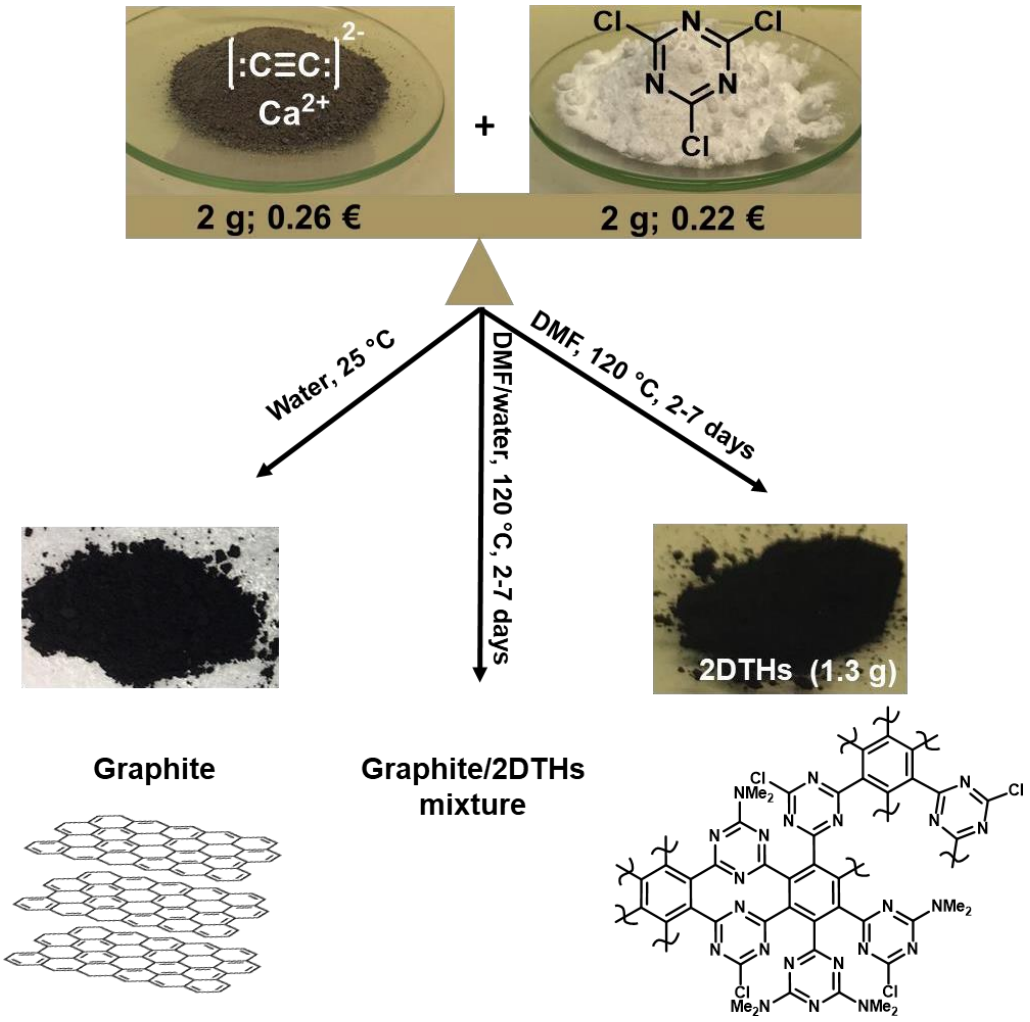

Figure 1. The product of reaction between calcium carbide and cyanuric chloride influenced by the water content of solvent strongly. While graphite was the main product in aqueous solutions, 2DTHs were obtained in dry DMF. The cost-effectiveness of the reaction is shown by the estimated prices and quantities of the precursors of two-dimensional triazine heterostructures (details can be found in S8-9). Prices of reagents were monitored from commercial suppliers (See page S3).

While the nitrogen content of the reaction product in water was close to zero, it was increased by decreasing the water content of the reaction. Under dry DMF conditions, according to elemental analysis the carbon/nitrogen ratio of 2DTHs was 2.6, rendering a C_3N_1 molecular formula for the two-dimensional triazine heterostructures (Table S1). This carbon/nitrogen ratio is higher than that of the expected structure, with C_2N_1 chemical formula. The reason for such a deviation can be formation of graphitic domains[49-50] in 2DTHs by acetylide cross-coupling and consequently trimerization. The topography and size of 2DTHs were further investigated by scanning force microscopy in quantitative nanomechanical mapping (SFM-QNM) of samples deposited on a freshly cleaved mica surface.

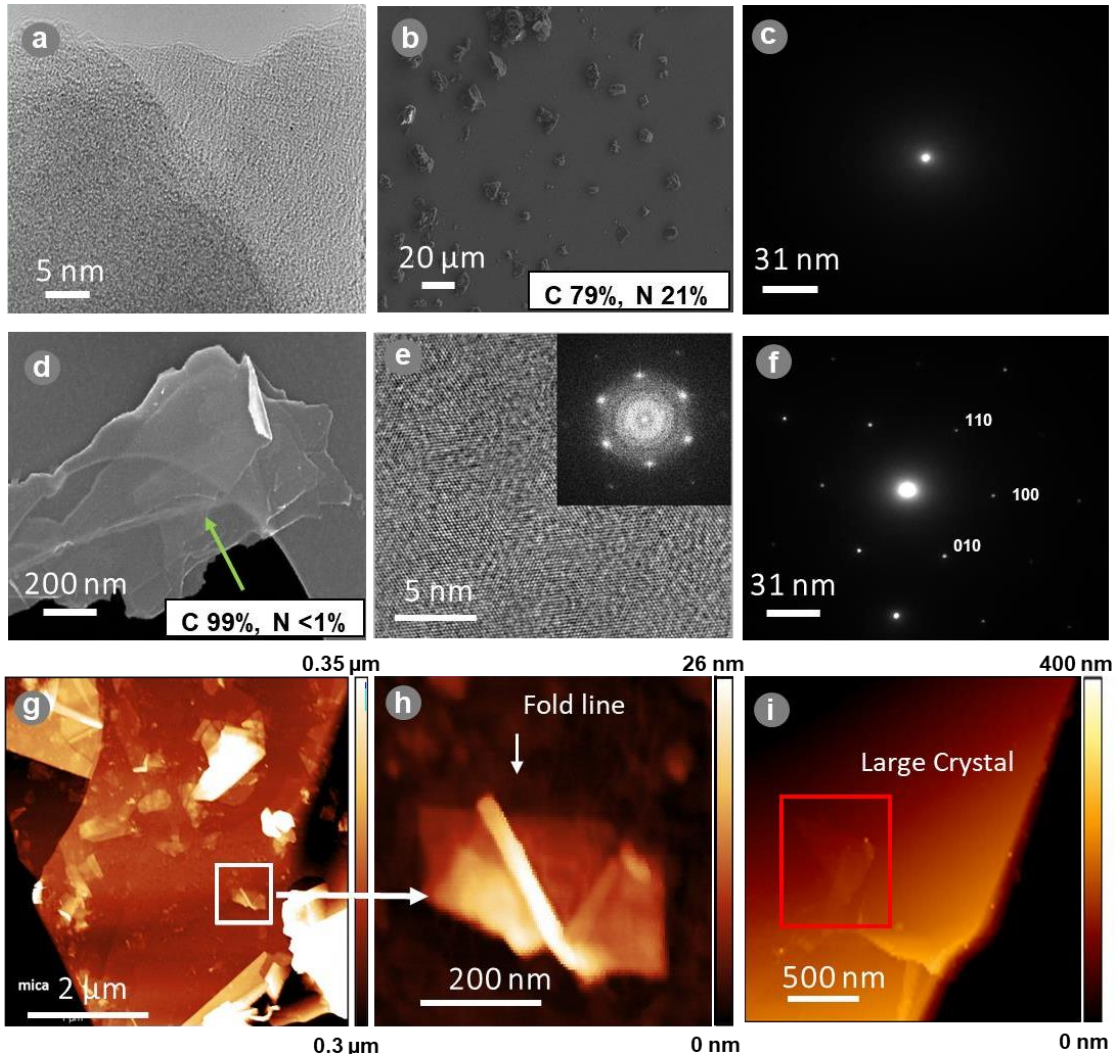

Figure 2. Two-dimensional triazine heterostructures were investigated by different microscopy methods including HRTEM, SEM and SFM. (**a**) and (**e**) HRTEM images of 2DTHs and graphite, respectively. (**b**) and (**d**) SEM images of 2DTHs and graphite respectively, showing sheet-like structure with clear edges for these nanomaterials. Also, elemental analysis of the areas indicated with the green arrow in (b) (C 79%, N 21%) and (d) (C 99%, N <1%. (**c**) and (**f**) Diffraction pattern and unit cell: 0.246nm of graphite and 2DTHS, showing the amorphous and crystalline materials. (**g**) SFM-QNM height image of the 2DTHs with plateaus and terraces. (**h**) A close up SFM-QNM height image of a typical layer with wrinkle line and back folding. Planar layer topography are evident from the height image. (**i**) large crystal image of graphite.

The SFM analysis revealed structures with lateral sizes up to 2-3 micrometers and thickness of 100 to 350 nm with layers and terraces including folds and wrinkles (Figure 2g,h). The height at terraces were 5-10 nm. Based on the observations of the SFM, a layered and ordered structure for 2DTHs was confirmed. Lateral dimensions as measured by SFM were found to be in the

range of 2-6 μm^2 (Figures 2g,h). Attenuated total reflection infrared spectroscopy (ATR-FTIR) spectrum of 2DTHs revealed a broad absorbance band at ~1394-1577 cm^{-1} corresponding to C=C and C=N bonds .[51] The absence of a C≡C absorbance band and appearance of C=C vibrations in the IR spectrum of 2DTHs is attributed to the trimerization of acetylide linkages and formation of benzene rings (Figure S3). ^{13}C solid-state cross-polarization magic-angle-spinning (CP-MAS) nuclear magnetic resonance (NMR) spectrum of 2DTHs showed a broad signal at 148-162 ppm which is related to the carbon atoms of triazine rings[51-52] and a signal at 27 ppm for $–NMe_2$ groups (Figure 3a). In this spectrum a broad signal centered at 126 ppm is assigned to benzene rings, which is a further confirmation for the trimerization of acetylide linkages (Figure 3a).

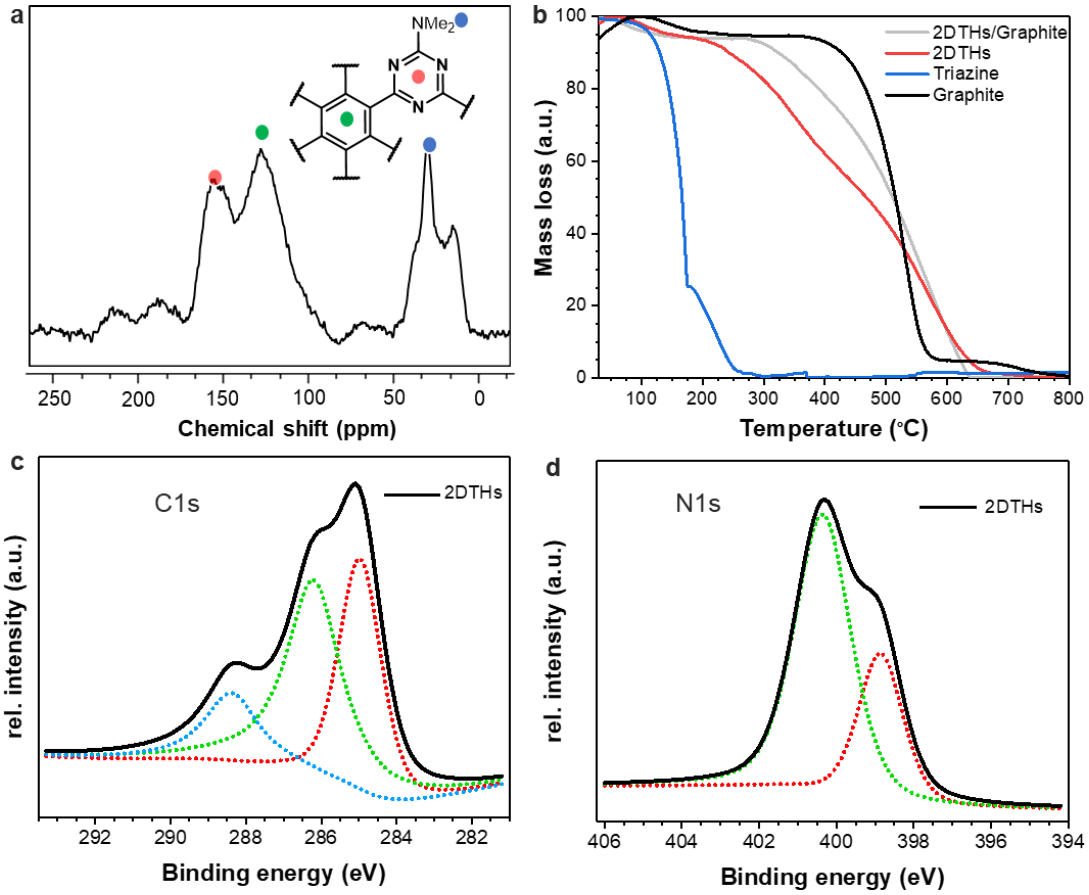

Figure 3. Characterization of 2DTHs by spectroscopy methods and thermal analysis. (**a**) ^{13}C CP-MAS-NMR spectrum of 2TDHs show distinguished signals for the triazine and benzene rings as well as dimethyl amine functional groups. (**b**) TGA thermograms of 2DTHs, triazine, graphite and graphite/2DTHs. (**c**) Highly resolved XPS spectra C1s peak and (**d**) N1s peak of 2DTHs. Fit parameters for each spectrum and interpretations are shown in Table S2.

The thermal behavior of 2DTHs was investigated by thermogravimetric analysis (TGA). While the reaction product in aqueous were decomposed at temperatures higher than ~500 °C, 2DTHs

showed weight loss at ~200-660 °C temperature range. There was a correlation between the nitrogen content of the products and their thermal stability. Materials with lower nitrogen contents, which are the product of reactions in aqueous solutions, showed higher thermal stability. This is an indicator for their higher graphitic contents. Weight losses at low and high temperature ranges are assigned to detachment of $–NMe_2$ functional groups and decomposition of the backbone of 2DTHs, respectively (Figure 3b). The structure of 2DTHs was further investigated by X-ray photoelectron spectroscopy (XPS). Carbon, nitrogen, as the main components, and oxygen were detected in the survey spectrum of 2DTHs (Figure S4). The highly-resolved C1s XPS spectrum (Figure 3c) showed two intense C 1s component peaks at 288.3 eV, representing carbon atoms of triazine rings,[53] 286.2 and 285.1 eV, corresponding to the carbons of benzene rings and $–NMe_2$ groups.[50, 52, 54] Two components in the N1s peak at 400.4 eV and 399.8 eV were assigned to the nitrogen atoms of triazine rings and $–NMe_2$ groups, respectively (Figure 3d).[52, 55] The absence of calcium peak in the survey spectrum of 2DTHs is a further prove for the successful removal of calcium content upon purification (Figure S4). In order to complement the characterization of the carbonaceous materials, Raman spectra of different structures including 2DTHs, graphite and HOPG as a reference were individually recorded and evaluated (Figure S5). A clear shift for the G peak of materials against nitrogen content was observed. In this regard, the G peak was shifted from, average position of ~1562.5 cm^{-1}, for 2DTHs, to ~1582 cm^{-1}, for graphite. G peak shift is known to be affected by factors such as; strain and doping, with further modifications due to C/N content.[56] Furthermore, 2DTHs demonstrated narrower Raman bands at ~1332 cm^{-1}, ~1564 cm^{-1} with an occasional weak and broad band at ~1610-1620 cm^{-1} in addition to a broad band centred at ~2700 cm^{-1}. These mentioned Raman bands resemble of those observed for graphite with a difference that the bands at ~1345 cm^{-1} and ~1620 cm^{-1} cannot be found for very crystalline and pure graphitic structure, since those two Raman bands correspond to D and D' peaks which are due to structural defects and charged particles near graphitic structure, respectively (Figure 4a,b). It is important to note that sp C≡C Raman band which exist within ~2100 cm^{-1} could not be found in the 2DTHs particles.[57-58] Therefore, no sp carbons remained from the CaC_2 precursor of the synthesis reaction. This agrees with solid NMR (Figure 3a) and ATR-FTIR (Figure S3) measurements. Thereafter, powder X-ray diffraction (PXRD) was used to investigate any long-range ordering in the structure of the synthesized materials. Broadened X-ray diffraction pattern is assigned to the (002) peak of graphitic carbon which located at 2θ = ~26.3° (Figure 4d) for the synthesized layered materials. Moreover, calcium carbide was also analyzed by PXRD (Figure S6), revealing no graphitic carbon content, demonstrating that this precursor is free of

graphite or any other analogous.[59] We further examined the reaction of calcium carbide, it was found that calcium carbide with only DMF (in the absence of triazine) did not result in any layered carbonaceous materials, further verifying that the 2DTHs was indeed converted from CaC_2 in the presence of triazine (See page S9). However, due to the polycrystalline/amorphous character of 2DTHs the XRD profile could not provide further information about the cell unit of 2DTHs.

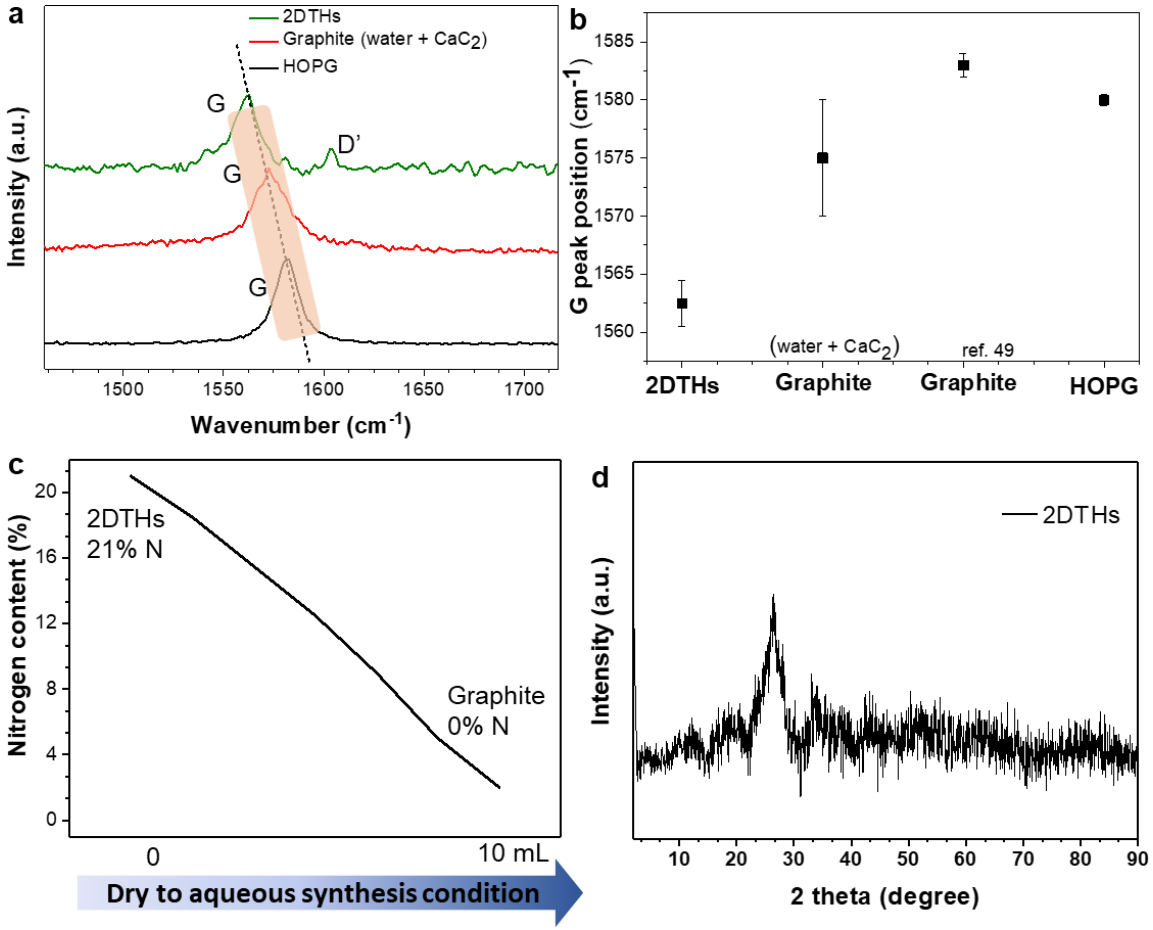

Figure 4. (**a**) and (**b**) A close up Raman spectra overlay of the G peak and D' peak regions of the 2DTHs planar particles, HOPG, graphite. In this image (**b**) the graphite is prepared based on the recent work.[49] (**c**) the corrolation between N content and water. (**d**) difractograms of synthesized 2DTHs.

After analyzing the chemical structure of two-dimensional heterostructures, the mechanism of their synthetic pathway and structure of intermediate were investigated. To avoid polymerization and keep reaction in the molecular level, two active sites of cyanuric chloride were blocked by phenol and 2-chloro-4,6-diphenoxy-1,3,5-triazine (**1**) was synthesized according to reported methods in literatures[60] (See Figures S7-9 for NMR and mass spectra). Since phenoxy groups decrease the electron deficiency of triazine ring, any nucleophilic

substitution of chlorine atom of 2-chloro-4,6-diphenoxy-1,3,5-triazine could be extended to the cyanuric chloride. Accordingly, 2-chloro-4,6-diphenoxy-1,3,5-triazine was reacted with calcium carbide in DMF at 120 °C. Different characterization methods showed that chlorine atom of 2-chloro-4,6-diphenoxy-1,3,5-triazine is substituted by DMF leading to N,N-dimethyl-4,6-diphenoxy-1,3,5-triazine-2-amine (**2**) (Figure 5a). The single X-ray crystallography revealed the structure of compound **2** and proved successful synthesis of this intermediate (Figure 5b). Moreover, ^{1}H-NMR showed a chemical shift for the phenoxy protons of compound (**1)** after reaction with DMF and a signal for $–NMe_2$ protons was appeared in the spectrum of compound (**2**) (Figure 5c). Comparison of ^{13}C NMR spectra of compounds (**1**) and (**2**) distinctly showed a chemical shift from 173.8 ppm to 167.4 ppm for –C–Cl after reaction with DMF. In agreement with the literature[61] these results confirmed substitution of the chlorine atom of compound (**1**) by $–NMe_2$ derived from DMF (Figure 5d). Structure of intermediate (**2)** was further proved by mass spectroscopy. Signals at 309.1357 and 331.1177 m/z are related to the molar mass of this compound accompanied by proton and sodium ion respectively (calculated for $C_{17}H_{16}N_4O_2$ [M+H] and [M+Na]: 309.13, 331.12, respectively, Figure S10). Reaction between compound (**2**) and calcium carbide resulted in compound (**3**). This reaction was monitored at intervals of two hours by Matrix-Assisted Laser Desorption/Ionization Time-of-Flight (MALDI-ToF) and electrospray ionization mass spectroscopy (ESI) for three days. A signal at 655.21 m/z (Figure S11) is assigned to compound (**3**) which is converted to compound (**4**) upon trimerization. Compound (**4**) accompanied by calcium ions and water molecules was detected by MALDI-ToF (Figure 5e). Fragments at 336 m/z and 639 m/z in the ESI mass spectrum of the above-mentioned reaction indicated building blocks consisting benzene rings with six substituents (Figures S12 and S13). Mechanism of reaction was further investigated by synthesizing 2,4-dichloro-6-phenoxy-1,3,5- triazine[62] and polymerization of this monomer in the same condition (Figure 1). In the MALDI-ToF spectrum of the product of this reaction distinguished peaks at 243n m/z intervals, where n is a natural number, showed a repeating unit with six-substituted benzene ring (Figure S14). This repeating unit is a further prove for nucleophilic substation of chlorine atoms of triazine followed by trimerization. Role of DMF in reaction between cyanuric chloride and calcium carbide was further proved by changing the solvent to toluene and mesitylene. Accomplishment of reaction in these solvents didn't result in any detectable product. This experiment proved the critical role of DMF in the production of two-dimensional triazine heterostructure. Complexation of intermediates with calcium ions hampered the rotation of acetylide linkages around C–C bonds and directed the consequent

reactions in two dimensions (Figure S15). The directing role of calcium ions was investigated by DFT functional in GPAW program (See page S20).

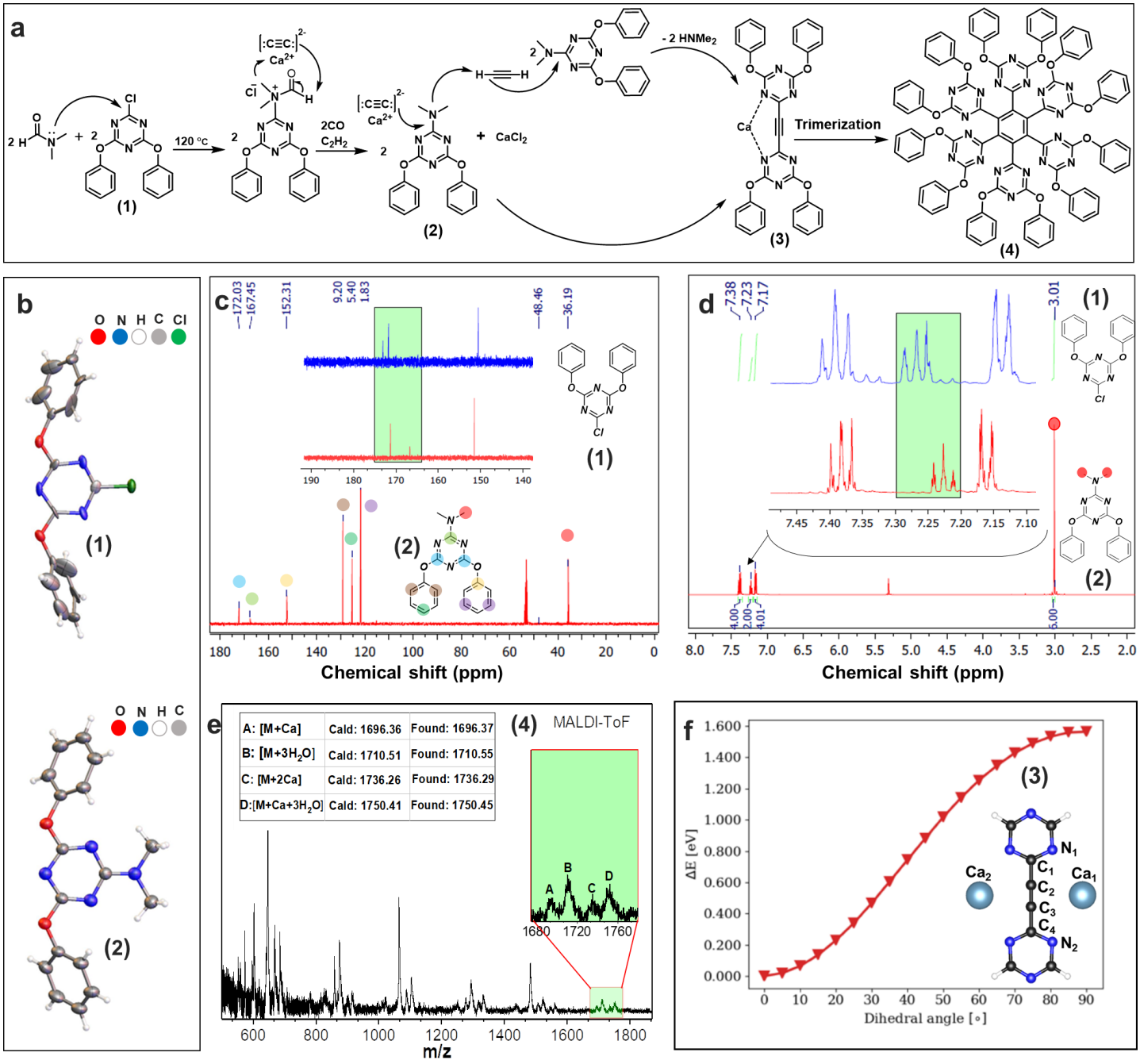

Figure 5. Investigation of the mechanism of reaction between cyanuric chloride and calcium carbide in DMF using model compounds. (**a**) Reaction between compound **1** and DMF resulted in intermediate **2**. Consequence nucleophilic reaction between compound **2** and calcium carbide resulted in compound **3** which converted to compound **4** upon trimerization. (**b**) single crystal XRD structure of compounds **1** and **2**. (**c**) and (**d**) ^{1}H- and ^{13}C-NMR spectra of compound **1** and compound **2**, respectively. (**e**) Expanded MALDI-ToF spectrum of reaction mixture. (**f**) The simulated structure of compound **3** coordinated with two calcium ions (on both sides) and the

total energy of the system with different dihedral angle with 5° each step (See detail Figure S15 and Table S3).

Coordination of calcium ions with nitrogen atoms of triazine rings in compound **3** causes 1.6 eV barrier energy for rotation around C_1–C_2 and C_3–C_4 (Figure 5f). This energy barrier is a driving force for growing triazine-benzene heterostructures in two dimensions (Figure 5f). According to literatures calcium ions are able to form complexes with nitrogen containing ligands including 1,10-phenanthroline, 4,4´-bipyridine and 2,2´-bipyridine.[63-65] While interactions between these ligands and calcium ions is not as strong as oxygen containing ligands,[66-67] they are able to induce enough rigidity for the two-dimensional coupling of monomers.[68-70] Weak interactions between calcium and monomers (building blocks) is important for the metal exclusion and purification of the final product. Metal ions with strong complexation ability cannot be excluded from the final product. A further proved for the directing role of calcium ions was achieved by adding ethylenediaminetetraacetic acid (EDTA) to the medium of reaction. When reaction between cyanuric chloride and calcium carbide was performed in DMF and in the presence of EDTA, any sheet like structure was not achieved (See Figure S16 for SEM and SFM data). This is due to the complexation of calcium ions with EDTA[71] and absence of any driving force to conjugate monomers in a sheet-like structure.

The composition of the reaction product was deeply affected by the water content of the reaction. Accomplishment of reaction in the presence of water led to a mixture of 2DTHs and graphitic materials. There was a direct correlation between the amount of graphitic materials and water content of the reaction medium. Under the dry conditions reaction between cyanuric chloride and calcium carbide produced 2DTHs without any graphitic materials. As the amount of water was increased, either in the reaction or purification steps, the content of graphitic materials was increased (Figure 4c). It is already reported that reaction between calcium carbide and water results in graphitic materials.[49] Therefore, the produced graphitic materials in our experiments are assigned to the same reaction. TEM and SEM images showed a layered structure for the graphitic materials with clear edges and several micrometer lateral sizes (Figure 2b). Moreover, the elemental analysis on the sheets showed close to 100% carbon content for graphitic materials. Moreover, the unit cell of the graphitic material was obtained from diffraction patterns corresponding to 0.246 nm (Figure 2f). Both the carbon content and the unit cell indicate that the crystalline material is graphite. Further investigations also showed that the graphite sheets were strained, which was clearly visible from the diffraction patterns.

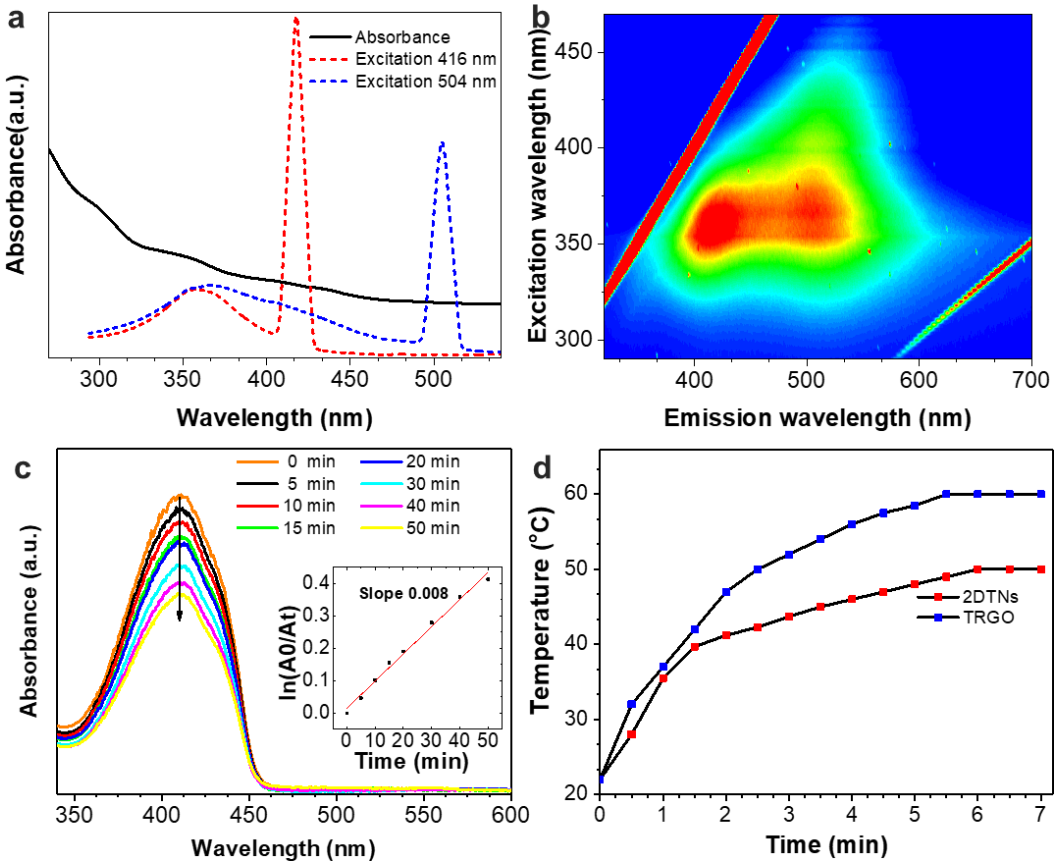

Figure 6. Physicochemical properties of 2DTHs including photodynamic, photothermal and photoluminescence properties were investigated by different methods. (**a**) Absorbance and photoluminescence emission of 2DTHs, (**b**) Photoluminescence map of 2DTHs. (**c**) Singlet oxygen generation kinetics of water dispersion of 2DTHs and (**d**) photothermal properties of 2DTHs under laser irradiation (808 nm, 0.5 W/cm^2). Thermally reduced graphene oxide (TRGO) was used as controls, concentration was (0.5 mg/ml in water, details can be found page S22).

The physicochemical properties of 2DTHs were investigated by different methods. Two dimensional triazine heterostructure showed a maximum UV absorption at 235 nm corresponding to n→π* transitions (Figure S17). Due to their huge π-conjugated system, 2DTHs are able to produce singlet oxygen under irradiation with NIR laser (808 nm) (Figure 6c). This property could be used for different proposes ranging from photodynamic therapy to photocatalyst applications. Laser irradiation of a water dispersion of 2DTHs elevated the medium temperature from 20 to 50 in 2 minutes (Figure 6d). Production of heat is less efficient than thermally reduced graphene oxide but in a suitable range for photothermal therapy.

Conclusion

The reaction between triazine and calcium carbide under defined conditions was mediated by dimethylformamide to produce triazine-benzene heterostructures on the gram scale. Calcium

carbide had multiple roles in the synthetic route of 2DTHs: It was the source of acetylide linkage, which created benzene rings upon trimerization, and induced coordinating calcium ions as two-dimensional directing metal centers. Water showed a high impact on the reaction route and in the presence of water graphitic materials were created in addition to 2DTHs. Taking advantage of their interesting physicochemical properties, straightforward synthesis and cheap precursors, the presented two-dimensional nanomaterial is an interesting new candidate opteoelectronic properties.

ACKNOWLEDGMENT

We thank the German Science Foundation (DFG) for financial Support within the grants SFB 658 and SFB 765. We would like to thank Dr. Andreas Schäfer and Maiko Schulze for solid-NMR experiments as well as we appreciate the effort of Vahid Ahmadi Soureshjani for MALDI-ToF experiments.

REFERENCES

1. Tomalia, D. A.; Baker, H.; Dewald, J.; Hall, M.; Kallos, G.; Martin, S.; Roeck, J.; Ryder, J.; Smith, P., A New Class of Polymers: Starburst-Dendritic Macromolecules. *Poly. J.* **1985,** *17*, 117.
2. Seymour, R. B., Polymers Are Everywhere. *J. Chem. Educ.* **1988,** *65*, 327-334.
3. Sakamoto, J.; van Heijst, J.; Lukin, O.; Schluter, A. D., Two-dimensional polymers: just a dream of synthetic chemists? *Angew. Chem. Int. Ed.* **2009,** *48* (6), 1030-69.
4. Stupp, S. I.; Son, S.; Lin, H. C.; Li, L. S., Synthesis of Two-Dimensional Polymers. *Science* **1993,** *259* (5091), 59.
5. Stupp, S. I.; Son, S.; Li, L. S.; Lin, H. C.; Keser, M., Bulk Synthesis of Two-Dimensional Polymers: The Molecular Recognition Approach. *J. Am. Chem. Soc.* **1995,** *117* (19), 5212-5227.
6. Makiura, R.; Tsuchiyama, K.; Pohl, E.; Prassides, K.; Sakata, O.; Tajiri, H.; Konovalov, O., Air/Liquid Interfacial Nanoassembly of Molecular Building Blocks into Preferentially Oriented Porous Organic Nanosheet Crystals via Hydrogen Bonding. *ACS Nano* **2017,** *11* (11), 10875-10882.
7. Payamyar, P.; King, B. T.; Öttinger, H. C.; Schlüter, A. D., Two-dimensional polymers: concepts and perspectives. *Chem. Commun.* **2016,** *52* (1), 18-34.
8. Dong, R.; Zhang, T.; Feng, X., Interface-Assisted Synthesis of 2D Materials: Trend and Challenges. *Chem. Rev.* **2018,** *118* (13), 6189-6235.
9. Chen, Y.; Li, M.; Payamyar, P.; Zheng, Z.; Sakamoto, J.; Schlüter, A. D., Room Temperature Synthesis of a Covalent Monolayer Sheet at Air/Water Interface Using a

Shape-Persistent Photoreactive Amphiphilic Monomer. *ACS Macro Lett.* **2014,** *3* (2), 153-158.

10. Servalli, M.; Celebi, K.; Payamyar, P.; Zheng, L.; Polozij, M.; Lowe, B.; Kuc, A.; Schwarz, T.; Thorwarth, K.; Borgschulte, A.; Heine, T.; Zenobi, R.; Schluter, A. D., Photochemical Creation of Covalent Organic 2D Monolayer Objects in Defined Shapes via a Lithographic 2D Polymerization. *ACS Nano* **2018,** *12* (11), 11294-11306.
11. Müller, V.; Hinaut, A.; Moradi, M.; Baljozovic, M.; Jung, T. A.; Shahgaldian, P.; Möhwald, H.; Hofer, G.; Kröger, M.; King, B. T.; Meyer, E.; Glatzel, T.; Schlüter, A. D., A Two-Dimensional Polymer Synthesized at the Air/Water Interface. *Angew. Chem.* **2018,** *130* (33), 10744-10748.
12. Burger, A.; Leonhard, H.; Rehage, H.; Wagner, R.; Schwoerer, M., Ultrathin crosslinked membranes at the interface between oil and water. *Macromol. Chem. Phys.* **1995,** *196* (1), 1-46.
13. Payamyar, P.; Kaja, K.; Ruiz-Vargas, C.; Stemmer, A.; Murray, D. J.; Johnson, C. J.; King, B. T.; Schiffmann, F.; Vandevondele, J.; Renn, A.; Gotzinger, S.; Ceroni, P.; Schutz, A.; Lee, L. T.; Zheng, Z.; Sakamoto, J.; Schluter, A. D., Synthesis of a covalent monolayer sheet by photochemical anthracene dimerization at the air/water interface and its mechanical characterization by AFM indentation. *Adv Mater* **2014,** *26* (13), 2052-8.
14. Murray, D. J.; Patterson, D. D.; Payamyar, P.; Bhola, R.; Song, W.; Lackinger, M.; Schluter, A. D.; King, B. T., Large area synthesis of a nanoporous two-dimensional polymer at the air/water interface. *J. Am. Chem. Soc.* **2015,** *137* (10), 3450-3.
15. Liu, J.; Zan, W.; Li, K.; Yang, Y.; Bu, F.; Xu, Y., Solution Synthesis of Semiconducting Two-Dimensional Polymer via Trimerization of Carbonitrile. *J. Am. Chem. Soc.* **2017,** *139* (34), 11666-11669.
16. Matsuoka, R.; Sakamoto, R.; Hoshiko, K.; Sasaki, S.; Masunaga, H.; Nagashio, K.; Nishihara, H., Crystalline Graphdiyne Nanosheets Produced at a Gas/Liquid or Liquid/Liquid Interface. *J. Am. Chem. Soc.* **2017,** *139* (8), 3145-3152.
17. Uribe-Romo, F. J.; Dichtel, W. R., Polymers stripped down. *Nat. Chem.* **2012,** *4*, 244.
18. Lafferentz, L.; Eberhardt, V.; Dri, C.; Africh, C.; Comelli, G.; Esch, F.; Hecht, S.; Grill, L., Controlling on-surface polymerization by hierarchical and substrate-directed growth. *Nat. Chem.* **2012,** *4* (3), 215-20.
19. Liu, Z.; Song, M.; Ju, S.; Huang, X.; Wang, X.; Shi, X.; Zhu, Y.; Wang, Z.; Chen, J.; Li, H.; Cheng, Y.; Xie, L.; Liu, J.; Huang, W., Wafer-Scale Ultrathin Two-Dimensional

Conjugated Microporous Polymers: Preparation and Application in Heterostructure Devices. *ACS Appl. Mater. Interfaces***,** *10* (4), 4010-4017.

20. Kissel, P.; Murray, D. J.; Wulftange, W. J.; Catalano, V. J.; King, B. T., A nanoporous two-dimensional polymer by single-crystal-to-single-crystal photopolymerization. *Nat. Chem.* **2014,** *6* (9), 774-8.
21. Gontarczyk, K.; Bury, W.; Serwatowski, J.; Wiecinski, P.; Wozniak, K.; Durka, K.; Lulinski, S., Hybrid Triazine-Boron Two-Dimensional Covalent Organic Frameworks: Synthesis, Characterization, and DFT Approach to Layer Interaction Energies. *ACS Appl. Mater. Interfaces.* **2017,** *9* (36), 31129-31141.
22. Kory, M. J.; Worle, M.; Weber, T.; Payamyar, P.; van de Poll, S. W.; Dshemuchadse, J.; Trapp, N.; Schluter, A. D., Gram-scale synthesis of two-dimensional polymer crystals and their structure analysis by X-ray diffraction. *Nat. Chem.* **2014,** *6* (9), 779-84.
23. Feng, X.; Schlüter, A. D., Towards Macroscopic Crystalline 2D Polymers. *Angew. Chem. Int. Ed.* **2018,** *57* (42), 13748-13763.
24. Huang, C.; Li, Y.; Wang, N.; Xue, Y.; Zuo, Z.; Liu, H.; Li, Y., Progress in Research into 2D Graphdiyne-Based Materials. *Chem. Rev.* **2018,** *118* (16), 7744-7803.
25. Zeng, M.; Xiao, Y.; Liu, J.; Yang, K.; Fu, L., Exploring Two-Dimensional Materials toward the Next-Generation Circuits: From Monomer Design to Assembly Control. *Chem. Rev.* **2018,** *118* (13), 6236-6296.
26. Grill, L.; Dyer, M.; Lafferentz, L.; Persson, M.; Peters, M. V.; Hecht, S., Nano-architectures by covalent assembly of molecular building blocks. *Nat. Nanotechnol.* **2007,** *2* (11), 687-91.
27. Liu, R.; Fan, S.; Xiao, D.; Zhang, J.; Liao, M.; Yu, S.; Meng, F.; Liu, B.; Gu, L.; Meng, S.; Zhang, G.; Zheng, W.; Hu, S.; Li, M., Free-Standing Single-Molecule Thick Crystals Consisting of Linear Long-Chain Polymers. *Nano Lett.* **2017,** *17* (3), 1655-1659.
28. Choi, I. Y.; Lee, J.; Ahn, H.; Lee, J.; Choi, H. C.; Park, M. J., High-Conductivity Two-Dimensional Polyaniline Nanosheets Developed on Ice Surfaces. *Angew. Chem. Int. Ed.* **2015,** *54* (36), 10497-10501.
29. Li, Y.; Zheng, S.; Liu, X.; Li, P.; Sun, L.; Yang, R.; Wang, S.; Wu, Z. S.; Bao, X.; Deng, W. Q., Conductive Microporous Covalent Triazine-Based Framework for High-Performance Electrochemical Capacitive Energy Storage. *Angew. Chem. Int. Ed.* **2018,** *57* (27), 7992-7996.

30. Lange, R. Z.; Hofer, G.; Weber, T.; Schlüter, A. D., A Two-Dimensional Polymer Synthesized through Topochemical [2 + 2]-Cycloaddition on the Multigram Scale. *J. Am. Chem. Soc.* **2017,** *139* (5), 2053-2059.
31. Kissel, P.; Erni, R.; Schweizer, W. B.; Rossell, M. D.; King, B. T.; Bauer, T.; Gotzinger, S.; Schluter, A. D.; Sakamoto, J., A two-dimensional polymer prepared by organic synthesis. *Nat. Chem.* **2012,** *4* (4), 287-91.
32. Zhang, T.; Hou, Y.; Dzhagan, V.; Liao, Z.; Chai, G.; Loffler, M.; Olianas, D.; Milani, A.; Xu, S.; Tommasini, M.; Zahn, D. R. T.; Zheng, Z.; Zschech, E.; Jordan, R.; Feng, X., Copper-surface-mediated synthesis of acetylenic carbon-rich nanofibers for active metal-free photocathodes. *Nat. Commun.* **2018,** *9* (1), 1140.
33. Huang, X.; Sheng, P.; Tu, Z.; Zhang, F.; Wang, J.; Geng, H.; Zou, Y.; Di, C.-a.; Yi, Y.; Sun, Y.; Xu, W.; Zhu, D., A two-dimensional π–d conjugated coordination polymer with extremely high electrical conductivity and ambipolar transport behaviour. *Nat. Commun.* **2015,** *6*, 7408.
34. Kambe, T.; Sakamoto, R.; Hoshiko, K.; Takada, K.; Miyachi, M.; Ryu, J. H.; Sasaki, S.; Kim, J.; Nakazato, K.; Takata, M.; Nishihara, H., pi-Conjugated nickel bis(dithiolene) complex nanosheet. *J. Am. Chem. Soc.* **2013,** *135* (7), 2462-5.
35. Bauer, T.; Zheng, Z.; Renn, A.; Enning, R.; Stemmer, A.; Sakamoto, J.; Schlüter, A. D., Synthesis of Free-Standing, Monolayered Organometallic Sheets at the Air/Water Interface. *Angew. Chem. Int. Ed.* **2011,** *50* (34), 7879-7884.
36. Dong, R.; Zheng, Z.; Tranca, D. C.; Zhang, J.; Chandrasekhar, N.; Liu, S.; Zhuang, X.; Seifert, G.; Feng, X., Inside Cover: Immobilizing Molecular Metal Dithiolene–Diamine Complexes on 2D Metal–Organic Frameworks for Electrocatalytic H2 Production (Chem. Eur. J. 10/2017). *Chem.A. Eur. J.* **2017,** *23* (10), 2234-2234.
37. Sakamoto, R.; Hoshiko, K.; Liu, Q.; Yagi, T.; Nagayama, T.; Kusaka, S.; Tsuchiya, M.; Kitagawa, Y.; Wong, W.-Y.; Nishihara, H., A photofunctional bottom-up bis(dipyrrinato)zinc(II) complex nanosheet. *Nat. Commun.* **2015,** *6*, 6713.
38. Wu, G.; Huang, J.; Zang, Y.; He, J.; Xu, G., Porous Field-Effect Transistors Based on a Semiconductive Metal–Organic Framework. *J. Am. Chem. Soc.* **2017,** *139* (4), 1360-1363.
39. Lahiri, N.; Lotfizadeh, N.; Tsuchikawa, R.; Deshpande, V. V.; Louie, J., Hexaaminobenzene as a building block for a Family of 2D Coordination Polymers. *J. Am. Chem. Soc.* **2017,** *139* (1), 19-22.

40. Dong, R.; Pfeffermann, M.; Liang, H.; Zheng, Z.; Zhu, X.; Zhang, J.; Feng, X., Large-Area, Free-Standing, Two-Dimensional Supramolecular Polymer Single-Layer Sheets for Highly Efficient Electrocatalytic Hydrogen Evolution. *Angew. Chem. Int. Ed.* **2015,** *54* (41), 12058-12063.

41. Clough, A. J.; Yoo, J. W.; Mecklenburg, M. H.; Marinescu, S. C., Two-Dimensional Metal–Organic Surfaces for Efficient Hydrogen Evolution from Water. *J. Am. Chem. Soc.* **2015,** *137* (1), 118-121.

42. Takada, K.; Sakamoto, R.; Yi, S.-T.; Katagiri, S.; Kambe, T.; Nishihara, H., Electrochromic Bis(terpyridine)metal Complex Nanosheets. *J. Am. Chem. Soc.* **2015,** *137* (14), 4681-4689.

43. Sun, X.; Wu, K. H.; Sakamoto, R.; Kusamoto, T.; Maeda, H.; Ni, X.; Jiang, W.; Liu, F.; Sasaki, S.; Masunaga, H.; Nishihara, H., Bis(aminothiolato)nickel nanosheet as a redox switch for conductivity and an electrocatalyst for the hydrogen evolution reaction. *Chem. Sci.* **2017,** *8* (12), 8078-8085.

44. Venkanna, P.; Rajanna, K. C.; Satish Kumar, M.; Bismillah Ansari, M.; Moazzam Ali, M., 2,4,6-Trichloro-1,3,5-triazine and N,N′-dimethylformamide as an effective Vilsmeier–Haack reagent for the synthesis of 2-chloro-3-formyl quinolines from acetanilides. *Tetrahedron Lett.* **2015,** *56* (37), 5164-5167.

45. Bandgar, B. P.; Joshi, N. S.; Kamble, V. T., 2,4,6-Trichloro-1,3,5-triazine catalyzed synthesis of thiiranes from oxiranes under solvent-free and mild conditions. *Tetrahedron Lett.* **2006,** *47* (27), 4775-4777.

46. Ranise, A.; Cesarini, S.; Spallarossa, A.; Sancassan, F.; Bondavalli, F.; Bruno, O.; Schenone, S.; Menozzi, G.; Fossa, P.; Mosti, L., Unprecedented One-Pot Stereoselective Synthesis of Knoevenagel-Type Derivatives via in situ Condensation of N-Methyleniminium Salts of Ethylenethiourea and Ethyleneurea with Active Methylene Reagents. *Synthesis* **2007,** *2007* (16), 2495-2502.

47. De Luca, L.; Giacomelli, G.; Porcheddu, A., Beckmann Rearrangement of Oximes under Very Mild Conditions. *J. Org. Chem.* **2002,** *67* (17), 6272-6274.

48. De Luca, L.; Giacomelli, G.; Porcheddu, A., An Efficient Route to Alkyl Chlorides from Alcohols Using the Complex TCT/DMF. *Org. Lett.* **2002,** *4* (4), 553-555.

49. Jia, Y.; Chen, X.; Zhang, G.; Wang, L.; Hu, C.; Sun, X., Topotactic conversion of calcium carbide to highly crystalline few-layer graphene in water. *J. Mater. Chem. A* **2018,** *6* (46), 23638-23643.

50. Casco, M. E.; Kirchhoff, S.; Leistenschneider, D.; Rauche, M.; Brunner, E.; Borchardt, L., Mechanochemical synthesis of N-doped porous carbon at room temperature. *Nanoscale* **2019,** *11* (11), 4712-4718.
51. Chen, Y.; Wang, X., Template-Free Synthesis of Hollow G-C3N4 Polymer with Vesicle Structure for Enhanced Photocatalytic Water Splitting. *J. Phys. Chem. C* **2018,** *122* (7), 3786-3793.
52. Xiang, Z.; Cao, D.; Huang, L.; Shui, J.; Wang, M.; Dai, L., Nitrogen-Doped Holey Graphitic Carbon from 2D Covalent Organic Polymers for Oxygen Reduction. *Adv. Mater.* **2014,** *26* (20), 3315-3320.
53. Tahir, M.; Mahmood, N.; Zhu, J.; Mahmood, A.; Butt, F. K.; Rizwan, S.; Aslam, I.; Tanveer, M.; Idrees, F.; Shakir, I.; Cao, C.; Hou, Y., One Dimensional Graphitic Carbon Nitrides as Effective Metal-Free Oxygen Reduction Catalysts. *Sci. Rep.* **2015,** *5*, 12389.
54. Chen, W.; Huang, L.; Yi, X.; Zheng, A., Lithium doping on 2D squaraine-bridged covalent organic polymers for enhancing adsorption properties: a theoretical study. *Phys. Chem. Chem. Phys.* **2018,** *20* (9), 6487-6499.
55. Faghani, A.; Donskyi, I. S.; Fardin Gholami, M.; Ziem, B.; Lippitz, A.; Unger, W. E.; Bottcher, C.; Rabe, J. P.; Haag, R.; Adeli, M., Controlled Covalent Functionalization of Thermally Reduced Graphene Oxide To Generate Defined Bifunctional 2D Nanomaterials. *Angew. Chem. Int. Ed.* **2017,** *56* (10), 2675-2679.
56. Ferrari, A. C.; Robertson, J., Raman spectroscopy of amorphous, nanostructured, diamond-like carbon, and nanodiamond. *Philosophical transactions. Series A, Mathematical, physical, and engineering sciences* **2004,** *362* (1824), 2477-512.
57. Cataldo, F., The role of Raman spectroscopy in the research on sp-hybridized carbon chains: carbynoid structures polyynes and metal polyynides. *J. Raman Spectrosc.* **2008,** *39* (2), 169-176.
58. Wang, J.; Zhang, S.; Zhou, J.; Liu, R.; Du, R.; Xu, H.; Liu, Z.; Zhang, J.; Liu, Z., Identifying sp-sp2 carbon materials by Raman and infrared spectroscopies. *Phys. Chem. Chem. Phys.* **2014,** *16* (23), 11303-9.
59. Konar, S.; Nylén, J.; Svensson, G.; Bernin, D.; Edén, M.; Ruschewitz, U.; Häussermann, U., The many phases of CaC 2. *J. Solid State Chem.* **2016,** *239*, 204-213.
60. Namazi, H.; Adeli, M., Solution proprieties of dendritic triazine/poly(ethylene glycol)/dendritic triazine block copolymers. *Journal of Polymer Science Part A: Poly. Chem.* **2005,** *43* (1), 28-41.

61. Chesniuk, A. A.; Mikhailichenko, S. N.; Zavodnov, V. S.; Zaplishny, V. N., Derivatives of sym-Triazine. 1. Synthesis and Conversions of Quaternary Methylammonium Salts of 2-Chloro-4,6-disubstituted 1,3,5-Triazines in Nucleophilic Substitution Reactions. *Chemistry of Heterocyclic Compounds* **2002,** *38* (2), 177-182.

62. Nguyen, T. A.; Luu, A. T.; Nguyen, T. H.; Le, N. M.; Tran, H. M.; Nguyen, L.-T. T.; Lee, J. Y.; Nguyen, H. T., Thiacalix[3]Triazine-centered regioregular poly(3-hexylthiophene) star: synthesis, structure and anion binding. *J. Polym. Res.* **2017,** *24* (11), 180.

63. Taqui Khan, M. M., TERNARY COMPLEXES OF TRANSITION METALIONS WITH ADENOSINE-5 ' -TRIPHOSPHATE AND 1,10-PHENANTHROLINE AU - Mohan, M. Srinivas. *J. Coord. Chem.* **1979,** *8* (4), 207-212.

64. Shamsipur, M., Fluorimetric Study of Complexation of Alkali and Alkaline Earth Cations with 1,10-Phenanthroline, 2,2′-Bipyridine and 8-Hydroxyquinoline in Nonaqueous Solvents AU - Ghasemi, Jahanbakhsh. *J.Coord. Chem.* **1992,** *26* (4), 337-344.

65. Murugavel, R.; Korah, R., Structural Diversity and Supramolecular Aggregation in Calcium, Strontium, and Barium Salicylates Incorporating 1,10-Phenanthroline and 4,4‘-Bipyridine: Probing the Softer Side of Group 2 Metal Ions with Pyridinic Ligands. *Inorg. Chem.* **2007,** *46* (26), 11048-11062.

66. Mitchell, P. R.; Sigel, H., Ternary complexes in solution. Enhanced stability of ternary metal ion/adenosine 5'-triphosphate complexes. Cooperative effects caused by stacking interactions in complexes containing adenosine triphosphate, phenanthroline, and magnesium, calcium, or zinc ions. *J. A. Chem. Soc.* **1978,** *100* (5), 1564-1570.

67. Noro, S.-i.; Mizutani, J.; Hijikata, Y.; Matsuda, R.; Sato, H.; Kitagawa, S.; Sugimoto, K.; Inubushi, Y.; Kubo, K.; Nakamura, T., Porous coordination polymers with ubiquitous and biocompatible metals and a neutral bridging ligand. *Nat. Commun.* **2015,** *6*, 5851.

68. Mortensen, J. J.; Hansen, L. B.; Jacobsen, K. W., Real-space grid implementation of the projector augmented wave method. *Phys. Rev. B* **2005,** *71* (3), 035109.

69. Enkovaara, J.; Rostgaard, C.; Mortensen, J. J.; Chen, J.; Dułak, M.; Ferrighi, L.; Gavnholt, J.; Glinsvad, C.; Haikola, V.; Hansen, H. A.; Kristoffersen, H. H.; Kuisma, M.; Larsen, A. H.; Lehtovaara, L.; Ljungberg, M.; Lopez-Acevedo, O.; Moses, P. G.; Ojanen, J.; Olsen, T.; Petzold, V.; Romero, N. A.; Stausholm-Møller, J.; Strange, M.; Tritsaris, G. A.; Vanin, M.; Walter, M.; Hammer, B.; Häkkinen, H.; Madsen, G. K. H.;

Nieminen, R. M.; Nørskov, J. K.; Puska, M.; Rantala, T. T.; Schiøtz, J.; Thygesen, K. S.; Jacobsen, K. W., Electronic structure calculations with GPAW: a real-space implementation of the projector augmented-wave method. *J. Phys. Condens. Matter* **2010,** *22* (25), 253202.

70. Marques, M. A. L.; Oliveira, M. J. T.; Burnus, T., Libxc: A library of exchange and correlation functionals for density functional theory. *Comput. Phys. Commun.* **2012,** *183* (10), 2272-2281.

71. Díaz-Cervantes, E.; García-Revilla, M. A.; Soto-Arredondo, K.; Villaseñor-Granados, T.; Martínez-Alfaro, M.; Robles, J., Computational study of metal complexes formed with EDTA, melatonin, and its main metabolites: implications in lead intoxication and clues to a plausible alternative treatment. *J Mol Model.* **2019,** *25* (1), 18.

Supporting Information

Gram-Scale, Metal- and Solvent-mediated Synthesis of Two- dimensional Triazine Heterostructures

Abbas Faghani,[a] Mohammad Fardin Gholami,[b] Matthias Trunk,[c] Johannes Müller,[b] Pradip Pachfule,[c] Sarah Vogel,[c] Philip Nickl,[a] Jingjing shao,[a] Sabrina Jürgensen,[d] Antonio Setaro,[d] Wolfgang E. S. Unger,[e] Raul Arenal,[f] Christoph T. Koch,[b] Beate Paulus,[a] Jürgen P. Rabe,[b] Stephanie Reich,[d] Arne Thomas,[c] Rainer Haag, [a] Mohsen Adeli,*[a,g]*

[a] *Institut für Chemie und Biochemie, Freie Universität Berlin, Takustraße 3, Berlin 14195, Germany.*

[b]*Department of Physics & IRIS Adlershof Humboldt Universität zu Berlin Newtonstrasse 15, 12489 Berlin Germany.*

[c]*Department of Chemistry / Functional Materials, Technische Universität Berlin, BA$_2$, Hardenbergstraße 40, 10623 Berlin, Germany.*

[d]*Department of Physics, Free University Berlin, Arnimallee 14, 14195 Berlin, Germany*

[e]*BAM – Federal Institute for Material Science and Testing, Division of Surface Analysis and Interfacial Chemistry, Unter den Eichen 44-46, 12205 Berlin, Germany*

[f]*Laboratorio de Microscopias Avanzadas (LMA), Instituto de Nanociencia de Aragon, Universidad de Zaragoza, 50018 Zaragoza, Spain. 5 Fundacion ARAID, 50018 Zaragoza, Spain.*

[g]*Faculty of Science, Department of Chemistry, Lorestan University, Khorramabad, Iran*

Table of Contents

1. Materials and methods:

Materials:

All the solvents and chemicals used were purchased from commercially available sources and used without further purification. 2,4,6-trichloro-1,3,5-triazine (cyanuric chloride or triazine), calcium carbide, 1-3-diphenylisobenzofuran (DBPF), Ethylenediaminetetraacetic acid (EDTA), acetic acid, methyl-2-pyrrolidone (NMP) and graphene were purchased from Sigma-Aldrich (Schnelldorf, Germany). Dimethylformamide (DMF), toluene, mesitylene, methanol, ethanol, chloroform, acetone, phosphate-buffered saline (PBS) and tetrahydrofuran, were purchased from Merck (Germany).

Methods and Instrumentations:

Attenuated total reflection infrared spectroscopy (ATR-IR): all measurements are performed on an ATR-IR-spectrometer FT/IR-4100 Firma Jasco equipped with a diamond window in a measurement range of 4000 – 550 cm-1.

Ultraviolet-Visible spectroscopy (UV-Vis): The measurements were performed on a Shimadzu UV-2450 spectrophotometer at room temperature. A 1cm path length quartz cuvette was used in the experiments.

Fluorescence spectroscopy: The measurements were performed on the Jasco FP-6500 fluorometer in the range of 500-800 nm.

Laser irradiation: The samples were irradiated with 100 W laser Voltcraft ESP1204 with wavelength of 785 nm. The temperature change was measured by thermo camera.

Thermal gravimetric analysis (TGA): The measurements were recorded by a STA 409 apparatus (Linseis) at temperatures range 25-800 ºC with a 10 ºC/min heating rate under air.

Elemental analysis (EA): EA was performed using ELEMENTAR apparatus with three columns and detector for carbon, nitrogen, hydrogen and sulfur elements.

Nuclear magnetic resonance spectroscopy (NMR): ^{1}H NMR and ^{13}C NMR spectra were recorded on a Jeol ECX 400 spectrometer or on a Bruker Biospin Avance 700 spectrometer (Bruker Corporation, Billerica, MA, USA) (at 295 K). Chemical shifts were reported in ppm

using the deuterated solvent peak as the internal standard and tetramethyl silane ($SiMe_4$) was used for internal calibration at 125 MHz with complete proton decoupling.

Electrospray ionization-time of flight (ESI-TOF): The measurements were performed on an Agilent 6210 ESI-TOF from Agilent Technologies, Santa Clara, CA, USA. The solvent flow rate was adjusted to 4 μL/min and the spray voltage set to 4 kV. The drying gas flow rate was set to 15 psi (1 bar). All the other parameters were adjusted for a maximum abundance of the relative $[M+H]^+$.

Matrix-Assisted Laser Desorption/Ionization Time-of-Flight Mass Spectroscopy (MALDI-ToF): was measured with a Bruker Ultra-flex TOF/TOF in the positive ion mode using a linear pathway (LP). Alpha-cyano-4-hydroxycinnamic acid was used as the matrix. The samples were prepared via the "dried-droplet method" by dropping 0.5 μL of methanolic solution of the sample mixture and letting them dry in air. The mixture was prepared by mixing 100 μl of a 2 mg ml-1 solution of the sample, 100 μl of a saturated matrix solution.

Powder X-ray diffraction (PXRD): PXRD data was collected on a Bruker D8 Avance diffractometer in reflection geometry operating with a Cu Kα anode (λ = 1.54178 Å) operating at 40 kV and 40 mA. Samples were ground and mounted as loose powders onto a Si sample holder. PXRD patterns were collected from 2 to 90 2θ degrees with a step size of 0.02 degrees and an exposure time of 2 seconds per step.

^{13}C Solid-state NMR (cross polarization magic-angle spinning (CP/MAS)): spectra were carried out on a Bruker Avance 400 MHz spectrometer operating at 100.6 MHz.

High resolution transmission electron microscopy (HRTEM): High resolution TEM was performed employing an imaging-side aberration-corrected FEI Titan-Cube microscope working at 80 kV, equipped with a Cs corrector (CETCOR from CEOS GmbH). Spatially-resolved electron energy loss spectroscopy (EELS) measurements were performed on probe-corrected scanning TEM (STEM) FEI Titan Low-Base operating at 80keV (fitted with a X-FEG® gun and Cs-probe corrector (CESCOR from CEOS GmbH)). Furthermore, to avoid the effects of electron beam damage, these measurements have been performed using a liquid-nitrogen-cooled cryo-holder at -170 ºC.

Scanning force microscopy (SFM): Scanning force microscopy in Quantitative nanomechanical mapping (SFM-QNM) and Scanasyst mode (SFM-Scanasyst) were performed using a Multimode 8 with Nanoscope 4 controller. An E or J scanner with maximum scan size of 10 and 100 µm were used for scanning the two-dimensional triazine heterostructures (2DTHs) samples. For SFM-QNM measurements, both cantilevers with spring constants of 2 N/m (OLTESPA) and 0.4 N/m (Scanasyst A ir–HR) were used. The sensitivity of cantilevers were first calibrated by thermal tuning process and then their spring constant were measured over Sapphire (Bruker) as a hard surface. The forces applied to the samples by the tips were within the ranges of 100-2000 pN. Measurements were carried out in 512 in 512 pixels resolution and speed of 6 minutes per image at room temperatures 25-27 ^{o}C. Samples of the 2DTHs were received as black powder. Additionally, samples were received in two types of exposed to oven or non-oven and a sample synthesized in presence of water during the purification process. The sample labeled oven, was exposed to ambient conditions oven at 400 ^{o}C for duration of 2 hours and these experiments were done on this sample. To investigate the 2DTHs material, various sample preparation methods and substrates were used. Surfaces such as; freshly cleaved muscovite mica (mica), Silicon oxide layer over Silicon wafers (Si wafer) and freshly cleaved highly oriented pyrolytic graphite (HOPG) were employed as substrates to support the 2DTHs particles. Furthermore, 2DTHs powder was dispersed in solvents such as, dimethylformamide (DMF), N-methyl-2-pyrrolidone (NMP), ethanol or methanol by use of 2 to 10 hours of bath ultra-sonication and then deposited onto substrates such as; mica, Si wafer, HOPG. Due to small dimensions of the particles of 2DTHs and their fine powder condition, commonly used method of mechanical exfoliation with tweezers is not possible. However, shearing of the powder between two hard substrates was tested to observe if helpful in exfoliation of those 2DTHs particles. It was observed that the 2DTHs particles can scratch the surface of mica if sheared over such surface as seen by SFM. Therefore, only Si wafer surface was used for shearing the 2DTHs powder as scratches could not be observed. Indeed, the Mohs scale hardness of the muscovite mica is between 2 – 2.5 and it is lower than that of SiO_2 layer of Si wafer 6.5 – 7.

X-ray photoelectron spectroscopy (XPS): XPS were recorded on a Kratos Axis Ultra DLD spectrometer equipped with a monochromated Al Kα X-ray source using an analyzer pass energy of 80 eV for survey spectra and 20 eV for the core level spectra. The electron emission angle was

60° and the source-to-analyzer angle was 60°. The binding energy scale of the instrument was calibrated following a Kratos Analytical procedure which uses ISO 15472 binding energy data. Spectra were recorded by setting the instrument to the hybrid lens mode and the slot mode providing approximately a 300 x 700 μm^2 analysis area using charge neutralization. All XPS spectra were processed with the UNIFIT program (version 2017). A Gaussian/Lorentzian sum function peak shape model GL (30) was used in combination with a Shirley background. If not otherwise denoted the L-G mixing for component peaks in all spectra were constrained to be identical. Peak fitting of C 1s spectra was performed by approximation of asymmetric peak for C–C sp^2 C 1s component. All spectra were calibrated about the Au4f signal at 84.0 eV. High-resolution core-level spectra were recorded in FAT (fixed analyser transmission) mode at a pass energy of 20 eV for all elements: O 1s, N 1s, C 1s, and Au4f.

Transmission electron microscopy (TEM) and scanning electron microscopy (SEM): The samples were prepared by setting up 1 mg/ml solutions of the 2DTHs particles with ethanol and leaving them in an ultrasonic bath for 120 mins. Droplets of these solutions were deposited on holey carbon transmission electron microscopy grids (TEM grids) to deposit 2DTHs particles on them. All measurements were performed on a JEOL TEM 2200FS operated at an acceleration voltage of 200kV.

Electron diffraction pattern analysis: We acquired the data in 4D-STEM (scanning transmission electron microscopy) mode with our Zeiss Gemini 500 microscope at 30kV acceleration voltage. The sample was mounted on a custom 4D-STEM sample holder. We scanned the electron beam over particles and took a diffraction pattern with the area detector (scintillator fiber coupled CMOS camera) for each scan position.

Energy electron loss spectroscopy (EELS): The measurements were performed on probe-corrected scanning TEM (STEM) FEI Titan Low-Base operating at 80keV (fitted with a X-FEG® gun and Cs-probe corrector (CESCOR from CEOS GmbH)).

Raman spectroscopy: The measurement of the 2DTHs samples were carried out mainly by deposition of the suspended 2DTHs and its precipitates from various solvents onto mica or SiO_2 layer of Si wafer. 2DTHs particles had (different) areas within range of 5-10 μm^2. Hundreds of particles were measured using either mapping or individual points using a 100X objective NA=0.9 (Mitutoyo, Olympus) at 532, 638 and 785 nm, with an Xplora one (Horiba) Raman

spectrometer with ~1.7cm^{-1} spectral resolution and power well lower than ~ 1 mW. A grating of 1800 grooves/mm was used in the setup. The instrument was calibrated using a Si spectral peak of a Si wafer in addition to the calibration against Neon lamp spectral lines. Special care was taken to assure that the accumulation times and laser power used, improve the signal to noise ratio but do not adversely affect the 2DTHs particles, i.e. preventing from thermally induced effects.[1]

Computational method: Were performed using the GPAW program[2, 3] employed the libxc implementation of the PBE functional by Perdew, Burke and Ernzerhof[4] using a LCAO expansion of the wave function[5] employing a double-ξ-polarized (dzp) basis set. During structure optimization, atomic positions were relaxed until the remaining forces were below 0.05 eV/°A.

2. Synthesis

Synthesis of graphite using CaC_2: The grind calcium carbide (1.00 g) was added into a round bottom flask (100 mL), then 10 mL deionized water was added dropwise into the flask (acetylene gas started to generate). After 30 minutes the reaction was entirely stopped, then 20 mL of HCl (10 wt%) was added slowly to the reaction mixture and was sonicated for 20 minutes to remove the impurities. Finally, black powder (0.05 g, yield, 5%) was obtained after several washing using centrifuge (7000 rpm, 15 minutes) with water, acetone and eventually dried at 80 °C in ambient air.

Synthesis of 2DTHs/graphite: Triazine (2.00 g, 10.84 mmol, 1 eq) and calcium carbide (2.09, 32.55 mol, 3 eq, the postal and murder was used to grind under inert gas), were mixed under an inert gas using schlenk flask (100 mL). After 15 minutes stirring in bulk, DMF (20 mL) was added to the mixture dropwise at room temperature. Caution: in this step gases released, and the reaction is exothermic. The resulted dark-brownish suspension was stirred for 72 hours at 120 °C. The reaction mixture was cooled to room temperature and a few drops of water slowly added via syringe to quench the reaction. Vacuum filtration (frit-P4) followed by washing with acetone, water, methanol, tetrahydrofuran and chloroform was carried out. Finally, soxhlet of the filtrate in methanol/water (24 h) and drying in the vacuum at 80 °C afforded 2DTHs/graphite as a dark-brownish powder (1.36 g, 68%). Note: prolongation for 7 days led to increasing the yield up to 1.74 g. Acid treatment of the 2DTHs/graphite was carried out to remove the Ca^{2+} ions and another possible derivative using hydrochloride acid (10 wt%). Hence, 500 mg of 2DTHs/graphite was dispersed in 30 mL of the acid and the mixture was stirred for 3 hours at 25 °C. Then the centrifuge (7000 rpm, 15 min) was used to precipitate the product, and following washing by water and acetone till the supernatant became transparent. The black product was then dried in the vacuum at 80 °C.

Synthesis of 2DTHs: Triazine (2.00 g, 10.84 mmol, 1 eq) and grind calcium carbide (2.09, 32.55 mol, 3 eq, were mixed under an inert gas using dry schlenk flask (100 mL). After 15 minutes stirring in bulk, dry DMF (20 mL) was added to the mixture dropwise at 25 °C and the temperature was increased up to 120 °C and reaction mixture was stirred for 72 hours. The reaction was cool to room temperature and diluted using 20 mL dry DMF, then transfer into two plastic falcon (50 mL) and kept intact for 5 minutes. Eventually, the supernatant was gently

separated and used for further purification as following; The supernatant was dialysis (benzylated tube MWCO: 2000) in dry DMF until no brownish color observed from the tubes. After dialysis a dark-brownish product was obtained and washed by HCl (10 wt%), water and acetone using centrifuge (10000 rpm, 10 minutes). The black product was then dried in the vacuum at 80 °C.

Control reaction: In order to examine further the role of DMF solvent in the process of 2D formation, the reaction was performed in the present of toluene and mesitylene as reaction solvents. The protocol was the same as 2DTHs synthesis, but we could not observe any product.

Control reactions: To have more information about the mechanism of the reaction, the calcium carbide with only DMF was mixed with same manner as 2DTHs, there was no product at all.

Similarly, triazine with only DMF was also examined with the same method for calcium carbide, no product was detected.

Control reaction in the presence of ethylenediaminetetraacetic acid (EDTA): In the same manner as synthesis of 2DTHs this control reaction was done. Briefly, triazine (1 g, 1 eq), calcium carbide (1.43 g, 3 eq) and EDTA (1 g) was mixed in bulk by following adding dropwise dry DMF (7 mL) in the mixture, the reaction was stirred for 3 days at 120 °C. A glass filter (P4) was used to wash the product with plenty of chloroform, acetone, dichloromethane and following by soxhlet in methanol for 24 hours, afterward the black product was dried in vacuum at 80 °C, 0.415 g.

Synthesis of 2-Chloro-4,6-diphenoxy-1,3,5-triazine (1). In the 250 mL flask triazine (3.688 g, 20 mmol) was dissolved in dry acetone (150 mL), then the solution was cooled down to 0 °C. In a separate flask, phenol (3.760 g, 40 mmol) was deprotonated with NaOH (1.600 g, 40 mmol) in water (150 mL) to make a transparent aqueous solution (a gentle heating might be beneficial).

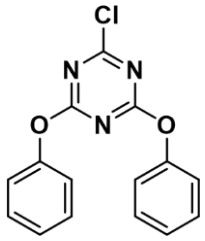

Then the aqueous deprotonated solution was slowly added to the triazine solution. The reaction mixture was stirring at 0 °C for 9 h, then the mixture was poured into water (150 mL) to make a white precipitate. The crude precipitate was filtered off, washed with water and ethanol. The thin white solid crystal was obtained by recrystallization with hexane. Yield: 70%.

Synthesis of 2,4-dicloro-6-phenoxy-1,3,5-triazine: Triazine (1.840 g, 10 mmol) was dissolved in dry acetone (80 mL) and the solution cooled -10 °C. Phenol (0.94 g, 10 mmol) was dissolved in water (80 mL) and reacted with NaOH (0.400 g, 10 mmol) in a separate glass vial at room temperature. This colorless solution then was dropwise added to the triazine solution, which was further stirred for 6 hours at 0 °C. Then a white precipitate was obtained by pouring the reaction mixture into water (70 mL) and filtered and was washed using ethanol and water. Finally, the purification was finished by recrystallization using n-hexane to afford white solid product. Yield 65%.

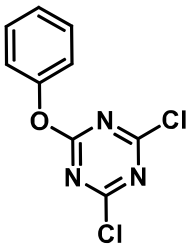

Synthesis of N,N-dimethyl-4,6-diphenoxy-1,3,5-triazin-2-amine (2): In a 100 ml flask the 2-Chloro-4,6-diphenoxy-1,3,5-triazine (3.000 g, 10 mmol) under inert gas was dissolved in dry DMF (20 mL), then the solution was stirred for 30 minutes at 25 °C. Grind calcium carbide (3.760 g, 40 mmol) was added to the solution. The reaction was stirred at 120 °C for 24 hours. The mixture was purified using Hex/EtOAc (7/3 v) silica gel column chromatography. Yield: 30%.

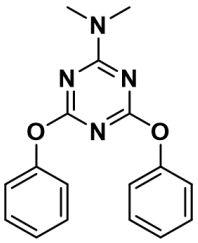

Trimerization product (4) and intermediate (3) monitoring reaction using MALDI-ToF and ESI mass: In the 100 ml flask the 2-Chloro-4,6-diphenoxy-1,3,5-triazine (3.000 g, 10 mmol) under inert gas was dissolved in dry DMF (20 mL), then the solution was stirred for 30 minutes at room temperature. Grind calcium carbide (3.760 g, 40 mmol) was added to the solution. The reaction was stirred at 120 °C for 4 days. The trimerization was monitored using MALDI-ToF at each 2 hours.

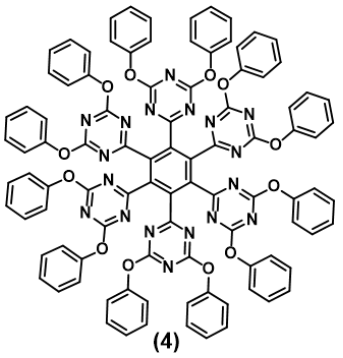
(4)

3. Characterization

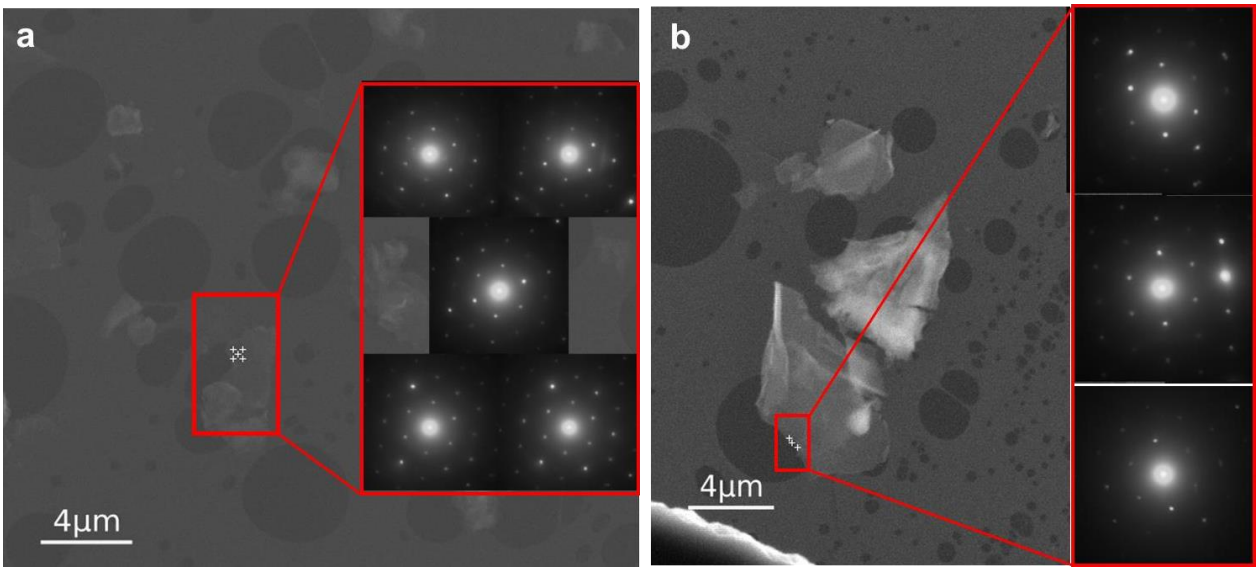

Figure S1. (**a**) and (**b**) SEM images and electron diffraction pattern analyses of synthesized graphite sheets, were acquired in spot mode by moving the spot to the marked pixel positions. In each image the red small rectangle image is a secondary electron (SE) image and the right rectangle images are diffraction patterns in transmission recorded with an electron sensitive camera.

The crystallinity and structure of the synthesized graphite were further explored using experimental electron diffraction analyses. Accordingly, the electron diffraction patterns showed graphitic structure with high crystallinity over areas of at least several hundred nanometers. In the pattern, the diffraction spots corresponding to a 2.2 Å unit cell could be clearly observed (**a**) and (**b**). This unit cell is match with the unit cell obtained by the reported chemical structure of graphene.

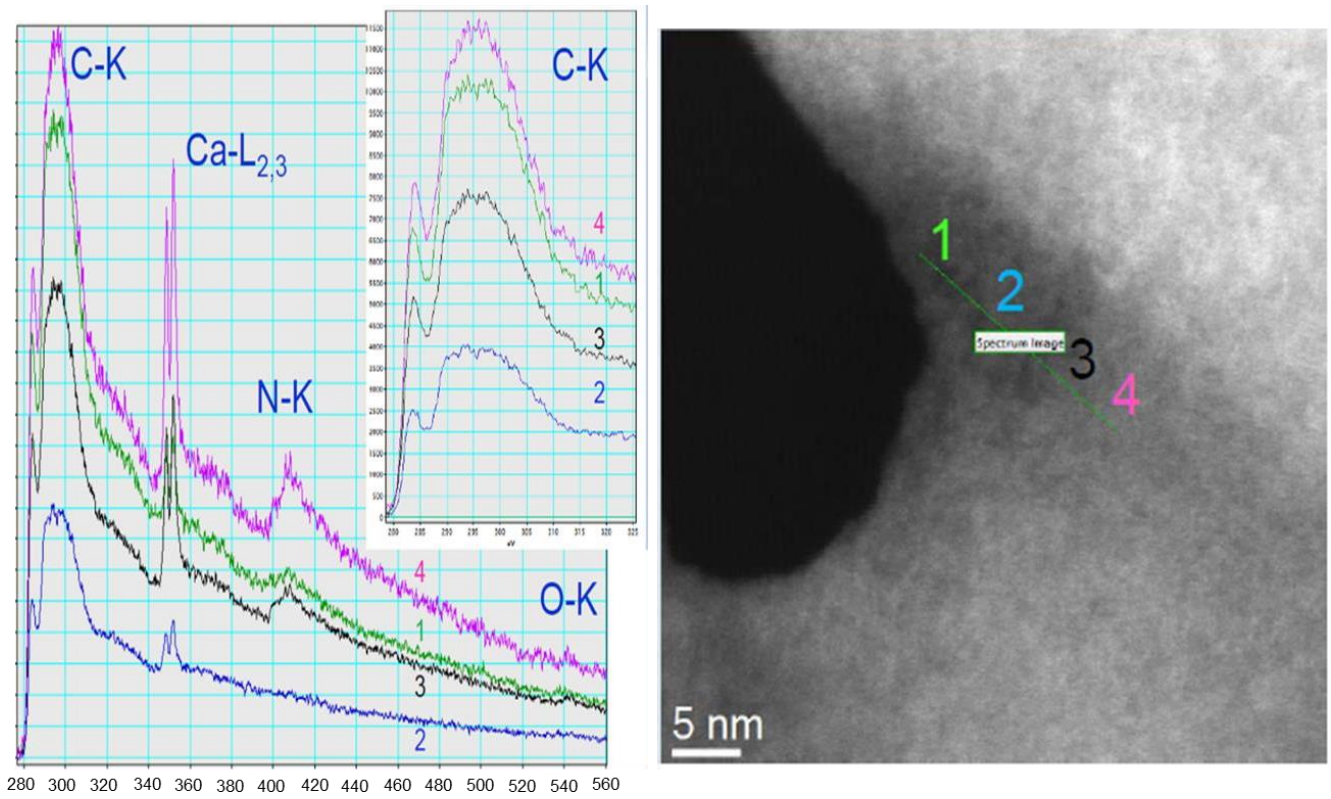

Figure S2. EELS spectra and HRTEM image of 2DTHs

Compound	C	N	H	C/N Found	C/N cal.
2DTHs	56.60	21.57	3.759	2.6	2.1
Graphite	91.12	0.63	0.112	-	-

Table S1. Elemental analysis and carbon to nitrogen ratio for 2DTHs calculated and experimental, also graphite produced from reaction of calcium carbide with water.

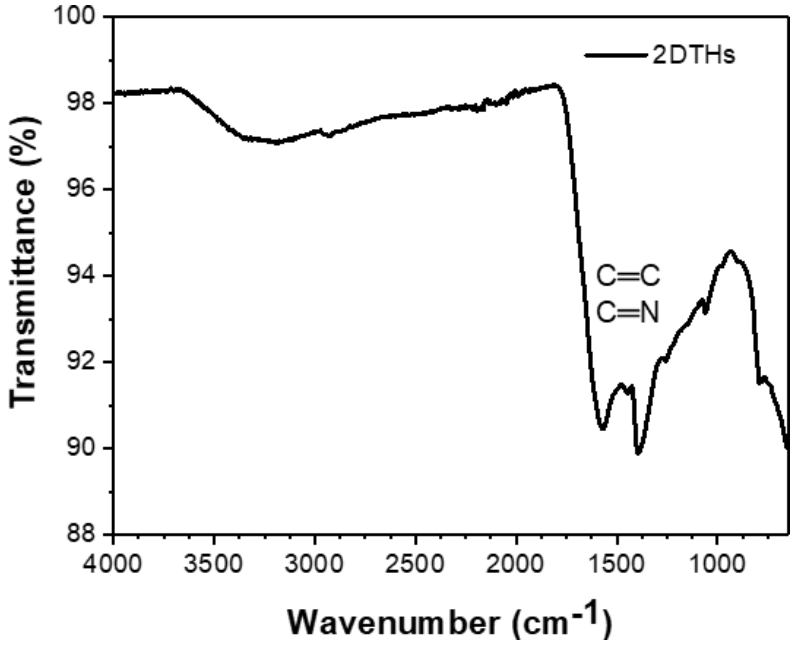

Figure S3. ATR-FTIR spectrum of 2DTHs, the main part of structure contains triazine and benzene rings, in which the vibration characteristic peaks can clearly been seen in the spectrum.

Table S2. Interpretation of the fitted components in the highly resolved XPS spectra.

Sample	Spectrum	Binding energy	L-G Mixing	FWHM	Interpretation	Relat. Area	Abs. Area [cps*eV]
2DTHs	C1s	285.0	0.37	2.02	C–C sp^2	0.37	4984
		281.1	0.37	2.02	C–C sp^3	0.30	4167
		288.5	0.37	2.02	C–N	0.33	4416
	N1s	398.9	0.28	1.42	Pyridinic component	0.35	3887
		400.5	0.28	1.99	Graphitic component	0,65	7190

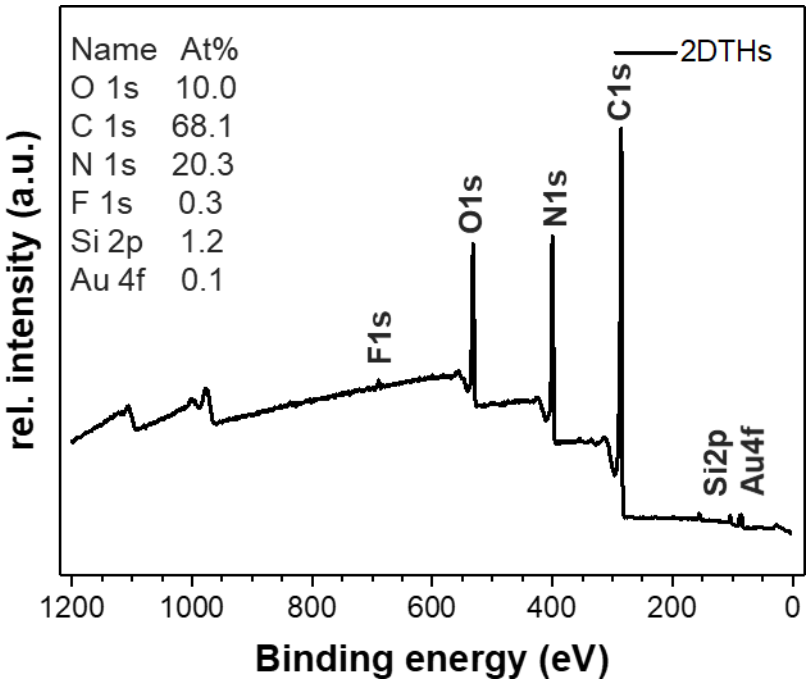

Figure S4. Survey XPS spectra of 2DTHs. Disappearing the calcium peak after washing process confirm the successful removal of metal ions.

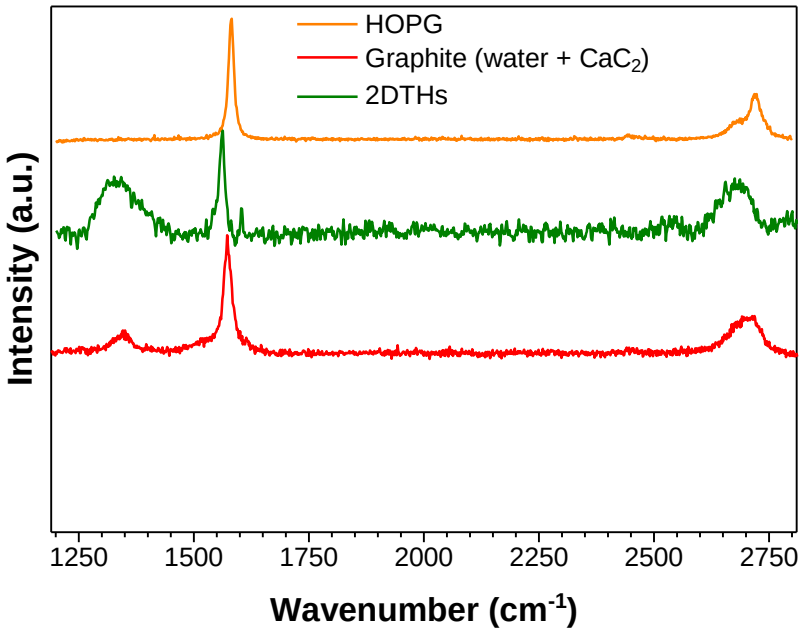

Figure S5. Raman spectra of Highly oriented pyrolytic graphite (HOPG), 2DTHs (green line) and graphite (water + CaC_2).

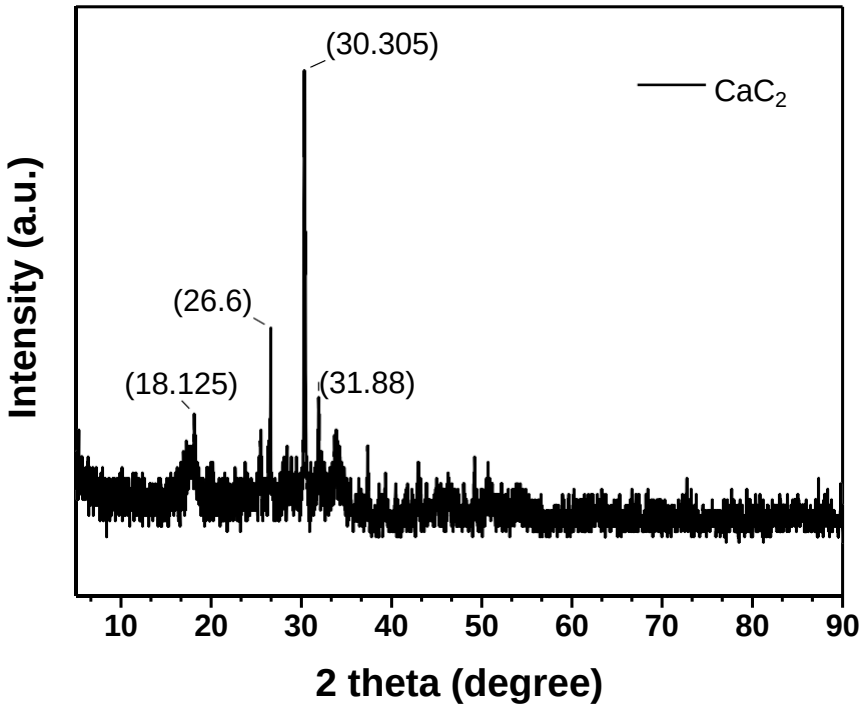

Figure S6. P-XRD of calcium carbide shows a graphitic peak and broadened background which is due to the amorphous areas in the structure.

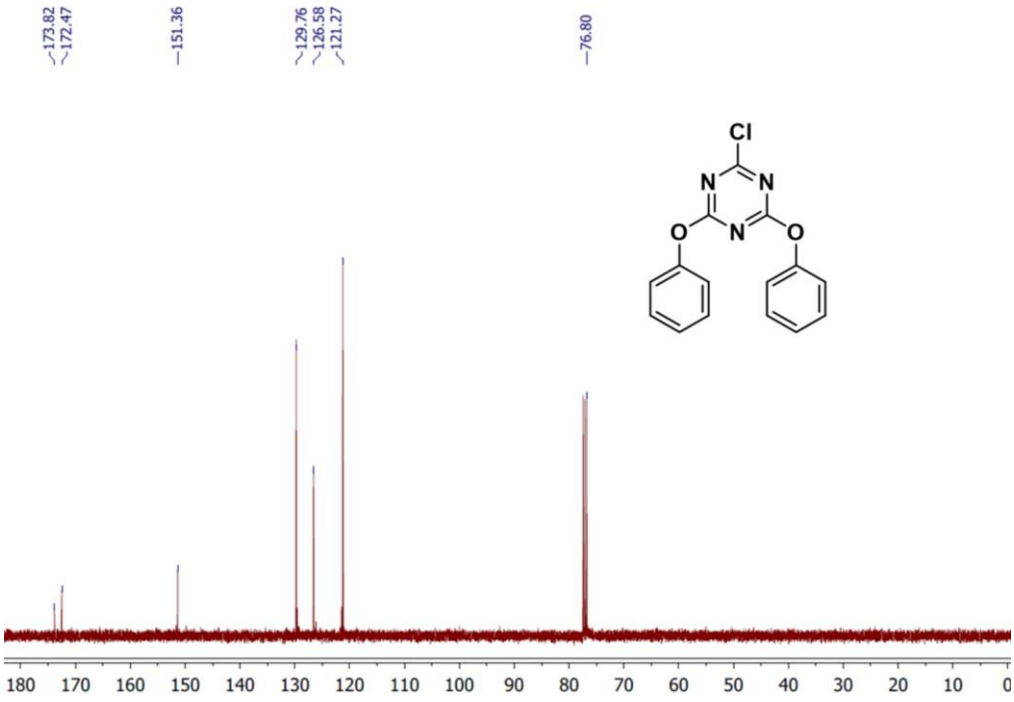

Figure S7. ^{13}C-NMR of 2-Chloro-4,6-diphenoxy-1,3,5-triazine (**1**), in $CDCl_3$.

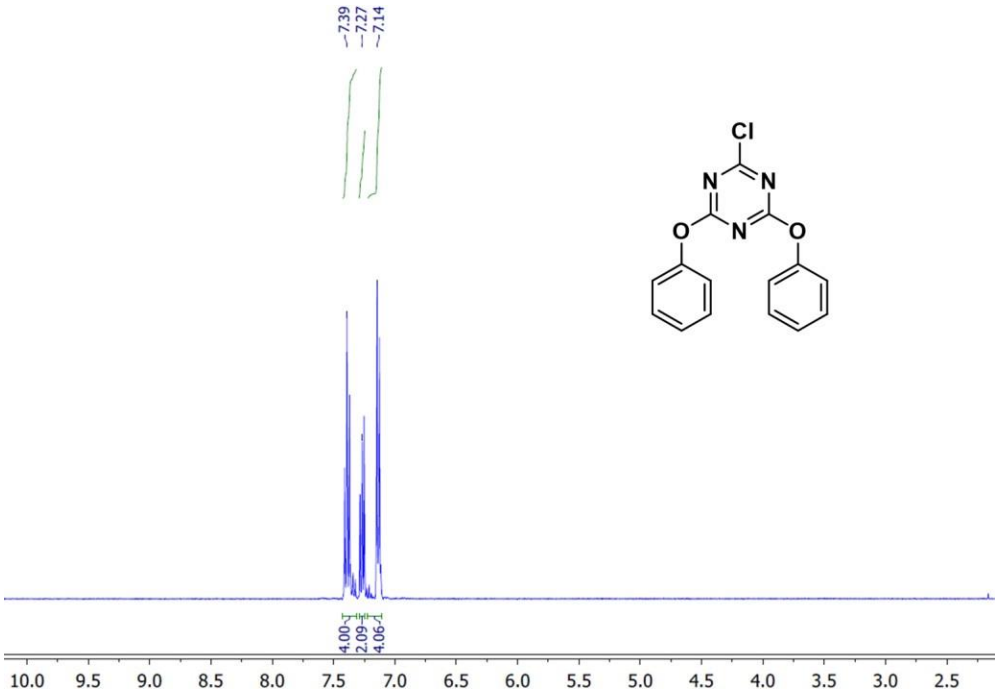

Figure S8. ^{1}H-NMR of 2-Chloro-4,6-diphenoxy-1,3,5-triazine (**1**) in $CDCl_3$.

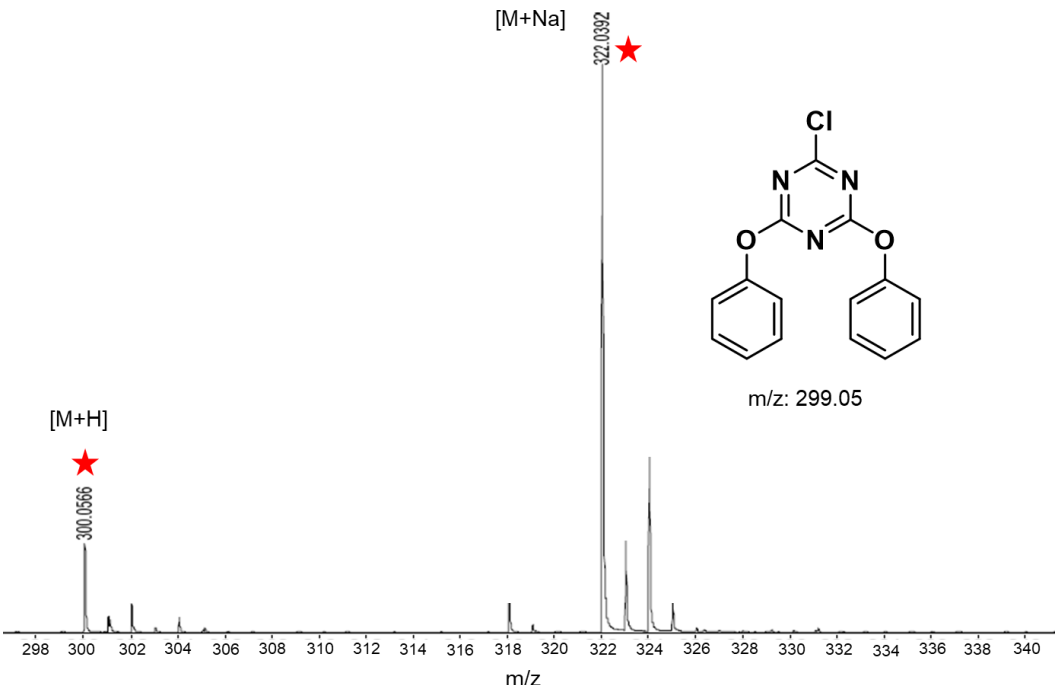

Figure S9. ESI Mass: m/z calcd for (**1**) $C_{17}H_{16}N_4O_2$ [M+Na] and [M+H]: 322.03, 300.05); founds: 322.0392 and 300.0566.

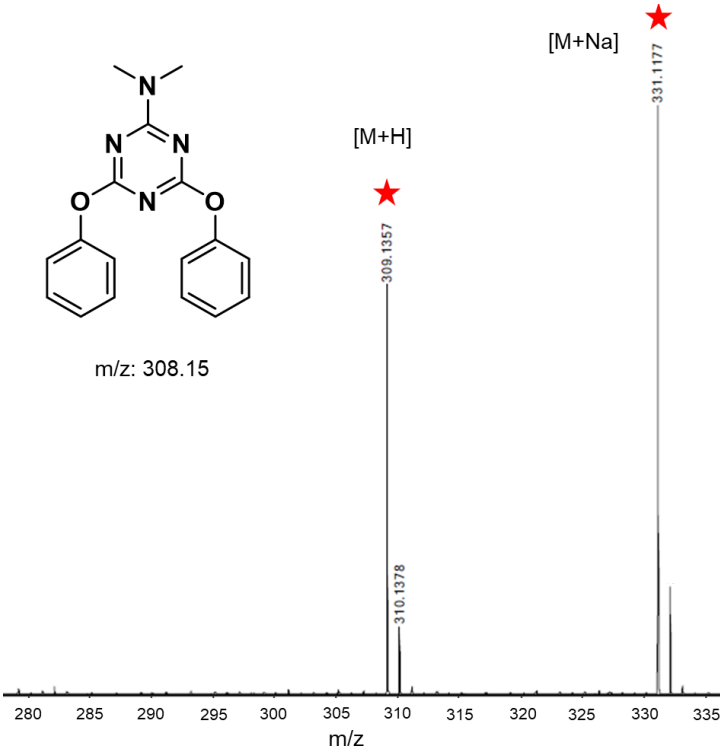

Figure S10. ESI Mass: m/z calcd for (**2**) $C_{17}H_{16}N_4O_2$ [M+Na] and [M+H]: 331.12, 309.13); founds: 331.1177 and 309.1357.

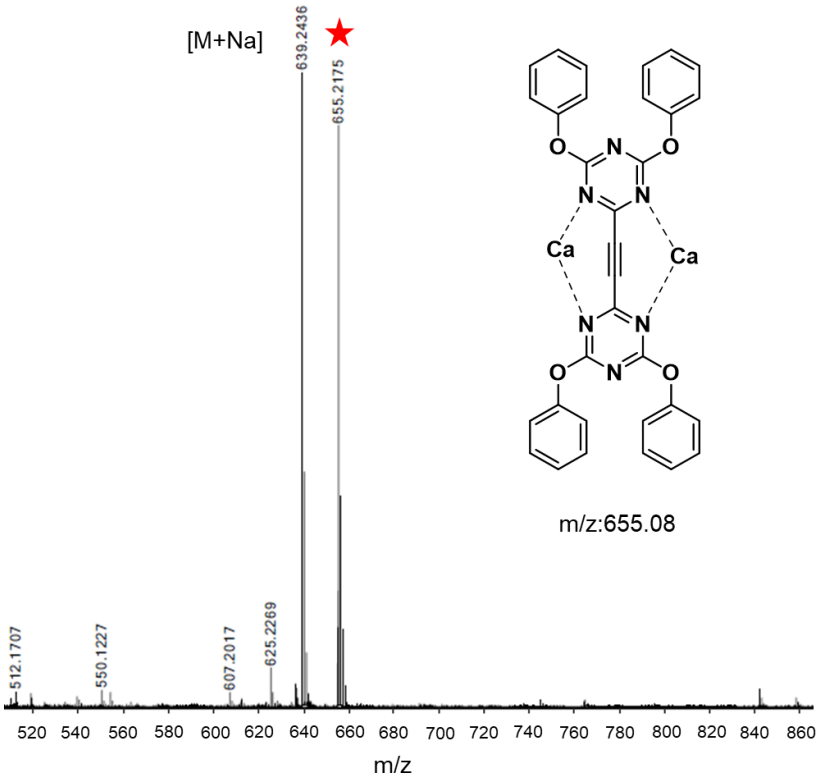

Figure S11. ESI Mass: m/z calcd for (**3**) $C_{32}H_{20}Ca_2N_6O_4$ [M+Na]: 655.21); found: 655.2175.

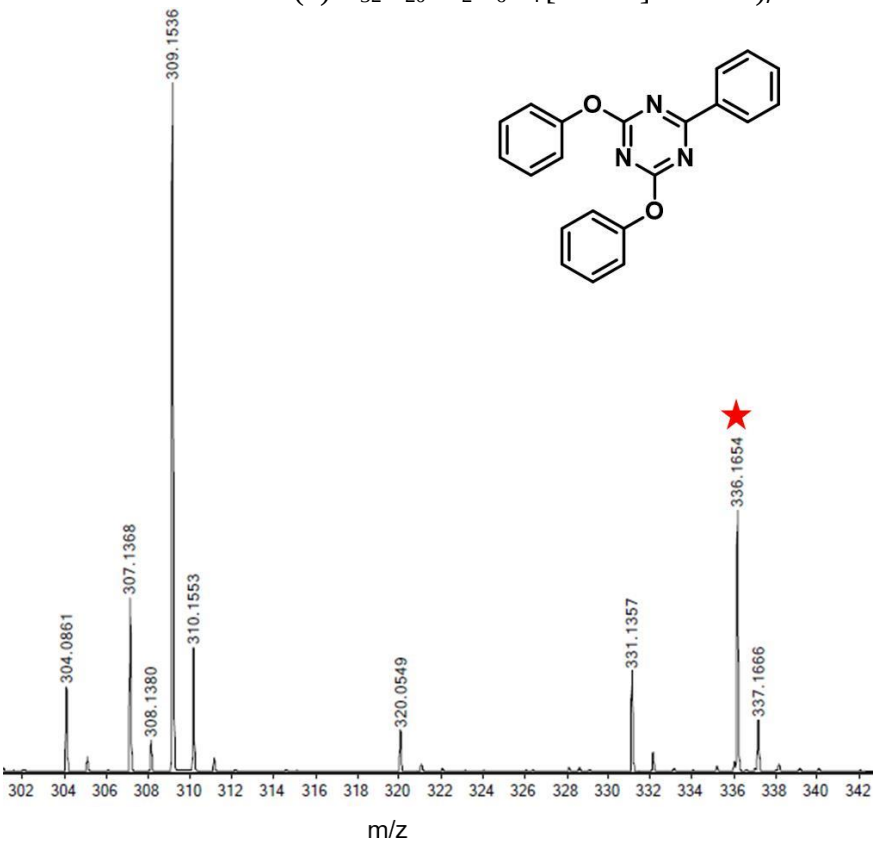

Figure S12. ESI Mass: 336 m/z

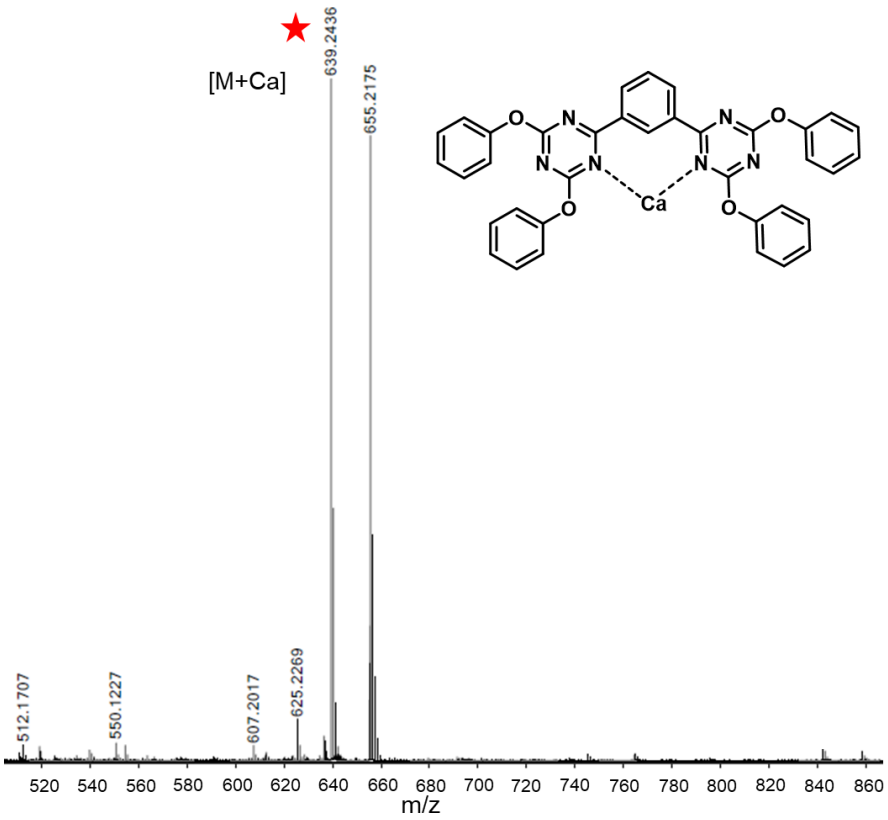

Figure S13. ESI Mass: 639 m/z.

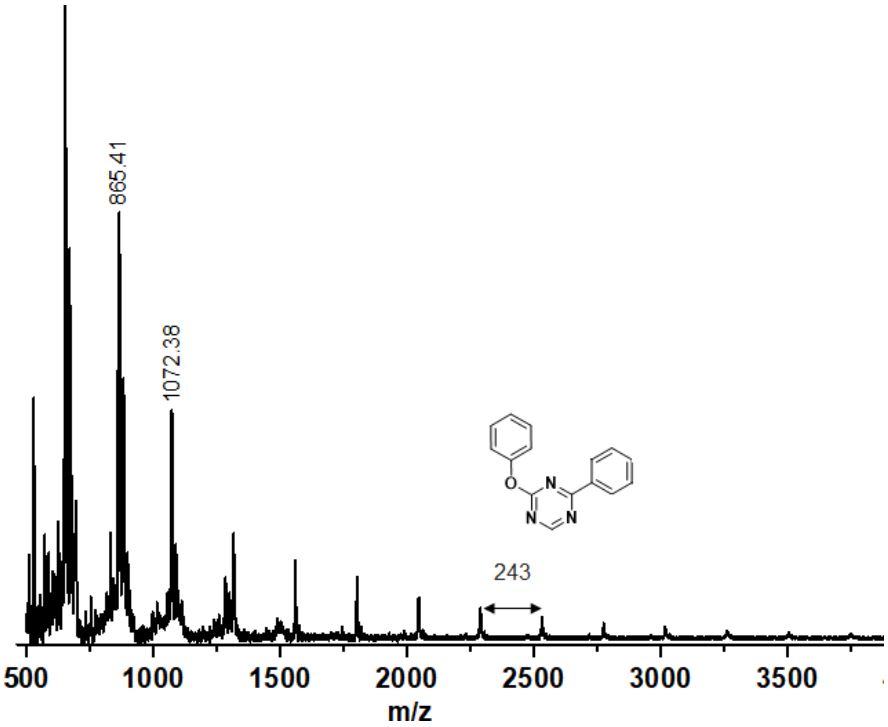

Figure S14. ESI Mass: 243 m/z as repeating unit for polymerization.

Computational analysis

As showed in figure S15, the initial model structure obtains the lowest energy when considered dihedral angle (marked with red line) is close to 90°. With the presence of two Ca^{2+} in the system, weak coordination with N_1, C_2, C_3, N_2 are observed, all distances between each Ca^{2+} and corresponding atom are listed in Table S3. For the initial structure the rotation barrier is only about 0.006 eV, which increases to 1.6 eV when Ca^{2+} are coordinated within the system (Figure 5f in the main text) This barrier is big enough to support the growth of the final 2D material.

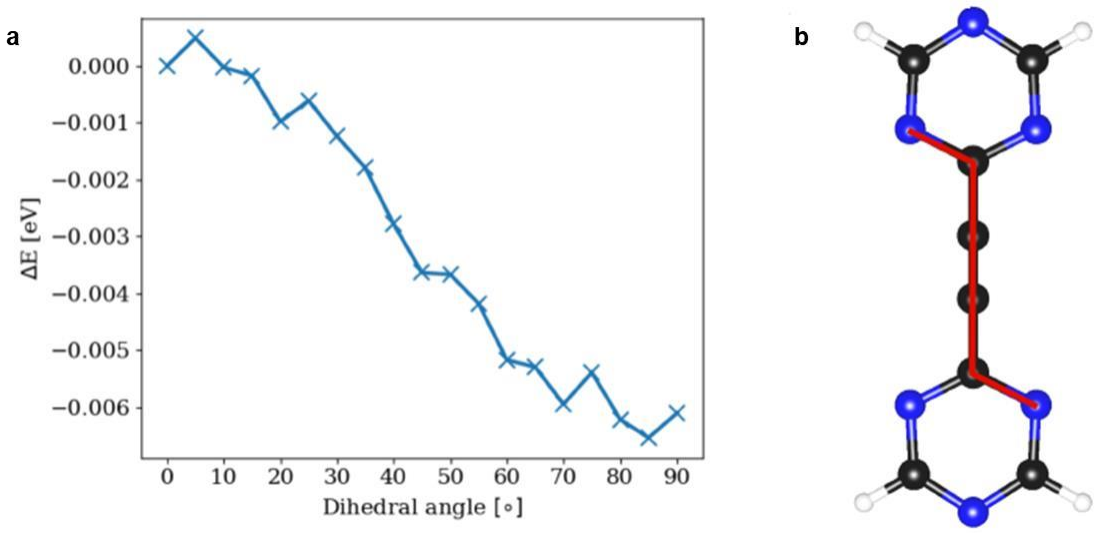

Figure S15. (**a)** Illustrates energy of the system against the dihedral angle with 5° each step. (**b)** The structure of the initial model molecule (considered dihedral angle is marked with red line) without Ca^{2+} in the system. It is noted that ΔE = E - E[Dihedral angle = 0°].

Table S3: Distance between each Ca^{2+} and labelled atoms of the initial model structure in Å.

	N_1	C_1	C_2	C_3	C_4	N_2
Ca_1	3.09	3.55	3.00	3.01	3.60	3.15
Ca_2	3.10	3.56	3.00	3.01	3.60	3.14

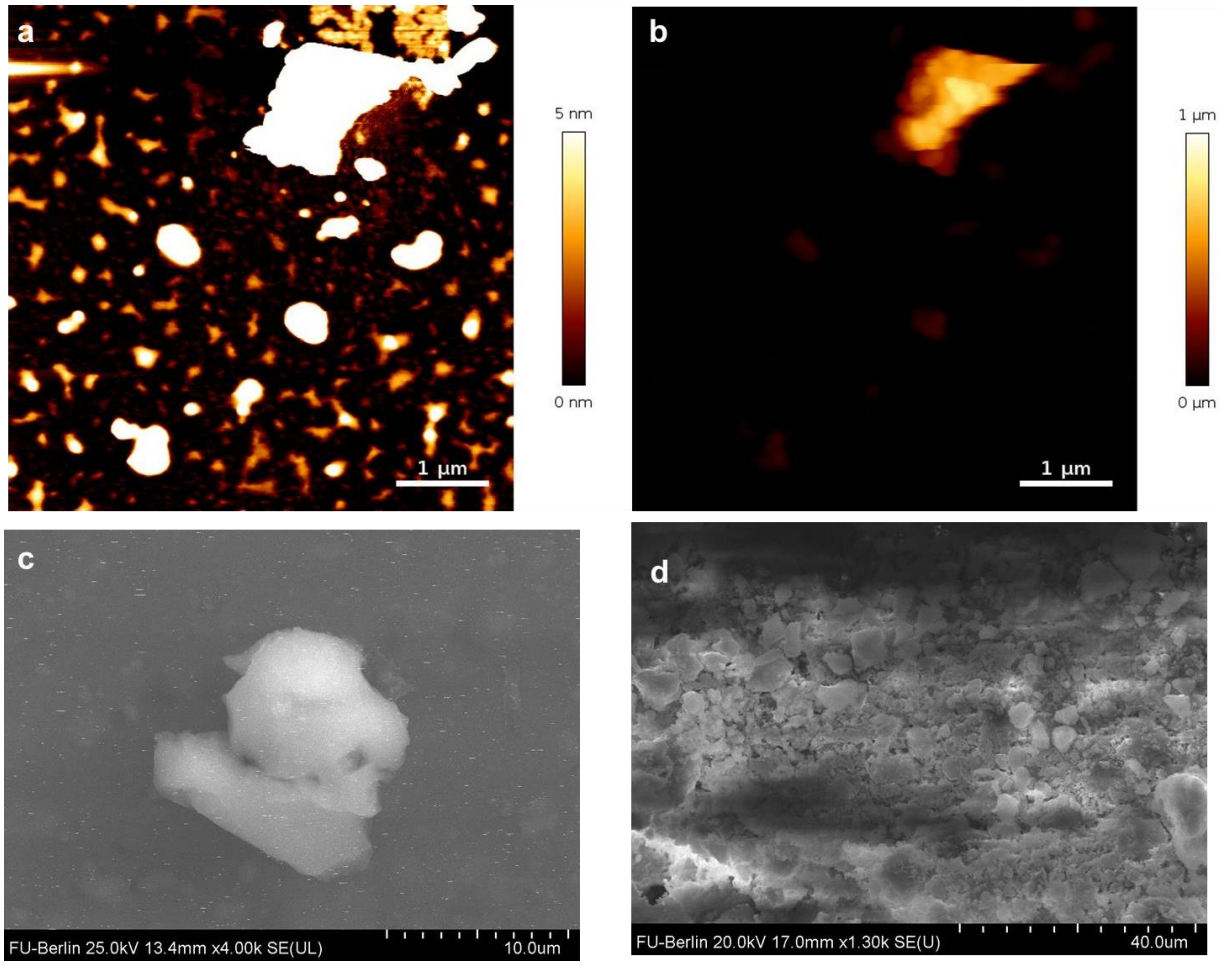

Figure S16. (**a**) and (**b**) scanning force microscopy (SFM). Control reaction of 2DTHs formation in the present of EDTA which not showed sheets like structures in the SFM images, also in (**c**) and (**d**) scanning electron microscope (SEM) images of the product, where no sheets were observed.

Photothermal and photodynamic experiments

The UV-Vis absorption spectroscopy measurements were performed in Ethanol. A solution of 1,3-Diphenylisobenzofuran (DBPF) was prepared in ethanol (3.7×10^{-7} mol (100 µg) in 1 mL ethanol). Similarly, the synthesized 2DTHs was dispersed (100 µg/mL) in EtOH by help of 10 minutes sonication. Then, 900 µl of prepared DBPF solution was mixed with 100 µl of 2DTHs in a Quartz UV-Vis cell (HELLMA GmbH, Quarzglas SUPRASIL 114-QS) with path length of 10 mm. Reference samples were prepared in Quartz cell containing only EtOH. Absorption spectra were measured with a double-beam UV–Vis spectrometer Shimadzu UV-2101PC. Samples were then exposed to a laser irradiation, diode infrared laser with 808 nm and power density of, 0.5 W/cm^2. Interval times of laser exposures were as follow, 5, 10, 15, 20, 25, 30, 35, 40, 45 and 50 minutes. UV-Vis absorption spectrum of 2DTHs was then measured in EtOH (Figure S17a). As it is demonstrated in the figure 5c (in the main text), exposure of the 2DTHs and DBPF in EtOH resulted in overall reduction in the absorption of the DBPF within the wavelengths 350-450 nm. Figure S17b, demonstrates the reference sample with only DBPF, showing a minimal change in absorption spectra in EtOH after exposure to the laser. Photothermal analysis was performed using near-infrared (NIR) laser (808 nm) and power density of 0.5 W/cm^2. Photothermal activity of 2DTHs was examined in two different concentration (0.5 mg/ml and 1 mg/ml) in deionized water and as comparison graphene was used in the same manner as 2DTHs by help of bath sonication at room temperature for 15 minutes. The temperature of the dispersion mixture raised over the time and detected via NIR camera.

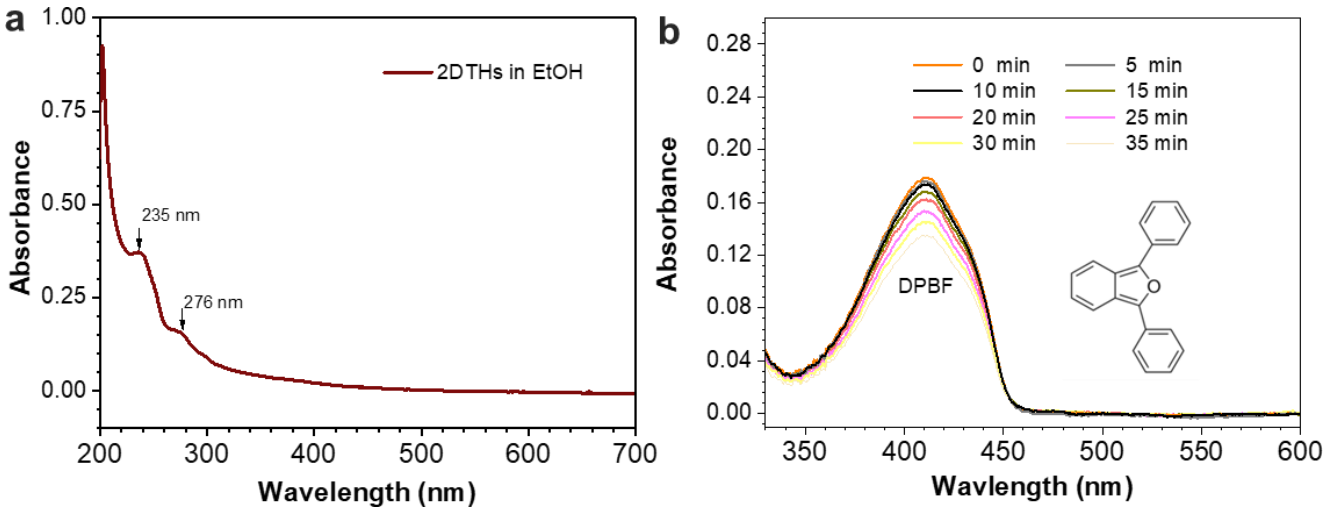

Figure S17. (**a**) UV-Vis spectrum of 2DTHs and (**b**) DBPF in EtOH.

References

]1[I. Calizo, A. A. Balandin, W. Bao, F. Miao, C. N. Lau, *Nano Lett.* **2007**, *7*, 2645-2649.

]2[P. E. Blöchl, *Phys. Rev. B* **1994**, *50*, 17953-17979.

]3[J. P. Perdew, Y. Wang, *Phys. Rev. B* **1992**, *45*, 13244-13249.

]4[J. P. Perdew, K. Burke, M. Ernzerhof, *Phys. Rev. Lett.* **1996**, *77*, 3865-3868.

]5[A. H. Larsen, M. Vanin, J. J. Mortensen, K. S. Thygesen, K. W. Jacobsen, *Phys. Rev. B* **2009**, *80*, 195112.

4 Summary and Outlook

Carbon materials have shown a great potential in the academic field and have been employed for plenty of applications. Graphene, a natural two dimensional polymer, and carbon nanotube (one dimensional analog) are meritorious candidates with fascinating physicochemical features. However, a chemical process is needed in order to customize their properties toward desired applications. Among different methods, covalent functionalization is the most promising approach for this purpose. On the other hand, the natural 2D polymer (graphene) inspired researchers to design and synthesize other 2D polymers. Nevertheless, the synthesis of 2DPs is still in its early stage and there is plenty of space for improvement in this field. Consequently, to expand these fascinating materials we conceived a new idea to functionalize graphene/carbon nanotube and synthesis of a 2D polymer by a new method. Scientific contribution of the thesis is in three main directions, which are addressing mentioned challenges for carbon nanotubes, graphene and 2D polymers.

In the first part we intend to investigate a controlled, reproducible, and mild covalent functionalization of graphene by a one-pot reaction between triazine and sodium azide to generate dichlorotriazine intermediate which could provide a selective and controlled modification approach through substitution the reactive chlorine of the triazine groups. The different reactivity of chlorine allows us to perform stepwise post-modification on graphene by manipulating the temperature from 25 up to 65 °C. As a result, defined bifunctional 2D nanomaterials (graphene) were provided and covered with hyperbranched polyglycerol (hPG) in a controlled and stepwise manner.

In the second part we intend to design and establish a new nondestructive covalent method to functionalize CNTs. We explored unique non-destructive covalent, gram-scale functionalization for CNT by a new nitrene [2+1] cycloaddition. By this method the reaction between CNT and dichlorotriazine intermediate resulted in dichlorotriazine functionality that rebuilds the extended π-system of CNTs, thereby preserving opteoelectronic properties of carbon nanotube.

Lastly, the challenge of in-solution synthesis of a 2D polymer was investigated and a new nanostructure was prepared. We introduced a metal-assisted method, in which calcium carbide and triazine are monomers and dimethylformamide is the solvent. This reaction was directed in two dimensions by calcium ions derived from calcium carbide and induced 2DTHs with amorphous structures. Calcium ions coordinated with nitrogen atoms of triazine (ligand-metal interaction), which prevented bond rotation and provide enough rigidity for the desired 2D

structure. We investigated the chemical structure and physicochemical properties of the obtained 2D structure and evaluated the mechanism of the related reactions. Based on our investigations, the water content of the reaction medium was one of the crucial factors that affected the structure of the product dramatically. While pure 2DTHs were obtained under dry conditions, graphite/2DTHs mixture or even pure graphite was obtained by increasing the water content of the reaction medium. Taking advantage of their straightforward and gram-scale synthesis as well as fluorescence, photothermal and photodynamic properties, the synthesized two-dimensional triazine heterostructures are promising materials for a wide range of future applications.

5 Kurzzusammenfassung

Kohlenstoffbasierte Nanomaterialien bieten ein großes Potential für die akademische Forschung und werden in vielen Anwendungen verwendet. Graphen, ein natürliches zweidimensionales Polymer (2DP), und Kohlenstoffnanoröhren (eindimensionale Analoga), sind zwei wichtige Vertreter dieser kohlenstoffbasierten Netzwerke mit außergewöhnlichen physikochemischen Eigenschaften. Allerdings sind chemische Modifikationen dieser Netzwerke notwendig, um ihre Eigenschaften anwendungsbezogen maßzuschneidern. Die kovalente Funktionalisierung der Nanomaterialien stellt hierbei den vielversprechendsten Ansatz dar. Das natürliche 2D-Polymer Graphen inspirierte Wissenschaftler synthetische 2D-Polymere zu designen und herzustellen. Nichtsdestotrotz sind die Synthesestrategien von 2DPs noch nicht sehr weit fortgeschritten, sodass in diesem Bereich ein großes Verbesserungspotential besteht. Um diesem Defizit entgegenzuwirken haben wir ein neues Funktionalisierungskonzept für Graphen/Kohlenstoffnanoröhrchen und eine Synthese eines 2D Polymeres entwickelt. Die vorliegende Arbeit gliedert sich inhaltlich in drei Teile, die sich jeweils mit den aufgeführten Herausforderungen bezüglich Kohlenstoffnanoröhren, Graphen und 2DPs beschäftigen. Im ersten Teil entwickelten wir eine kontrollierte, reproduzierbare, milde und kovalente Funktionalisierung von Graphen in einer *one pot*-Reaktion unter Verwendung von Triazine und Natriumazid. Hierbei wird ein Dichlortriazin-Intermediat erzeugt, dass eine selektive und kontrollierte Modifizierung des Graphens durch Substitution mit den reaktiven Chlorsubstituenten des Triazines ermöglicht. Die unterschiedlichen Reaktivitäten dieser Chlorsubstituenten ermöglichen die schrittweise Postmodifizierung des Graphens durch Variation der Reaktionstemperaturen im Bereich von 25 °C bis 65 °C. Als Produkte wurden definierte, bifunktionelle 2D Nanomaterialien (Graphen) erhalten, welche mit hochverzweigten Polyglycerol (hPG) kontrolliert, stufenweise modifiziert werden konnten. Im zweiten Teil beabsichtigten wir eine neuartige, nicht-destruktive Synthesemethode zur kovalenten Funktionalisierung von Kohlenstoffnanoröhren zu designen and zu etablieren. Entdeckt haben wir eine einzigartige, nicht-destruktive Methode zur kovalenten Funktionalisierung von Kohlenstoffnanoröhren im Gramm-Maßstab, die über eine Nitrenbasierte [2+1]-Cycloaddition verläuft. Diese Methode erreicht bei Kohlenstoffnanoröhrchen mit dem Dichlorotriazine-Intermediat eine Dichlorotriazine-Funktionalisierung und stellt das konjugierte π-System wieder her, sodass die optoelektronischen Eigenschaften der Kohlenstoffnanoröhren erhalten bleiben.

Im Rahmen des dritten Projekts, wurde eine neue Synthesemethode für zweidimensionale Polymere durch kontrolliertes Wachstum in Lösung entwickelt und verbessert. Dazu haben wir eine metallassistierte und lösungsmitteldirigierende Methode eingeführt, in der Calciumcarbid und Triazine als Monomere und DMF als Lösungsmittel dienen. Das kontrollierte, zweidimensionale Wachstum konnte durch die Calciumionen aus Calciumcarbid gesteuert werden und lieferte 2DTHs mit amorphen Strukturen. Die Calciumionen koordinieren über Ligand-Metall-Wechselwirkungen an die Stickstoffatome der Triazingruppen, wodurch die Bindungsrotationen verhindert werden und eine ausreichende Festigkeit der gewünschten 2D Struktur erreicht wird. Darüber hinaus haben wir die chemische Struktur, die physikochemischen Eigenschaften und die zugrundeliegenden Reaktionsmechanismen der 2D Strukturen untersucht. Der Wassergehalt im Reaktionsmedium stellte sich hierbei als bedeutender Faktor heraus, da er einen bedeutenden Einfluss auf die Struktur des Produkts hatte. Während reine 2DTHs unter wasserfreien Bedingungen erhalten wurden, war es durch die Erhöhung des Wassergehalts im Reaktionsmedium möglich, Graphen/2DTHs-Mischungen oder sogar reines Graphen zu erhalten. In Anbetracht der effizienten, skalierbaren Synthese, des Fluoreszenzverhaltens, sowie der photothermischen und photodynamischen Eigenschaften stellen die erhaltenen zweidimensionale Triazine-Heterostrukturen ein vielversprechendes Material für zahlreiche potenzielle Anwendungen in der Zukunft dar.

6 References

[1] S. Nasir, M. Z. Hussein, Z. Zainal, N. A. Yusof, *Materials* **2018**, *11*, 295-319.

[2] G. A. Csáthy, J. K. Jain, *Nat. Phys* **2019**.

[3] R. Hoffmann, A. A. Kabanov, A. A. Golov, D. M. Proserpio, *Angew. Chem. Int. Ed.* **2016**, *55*, 10962-10976.

[4] A. Balaban, C. C. Rentia, E. Ciupitu, *Rev Roum Chim* **1968**, *13*, 231.

[5] Q.-S. Du, P.-D. Tang, H.-L. Huang, F.-L. Du, K. Huang, N.-Z. Xie, S.-Y. Long, Y.-M. Li, J.-S. Qiu, R.-B. Huang, *Sci. Rep.* **2017**, *7*, 40796-40807.

[6] R. Totani, C. Grazioli, T. Zhang, I. Bidermane, J. Lüder, M. de Simone, M. Coreno, B. Brena, L. Lozzi, C. Puglia, *J. Chem. Phys.* **2017**, *146*, 054705-054712.

[7] Z. Shunhong, Z. Jian, W. Qian, C. Xiaoshuang, K. Yoshiyuki, J. Puru, *Радиоэлектроника. Наносистемы. Информационные технологии* **2015**, *7*.

[8] O. Rahaman, B. Mortazavi, A. Dianat, G. Cuniberti, T. Rabczuk, *FlatChem* **2017**, *1*, 65-73.

[9] M.-Q. Le, *Comput. Mater. Sci.* **2017**, *136*, 181-190.

[10] J.-W. Jiang, J. Leng, J. Li, Z. Guo, T. Chang, X. Guo, T. Zhang, *Carbon* **2017**, *118*, 370-375.

[11] Y.-Q. Zhang, N. Kepčija, M. Kleinschrodt, K. Diller, S. Fischer, A. C. Papageorgiou, F. Allegretti, J. Björk, S. Klyatskaya, F. Klappenberger, *Nat. Commun.* **2012**, *3*, 1286-1294.

[12] G. Li, Y. Li, H. Liu, Y. Guo, Y. Li, D. Zhu, *Chem.Comm.* **2010**, *46*, 3256-3258.

[13] M. M. Haley, S. C. Brand, J. J. Pak, *Angew. Chem. Int. Ed.* **1997**, *36*, 836-838.

[14] Z. Wang, X.-F. Zhou, X. Zhang, Q. Zhu, H. Dong, M. Zhao, A. R. Oganov, *Nano Lett.* **2015**, *15*, 6182-6186.

[15] L. F. C. Pereira, B. Mortazavi, M. Makaremi, T. Rabczuk, *RSC Adv.* **2016**, *6*, 57773-57779.

[16] H. Sun, S. Mukherjee, C. V. Singh, *Phys. Chem. Chem. Phys.* **2016**, *18*, 26736-26742.

[17] N. Yedla, P. Gupta, T. Y. Ng, K. Geethalakshmi, *Mater. Chem. Phys.* **2017**, *202*, 127-135.

[18] M. A. Hudspeth, B. W. Whitman, V. Barone, J. E. Peralta, *ACS nano* **2010**, *4*, 4565-4570.

[19] M.-J. Sun, X. Cao, Z. Cao, *ACS Appl. Mater. Interfaces* **2016**, *8*, 16551-16554.

[20] Y. Chen, K. Fu, S. Zhu, W. Luo, Y. Wang, Y. Li, E. Hitz, Y. Yao, J. Dai, J. Wan, V. A. Danner, T. Li, L. Hu, *Nano Lett.* **2016**, *16*, 3616-3623.

[21] S. K. Krishnan, E. Singh, P. Singh, M. Meyyappan, H. S. Nalwa, *RSC Adv.* **2019**, *9*, 8778-8881.

[22] K. S. Novoselov, A. K. Geim, S. V. Morozov, D. Jiang, Y. Zhang, S. V. Dubonos, I. V. Grigorieva, A. A. Firsov, *science* **2004**, *306*, 666-669.

[23] A. Dato, *Mater. Res.* **2019**, *34*, 214-230.

[24] M. J. Allen, V. C. Tung, R. B. Kaner, *Chem. Rev.* **2009**, *110*, 132-145.

[25] S. Park, R. S. Ruoff, *Nat. Nanotechnol.* **2009**, *4*, 217-224.

[26] C. Lee, X. Wei, J. W. Kysar, J. Hone, *science* **2008**, *321*, 385-388.

[27] A. A. Balandin, *Nat. mater.* **2011**, *10*, 569-589.

[28] A. S. Mayorov, R. V. Gorbachev, S. V. Morozov, L. Britnell, R. Jalil, L. A. Ponomarenko, P. Blake, K. S. Novoselov, K. Watanabe, T. Taniguchi, *Nano lett.* **2011**, *11*, 2396-2399.

[29] M. Terrones, *Int. Mater. Rev.* **2004**, *49*, 325-377.

[30] P. Avouris, M. Freitag, V. Perebeinos, *Nat. Photonics* **2008**, *2*, 341-350.

[31] F. Wang, G. Dukovic, L. E. Brus, T. F. Heinz, *Science* **2005**, *308*, 838-841.

[32] A. Sharma, V. Singh, T. L. Bougher, B. A. Cola, *Nat. nanotechnol.* **2015**, *10*, 1027-1032.

[33] S. Y. Hong, G. Tobias, K. T. Al-Jamal, B. Ballesteros, H. Ali-Boucetta, S. Lozano-Perez, P. D. Nellist, R. B. Sim, C. Finucane, S. J. Mather, *Nat. mater.* **2010**, *9*, 485-490.

[34] M. Mihajlovic, M. Mihajlovic, P. Y. W. Dankers, R. Masereeuw, R. P. Sijbesma, *Macromol. Biosci.* **2019**, *19*, 1800173-1800185.

[35] A. K. Geim, K. S. Novoselov, *Nat. Mater.* **2007**, *6*, 183-191.

[36] J. L. Bahr, E. T. Mickelson, M. J. Bronikowski, R. E. Smalley, J. M. Tour, *Chem.Commun.* **2001**, 193-194.

[37] F. Tournus, S. Latil, M. Heggie, J.-C. Charlier, *Phys. Rev. B* **2005**, *72*, 075431-075436.

[38] E. M. Pérez, N. Martín, *Chem. Soc. Rev.* **2015**, *44*, 6425-6433.

[39] A. T. Lawal, *Mater Res Bull* **2016**, *73*, 308-350.

[40] J. H. Ahn, J.-H. Kim, N. F. Reuel, P. W. Barone, A. A. Boghossian, J. Zhang, H. Yoon, A. C. Chang, A. J. Hilmer, M. S. Strano, *Nano lett.* **2011**, *11*, 2743-2752.

[41] C. M. Tîlmaciu, M. C. Morris, *Front Chem* **2015**, *3*, 59-80.

[42] R. V. Mundra, X. Wu, J. Sauer, J. S. Dordick, R. S. Kane, *Curr Opinn Biotech* **2014**, *28*, 25-32.

[43] C. F. Blanford, C. E. Foster, R. S. Heath, F. A. Armstrong, *Faraday Disuss* **2009**, *140*, 319-335.

[44] M. G. Bellino, G. J. Soler- Illia, *small* **2014**, *10*, 2834-2839.

[45] K. Besteman, J.-O. Lee, F. G. Wiertz, H. A. Heering, C. Dekker, *Nano lett.* **2003**, *3*, 727-730.

[46] S. J. Aravind, S. Ramaprabhu, *Sensor Actuat B-Chem* **2011**, *155*, 679-686.

[47] Y.-L. Zhao, J. F. Stoddart, *Acc. Chem. Res.* **2009**, *42*, 1161-1171.

[48] C. Gao, Z. Guo, J.-H. Liu, X.-J. Huang, *Nanoscale* **2012**, *4*, 1948-1963.

[49] R. J. Chen, S. Bangsaruntip, K. A. Drouvalakis, N. W. S. Kam, M. Shim, Y. Li, W. Kim, P. J. Utz, H. Dai, *PNAS* **2003**, *100*, 4984-4989.

[50] X. Wang, H. Wang, Y. Huang, Z. Zhao, X. Qin, Y. Wang, Z. Miao, Q. Chen, M. Qiao, *Biosens. Bioelectron* **2010**, *26*, 1104-1108.

[51] R. Haddad, S. Cosnier, A. Maaref, M. Holzinger, *Analyst* **2009**, *134*, 2412-2418.

[52] M. Holzinger, J. Baur, R. Haddad, X. Wang, S. Cosnier, *Chem. Commun.* **2011**, *47*, 2450-2452.

[53] M. Holzinger, L. Bouffier, R. Villalonga, S. Cosnier, *Biosens. Bioelectron* **2009**, *24*, 1128-1134.

[54] L. Zhu, R. Yang, J. Zhai, C. Tian, *Biosens. Bioelectron* **2007**, *23*, 528-535.

[55] R. Cui, H. Huang, Z. Yin, D. Gao, J.-J. Zhu, *Biosens. Bioelectron* **2008**, *23*, 1666-1673.

[56] A. Setaro, *Journal of Physics: Condens Matter* **2017**, *29*, 423003-423023.

[57] S. Ryu, M. Y. Han, J. Maultzsch, T. F. Heinz, P. Kim, M. L. Steigerwald, L. E. Brus, *Nano lett.* **2008**, *8*, 4597-4602.

[58] D. e. Jiang, B. G. Sumpter, S. Dai, *J. Chem. Phys.* **2007**, *126*, 134701-134708.

[59] S. Niyogi, M. Hamon, H. Hu, B. Zhao, P. Bhowmik, R. Sen, M. Itkis, R. Haddon, *Accounts Chem Res* **2002**, *35*, 1105-1113.

[60] T. Kuila, S. Bose, A. K. Mishra, P. Khanra, N. H. Kim, J. H. Lee, *Prog Mater Sci* **2012**, *57*, 1061-1105.

[61] T. Kuila, S. Bose, C. E. Hong, M. E. Uddin, P. Khanra, N. H. Kim, J. H. Lee, *Carbon* **2011**, *49*, 1033-1037.

[62] C. Shan, H. Yang, D. Han, Q. Zhang, A. Ivaska, L. Niu, *Langmuir* **2009**, *25*, 12030-12033.

[63] H. Yang, C. Shan, F. Li, D. Han, Q. Zhang, L. Niu, *Chem. Commun.* **2009**, 3880-3882.

[64] H. Bao, Y. Pan, Y. Ping, N. G. Sahoo, T. Wu, L. Li, J. Li, L. H. Gan, *Small* **2011**, *7*, 1569-1578.

[65] A. Lerf, H. He, M. Forster, J. Klinowski, *J. Phys. Chem. B* **1998**, *102*, 4477-4482.

[66] S. Park, R. S. Ruoff, *Nat. Nanotechnol.* **2009**, *4*, 217-224.

[67] V. Georgakilas, M. Otyepka, A. B. Bourlinos, V. Chandra, N. Kim, K. C. Kemp, P. Hobza, R. Zboril, K. S. Kim, *Chem. Rev.* **2012**, *112*, 6156-6214.

[68] W. Gao, L. B. Alemany, L. Ci, P. M. Ajayan, *Nat. Chem.* **2009**, *1*, 403-480.

[69] I. Coldham, R. Hufton, *Chem. Rev.* **2005**, *105*, 2765-2810.

[70] C. K. Chua, M. Pumera, *Chem. Soc. Rev.* **2013**, *42*, 3222-3233.

[71] G. Sakellariou, H. Ji, J. W. Mays, N. Hadjichristidis, D. Baskaran, *Chem. Mater.* **2007**, *19*, 6370-6372.

[72] I. Kumar, S. Rana, J. W. Cho, *Chem. Eur. J.* **2011**, *17*, 11092-11101.

[73] C. Gao, H. He, L. Zhou, X. Zheng, Y. Zhang, *Chem. Mater.* **2008**, *21*, 360-370.

[74] M. Holzinger, O. Vostrowsky, A. Hirsch, F. Hennrich, M. Kappes, R. Weiss, F. Jellen, *Angew. Chem. Int. Ed.* **2001**, *40*, 4002-4005.

[75] J. Choi, K.-j. Kim, B. Kim, H. Lee, S. Kim, *J. Phys. Chem. C* **2009**, *113*, 9433-9435.

[76] S. J. Pastine, D. Okawa, B. Kessler, M. Rolandi, M. Llorente, A. Zettl, J. M. Fréchet, *J. Am. Chem. Soc.* **2008**, *130*, 4238-4239.

[77] J. Park, M. Yan, *Accounts Chem Res* **2012**, *46*, 181-189.

[78] J. F. Keana, S. X. Cai, *J. Org. Chem.* **1990**, *55*, 3640-3647.

[79] S. X. Cai, J. Nabity, M. Wybourne, J. F. Keana, *Chem. Mater.* **1990**, *2*, 631-633.

[80] L.-H. Liu, M. M. Lerner, M. Yan, *Nano Lett.* **2010**, *10*, 3754-3756.

[81] M. Holzinger, O. Vostrowsky, A. Hirsch, F. Hennrich, M. Kappes, R. Weiss, F. Jellen, *Angew. Chem. Int. Ed.* **2001**, *113*, 4132-4136.

[82] M. Holzinger, J. Abraham, P. Whelan, R. Graupner, L. Ley, F. Hennrich, M. Kappes, A. Hirsch, *J. Am. Chem. Soc.* **2003**, *125*, 8566-8580.

[83] E. Cho, H. Kim, C. Kim, S. Han, *Chem. Phys. Lett.* **2006**, *419*, 134-138.

[84] H. F. Bettinger, *Chem. Eur. J.* **2006**, *12*, 4372-4379.

[85] X. Lu, F. Tian, Q. Zhang, *J. Phys. Chem. B* **2003**, *107*, 8388-8391.

[86] A. Hirsch, *Top Curr Chem* **2005**, *245*, 193-237.

[87] X. Zhong, J. Jin, S. Li, Z. Niu, W. Hu, R. Li, J. Ma, *Chem.Commun.* **2010**, *46*, 7340-7342.

[88] M. Kanungo, H. Lu, G. G. Malliaras, G. B. Blanchet, *Science* **2009**, *323*, 234-237.

[89] C. M. Rosser, S. C. Coote, J. P. Kirby, P. O'Brien, D. Caine, *Org. Lett.* **2004**, *6*, 4817-4819.

[90] A. G. Nasibulin, P. V. Pikhitsa, H. Jiang, D. P. Brown, A. V. Krasheninnikov, A. S. Anisimov, P. Queipo, A. Moisala, D. Gonzalez, G. Lientschnig, *Nat. Nanotechnol.* **2007**, *2*, 156-161.

[91] M. A. Hamon, K. L. Stensaas, M. A. Sugar, K. C. Tumminello, A. K. Allred, *Chem. Phys. Lett.* **2007**, *447*, 1-4.

[92] Y.-f. Zhang, Z.-f. Liu, *J. Phys. Chem. B* **2004**, *108*, 11435-11441.

[93] V. Georgakilas, A. B. Bourlinos, R. Zboril, T. A. Steriotis, P. Dallas, A. K. Stubos, C. Trapalis, *Chem. Commun.* **2010**, *46*, 1766-1768.

[94] J. L. Delgado, P. de la Cruz, F. Langa, A. Urbina, J. Casado, J. T. L. Navarrete, *Chem. Commun.* **2004**, 1734-1735.

[95] X. Lu, F. Tian, N. Wang, Q. Zhang, *Org. lett.* **2002**, *4*, 4313-4315.

[96] L. Zhang, J. Yang, C. L. Edwards, L. B. Alemany, V. N. Khabashesku, A. R. Barron, *Chem. Commun.* **2005**, 3265-3267.

[97] C. Ménard-Moyon, F. Dumas, E. Doris, C. Mioskowski, *J. Am. Chem. Soc.* **2006**, *128*, 14764-14765.

[98] S. Sarkar, E. Bekyarova, S. Niyogi, R. C. Haddon, *J. Am. Chem. Soc.* **2011**, *133*, 3324-3327.

[99] M. J. O'connell, S. M. Bachilo, C. B. Huffman, V. C. Moore, M. S. Strano, E. H. Haroz, K. L. Rialon, P. J. Boul, W. H. Noon, C. Kittrell, *Science* **2002**, *297*, 593-596.

[100] Y. Wu, Y.-m. Lin, A. A. Bol, K. A. Jenkins, F. Xia, D. B. Farmer, Y. Zhu, P. Avouris, *Nature* **2011**, *472*, 74-78.

[101] I. Gierz, C. Riedl, U. Starke, C. R. Ast, K. Kern, *Nano Lett.* **2008**, *8*, 4603-4607.

[102] G. Gordeev, A. Setaro, M. Glaeske, S. Jürgensen, S. Reich, *Phys Status Solidi B* **2016**, *253*, 2461-2467.

[103] Y. Piao, B. Meany, L. R. Powell, N. Valley, H. Kwon, G. C. Schatz, Y. Wang, *Nat. chem.* **2013**, *5*, 840-845.

[104] S. Mallakpour, A. Abdolmaleki, S. Borandeh, *Appl. Surf. Sci.* **2014**, *307*, 533-542.

[105] J. Zhang, H. Yang, G. Shen, P. Cheng, J. Zhang, S. Guo, *Chem. Commun.* **2010**, *46*, 1112-1114.

[106] R. K. Singh, R. Kumar, D. P. Singh, *RSC Adv.* **2016**, *6*, 64993-65011.

[107] T. S. Sreeprasad, V. Berry, *Small* **2013**, *9*, 341-350.

[108] A. B. Kaiser, C. Gómez-Navarro, R. S. Sundaram, M. Burghard, K. Kern, *Nano Lett.* **2009**, *9*, 1787-1792.

[109] M. S. Platz, *Acc. Chem. Res.* **1995**, *28*, 487-492.

[110] J. Li, G. Jia, Y. Zhang, Y. Chen, *Chem. Mater.* **2006**, *18*, 3579-3584.

[111] Y.-S. Lee, N. Marzari, *Phys. Rev. Lett.* **2006**, *97*, 116801-116805.

[112] K. Zhang, Q. Zhang, C. Liu, N. Marzari, F. Stellacci, *Adv. Funct. Mater.* **2012**, *22*, 5216-5223.

[113] A. Setaro, M. Adeli, M. Glaeske, D. Przyrembel, T. Bisswanger, G. Gordeev, F. Maschietto, A. Faghani, B. Paulus, M. Weinelt, *Nat. commun.* **2017**, *8*, 14281-14288.

[114] G. Guday, I. S. Donskyi, M. F. Gholami, G. Algara- Siller, F. Witte, A. Lippitz, W. E. Unger, B. Paulus, J. P. Rabe, M. Adeli, *Small* **2019**, 1805430-1805438.

[115] Z. Tu, H. Qiao, Y. Yan, G. Guday, W. Chen, M. Adeli, R. Haag, *Angew. Chem. Int. Ed.* **2018**, *130*, 11368-11372.

[116] Z. Tu, K. Achazi, A. Schulz, R. Mülhaupt, S. Thierbach, E. Rühl, M. Adeli, R. Haag, *Adv. Funct. Mater.* **2017**, *27*, 1701837-1701848.

[117] K. H. Tan, S. Sattari, I. S. Donskyi, J. L. Cuellar-Camacho, C. Cheng, K. Schwibbert, A. Lippitz, W. E. Unger, A. Gorbushina, M. Adeli, *Nanoscale* **2018**, *10*, 9525-9537.

[118] M. F. Gholami, D. Lauster, K. Ludwig, J. Storm, B. Ziem, N. Severin, C. Böttcher, J. P. Rabe, A. Herrmann, M. Adeli, *Adv. Funct. Mater.* **2017**, *27*, 1606477-1606489.

[119] Z. Beiranvand, A. Kakanejadifard, I. Donskyi, A. Faghani, Z. Tu, A. Lippitz, P. Sasanpour, F. Maschietto, B. Paulus, W. Unger, *RSC Adv.* **2016**, *6*, 112771-112775.

[120] B. Ziem, J. Rahn, I. Donskyi, K. Silberreis, L. Cuellar, J. Dernedde, G. Keil, T. C. Mettenleiter, R. Haag, *Macromol. Biosci.* **2017**, *17*, 1600499-1600508.

[121] B. Ziem, H. Thien, K. Achazi, C. Yue, D. Stern, K. Silberreis, M. F. Gholami, F. Beckert, D. Gröger, R. Mülhaupt, *Adv Healthc Mater* **2016**, *5*, 2922-2930.

[122] I. S. Donskyi, K. Achazi, V. Wycisk, K. Licha, M. Adeli, R. Haag, *Langmuir* **2017**, *33*, 6595-6600.

[123] B. Ziem, W. Azab, M. Gholami, J. Rabe, N. Osterrieder, R. Haag, *Nanoscale* **2017**, *9*, 3774-3783.

[124] I. Donskyi, M. Drüke, K. Silberreis, D. Lauster, K. Ludwig, C. Kühne, W. Unger, C. Böttcher, A. Herrmann, J. Dernedde, *Small* **2018**, *14*, 1800189-1800196.

[125] H. Staudinger, *Berichte der deutschen chemischen Gesellschaft (A and B Series)* **1920**, *53*, 1073-1085.

[126] R. Mülhaupt, *Angew. Chem. Int. Ed.* **2004**, *43*, 1054-1063.

[127] M. Servalli, A. D. Schlüter, *Annu. Rev. Mater. Sci.* **2017**, *47*, 361-389.

[128] P. Miró, M. Audiffred, T. Heine, *Chem. Soc. Rev.* **2014**, *43*, 6537-6554.

[129] M. M. Ugeda, A. J. Bradley, S.-F. Shi, H. Felipe, Y. Zhang, D. Y. Qiu, W. Ruan, S.-K. Mo, Z. Hussain, Z.-X. Shen, *Nat. mater.* **2014**, *13*, 1091-1095.

[130] A. A. Balandin, S. Ghosh, W. Bao, I. Calizo, D. Teweldebrhan, F. Miao, C. N. Lau, *Nano lett.* **2008**, *8*, 902-907.

[131] X. Li, H. Zhu, *J. Materiomics.* **2015**, *1*, 33-44.

[132] S. J. Kim, K. Choi, B. Lee, Y. Kim, B. H. Hong, *Annu. Rev. Mater. Sci.* **2015**, *45*, 63-84.

[133] A. Reina, X. Jia, J. Ho, D. Nezich, H. Son, V. Bulovic, M. S. Dresselhaus, J. Kong, *Nano lett.* **2008**, *9*, 30-35.

[134] Y. H. Lee, X. Q. Zhang, W. Zhang, M. T. Chang, C. T. Lin, K. D. Chang, Y. C. Yu, J. T. W. Wang, C. S. Chang, L. J. Li, *Adv. Mater.* **2012**, *24*, 2320-2325.

[135] J. Yu, J. Li, W. Zhang, H. Chang, *Chem. Sci.* **2015**, *6*, 6705-6716.

[136] K. Novoselov, D. Jiang, F. Schedin, T. Booth, V. Khotkevich, S. Morozov, A. Geim, *PNAS* **2005**, *102*, 10451-10453.

[137] G. Liu, N. Komatsu, *ChemPhysChem* **2016**, *17*, 1557-1567.

[138] M. Jedrzejczak-Silicka, M. Trukawka, M. Dudziak, K. Piotrowska, E. Mijowska, *Nanomaterials* **2018**, *8*, 605-627.

[139] C. Du, M. Li, M. Cao, S. Song, S. Feng, X. Li, H. Guo, B. Li, *ACS Appl. Mater. Interfaces* **2018**, *10*, 34674-34682.

[140] P. A. Denis, *Phys. Chem. Chem. Phys.* **2015**, *17*, 5393-5402.

[141] C. Sun, Y. Wang, Y. Jiang, Z.-D. Yang, G. Zhang, Y. Hu, *New J Chem* **2019**, *43*, 377-385.

[142] J. M. Englert, C. Dotzer, G. Yang, M. Schmid, C. Papp, J. M. Gottfried, H.-P. Steinrück, E. Spiecker, F. Hauke, A. Hirsch, *Nat. Chem.* **2011**, *3*, 279-286.

[143] G. Gee, E. K. Rideal, *Proceedings of the Royal Society of London. Series A-Mathematical and Physical Sciences* **1935**, *153*, 116-128.

[144] G. Gee, *Proceedings of the Royal Society of London. Series A-Mathematical and Physical Sciences* **1935**, *153*, 129-141.

[145] J. Sakamoto, J. van Heijst, O. Lukin, A. D. Schlüter, *Angew. Chem. Int. Ed.* **2009**, *48*, 1030-1069.

[146] S. Stupp, S. Son, L. Li, H. Lin, M. Keser, *J. Am. Chem. Soc.* **1995**, *117*, 5212-5227.

[147] J. Michl, T. F. Magnera, *PNAS* **2002**, *99*, 4788-4792.

[148] P. Kissel, R. Erni, W. B. Schweizer, M. D. Rossell, B. T. King, T. Bauer, S. Götzinger, A. D. Schlüter, J. Sakamoto, *Nat. chem.* **2012**, *4*, 287-291.

[149] J. W. Colson, W. R. Dichtel, *Nat. chem.* **2013**, *5*, 453-465.

[150] Y. Zang, T. Aoki, M. Teraguchi, T. Kaneko, L. Ma, H. Jia, *Poly. Rev.* **2015**, *55*, 57-89.

[151] D. Rodriguez-San-Miguel, P. Amo-Ochoa, F. Zamora, *Chem. Commun.* **2016**, *52*, 4113-4127.

[152] P. Kissel, D. J. Murray, W. J. Wulftange, V. J. Catalano, B. T. King, *Nat. Chem.* **2014**, *6*, 774-778.

[153] M. Servalli, *CHIMIA* **2017**, *71*, 359-368.

[154] G. Blotny, *Tetrahedron* **2006**, *62*, 9507-9522.

[155] M. B. Steffensen, E. Hollink, F. Kuschel, M. Bauer, E. E. Simanek, *J Polym Sci Pol Chem* **2006**, *44*, 3411-3433.

[156] H. Duan, L. Wang, D. Qin, X. Li, S. Wang, Y. Zhang, *ynth. Commun.* **2011**, *41*, 380-384.

[157] T.-Y. Zhou, F. Lin, Z.-T. Li, X. Zhao, *Macromolecules* **2013**, *46*, 7745-7752.

[158] H. Yu, D. T. L. Alexander, U. Aschauer, R. Häner, *Angew. Chem. Int. Ed.* **2017**, *56*, 5040-5044.

[159] K. Baek, G. Yun, Y. Kim, D. Kim, R. Hota, I. Hwang, D. Xu, Y. H. Ko, G. H. Gu, J. H. Suh, C. G. Park, B. J. Sung, K. Kim, *J. Am. Chem. Soc.* **2013**, *135*, 6523-6528.

[160] D. Kim, E. Kim, J. Lee, S. Hong, W. Sung, N. Lim, C. G. Park, K. Kim, *J. Am. Chem. Soc.* **2010**, *132*, 9908-9919.

[161] T. Y. Zhou, Q.-Y. Qi, Q.-L. Zhao, J. Fu, Y. Liu, Z. Ma, X. Zhao, *Poly. Chem.* **2015**, *6*, 3018-3023.

[162] S. Q. Xu, X. Zhang, C.-B. Nie, Z.-F. Pang, X.-N. Xu, X. Zhao, *Chem. Commun.* **2015**, *51*, 16417-16420.

[163] M. Vybornyi, Y. Bur-Cecilio Hechevarria, M. Glauser, A. V. Rudnev, R. Häner, *Chem. Commun.* **2015**, *51*, 16191-16193.

[164] C. Grivas, C. Li, P. Andreakou, P. Wang, M. Ding, G. Brambilla, L. Manna, P. Lagoudakis, *Nat. Commun.* **2013**, *4*, 2376-2385.

[165] D. Sheberla, L. Sun, M. A. Blood-Forsythe, S. Er, C. R. Wade, C. K. Brozek, A. Aspuru-Guzik, M. Dincă, *J. Am. Chem. Soc.* **2014**, *136*, 8859-8862.

[166] R. Dong, Z. Zheng, D. C. Tranca, J. Zhang, N. Chandrasekhar, S. Liu, X. Zhuang, G. Seifert, X. Feng, *Chem. Eur. J.* **2017**, *23*, 2234-2234.

[167] P. Puthiaraj, Y.-R. Lee, S. Zhang, W.-S. Ahn, ***J***. *Mater. Chem. A* **2016**, *4*, 16288-16311.

[168] P. Kuhn, M. Antonietti, A. Thomas, *Angew. Chem. Int. Ed.* **2008**, *47*, 3450-3453.

[169] M. G. Schwab, B. Fassbender, H. W. Spiess, A. Thomas, X. Feng, K. Müllen, *J. Am. Chem. Soc.* **2009**, *131*, 7216-7217.

[170] M. X. Tan, Y. N. Sum, J. Y. Ying, Y. Zhang, *Energ Environ Sci* **2013**, *6*, 3254-3259.

[171] A. Modak, M. Pramanik, S. Inagaki, A. Bhaumik, *J. Mater. Chem. A* **2014**, *2*, 11642-11650.

[172] S. Ren, R. Dawson, A. Laybourn, J.-x. Jiang, Y. Khimyak, D. J. Adams, A. I. Cooper, *Poly. Chem.* **2012**, *3*, 928-934.

[173] Z. Xiang, D. Cao, L. Huang, J. Shui, M. Wang, L. Dai, *Adv. Mater.* **2014**, *26*, 3315-3320.

[174] P. Puthiaraj, S.-S. Kim, W.-S. Ahn, *Chem Eng J* **2016**, *283*, 184-192.

[175] X. Zhu, S. M. Mahurin, S.-H. An, C.-L. Do-Thanh, C. Tian, Y. Li, L. W. Gill, E. W. Hagaman, Z. Bian, J.-H. Zhou, J. Hu, H. Liu, S. Dai, *Chem.Commun.* **2014**, *50*, 7933-7936.

[176] W. Huang, J. H.-C. Liu, P. Alayoglu, Y. Li, C. A. Witham, C.-K. Tsung, F. D. Toste, G. A. Somorjai, *J. Am. Chem. Soc.* **2010**, *132*, 16771-16773.

[177] A. M. Stemig, T. A. Do, V. M. Yuwono, W. A. Arnold, R. L. Penn, *Environ. Sci. Nano.* **2014**, *1*, 478-487.

[178] I. Langmuir, *J. Am. Chem. Soc.* **1917**, *39*, 1848-1906.

[179] I. Langmuir, *J. Chem. Soc. Faraday Trans.* **1920**, *15*, 62-74.

[180] P. Payamyar, K. Kaja, C. Ruiz- Vargas, A. Stemmer, D. J. Murray, C. J. Johnson, B. T. King, F. Schiffmann, J. VandeVondele, A. Renn, *Adv. Mater.* **2014**, *26*, 2052-2058.

[181] T. Kunitake, in *Macromolecular Symposia, Vol. 98*, Wiley Online Library, **1995**, pp. 45-51.

[182] F. Porteu, S. Palacin, A. Ruaudel- Teixier, A. Barraud, in *Makromolekulare Chemie. Macromolecular Symposia, Vol. 46*, Wiley Online Library, **1991**, pp. 37-45.

[183] R. Sakamoto, K. Hoshiko, Q. Liu, T. Yagi, T. Nagayama, S. Kusaka, M. Tsuchiya, Y. Kitagawa, W.-Y. Wong, H. Nishihara, *Nat. commun.* **2015**, *6*, 6713-7622.

[184] R. Dong, M. Pfeffermann, H. Liang, Z. Zheng, X. Zhu, J. Zhang, X. Feng, *Angew. Chem. Int. Ed.* **2015**, *54*, 12058-12063.

[185] H. Sahabudeen, H. Qi, B. A. Glatz, D. Tranca, R. Dong, Y. Hou, T. Zhang, C. Kuttner, T. Lehnert, G. Seifert, *Nat. commun.* **2016**, *7*, 13461-13469.

[186] D. J. Murray, D. D. Patterson, P. Payamyar, R. Bhola, W. Song, M. Lackinger, A. D. Schlüter, B. T. King, *J. Am. Chem. Soc.* **2015**, *137*, 3450-3453.

[187] M. Cohen, G. Schmidt, *J. Chem. Soc.* **1964**, 1996-2000.

[188] R. Z. Lange, G. Hofer, T. Weber, A. D. Schlüter, *J. Am. Chem. Soc.* **2017**, *139*, 2053-2059.

[189] K. Novak, V. Enkelmann, G. Wegner, K. B. Wagener, *Angew. Chem. Int. Ed* **1993**, *32*, 1614-1616.

[190] R. Bhola, P. Payamyar, D. J. Murray, B. Kumar, A. J. Teator, M. U. Schmidt, S. M. Hammer, A. Saha, J. Sakamoto, A. D. Schlüter, *J. Am. Chem. Soc.* **2013**, *135*, 14134-14141.

[191] S.-Y. Ding, W. Wang, *Chem. Soc. Rev.* **2013**, *42*, 548-568.

[192] X. Feng, X. Ding, D. Jiang, *Chem. Soc. Rev.* **2012**, *41*, 6010-6022.

[193] A. P. Cote, A. I. Benin, N. W. Ockwig, M. O'keeffe, A. J. Matzger, O. M. Yaghi, *science* **2005**, *310*, 1166-1170.

[194] J. W. Colson, A. R. Woll, A. Mukherjee, M. P. Levendorf, E. L. Spitler, V. B. Shields, M. G. Spencer, J. Park, W. R. Dichtel, *Science* **2011**, *332*, 228-231.

[195] C. Gianelli, L. Sambri, A. Carlone, G. Bartoli, P. Melchiorre, *Angew. Chem. Int. Ed.* **2008**, *120*, 8828-8830.

[196] S. J. Rowan, S. J. Cantrill, G. R. Cousins, J. K. Sanders, J. F. Stoddart, *Angew. Chem. Int. Ed.* **2002**, *41*, 898-952.

[197] Y. Jin, C. Yu, R. J. Denman, W. Zhang, *Chem. Soc. Rev.* **2013**, *42*, 6634-6654.

[198] D. N. Bunck, W. R. Dichtel, *J. Am. Chem. Soc.* **2013**, *135*, 14952-14955.

[199] I. Berlanga, M. L. Ruiz- González, J. M. González- Calbet, J. L. G. Fierro, R. Mas-Ballesté, F. Zamora, *Small* **2011**, *7*, 1207-1211.

[200] W. Dai, F. Shao, J. Szczerbiński, R. McCaffrey, R. Zenobi, Y. Jin, A. D. Schlüter, W. Zhang, *Angew. Chem. Int. Ed.* **2016**, *55*, 213-217.

[201] T. Bauer, Z. Zheng, A. Renn, R. Enning, A. Stemmer, J. Sakamoto, A. D. Schlüter, *Angew. Chem. Int. Ed.* **2011**, *50*, 7879-7884.

[202] R. Matake, Y. Niwa, H. Matsubara, *Org. Lett.* **2015**, *17*, 2354-2357.

[203] K. S. Rodygin, G. Werner, F. A. Kucherov, V. P. Ananikov, *Chem. Asian J.* **2016**, *11*, 965-976.

[204] W. Zhang, H. Wu, Z. Liu, P. Zhong, L. Zhang, X. Huang, J. Cheng, *Chem.Commun.* **2006**, 4826-4828.

[205] Y. Jia, X. Chen, G. Zhang, L. Wang, C. Hu, X. Sun, *J. Mater. Chem. A* **2018**, *6*, 23638-23643.

[206] M. E. Casco, S. Kirchhoff, D. Leistenschneider, M. Rauche, E. Brunner, L. Borchardt, *Nanoscale* **2019**, *11*, 4712-4718.

[207] D. Matochová, M. Medved', A. Bakandritsos, T. Steklý, R. Zbořil, M. Otyepka, *J. Phys. Chem. Lett.* **2018**, *9*, 3580-3585.

7 Appendix

7.1 Publications and contributions

Publications

1. **A. Faghani**, Mohammad Fardin Gholami, M. Trunk, P. Pachfule, J. Müller, P. Nickl, J. Shao, A. Setaro, W. E. S. Unger, R. Arenal, S. Reich, C. T. Koch, B. Paulus, J. P. Rabe, A. Thomas, R. Haag, M. Adeli. *Gram-Scale, Metal- and Solvent Mediated Synthesis of Two-dimensional Triazine Heterostructures*, **2019**, submitted.
2. K. H. Tan, S. Sattari, S. Beyranvand, **A. Faghani**, K. Ludwig, K. Schwibbert, C. Böttcher, R. Haag, and M. Adeli, Langmuir, **2019**, *35* (13), 4736–4746. *Thermoresponsive Amphiphilic Functionalization of Thermally Reduced Graphene Oxide to Study Graphene/Bacteria Hydrophobic Interactions*.
3. **A. Faghani**, I. S. Donskyi, M. F. Gholami, B. Ziem, A. Lippitz, W. E. S. Unger, C. Böttcher, J. P. Rabe, R. Haag and M. Adeli, *Angew. Chem. Int. Ed.*, **2017**, *56 (10)*, 2675–2679. *Controlled Covalent Functionalization of Thermally Reduced Graphene Oxide under Mild Conditions as Defined Bifunctional 2D Nanomaterials.*
4. A. Setaro, M. Adeli, M. Glaeske, D. Przyrembel, T. Bisswanger, G. Gordeev, F. Maschietto, **A. Faghani**, B. Paulus, M. Weinelt, R. Arenal, R. Haag, and S. Reich, *Nat. Commun.*, **2017**, *8*, 14281. *Preserving π-conjugation in covalently functionalized carbon nanotubes for optoelectronic applications.*
5. M. Khani, E. Mehdipour, **A. Faghani**, G. Guday, I. S. Donskyi, W. E. S. Unger, R. Haag and Mohsen Adeli, *RSC Adv.*, **2016**, *6*, 115055. *Preparation of graphene oxide by cyanuric chloride as an effective and non-corrosive oxidizing agent.*
6. Z. Beiranvand, A. Kakanejadifard, I. S. Donskyi, **A. Faghani**, Z. Tu, A. Lippitz, P. Sasanpour, F. Maschietto, B. Paulus, W. E. S. Unger, R. Haag and M. Adeli, *RSC Adv.*, **2016**, *6*, 112771. *Functionalization of fullerene at room temperature: toward new carbon vectors with improved physicochemical properties.*

7.2 Curriculum vitae

The CV is not included for personal reasons.